CIRCULATING FLUIDIZED BED HYDRODYNAMICS IN A RISER OF SQUARE CROSS-SECTION

By

Jiahua Zhou

B.A.Sc., Zhejiang University, 1987
M.A.Sc., Zhejiang University, 1989

A THESIS SUBMITTED IN PARTIAL FULFILLMENT OF

THE REQUIREMENTS FOR THE DEGREE OF

DOCTOR OF PHILOSOPHY

in

THE FACULTY OF GRADUATE STUDIES

(Department of Chemical Engineering)

We accept this thesis as conforming

to the required standard

THE UNIVERSITY OF BRITISH COLUMBIA

April 1995

In presenting this thesis in partial fulfilment of the requirements for an advanced degree at the University of British Columbia, I agree that the Library shall make it freely available for reference and study. I further agree that permission for extensive copying of this thesis for scholarly purposes may be granted by the head of my department or by his or her representatives. It is understood that copying or publication of this thesis for financial gain shall not be allowed without my written permission.

(Signature)

Department of CHEMICAL ENGINEERING

The University of British Columbia
Vancouver, Canada

Date JULY 25, 1995

DE-6 (2/88)

Abstract

Hydrodynamic experiments were carried out in a cold-model circulating fluidized bed riser of 146 mm × 146 mm square cross-section and 9.14 m height. Ottawa sand particles of mean diameter 213 μm, particle density 2640 kg/m^3 and loosely packed bed voidage 0.43 were used as the bed material. Fibre optic probes were employed to measure both local time-mean voidage and particle velocity.

A core-annulus flow structure was found to exist in the square riser as for risers of circular cross-section investigated by earlier workers. The voidage generally decreases laterally from the axis towards the wall. However, M-shaped lateral voidage profiles, which can also be distinguished in earlier reported data from circular risers, were found in a number of cases, with voidage first increasing from the wall, reaching a maximum, then decreasing somewhat towards the axis. In the corners, the voidage was lower while the descending particle velocity was higher than for other near-wall locations at the same cross-section. Bimodal and tri-modal probability distributions of particle concentration were found in some cases. The velocity of those particles which are ascending was found to be low at the wall and to increase towards the axis; there was a maximum in the lateral profile of descending particle velocity at a small distance from the wall. The velocity of particle downflow was found to be in the range 0.8 to 1.5 m/s. A theoretical model has been established to predict the velocity of descending clusters near the wall. The model suggests that the aspect ratio of ellipsoidal clusters has only a limited influence on the cluster velocity. The thickness of the outer annular zone first decreased with height until a minimum was reached 3 to 4 m above the distributor, then increased towards the top because net solids mass flux was outward towards the wall near the bottom and inward towards the axis near the top of the column. Significant differences were found between core-annulus boundaries defined as the location of zero vertical solids flux and zero vertical mean particle velocity, with the annulus thickness based on the latter definition being smaller.

Wall roughness, introduced by affixing sand paper to the entire wall surface, was found to lead to an increase in voidage near the wall, while having little influence on the voidage near the axis. More uniform lateral voidage profiles were obtained for the rough-walled riser. Neither bimodal nor trimodal probability distributions of particle concentration were found for the rough-walled column, nor were there any M-shaped voidage profiles. Wall roughness increased the ascending particle velocity somewhat, while having little influence on the descending particle velocity near the wall. In a riser with simulated membrane walls, the valleys formed by the fin and two adjacent membrane tubes protect particles from the gas. Particle streamers near the wall then tend to move downwards in the fin region, leading to higher voidages and increase descending particle velocities than in the crest region or for flat smooth walls. It was found that wall features such as roughness and membrane tubes have significant influence on the gas-solids flow structure near the wall of circulating fluidized bed risers. Little influence of wall roughness and membrane tube could be detected near the axis of the column.

A sampling probe and piezoelectric probe were used to measure lateral solids mass flux and momentum flux. Except at the very bottom of the riser, cross-flow fluxes were always substantially lower than (axial) net circulation fluxes, but high enough to assure considerable interchange between the wall and core regions. Lateral fluxes were highest at the bottom of the riser, relatively constant at intermediate levels, then increased slightly near the top. The solids momentum flux was found to increase with height in the lower part of the column, and then decrease in the upper part. The lateral particle velocity was as high as 2 to 3 m/s on the axis of the riser.

Table of Contents

List of Tables

List of Figures

Acknowledgment

I would like to express my sincere gratitude to my main supervisor, Dr. J.R. Grace for his continuous guidance and support over the entire course of this work. My appreciation also goes to the co-supervisors, Dr. C.H.M. Brereton and C.J. Lim for their ideas, discussion and assistance. I am indebted to Professor S. Qin of the Institute of Chemical Metallurgy, Beijing for his input with respect to instrumentation. Appreciation is expressed to Dr. J.-X. Zhu and Dr. K.S. Lim for their discussion and assistance. The equipment owes a great deal to the Chemical Engineering Workshop and Stores. I also wish to thank everybody in the Fluidization Group for helpful discussions. Financial support from the operating funds of the Natural Sciences and Engineering Research Council of Canada is gratefully acknowledged.

Finally I want to express my appreciation to my wife Yamei for her encouragement and support.

Chapter 1

Introduction

Gas-solid fluidization has been widely investigated in the latter half of this century because of its important role throughout the chemical process industries, as well as in diverse areas such as electrical power generation, food processing, pharmaceuticals manufacture, mineral processing, etc. The beds are useful both as chemical reactors (gas-solid and solid-catalyzed), when gas and solid particles must be brought into contact, and in certain physical processes (e.g. drying of particulate material, coating, quenching).

Particles in fluidization systems for air at atmospheric pressure and temperature were classified by Geldart (1972, 1973) into four groups (A, B, C, and D) depending on their particle size and particle density. Grace (1986) extended Geldart's methods to gases other than air and to pressures and temperature other than atmospheric. Different fluidization regimes, in particular homogeneous, bubbling, turbulent, and fast fluidization have long been recognized and studied.

1.1 Fast Fluidization

This thesis is concerned with the fast fluidization regime, which requires that the superficial gas velocity, U_g, be greater than the transport velocity, U_{TR} (Bi, 1994). Beyond fast fluidization, there is dilute pneumatic transport at even higher superficial gas velocities. For fast fluidization and pneumatic transport, to keep the system operating, continuous feeding of particles is necessary to replace particles being carried out of the system rapidly by the high-velocity gas.

Yerushalmi et al. (1976) were the first to use the term "fast fluidization" to indicate a regime between turbulent fluidization and pneumatic transport. The onset of fast fluidization was

defined as the point above which bed density becomes strongly dependent on solids feed rate. This is shown in Figs 1.1 and 1.2. Yerushalmi and Cankurt (1979), as illustrated in Fig. 1.3, described the transport velocity as a superficial gas velocity below which a sharp change in pressure gradient (or choking) occurs. They further defined fast fluidization as the regime above the minimum transport velocity for any solid circulation rate as indicated in Figs 1.4 and 1.5. However, Rhodes and Geldart (1986) and Schnitzlein and Weinstein (1988) could not identify a transport velocity in their systems. Kato et al. (1992) reported that the transport velocity varies greatly with the design of apparatus. These conflicting reports on the transport velocity indicate that the transition to the fast fluidization regime is not well understood.

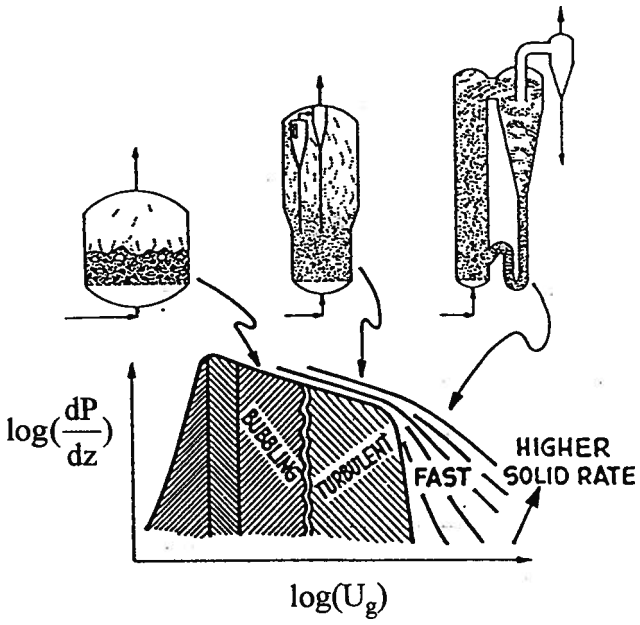

Fig. 1.1 Fluidization phase diagram for a fine powder, showing schematic diagrams of equipment suitable for the bubbling, turbulent and fast fluidization regimes (Yerushalmi et al., 1976).

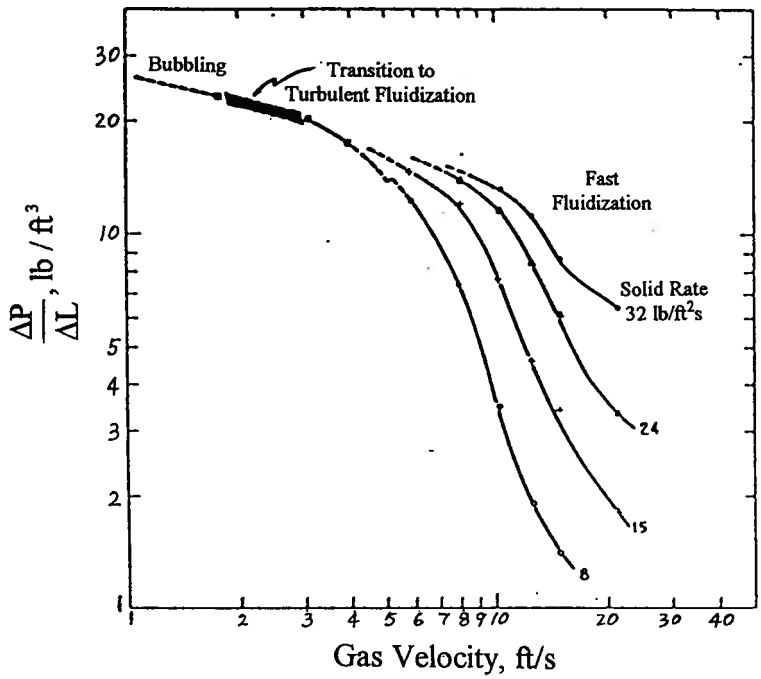

Fig. 1.2. Phase diagram showing fluidization regime for fluid cracking catalyst (Yerushalmi et al., 1976).

A "fast fluidized bed" (termed circulating fluidized bed in this thesis) has been described (Yerushalmi et al, 1976) as a dense entrained suspension characterized by an aggregative state in which many of the solid particles are segregated in relatively large, densely packed clusters and strands. The particle aggregation was used to explain the ability to operate with high relative gas-solids slip velocities, often much higher than single particle terminal velocities. Grace and Tuot (1979) explained the formation of the clusters and strands in terms of flow instability. Arena et al. (1989) described flow instability as the reason for clusters in circulating fluidized bed risers.

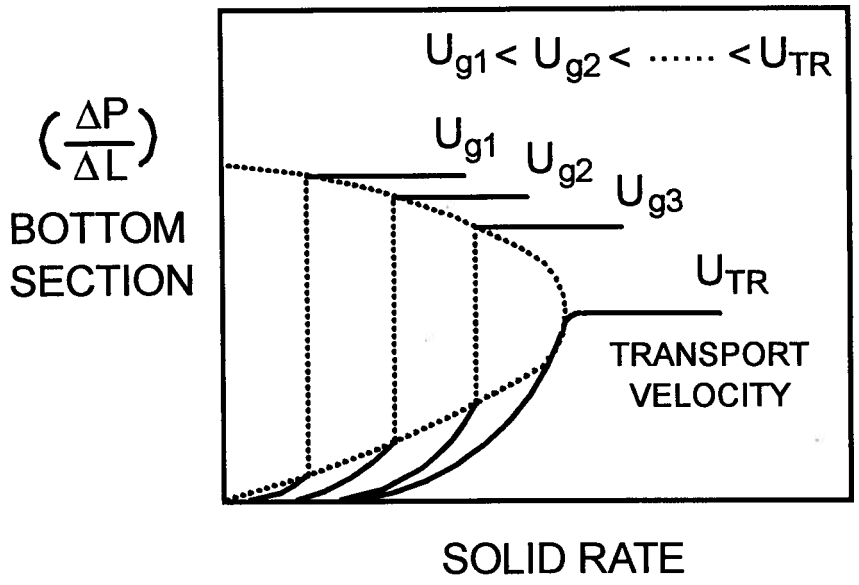

(a)

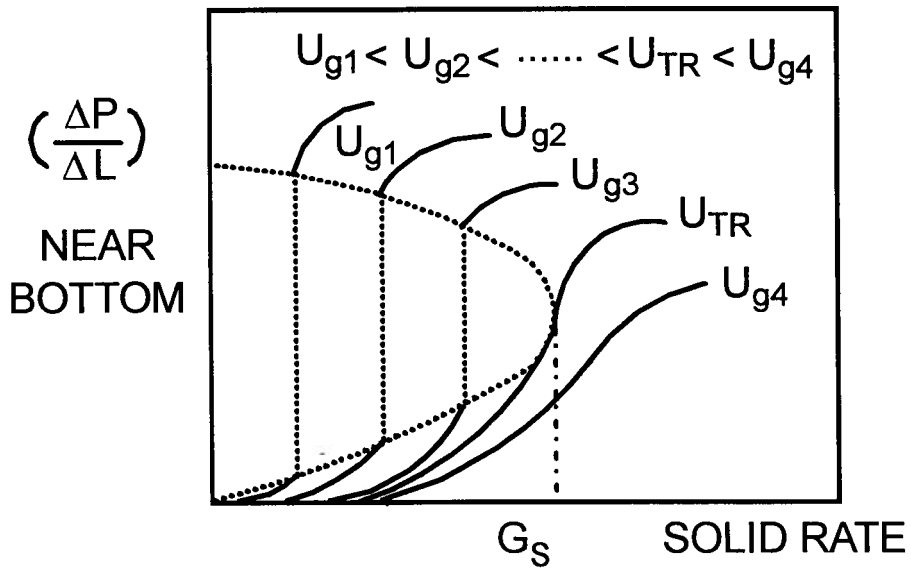

(b)

Fig. 1.3. Qualitative representation of pressure gradients measured in a modified 152 mm diameter system by Yerushalmi and Cankurt (1979).
(a) across the bottom section (609 mm in height).
(b) between pressure taps at heights of 609 mm and 2286 mm above the bottom of the riser.

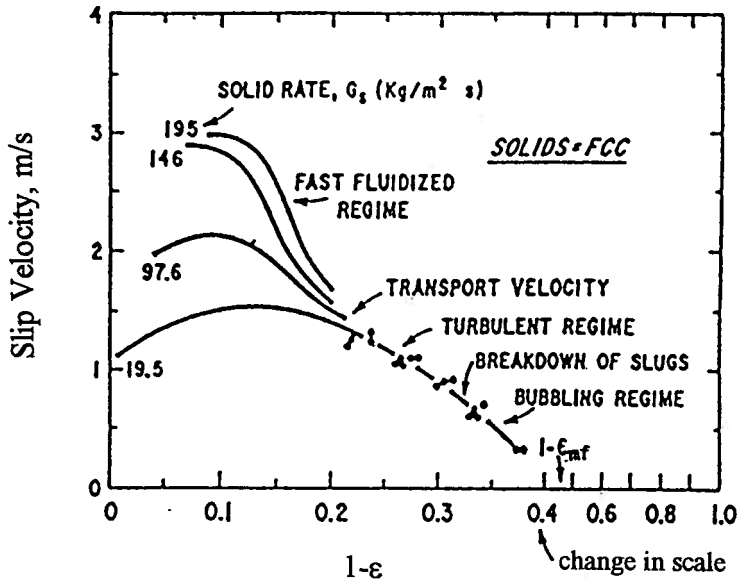

Fig. 1.4. Fluidization data for a fluid cracking catalyst: slip velocity vs. solid concentration obtained in a 152 mm i.d. riser (Yerushalmi & Cankurt, 1979).

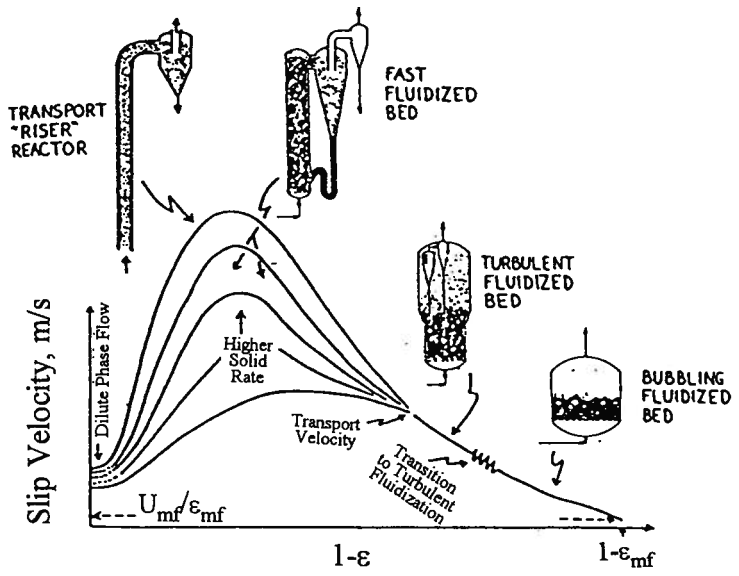

Fig. 1.5. Qualitative fluidization map for fine solids due to Yerushalmi & Cankurt (1979).

Since 1980, many flow regime diagrams for fast fluidization have been proposed, and there have been various definitions of fast fluidization (Li and Kwauk; 1980, Yang, 1983; Takeuechi et al., 1986;. Grace 1986; Karri and Knowlton, 1990; Perales et al., 1990). Here just two are introduced. As shown in Fig. 1.6, Grace (1986) indicated various regimes in which current industrial gas-solid reactors operate. From the diagram, one can see a region in which circulating fluidized beds usually operate. The boundaries shown in Fig. 1.6 are not intended to correspond fully to flow regime boundaries. When more experimental data are available, the diagram can be further expanded in the future.

Although many flow regime diagrams have been proposed, fast fluidization has not been consistently defined because the mechanism of the transition from other regimes to fast fluidization has not been fully clarified. In this thesis no attempt is made to account for the transition between flow regimes. This is the subject of a parallel study (Bi, 1994). Our goal here is to try to provide systematic and complete information on the flow structure in a circulating fluidized bed.

The term circulating fluidized bed (CFB) was first proposed by Reh in 1971. Fast fluidization is usually the flow regime in which CFB risers are operated. A CFB system consists of a riser in which solid particles are suspended in the air flow, a gas-solids separator, and a solids recycling system to return solid particles from the separator back to the base of the riser.

In the last two decades, CFBs, having been accepted worldwide as an advanced technology for combustion and other chemical reactions, have developed quickly because of many advantages. For example, in circulating fluidized bed combustion (CFBC) systems, the primary advantages are:

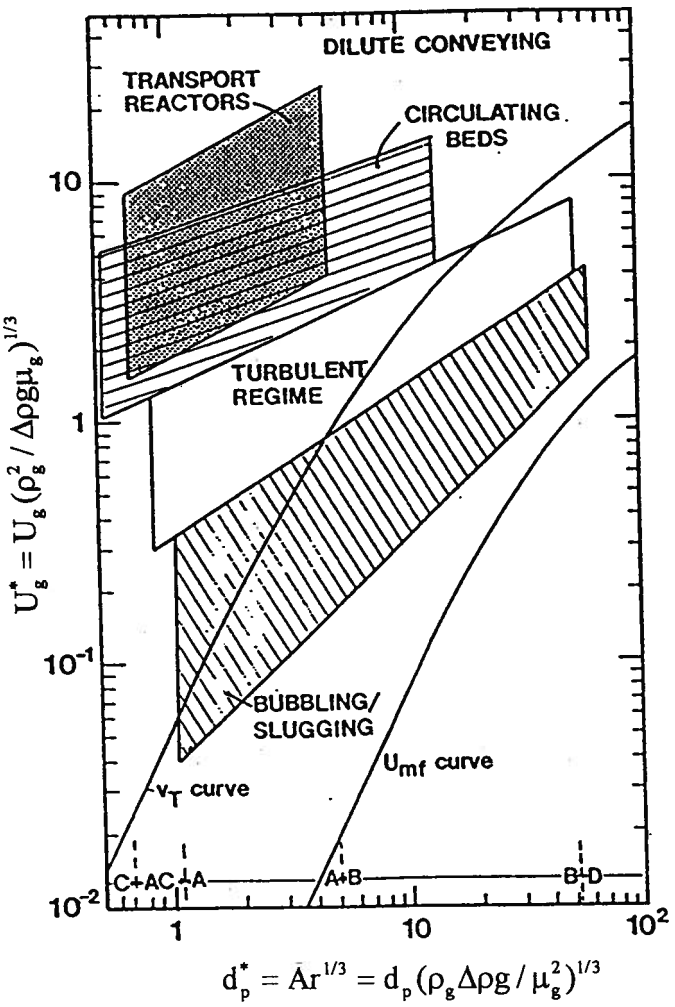

Fig. 1.6. Fluidization regime map showing practical operating regions of the various hydrodynamic regime Grace (1986). Approximate boundaries between the different powder groups proposed by Geldart are shown at the bottom (Grace, 1990).

1. Improved fuel combustion efficiency because of the recirculation of incompletely burned fuel particles to the reaction chamber.

2. Low SO_X emissions due to in situ sulphur capture by limestone or dolomite and the reutilization of fine sorbent particles which are collected by the gas-solids separators and returned to the riser.

3. Low NO_X emissions due to the staged introduction of primary and secondary air and relatively low combustion temperatures.

4. Good turndown ratio because suspension density can be varied readily by controlling solids circulation rate, allowing the suspension-to-wall heat transfer coefficient to be changed.

5. Good gas-solids contacting and favourable heat and mass transfer.

Because of their advantages, CFB reactors have also been employed in other industrial applications such as gasification, ore roasting, calcination, and fluid catalytic cracking (FCC). In 1992, over 250 FCC units were processing one quarter of the world's crude oil production and by the end of 1995 some 400 CFB combustion units with a total thermal power of 23,000 MW will be in operation (Werther, 1993).

1.2 Scope of work

Most CFB fundamental studies on such subjects as hydrodynamics and heat and mass transfer have been for idealized conditions far removed from those employed in industrial applications. Although many applications, especially CFB combustors, involve risers of rectangular cross-section, almost all available hydrodynamic data are from risers of circular cross-section; hence corner effects have been ignored. Different, even contradictory, phenomena have

been reported. There is also a lack of reliable hydrodynamic data on some subjects, especially on the flow near the wall and solids lateral cross-flow. The lack of reliable experimental data leads to difficulties and poor accuracy in modelling hydrodynamics and heat and mass transfer in CFB risers. Therefore, comprehensive experiments are needed to investigate systematically CFB hydrodynamics and, in particular, to provide as complete data as possible on various measures. Better and more complete data on hydrodynamics can improve CFB design and operation, as well as providing a knowledge base for CFB scale-up.

This work investigates hydrodynamics in a CFB riser of square cross-section. The study involves measurements of local particle concentration, particle velocity and cross-flow fluxes, including both solids mass flux and momentum flux, all for the same experimental conditions, using recently developed measurement techniques. The influence of the corners on hydrodynamics, showing the difference between risers of square and circular cross-sections, is examined. The influences of wall roughness and membrane walls are also investigated to provide an even more comprehensive treatment. Operating conditions similar to those in commercial units (except for temperature and scale) were chosen. The purpose of this project is not to study the scaling rules for CFB, but to provide a comprehensive basis for both modelling and scale-up.

Chapter 2 describes in detail the equipment in which most of the experimental work was carried out. Since most of this work was experimental, measurement techniques are key to the success of this work. In Chapter 2, the criteria for selection of instrumentation are also introduced. To make the thesis more readable, detailed information on instrumentation is given separately in the chapter where the specific technique is utilized.

In Chapters 3 and 4, before showing experimental results on local particle concentration and particle velocity profiles respectively, previous work is reviewed on the specific topics to provide the background for the work, followed by a detailed description of the fibre optic probes

used to measure particle concentration and particle velocity and their calibration. Measurements of particle concentration and particle velocity provide not only information on particle flow near the corners, but also on the configuration of the boundary between core and annulus. The influence of operating conditions, in particular superficial gas velocity and solids circulation rate, on hydrodynamics is discussed in the light of the experimental results. Comparisons are also made between our experimental results and those from earlier studies.

Chapters 5 and 6 discuss respectively the influence of wall roughness and membrane walls on the basic profiles, i.e. particle concentration and particle velocity profiles in the CFB riser. Sand-paper attached to the walls was used to simulate rough walls. Plexiglass half-round rods were affixed to the inside surface of the riser to simulate membrane walls. Solids flow near both the crest and the fin area is investigated.

A detailed study of solids cross-flow is presented in Chapter 7. Lateral solids mass flux was measured by a solids sampling probe. Both the direction and the magnitude of the cross-flow mass flux are obtained. A piezoelectric probe has been developed and calibrated to measure the horizontal component of lateral solids momentum flux. Lateral particle velocity at the axis of the riser is estimated by dividing the lateral solids momentum flux by the lateral solids mass flux. Combining information on solids cross-flow with the results from Chapters 3, 4 and 7 allows solids flow in the CFB riser to be mapped.

Conclusions of this work are provided in Chapter 8 together with recommendations for future investigation in the field of CFB hydrodynamics.

Chapter 2

Experimental Set-up

2.1 Apparatus

To investigate the influence of column configuration on hydrodynamics, a new riser of square cross-section was designed and installed beside the one with circular cross-section used by Brereton (1987) to study the hydrodynamics in a CFB riser. Design criteria and constraints provided by Brereton (1987) were carefully considered. No change was made to the solids separation and recirculation systems used by Brereton (1987). The CFB system, illustrated in Fig. 2.1, consists of the riser, two cyclones, a standpipe for storing recirculating solids and an L-valve to feed solids back into the riser.

The column is constructed of carbon steel with wall thickness of 1/8" (3 mm), giving an inside cross-sectional area of 146 mm × 146 mm. The riser is made of seven sections of heights 610, 610, 1219, 2438, 2438, 1219, 610 mm, respectively from bottom to top, giving a total height of 9.14 m. Sections are connected to each other by flanges. Rubber gaskets are used between flanges for sealing. Smooth connections were assured. The length of the solids recirculation system was adjusted to fit the new riser, since the previous (152 mm diameter) circular cross-section riser used by Brereton was 9.3 m tall.

Pairs of plexiglass windows, 4" (102 mm) in width, are mounted on facing surfaces for visual observation. The windows are 20" (508 mm) high in the two bottom sections and one top section, while the height of the windows in the other sections is 32" (813 mm). The plexiglass

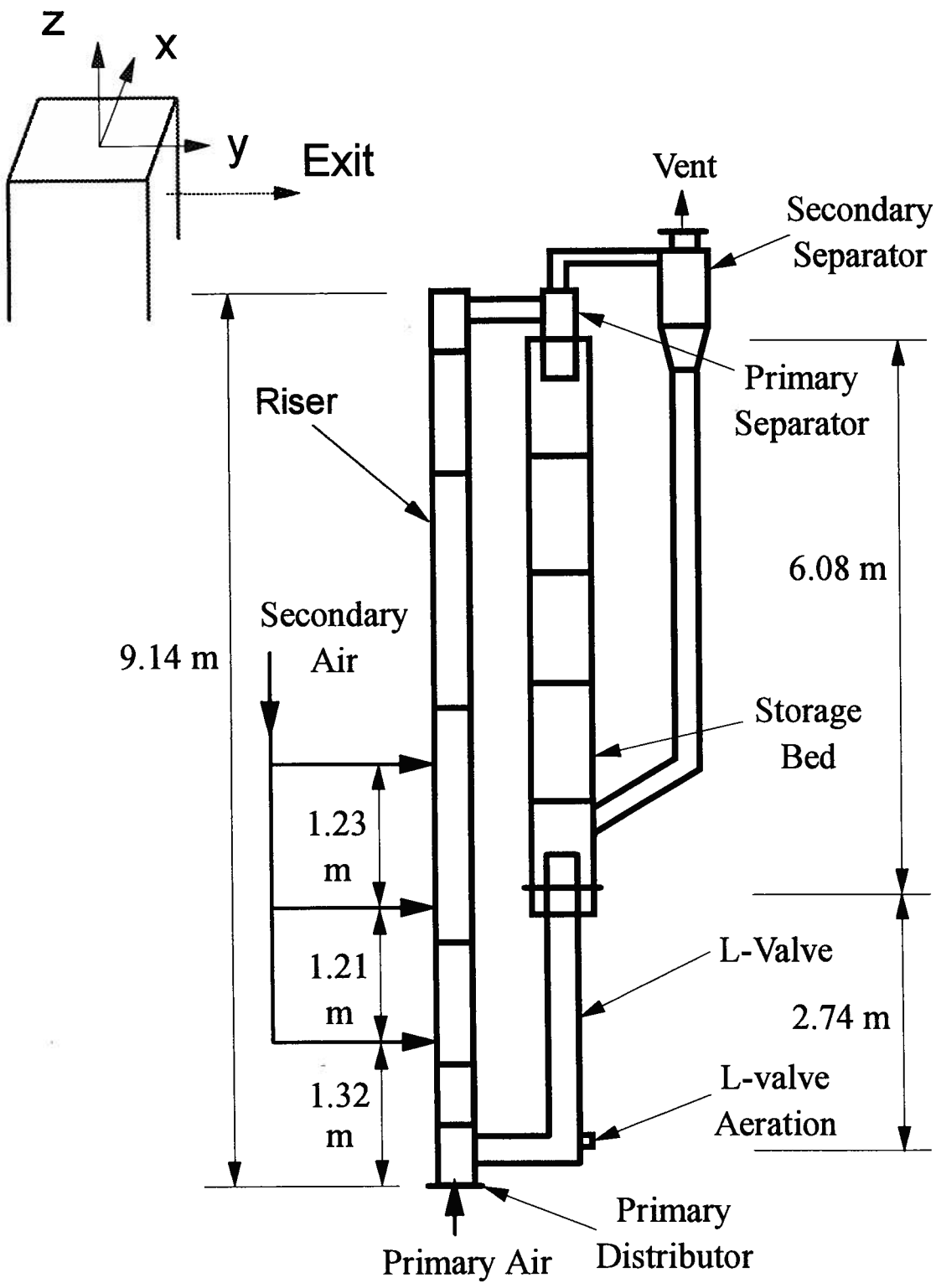

Fig. 2.1. Schematic of the circulating fluidized bed system.

windows were specially designed to ensure a smooth inside surface, because roughness may affect the hydrodynamics in the riser. There are measuring ports of inside diameter 1.5" (38 mm) and thickness 1/4" (6.4 mm) on some of the windows which can be mounted to sections of different height. Pressure taps of diameter 12.7 mm (0.5") and measurement ports of diameter 38 mm (1.5") are fixed to the two facing steel walls of each section.

Air is provided through a 3" (76.2 mm) pipe by a 0.15 m^3/s, 34 kPa Sutorbuilt blower, model 7HV (Brereton, 1987), to the windbox at the base of the column. The blower air enters the riser through a multi-orifice distributor of 17% free area with 196 holes of 4.76 mm (3/16") diameter and 9.53 mm (3/8") pitch. The superficial gas velocity was measured with an orifice meter. The highest superficial gas velocity in the experiments was 8 m/s. Secondary air can be introduced into the riser through two pairs (four ports at each level) of directly opposed ports of 38 mm (1.5") diameter located 1320, 2530 and/or 3760 mm above the distributor on all four walls for possible future study of the influence of secondary air injection on CFB hydrodynamics. However, no secondary air was employed in this study.

At the top of the column, entrained solids are carried by the gas from the riser through a 102 mm (4") ID horizontal pipe into the primary cyclone, where most of the particles are captured and fall into the standpipe for recirculation. Most fine particles not captured by the primary cyclone are removed by a secondary cyclone and returned to the standpipe. Air leaving the secondary cyclone is vented outside the building. A butterfly valve was installed in the standpipe to measure the solids circulation rate. A detailed description of the standpipe and both the primary and the secondary cyclones is provided by Burkell (1986) and Brereton (1987).

Solids in the standpipe enter the vessel from the L-valve through a 146 mm ID pipe centered 114 mm (4.5") above the distributor. The solids circulation rate is controlled by varying the flow of air supplied to the L-valve. Aeration was applied to the L-valve at two points, one

located at the axis and the other 121 mm above the axis of the horizontal section to achieve a wide range of solids circulation rates. Rotameters are used to monitor the air flowrates. Pressure regulators are employed to stabilize the aeration flow rates, because the solids circulation rate is very sensitive to the pressure and flowrate of air supplied to the L-valve.

The time-of-descent technique (Burkell, 1986; Burkell et al., 1988) was employed to measure the solids circulation rate, defined here in terms of the amount of solids returned to the riser. This method involves measuring the time for identifiable particles to descend through a known distance in a transparent section of a smooth-walled standpipe through which the solids return in moving packed bed flow. Thus the solids circulation rate can be obtained from

$$G_s = \frac{L_i \rho_{bulk} A_l}{t_i A_t} \tag{2.1}$$

where A_l is the cross-sectional area of the standpipe in which the identified particles are descending, A_t is the cross-sectional area of the riser, L_i is the known distance, t is the time for the identified particles to traverse the known distance, and ρ_{bulk} is the loosely packed particle density. The technique was compared with the butterfly valve method by Burkell et al. (1988) and agreement from the two techniques was generally good providing the location of the descent measurements was properly chosen.

2.2 Particles

Ottawa sand of surface-to-volume mean diameter 213 μm, particle density 2640 kg/m^3 and loosely packed bed voidage 0.43 was used as the bed material. This sand has a minimum fluidization velocity of 0.048 m/s (Grace, 1982) and a terminal velocity of 1.41 m/s. The particle size distribution from a sieve analysis is provided in Table 2.1.

Table 2.1. Size distribution of sand particles.

Diameter (μm)	Weight percentage (%)
0-38	0.03
38-53	0.02
53-75	0.10
75-90	0.56
90-106	1.20
106-125	2.72
125-212	46.19
212-250	22.65
250-300	16.83
300-355	6.47
355-425	2.65
425-600	0.59

2.3 CFB System Operation

For safety purposes, operating procedures for start-up and shut-down were established as follows:

Procedures for start-up:

1. Open compressor bypass.

2. Start compressor.
3. Fully open valve on the primary air line.
4. Gradually close the valve on the bypass line until desired superficial gas velocity is reached.
5. Start feeding solids from the storage standpipe to the riser by turning on aeration to the L-valve until the desired solids circulation rate is reached.
6. Adjust both superficial gas velocity and solids circulation rate until the desired operating condition is reached.

While waiting for steady state conditions to be achieved (usually requiring around 20 minutes), the system needs checking from the bottom to the top to make sure that there are no problems.

Procedures for shut-down:

1. Terminate solids circulation by shutting off aeration to the L-valve.
2. After the riser is emptied, open the valve on the bypass line.
3. Stop the compressor.

2.4 Selection of Instrumentation

The selection of a particular measuring method depends on specific data requirements, bed structure, cost, environment and accessibility for sensor installation. Each of the techniques has certain limitations. Some of the methods require further laboratory-scale evaluations. Each technique must be assessed based on the requirements of the intended study and anticipated particle size, range, concentration and velocities.

After considering these factors, fiber optic probes, described in greater detail in Chapter 3 and 4, were chosen to measure particle velocity in this study. With this technique, measurement of local particle concentration and particle velocity with high accuracy can be conducted either at the wall or inside the riser. The probes can be used both in the bottom region of the riser where particle concentration is high and in the upper dilute region.

U-tube manometers are used to measure pressure profiles along the height of the riser. They provide reliable readings of pressure drops in the circulating fluidized bed. A sampling probe and a piezo-electric probe have been developed to measure solids cross-flow mass flux and momentum flux respectively. They are simple in principle and straightforward to use.

A detailed description of each measurement technique and its calibration is given in the chapter where the corresponding measurements are presented.

Chapter 3

Voidage Profiles

3.1 Introduction

Both radial and axial voidage profiles have been widely studied in CFBs during the last decade. It was recognized in early studies of CFB hydrodynamics that there are axial variations in voidage, with a relatively dense region near the solids re-entry point located near the bottom of the riser (Yerushalmi et al., 1978). Li and Kwauk (1980), using a needle-type capacitance probe, found an S-shaped axial voidage profile with an inflection point which could serve to delineate a dense phase at lower positions and a dilute phase in the upper portion of the riser. Hartge et al. (1986) measured the vertical voidage profile with pressure transducers, a needle capacitance probe, and fiber optic probes. Their results can be well described by an S-shaped voidage profile. Schnitzlein and Weinstein (1988), Cen et al. (1988), and Li et al. (1988) confirmed this shape of profile.

S-shaped voidage profiles are, however, not always found (Bai et al., 1992; Brereton and Stromberg, 1986; Rhodes and Geldart, 1986; Li et al., 1988). The exit configuration, solids inventory, gas velocity and particle circulation rate are key factors that may change the shape of the voidage profile along the riser. An exponential decay function was found to be able to represent the axial profiles voidage throughout the riser from the bottom to the top by Arena et al. (1986) who obtained a simple exponential distribution from direct voidage measurements, while an S-shaped distribution was obtained from pressure drop signals neglecting solids acceleration.

Brereton (1987) proposed that S-shape solids concentration profiles exist for relatively high solids circulation rate, while profiles represented by an exponential decay function occur for

low solids circulation rates. Bai et al. (1992) concluded that exponential axial voidage profiles exist for normal CFBs. When a very weakly restrictive entrance structure is present, the profiles have an S-shape. This conclusion is similar to that of Brereton (1987), because the tendency to be "restrictive" is measured by the ability to achieve high solids circulation rates.

The exit structure was found by Brereton and Stromberg (1986) to influence the axial voidage profile in CFB risers. In a riser with an abrupt exit, a C-shape axial voidage distribution was found with low voidage at both the bottom and the top of the column and high voidage in the middle. This was confirmed by Jin et al. (1988). Different means of measurement and different column configurations used by different authors may also be responsible for the discrepancies.

The radial variation of particle concentration in a circulating fluidized bed was first determined by Gajdos and Bierl (1978) who employed local solids flux probes and X-rays. They found a lean core surrounded by a relative dense annulus. With an X-ray source and a chordal absorptometer, Weinstein et al. (1986) confirmed this structure. A core-annulus distribution of particle concentration was also confirmed by Dry (1986) using a small heat pulse as a tracer, by Brereton (1987) with a capacitance probe, and by Horio et al. (1988) and Hartge et al. (1988) with fiber optic probes.

These results clearly indicate the existence of a core-annulus flow structure with very significant radial concentration gradients and with the boundary between core and annulus not clearly defined. Various core/annulus two-zone models have been employed to describe circulating fluidized beds. Bader et al. (1988) defined the core-annulus distribution in terms of a low density, high velocity gas-solids core surrounded by a slow-moving, high solids density annular region. Brereton et al. (1987) proposed a core-annulus model in which gas is assumed to travel rapidly upwards in the core, while gas either moves upwards much more slowly or is pulled

downwards in the outer annular region. A similar assumption was also made by other workers, e.g. Bolton and Davidson (1988), Berruti and Kalogerakis (1989) and Rhodes (1990).

Brereton and Grace (1993) introduced an intermittency index to compare the two-phase nature of flow in circulating fluidized beds. Their study indicates that neither perfect cluster flow nor perfect core-annulus flow exists in CFB risers. The flow structure tends to change with height, with cluster-like structures more common near the bottom of the riser, and a core-annulus structure more predominant towards the top. Some clusters or strands exist in the center of the riser, even at low solids concentration (Brereton and Stromberg, 1986; Horio et al., 1988).

Solids concentration profiles depend not only on primary and secondary gas flow rates and the solids circulation rate (Yerushalmi and Cankurt, 1979; Li and Kwauk, 1980; Brereton, 1987) but also on the properties of the particles (Weinstein et al., 1984). The geometry of the riser has also been found to have considerable influence on the hydrodynamics of circulating fluidized beds (Brereton and Stromberg, 1986; Jin et al., 1988; Schnitzlein and Weinstein, 1988; Wu et al., 1990; Brereton and Grace, 1994).

Almost all previous cold-model hydrodynamic research has been carried out on risers of circular cross-section. However, risers of square and rectangular cross-sections are widely employed in CFB applications such as combustion. In these risers, the corners are expected to have considerable influence on both lateral and axial voidage profiles. This chapter presents both lateral and axial profiles of voidage in a cold model circulating fluidized bed riser of a square cross-section.

3.2 Instrumentation

Various techniques have been used to measure voidage in fluidized beds. The three most popular techniques, i.e. X-ray or γ-ray transmission, capacitance probes and optical fibre probes, are briefly reviewed here.

An X-ray technique was used by Weinstein et al. (1986) in a circulating fluidized bed to obtain bed voidage profiles. X-ray and/or γ-ray transmission techniques have been used for many years in conventional fluidized beds to detect bubbles and to measure bed voidage (e.g. Baumgarten and Pigford, 1960; Rowe and Partridge, 1965). A radioactive source emits a beam of X-rays or γ-rays across the vessel through its walls to the detector. The detector consists of a Geiger counter that produces an electrical impulse in response to each photon passing through the tube reaching the detector. These pulses are integrated and transformed into a DC signal proportional to the radiation received at the counter. In the case of a fluidized bed, the concentration of particles along a chord is detected by the attenuation of the measured X-ray or γ-ray signal.

Significant differences in electrical properties such as capacitance between air and a packed bed of solid particles provide the basis for electrical properties measurement techniques. Local measurements of capacitance are related to the local state of the fluidized bed. Hartge et al. (1985) traversed a needle probe through a circulating fluidized bed riser and correlated the resulting capacitance with voidage.

Capacitance probes have been employed often because they work well with nonconducting materials. For example, Brereton and Stromberg (1985) measured radial voidage profiles in a circulating fluidized bed using a needle capacitance probe. Various probe configurations have been used, ranging from parallel plates to needle-shaped probes. Probe

configuration is an important consideration, as different geometries have varying responses. Also, the geometry can alter local flow conditions. Hence, configurations are required which minimize disturbances.

The basic mechanism of a capacitance probe is very simple. The capacitance of a solid medium differs markedly from that of a gas. Therefore, changes of void fraction in the zone where the probe is located create changes in the dielectric constant, which in turn alter the system capacitance. A capacitance probe can provide a measure of local changes in instantaneous values of particle concentration. A capacitance measuring system can be capable of responding at frequency of up to about 100 kHz (Brereton, 1987). The technique can also be used for high temperature and high pressure systems. However, a capacitance probe needs calibration for different bed materials and is not applicable for conductive bed materials. Also, the measuring volume of the probe is not precisely defined. Another disadvantage is the sensitivity of capacitance measurements to moisture, which changes the dielectric constant and thus alters the capacitance.

3.2.1 Fundamentals of Fibre Optic Probes

Fiber optic probes can be used to measure both voidage and particle velocity in circulating fluidized beds. This technique has the advantages of simplicity, high accuracy and potential low cost. Thus it is widely used for the study of hydrodynamics in fluidized beds. Some examples are summarised in Table 2.1.

Krohn (1982) divided fiber optic sensors into two basic classifications. First, for what is referred to as an intrinsic fiber optic sensor, the transmission of the fiber is directly affected by the physical phenomena being sensed. The second classification is for fiber optic position sensors

Table 3.1. Examples of fibre optic probes used to measure voidage and particle velocity.

Worker	Bed Type	Bed Material	d_p (mm)	U_g (m/s)	G_s (kg/m^{2}s)	ρ_s (kg/m^3)	Measuring Parameter
Patrose et al. et al. (1982)	Fluidized bed	Glass Beads	0.2-0.7			2.47	v_p
Randelman et al. (1983)	Spouted Bed	Glass Spheres	0.95	0.328			v_p
Nakajima (1990)	Turbulent Bed	FCC, Silica Sand	0.064 0.087	0.13-1.33 0.27-1.59		880 1200	Bubble Fraction
Kato et al. (1990)	CFB	FCC	0.74	2.4, 3.0, 4.0		1770	Bed Voidage
Reh et al. (1990)	Fluidized Bed	Glass Beads, Alumina Particles	0.04-0.08 0-0.11				Bed Voidage
Bai et al (1991)	CFB	FCC	0.059	2-3	30-180	1545	v_p & Bed Voidage
Morooka et al. (1990)	Fluidized Bed	FCC	0.065-0.068	0.15-5.0		960-1110	v_p & Bed Voidage
Ishii et al. (1990)	CFB	FCC, FCC	0.0613 0.0464	0.8, 1.2 0.4, 0.6	8 4	1780 1780	v_p & Bed Voidage
Rhodes et al. (1990)	CFB	Aluminum Trihydride Powder	0.07	2-5	8-80	2430	v_p & Bed Voidage
Nowak et al. (1990)	CFB	98% FCC + 2% Alumina	0.046 3	6-10	4.3-34	2300	v_p & Bed Voidage
Kojima et al. (1989)	CFB	FCC	0.06	0.5-2		1000	v_p
Horio et al. (1988)	CFB	FCC	0.06	1.1-1.3		1000	Cluster Velocity & Voidage
Hartge et al. (1988)	CFB	Bed Ash, FCC	0.12 0.085	3.8-5.4 1.2-5.4	27-70 7-70		v_p & Bed Voidage

which transit position change in a device (transducer) that is sensitive to physical property changes. Five types of sensors with different working principles — intensity modulated, transmissive, reflective, micro bending and intrinsic concepts — are in common use. To measure local voidages and particle velocities in circulating fluidized beds in this work, the reflective concept is used.

Reflective fiber optic sensors are excellent position sensors. The configuration is shown in Fig. 3.1. The sensor consists of two bundles of fibers, one of which transmits light to a reflecting target, while the other bundle traps reflected light and transmits it to a detector. The intensity of the detected light depends on how far the reflecting target is from the fiber optic probe (Krohn, 1982).

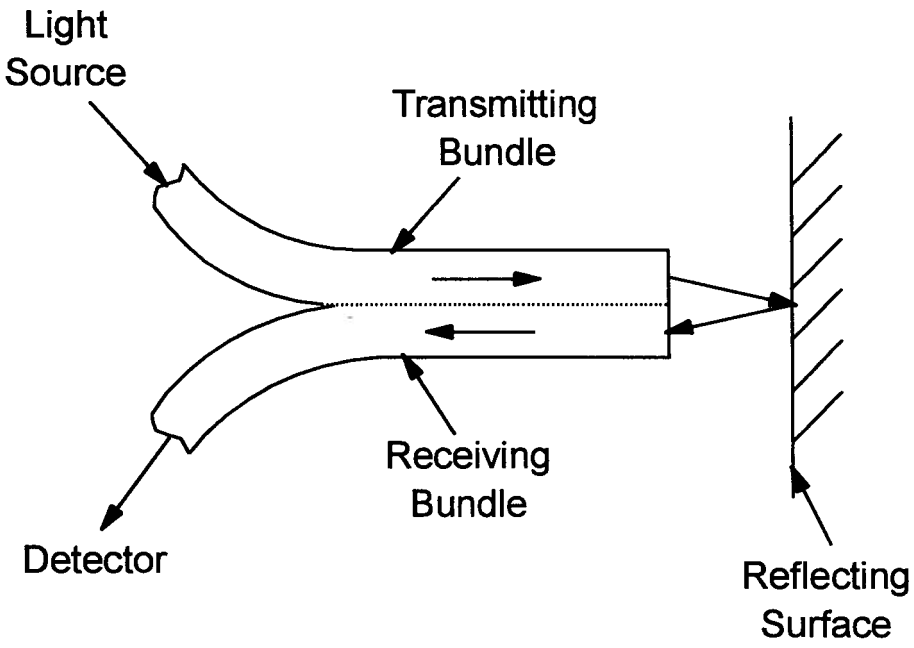

Fig. 3.1 Configuration of reflective fibre probe.

In fiber optic measuring systems, stable illumination light sources are needed to ensure accurate measurements. Several illumination light sources have been used. Oki et al. (1975) used a tungsten lamp as a light source, while Patrose and Caram (1982), Hartge et al. (1988), Nakajima et al. (1990) employed lasers. Kojima et al. (1989) and Nowak et al. (1990) used mercury lamps to produce ultraviolet light as their light source. A quartz lamp was utilized by Randelman et al. (1983), while Matsuno et al. (1983) employed an incandescent electric lamp and a halogen lamp as light sources.

3.2.2 System and Principle

A fiber optic probe system used to measure bed voidage consists of a light source, optical fibers, a photomultiplier, voltage integrator, data recorder, A/D converter and computer. Two bundles of fibers are used. One carries light from the light source and projects it onto a swarm of particles. The other transmits light reflected by the particles to a photo-multiplier where light signals are converted to electrical signals with the voltage output proportional to the intensity of reflected light. There are usually two ways to measure particle concentration, depending on the method of signal treatment after the light-receiver according to Matsuno et al. (1983). Figure 3.2. shows the difference between these two methods.

(1) When the particle diameter is smaller than the core diameter of the optic fiber, type I treatment is applied. In this case, the output signals of pulses generated by all the particles existing within a dotted circle in Fig. 3.2 are integrated. The integrated value of voltage from the voltage integrator is transmitted to a computer by an A/D converter. The integrated values of voltage can be correlated with the concentration of particles using a calibration. In this method, a swarm of particles is detected rather than single particles, so that instantaneous concentrations can be measured.

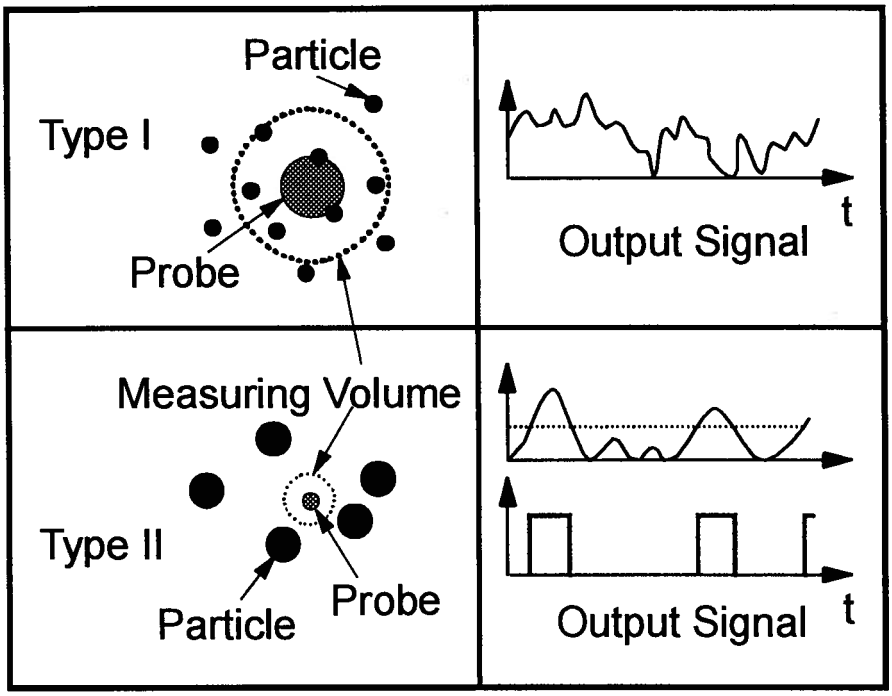

Fig. 3.2 Type I: Detection of swarm of particles;
Type II: Detection of a single particle (Matsuno et al., 1983)

(2) When the particle diameter is greater than the core diameter of the optic fiber, type II treatment is used. In this case, a single particle is detected by the optic fiber probe. The output signals from the light receiver are converted to the pulse at any threshold level V_s. Therefore, the pulse count corresponds to the number of particles. Using this method, particle velocity should be known to convert the number of particles in a time interval to particle concentration. Thus this method requires a long time to measure particle concentration with high accuracy, and only average concentrations can be measured.

In this work, the former method is employed. The fiber optic probe system, similar to that described by Qin and Liu (1982), includes a light source, optical fibers, a photomultiplier, an A/D converter and a computer. Quartz fibers are used, each with a diameter of 0.015 mm. The outside diameter of the probe is 3 mm. The duration of each measurement was 60 seconds at a sampling frequency of 483 Hz. For each experimental point, at least four 60 s measurements were usually taken to obtain an average value.

The size of the measuring volume depends on the local voidage. Tests, gradually approaching the tip of the fibre optic voidage probe with a small piece of stainless steel plate in a calibration beaker described latter, indicated that the measuring distance was approximately 7 mm for ε approaching 1 and about 4 mm for ε=0.9. It was clearly less than 4 mm in the wall region where voidage changes most rapidly.

3.2.3 Calibration Method

As no method for direct conversion of integrated electric signals to particle concentration exists, the system must first be calibrated. Two calibration methods are available:

(1). Matsuno et al. (1983) used the system shown in Fig. 3.3 to calibrate their optical fiber. Particles from a sieve were made to fall uniformly by vibrating the sieve. The particle concentration in the zone where particle terminal velocity is achieved can be calculated by:

$$C_p = \frac{\Delta W}{A_s v_T \Delta t} \tag{3.1}$$

where ΔW is the cumulative weight of particles passing through the cross-sectional area A_s within time interval Δt, and v_T is the terminal velocity of the particles. The optical fiber was set far

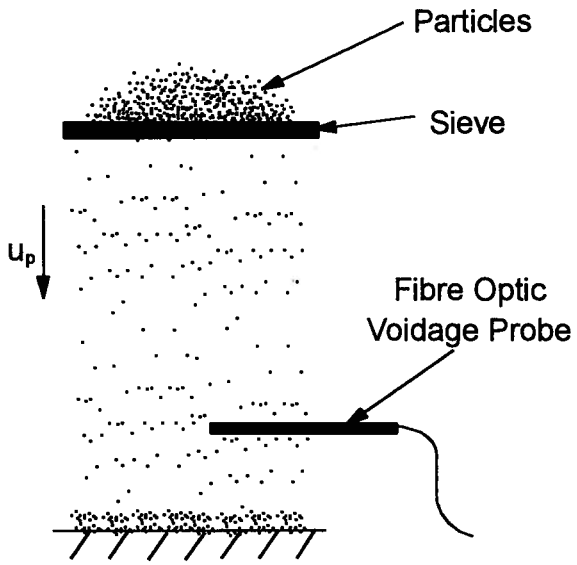

Fig. 3.3. Calibration method for fibre optic voidage probe employed by Matsuno et al, 1983.

enough below the sieve so that the particle terminal velocity was achieved. The integration time was set at two-second intervals. Four types of glass beads of average diameter 56.5 μm and density 2520 kg/m^3 were used. Fig. 3.4 shows that the calibration curve was approximately linear. Scatter was said to be due to the manual vibration of the sieve. The particle size distribution may also be responsible for some data scatter, because the terminal velocities are different. Another systematic error of this method comes from the application of single-particle terminal velocity in Equation (3.1). Matsen (1982) demonstrates that the terminal velocity of particles for particle concentration of 1% can be as much as twice the terminal velocity of single particles.

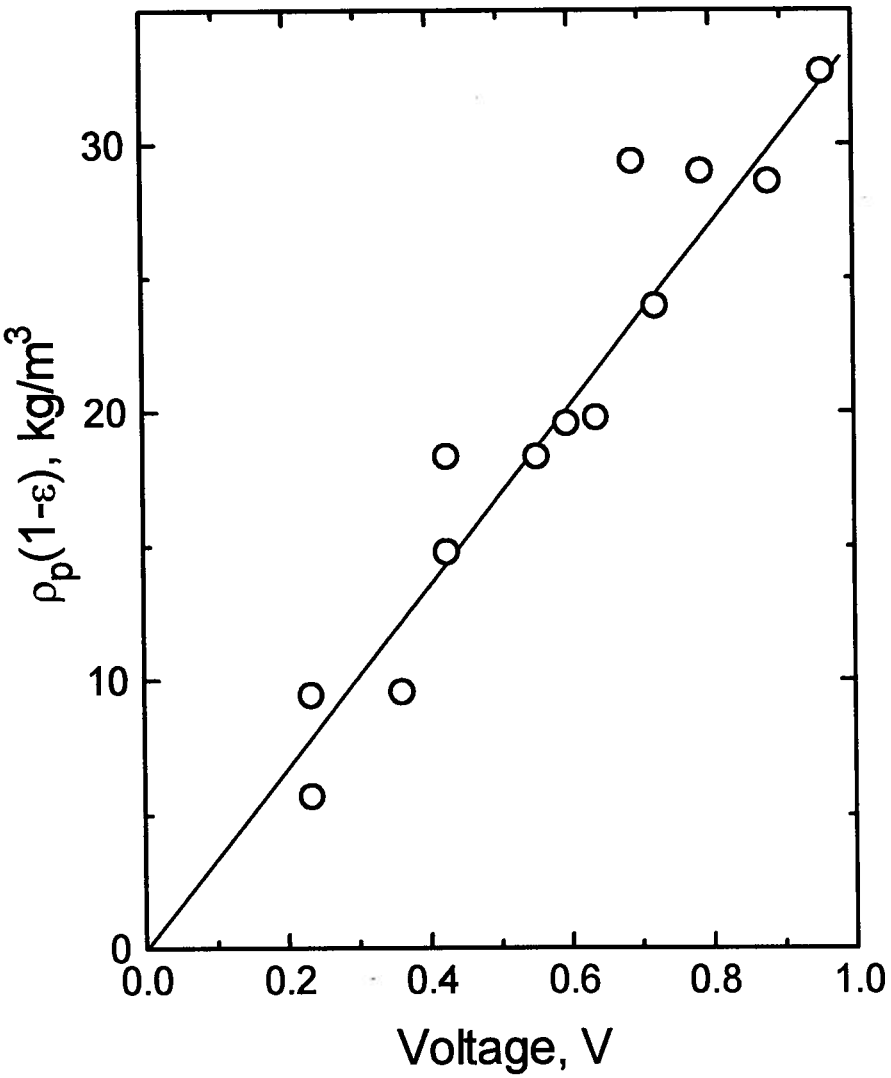

Fig. 3.4. Calibration curve for fibre optic voidage probe by Matsuno et al. (1983)

(2). For the second method, the calibration is carried out in a liquid-solid fluidized bed because particles are quite uniformly distributed in such a system. Voidage can be obtained from the height, H, of the expanded bed as:

$$\varepsilon = 1 - \frac{H_o}{H}(1-\varepsilon_o) \tag{3.2}$$

where H_o is the height of a packed bed and ε_o is the voidage of the packed bed. A set of bed voidage data can be obtained by changing fluid velocity to achieve different bed heights, H. To reduce the influence of an axially non-uniform voidage distribution, the calibration can be carried out at different bed heights, and an average value can be obtained. This method of calibration for the fibre optic voidage probe was used by Qin and Liu (1982) for glass beads of diameter 900 μm and 300 μm. As shown in Fig. 3.5, a plot of bed voidage vs output signal gives a nearly linear relationship. A linear relationship was confirmed by Hartge et al. (1986) for sand particles of diameter 56 μm as shown in Fig. 3.6 and by Boiarski (1985) for fine polystyrene beads. It is interesting to note that in both Figs 3.5 and 3.6 the output of the fibre optic probe is not zero at unit voidage. It is suspected that dust and bubbles in the liquid-solid systems of Qin and Liu (1982) and Hartge et al. (1986) is probably responsible for the non-zero output signal of the fibre optic probes at the unit voidage.

Lischer and Louge (1992) simulated the calibration in liquid-solid systems by using a ray-tracing Monte Carlo algorithm. They showed that the accuracy of optical fiber measurements increases with a decreasing ratio of particle diameter to probe diameter, d_p/d_f. They also found that for transparent materials such as glass beads, water calibration may cause problems. The same particles should be used in the calibration to reduce errors. No other similar study on the performance of optical fiber probes for determining particle concentrations has been reported.

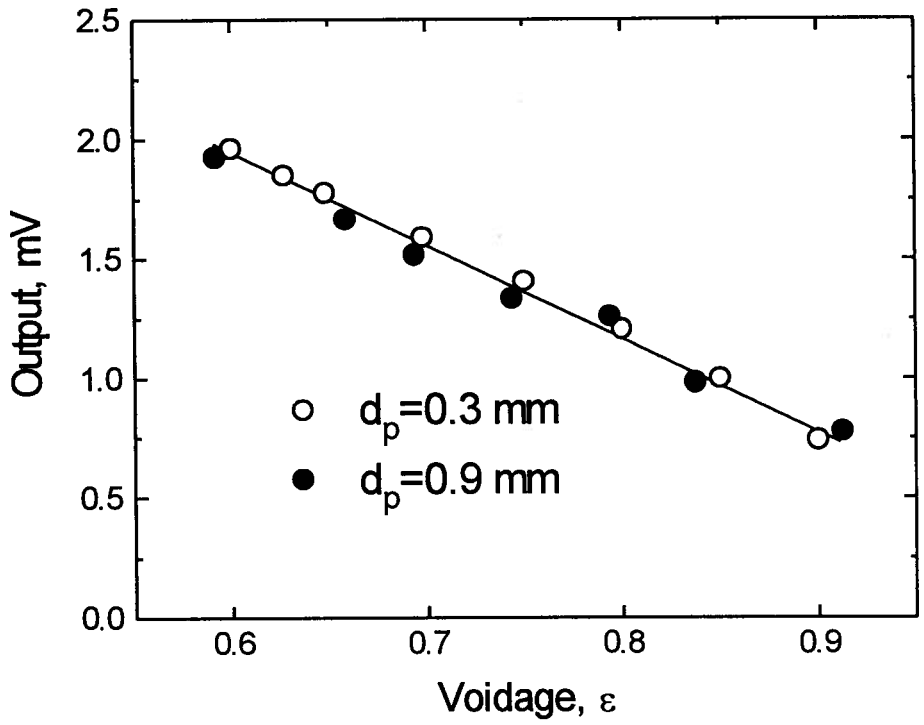

Fig. 3.5. Calibration curve for fibre optic voidage probe obtained by Qin and Liu (1982).

In our calibration, since d_p/d_f is only 0.07 and sand is opaque, the calibration should give reasonable results according to Lischer and Louge (1992).

To further check the linear output of the fiber optic particle concentration probe, calibration using the same particles as in the experiments was conducted in two liquid-solid systems. For voidages less than 0.8, the calibration was carried out in a liquid-solid fluidized bed similar to the one used by Qin and Liu (1982). Calibration results are illustrated by the open

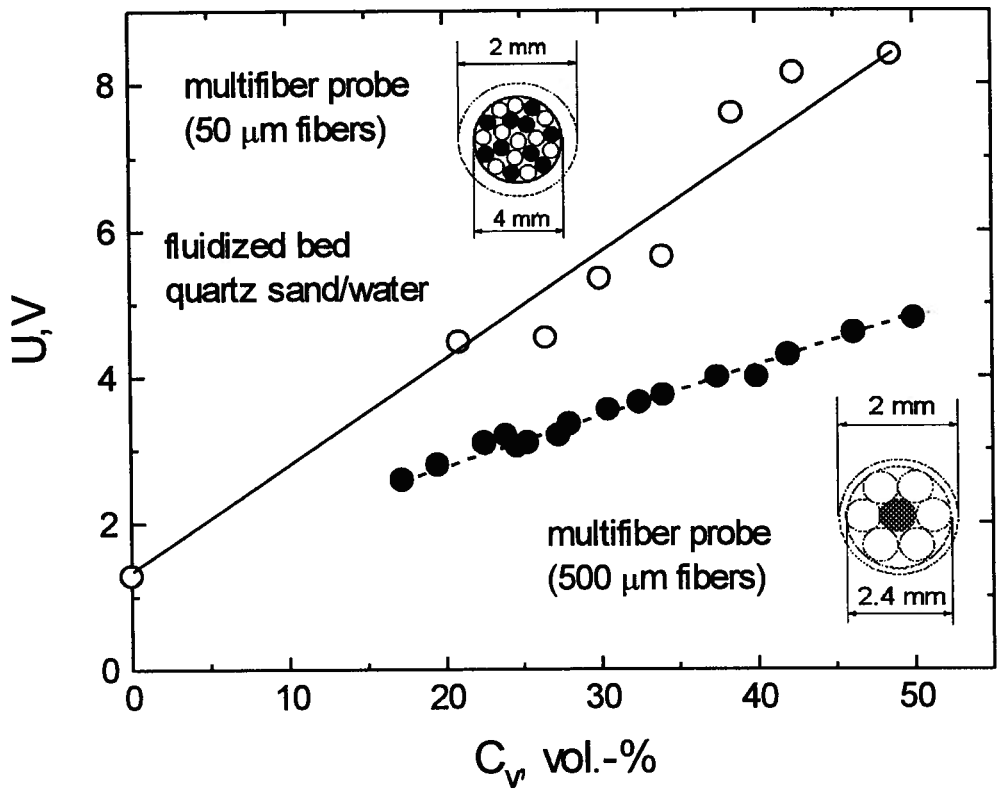

Fig. 3.6. Calibration curve for fibre optic voidage probe by Hartge et al., 1986. Blackened fibres are light transmiters, while open fibres are receivers.

symbols in Fig. 3.7. Calibrations at voidages of 0.8 and above are difficult in liquid-solid fluidized beds because the bed surface is obscure. Therefore, calibrations at higher voidages were carried out in a beaker. A known volume of solid particles was put into a beaker and mixed with water of known volume. The liquid-solid mixture was then stirred until the particles are uniformly distributed in the water. Liquid-solid systems having different voidage can be achieved by mixing different volumes of particles into the water. Before the tests, the liquid-solid systems were checked to be free of bubbles and dust, so that the output of the fibre optic probe was zero at unit

voidage to ensure the accuracy of each test. Results from the beaker are also shown by the closed symbols in Fig. 3.7. It is seen from Fig. 3.7 that the calibrations from both systems were very nearly linear over the entire voidage range of interest.

The linear relationship between the voidage and the output of the fibre optic voidage probe in a gas-solid system was verified by a dropping test as indicated in Fig. 3.8. The solids recirculation system which is described in detail in Chapter 2 was employed to carry out the test. Particle velocity at the measuring location was measured by the fibre optic particle velocity probe

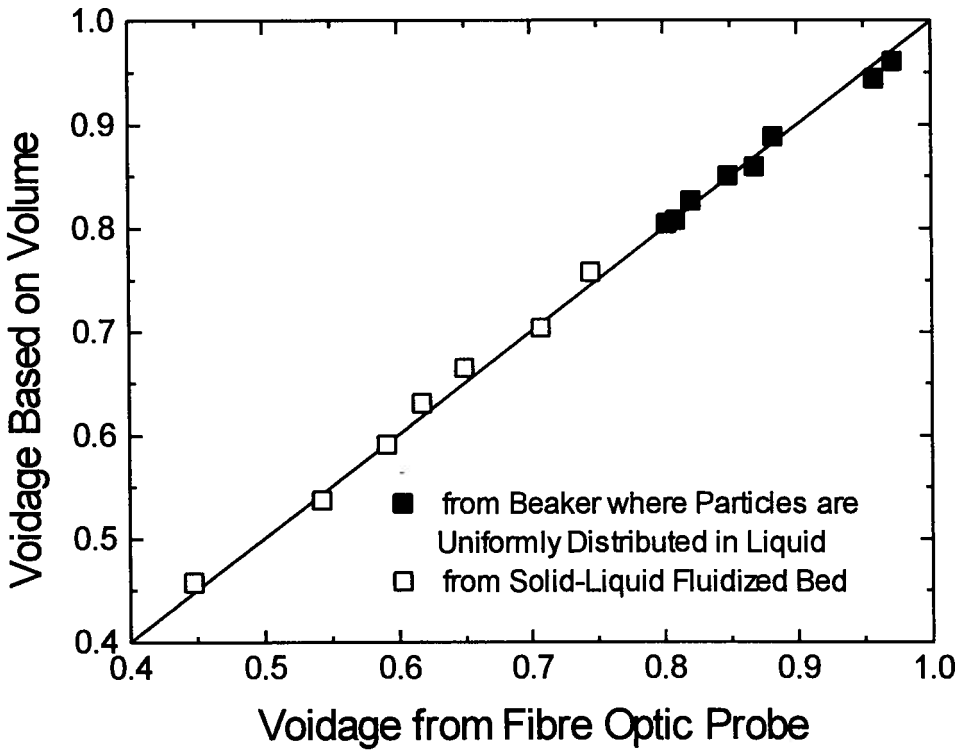

Fig. 3.7. Calibration curve for fibre optic voidage probe.

described in detail in Chapter 4. The solids flux was obtained by capturing and weighing the amount of particles descending through a known area over a known time interval. From these measurements, the voidage was calculated. The test results, indicated in Fig. 3.9, provide further evidence of a linear relationship between voidage and the output of the voidage probe. Since the output of the fibre optic voidage probe has a linear relationship with the measured particle concentration, in-situ calibration is required at only two points, one corresponding to the loosely packed bed voidage and the other to a voidage of unity.

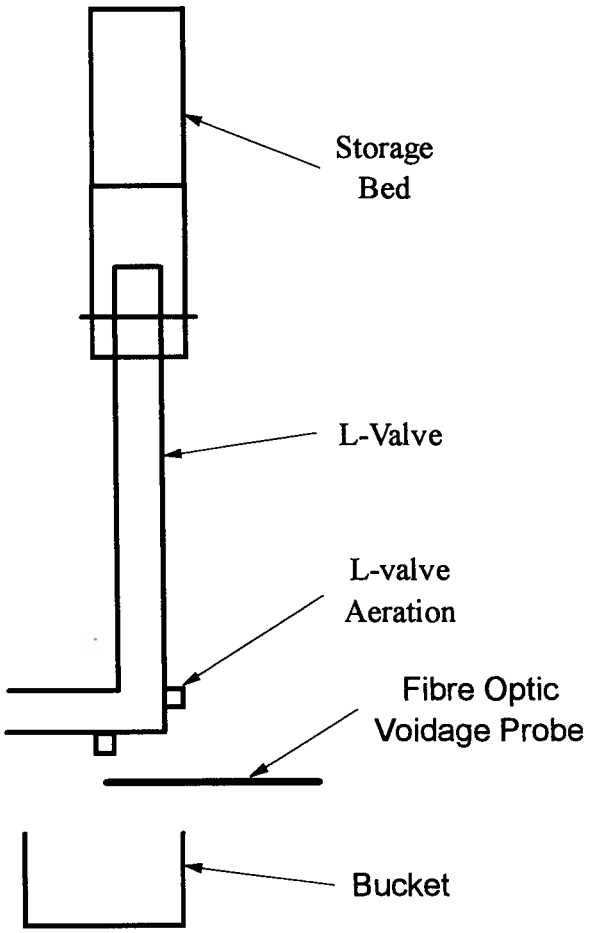

Fig. 3.8. Schematic of gas-solid system used to confirm a linear relationship between voltage and solids concentration for the fibre optic voidage probe.

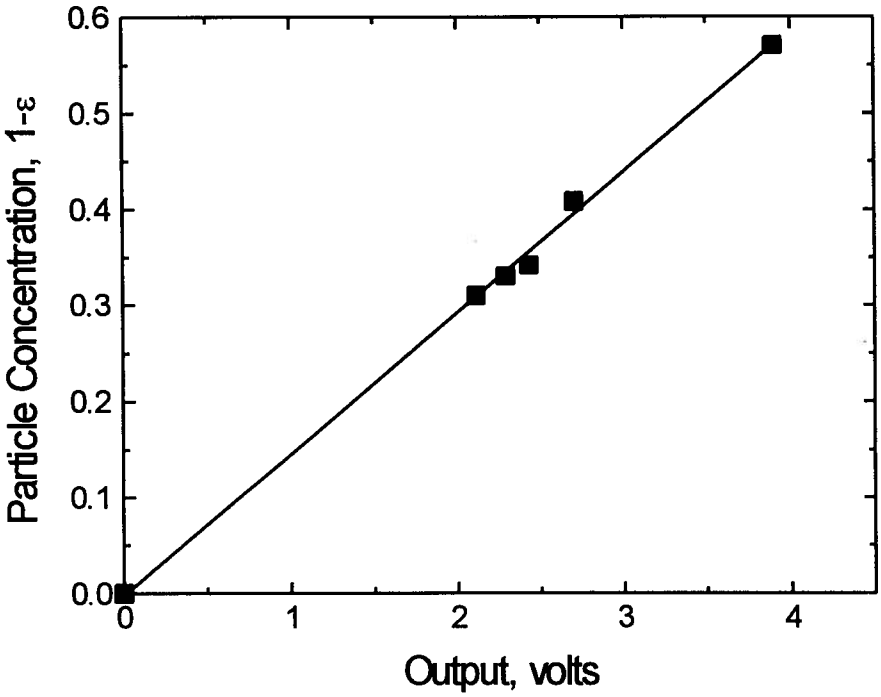

Fig. 3.9. Verification of the linear relationship for the fibre optic voidage probe using the gas-solid system shown schematically in Fig. 3.8.

Measurements in the CFB riser were taken at heights of 0.25, 0.79, 1.83, 3.45, 5.13, 6.20, 7.06, and 8.98 m above the distributor to obtain axial profiles of voidage. Lateral profiles involved measurements at 0.0, 26.0, 47.0, 60.0, 66.5, and 73.0 mm from the riser axis. The coordinates used on all figures appear in Fig. 2.1.

Before starting each test, the windows near the measurement location were covered with black plastic bags to prevent unwanted light from penetrating into the riser. A special fitting was

used to mount the fibre optic probe to the riser so that the probe could be moved laterally without shutting down the CFB system. After the measuring system and a personal computer were hooked up, measurements were started.

3.3 Results and Discussion

3.3.1 Basic Profiles

Figure 3.10 shows a typical trace of local instantaneous voidage versus time. The instantaneous local voidage shows rapid fluctuations. Axial profiles of local time-average voidages under several different operating conditions are presented in Figs 3.11 to 3.14. Generally speaking, the time-mean voidage at the bottom of the riser is low and gradually increases towards the top. This is true both in the wall region and at the center. More significant changes in voidage with height occur at the wall than in the central region.

Figures 3.12 and 3.13 show that local time-mean voidage decreases with increasing solids circulation rate. As portrayed in Fig. 3.14, the time-mean voidage increases with increasing gas velocity. Superficial gas velocity and solids circulation rate exert more influence on the voidage at the wall than in the core. From Figs 3.11, 3.12, and 3.14, we find that voidages near the wall are not always lowest at the distributor. For high circulation rates and/or low superficial gas velocities and in the wall region ($0.8<y/Y<1$), voidage decreases from just above the distributor to a height just above where the particles re-enter the riser. Voidage then increases along the column height.

From Figs 3.11 to 3.14, one can also observe the influence of the riser exit at the top of the riser. Due to the abrupt exit, there is a strong exit effect. Because many particles hitting the top of the riser tend to rebound, particle concentration near the exit becomes high. Compared

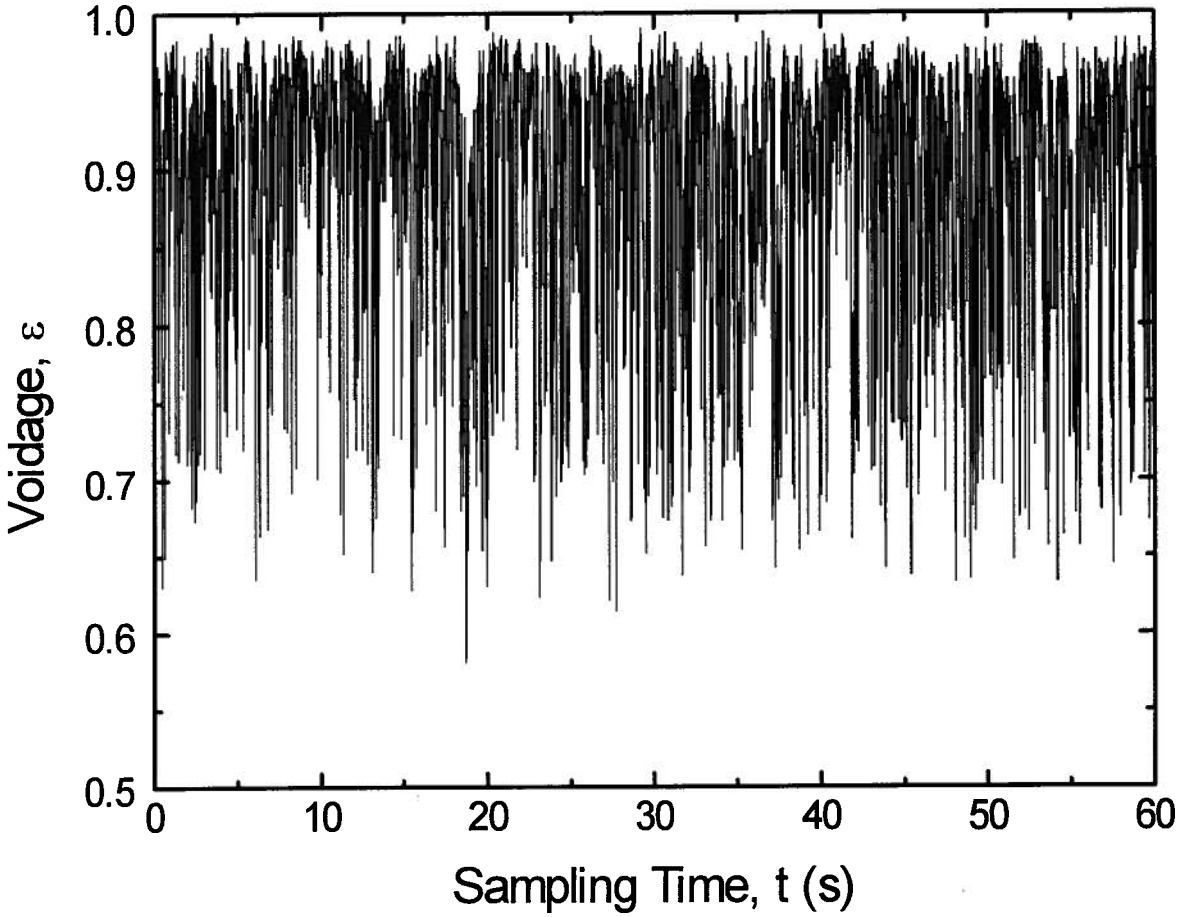

Fig. 3.10. Local instantaneous voidage versus time for a point near the top of the riser. (U_g=5.5 m/s, G_s=40 kg /m^{2}s, x/X=0, y/Y=-1, z=8.98 m and $\bar{\varepsilon}$ = 0.9).

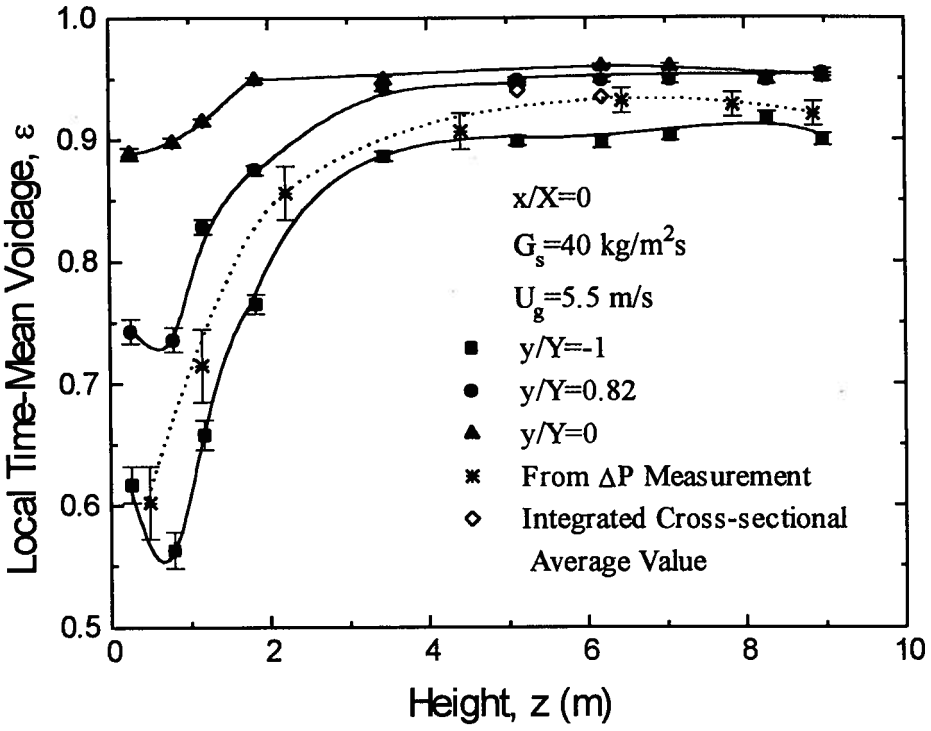

Fig. 3.11. Axial profiles of local time-mean voidage for x/X=0, U_g=5.5 m/s and G_s=40 kg /m^2s.

with the exit effect in a riser of circular cross-section (Brereton and Grace, 1994), there appears to be a more severe exit effect in the square column. Figures 3.11 to 3.14 indicate that the abrupt exit influenced an extensive zone. The extent of the region of influence may be related to the corners in the square column since corners can shelter particles rebounding from the top of the riser, while downward-moving particles are more difficult to strip from the corners than those traveling downwards along a smooth surface. Hence particles move downwards a longer distance in the corners of a square column than in a circular column. Similar reasoning may explain why particle concentration is higher in the lower part of the square riser for a given gas velocity and solids circulation rate.

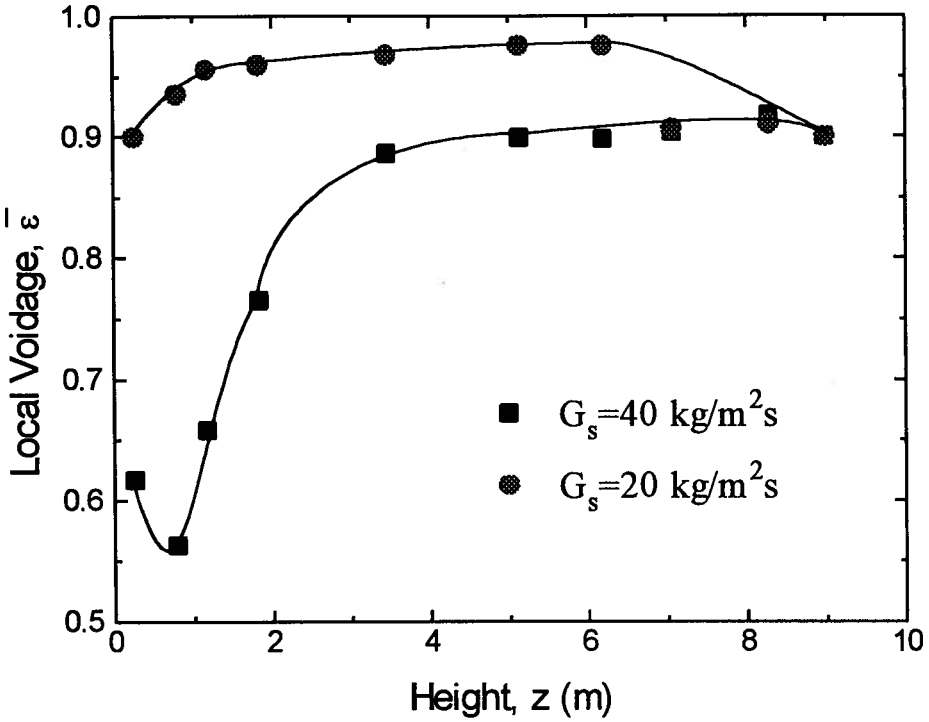

Fig. 3.12. Axial profiles of time-mean voidage at the wall for two different solids circulation rates for x/X=0, y/Y=-1 and U_g=5.5 m/s.

None of the profiles in Figs 3.11 to 3.14 is S-shaped. Thus the model of Li and Kwauk (1980) is not applicable to this study. The voidage profile in the lower part of the column from the location at which the solids re-enter the riser can be described by

$$\frac{\bar{\varepsilon}-\bar{\varepsilon}_o}{1-\bar{\varepsilon}_o}=\exp\left(-\frac{\zeta}{z-z_o}\right) \tag{3.3}$$

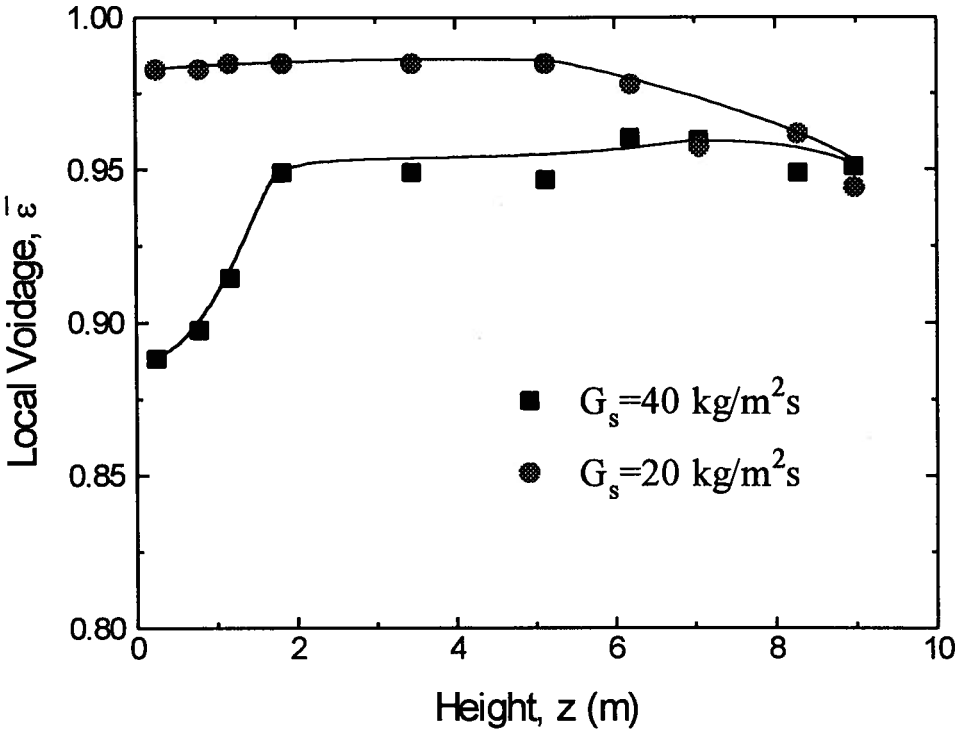

Fig. 3.13. Axial profiles of local time-mean voidage at the axis for two different solids circulation rates for x/X=0, y/Y=0 and U_g=5.5 m/s.

where z is the height above the distributor, $\bar{\varepsilon}$ is cross-sectional average voidage, $\bar{\varepsilon}_o$ is the cross-sectional average voidage at the solids re-entry location, z_o is the height of solids recirculation location and ζ is a decay constant. Rewriting Equation (3.3) in terms of solids suspension density, we obtain:

$$\bar{\rho}_{susp} = \bar{\rho}_o(1 - \exp(-\frac{\zeta}{z - z_o})) \tag{3.4}$$

where $\bar{\rho}_{susp}$ is the solids suspension density and $\bar{\rho}_o$ is the solids suspension density at the solids re-entry location. To find $\bar{\rho}_o$, the same approach as used by Senior and Brereton (1992) was adopted here, i.e. assume that

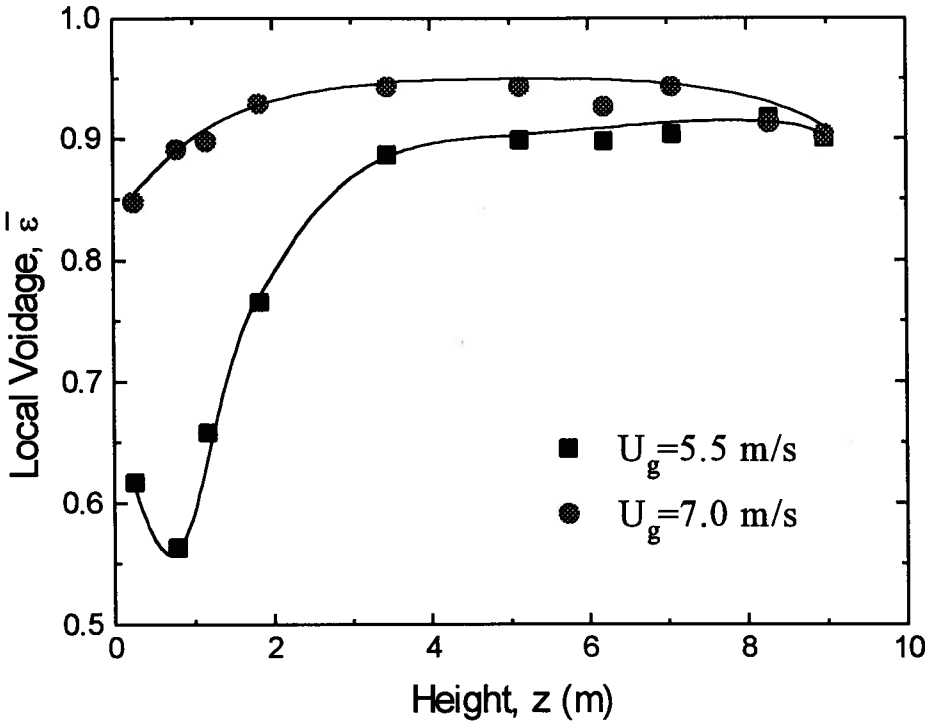

Fig. 3.14. Axial profiles of local time-mean voidage at the wall with two different superficial gas velocities for x/X=0, y/Y=-1 and G_s=40 kg/m^{2}s.

$$(1-\bar{\varepsilon}_o) = C_o U_g^{*C_1} \left(\frac{G_s}{\rho_p (U_g - v_T)}\right)^{C_2} \tag{3.5}$$

where C_o, C_1, and C_2 are constants, G_s is the solids circulation rate, U_g is the superficial gas velocity, v_T is the particle terminal velocity, ρ_p is the solids density, and $U_g^* = U_g \left\{\rho_g^2 / [g(\rho_p - \rho_g)\mu_g]\right\}^{\frac{1}{3}}$ is the dimensionless velocity given by Grace (1986) with g being the gravitational acceleration, ρ_g the gas density, and μ_g the gas viscosity. By correlating $\bar{\varepsilon}_o$ in

Equation (3.5) and ζ in Equation (3.3) against U_g and G_s, from the experiments, we obtain C_o=2.3 x 10^4, C_1=-1.4, C_2=1.6, and ζ=0.8 m.

Figure 3.15 compares the predictions of to Equation (3.4) with solids suspension densities obtained from pressure drop measurements. The fitted equation generally fits well except near the top of the riser where there is a significant exit effect.

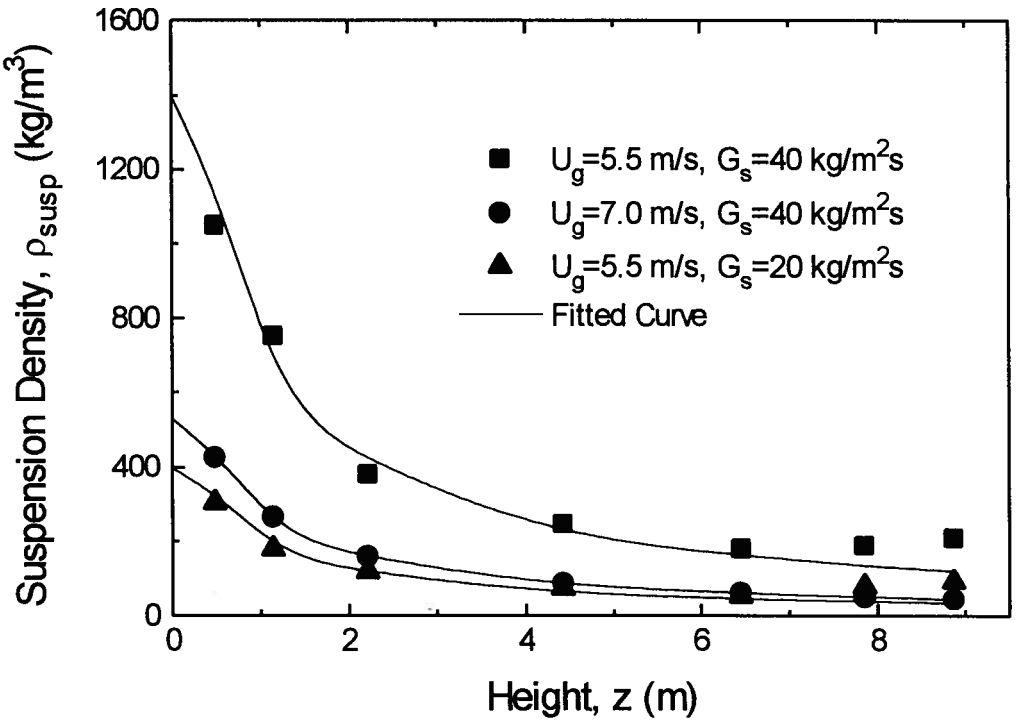

Fig. 3.15. Axial suspension density profiles compared with fitted curves corresponding to equation (3.4) with ζ=0.8 m.

An axial profile of voidage calculated from differential pressure measurements along the height of the riser is plotted as a dotted line in Fig. 3.11 in comparison with results from fiber optic probe measurement. Results obtained from the optical fiber follow the same trend as those from the ΔP measurement. To further check the results, local voidages from the fiber optic probe were integrated at two heights, 5.13 m and 6.20 m, assuming symmetry about the axis to obtain cross-sectional average voidages as indicated in Fig. 3.11. The results are seen to be in reasonable agreement.

Lateral profiles of voidages 0.79 m above the bottom are shown in Fig. 3.16. The particle concentration is high at the wall and low in the central region. Particles generally move downwards in the wall region. These observations are very similar to those in risers of circular cross-section. They show that there is also a core-annulus structure in a riser of square cross-section. In the dilute core region, particles generally move upwards with the voidage usually 0.94 to 0.99, depending on the operating conditions. In the annulus, particle concentration is high and particles mainly move downwards, with occasional upward movement, with voidages from 0.88 to 0.95 for the developed region. The lateral profile of voidage changes greatly near the wall and is more uniform in the core.

Figure 3.17 shows cross-sectional voidage profiles. Voidage is seen to be higher at the center and lower at the wall, as in columns of circular cross-section. Particles in the corner region of risers of square cross-section are protected by two walls and are more difficult to strip out of the corners than for risers of circular cross-section. Thus voidage becomes even lower towards the corner. From visual observations, particles in the corner region move downwards.

As indicated in Fig. 3.18, the riser exit also causes an asymmetric lateral distribution of voidage near the top of the riser, with the time-mean voidage on the exit side being lower than on the opposite side. There are two possible reasons. Because of the exit, gas and particles reaching

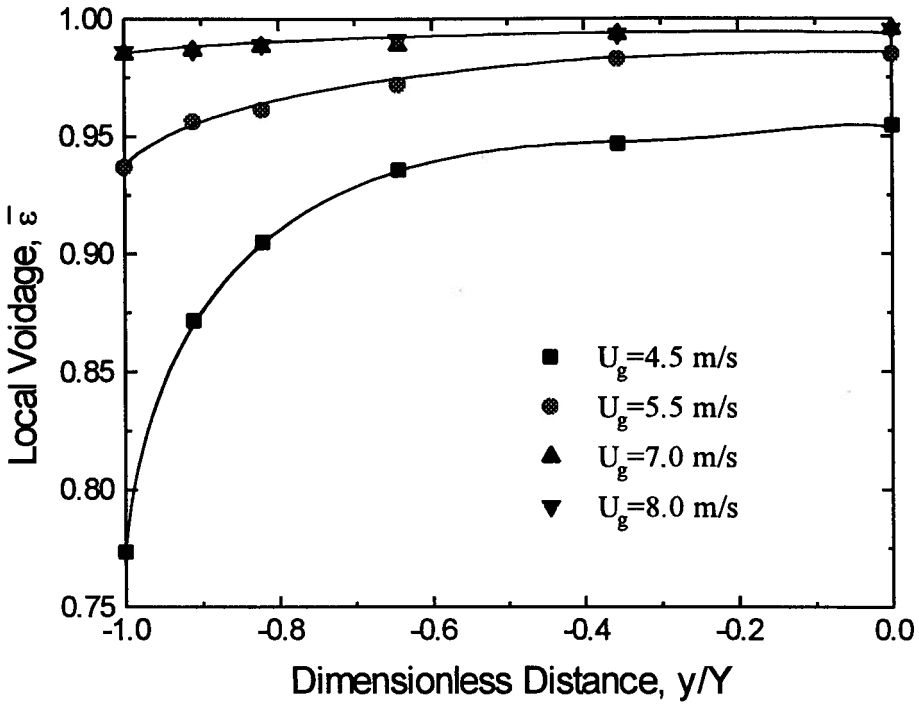

Fig. 3.16. Lateral profiles of local time-mean voidage near the bottom of the riser at four different gas velocities for x/X=0, z=0.79 and G_s=20 kg/m^{2}s.

the top of the riser must have a horizontal component towards the exit. As a consequence, particle concentration is higher on this side. When a plexiglass horizontal duct was employed in this study connecting the riser exit to the primary cyclone, particles were found to pile up on the lower surface of the horizontal duct. With enough accumulation of particles, some particles may slip back periodically from the horizontal duct and move downwards along the near wall of the riser, thus, causing higher particle concentration on the exit side, as observed by Glicksman et al. (1993). Visual observations indicated that particles rebounding from the top tend to move downwards in the corners of the riser where they are sheltered from the upflowing gas.

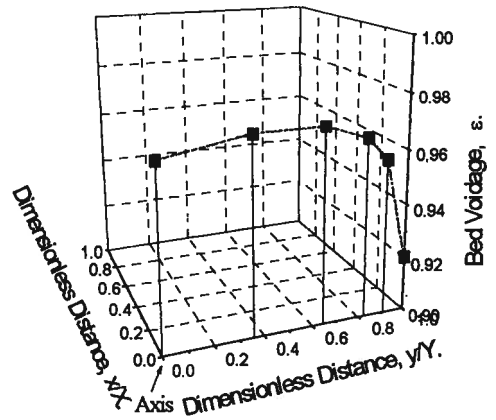

x/X=0

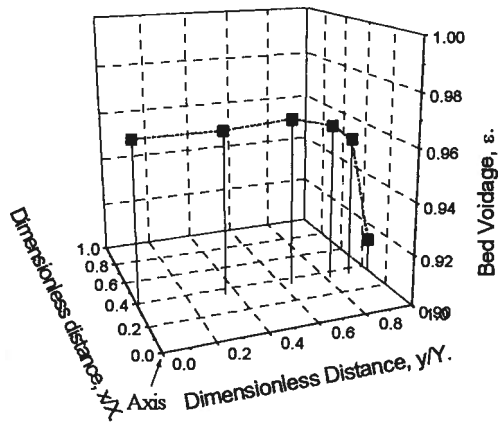

x/X=0.37

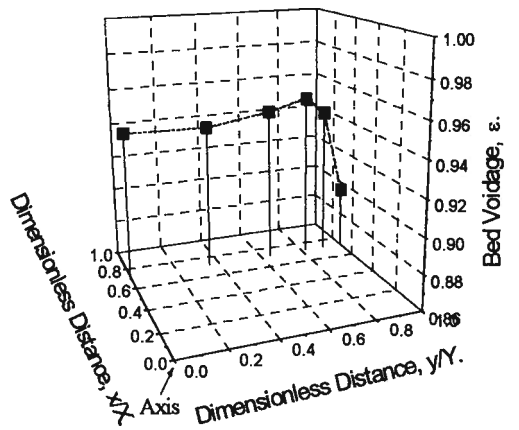

x/X=0.72

Fig. 3.17. Lateral profiles of local time-mean voidage for U_g=7.0 m/s, G_s=40 kg/m^{2}s and z=6.20 m.

Another interesting finding is that time-mean voidages are not always highest on the axis of the column. As seen in Fig. 3.18, the voidage sometimes reaches a maximum at a location of about 0.6 to 0.8 of the half-width of the column and then decreases slightly towards the center. From close scrutiny of the literature, a similar trend can also be found in risers of circular cross-section (e.g. Weinstein et al., 1986; Hartge et al., 1988; Kato et al., 1990; Nowak et al., 1990; Bai et al., 1991; Herb et al., 1992). Since different measurement techniques such as X-rays, capacitance probes and fiber optic probes were used by these authors, it cannot be attributed to the measuring technique. However, the M-shaped* profiles appear to be more distinguishable in our riser of square cross-section.

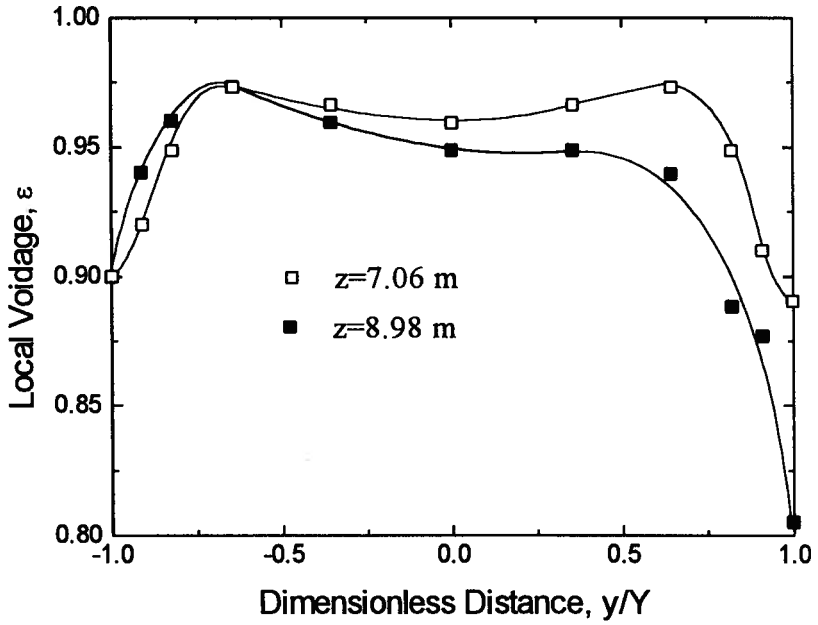

Fig. 3.18. Lateral profiles of voidage for x/X=0, U_g=5.5 m/s, G_s=40 kg/m^{2}s.

* "W-shaped solids concentration profile" is more accurate than "M-shaped voidage profile". Since "M-shaped voidage profile" was used in a published paper Zhou et al. (1994), the term is also employed here.

The M-shaped profile is also in good accord with the radial gas velocity profiles obtained by Gel'perin et al. (1976) using a total pressure probe and Tsuji et al. (1984) employing a laser-Doppler velocimeter. Both studies found that the gas velocity was not a maximum at the center. Instead, it increased sharply at first until a maximum was reached and then decreased slowly towards the center. The radial dimensionless position where the gas velocity reached its maximum was similar to that where the voidage reached a maximum in our column.

By using an optical fibre image system, Wei et al. (1993) obtained pictures which suggest a high voidage circular area between center and wall regions. Photographs obtained by Wei et al. (1993) are reproduced in Fig. 3.19. Particles are shown as black areas in the picture. Similar results were obtained using a laser sheet technique by Horio et al. (1993) in a riser of circular cross-section, further validating our finding of M-shaped lateral voidage profiles.

The M-shaped profiles may be due to cross-sectional non-uniformity of gas turbulence intensity. In the core region, gas moves upwards, while in the annulus, descending particles drag gas downwards (Brereton, 1987). At the interface between the core and annulus layers, the shear rate is high, at least 1000 times that in the core of the riser (Senior, 1992). Turbulence is likely to be generated at the shear boundary. Hence, there may well be more radial particle diffusion in this vicinity than near the axis of the column, causing the particle concentration to be a little higher at the center of the riser. Yang et al. (1992) measured lateral profiles of gas and particle velocities in a circulating fluidized bed riser. They found a region between the axis and the wall where the gas-solids slip velocity and gas fluctuation velocities reach maximum values. If this is correct, then this phenomenon should be more distinguishable for small particles, e.g. FCC particles, because small particles are more likely to be influenced by gas motion and turbulence than by particle collisions

(Senior, 1992). Upon checking the bed materials in the literature for which this phenomenon was shown, we find that in most cases when M-shaped profiles can be distinguished the particle diameters were smaller than 100 μm.

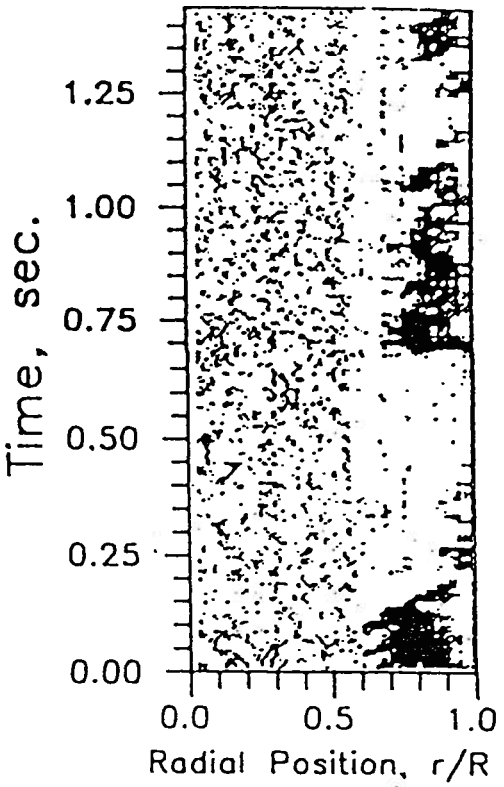

Fig. 3.19. Picture from Wei et al. (1993) showing a high voidage circular area between axis and wall regions.

Tung et al. (1988) reported that, in a circular riser, local voidage in the riser can be correlated in terms of the cross-sectional average voidage and the dimensionless lateral position, with voidage independent of operating conditions, scale, particle properties and vertical position. Their correlation was

$$\bar{\varepsilon} = \bar{\varepsilon}_{av}^{(\phi^2+0.19)} \qquad \text{for} \quad \phi = r/R \leq 0.75 \tag{3.6}$$

$$\bar{\varepsilon} = \bar{\varepsilon}_{av}^{(3.62\phi^{6.47}+0.191)} \qquad \text{for} \quad \phi = r/R \geq 0.75 \tag{3.7}$$

where $\bar{\varepsilon}_{av}$ is the cross-sectional average voidage. Zhang et al. (1991) used a single equation,

$$\bar{\varepsilon} = \bar{\varepsilon}_{av}^{(0.191+\phi^{2.5}+3\phi^{11})} \tag{3.8}$$

to represent the whole range. Equations (3.6), (3.7) and (3.8) do not fit the experimental data in this study.

Similar lateral voidage profiles, with local voidage only dependent on the cross-sectional average voidage and the dimensionless radial position, were confirmed in a circular riser by Rhodes et al. (1992) who proposed a semi-empirical equation

$$\frac{1-\bar{\varepsilon}}{1-\bar{\varepsilon}_{av}} = 2\left(\frac{r}{R}\right)^2 \tag{3.9}$$

to simulate the lateral voidage profiles. Equation (3.9) also does not fit our experimental results very well. One flaw of Equation (3.9) is that the calculated voidage at the axis of the riser is always predicted to be unity. The lack of agreement in this study with the equations of Tung et al. (1988), Wang et al. (1991) and Rhodes et al. (1992) is probably related to the different bed materials used. Equations (3.6) to (3.9) were obtained for Group A particles, while Group B particles were used in this work. The different riser configuration is also likely to have been a factor, with the corners having some influence on the lateral voidage profiles.

An empirical equation somewhat similar in form to the Rhodes' semi-empirical equation

$$\frac{\frac{2\bar{\varepsilon}_{av}+1}{3}-\bar{\varepsilon}}{1-\bar{\varepsilon}_{av}}=\left(\frac{y}{Y}\right)^4 \tag{3.10}$$

was written based on the experimental data from the square riser. Here Y is the half-width of the column and y is the lateral distance from the axis. Figure 3.20 compares the calculation results from Equation (3.10) with experimental data obtained in the developed region. In the core region ($y/Y \leq 0.9$), the empirically modified equation fits the experimental data very well.

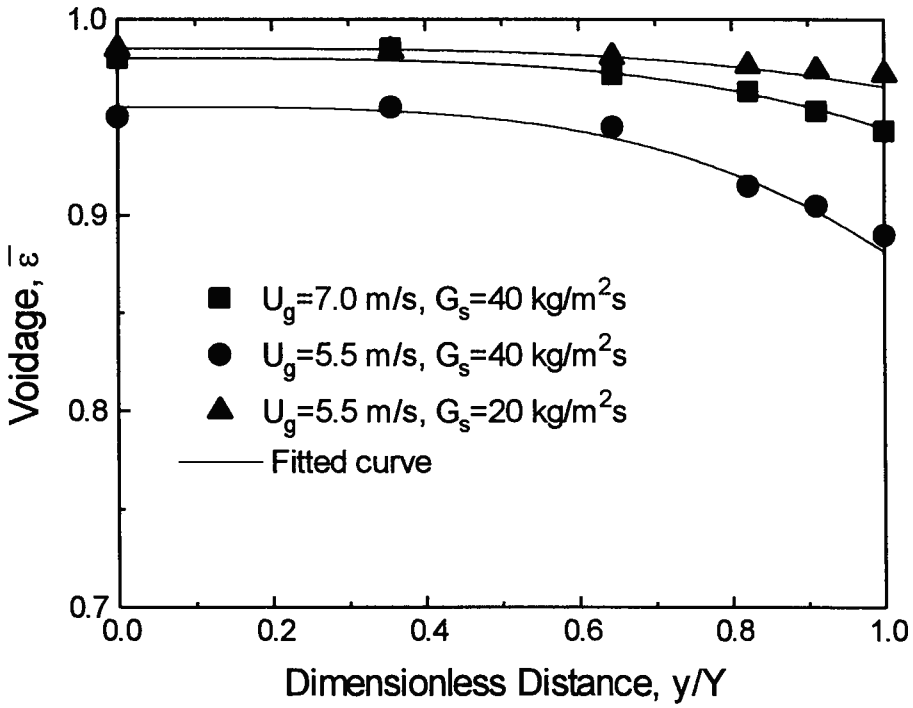

Fig. 3.20. Comparison between simulation results and experimental data showing similar lateral voidage profiles: x/X=0, z=5.13 m .

However, there are deviations in the wall region. Equation (3.10) gives reasonable results for the voidage at the axis.

3.3.2. Probability Analysis

Probability distributions of particle concentration for different heights at the center and wall regions are shown in Figs 3.21 and 3.22. At a high solids circulation rate and low superficial gas velocity, two peaks may be found as shown for the lowest levels in Fig. 3.21. This indicates that in the wall region over the lower part of the riser, there are two dominant particle concentrations, both high. Rhodes et al. (1992), using high speed video photography, reported that at high solids fluxes, there was a substantial bulk downflow of particles at the wall, with the voidage of this bulk downflow higher than that of the particle downflow in swarms. This may account for the bimodal distributions. A bimodal distribution is found only in the lower region of the riser, with no bimodal distributions at the axis nor near the top. In the work of Rhodes et al. (1992) the bulk downflow disappeared at low solid fluxes. For the modest solids circulation rate and relatively high superficial gas velocity, only one peak can be seen in the probability distribution of particle concentration at the wall.

Louge et al. (1990), using a capacitance probe, did not find a bimodal probability distribution of voidage at any location in their riser. The large measuring volume of the probe may account for the lack of a bimodal distribution. The high measuring location may be another factor since bimodal distributions were only found in the lower part of the riser in the present work.

Figure 3.23 demonstrates that the particle concentration in the core is more uniform than

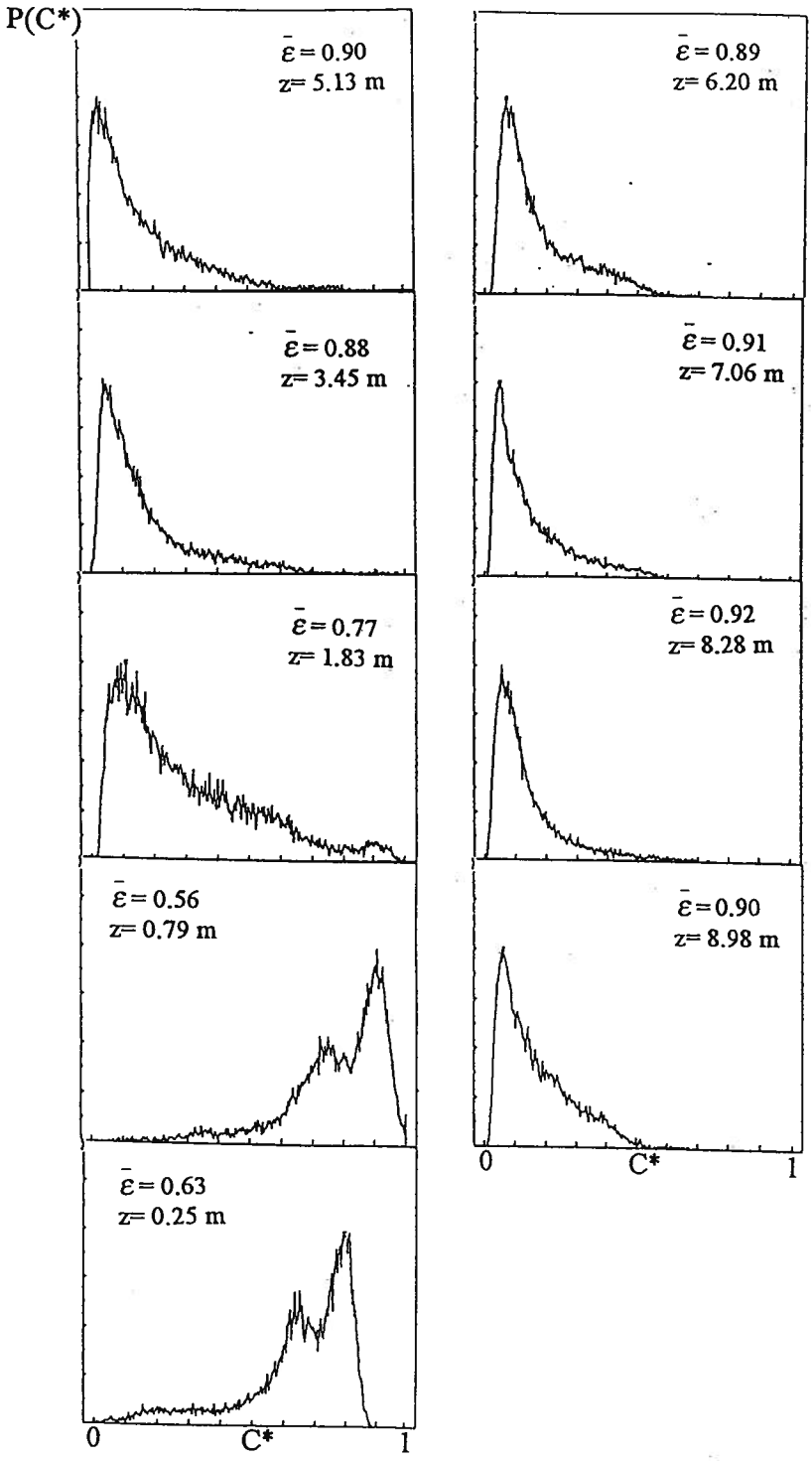

Fig. 3.21. Axial profiles of probability distribution of local time-mean particle concentration, $C^* = (1-\varepsilon)/(1-\varepsilon_o)$ at the wall for U_g=5.5 m/s, G_s=40 kg/m^{2}s, x/X=0 and y/Y=-1. C*=1 corresponds to packed bed particle concentration, i.e. ε_o=0.43.

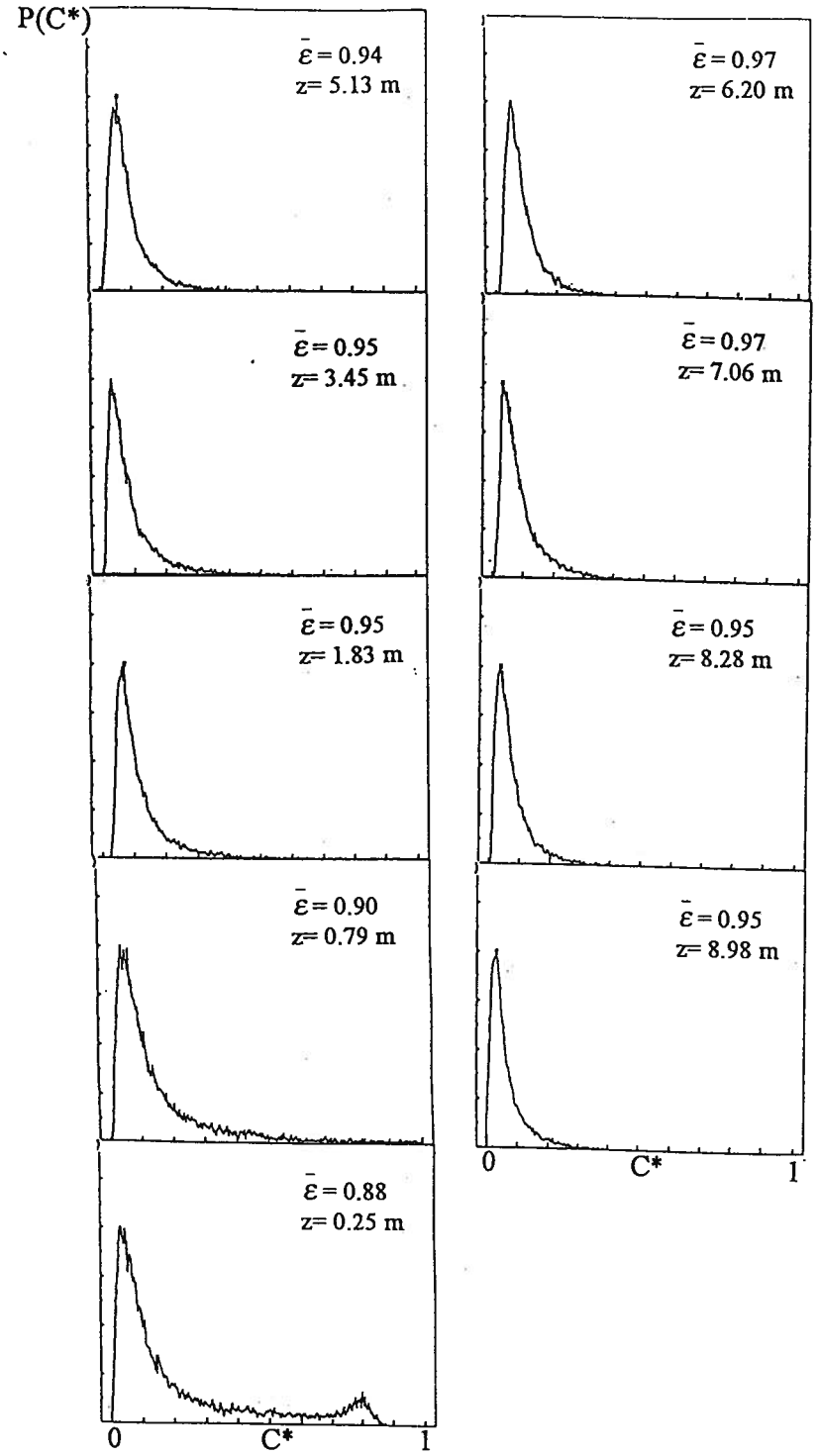

Fig. 3.22. Axial profiles of probability distribution of local time-mean particle concentration, $C^* = (1-\varepsilon)/(1-\varepsilon_o)$ at the axis for U_g=5.5 m/s, G_s=40 kg/m^{2}s, x/X=0 and y/Y=0. C*=1 corresponds to packed bed particle concentration, i.e. ε_o=0.43.

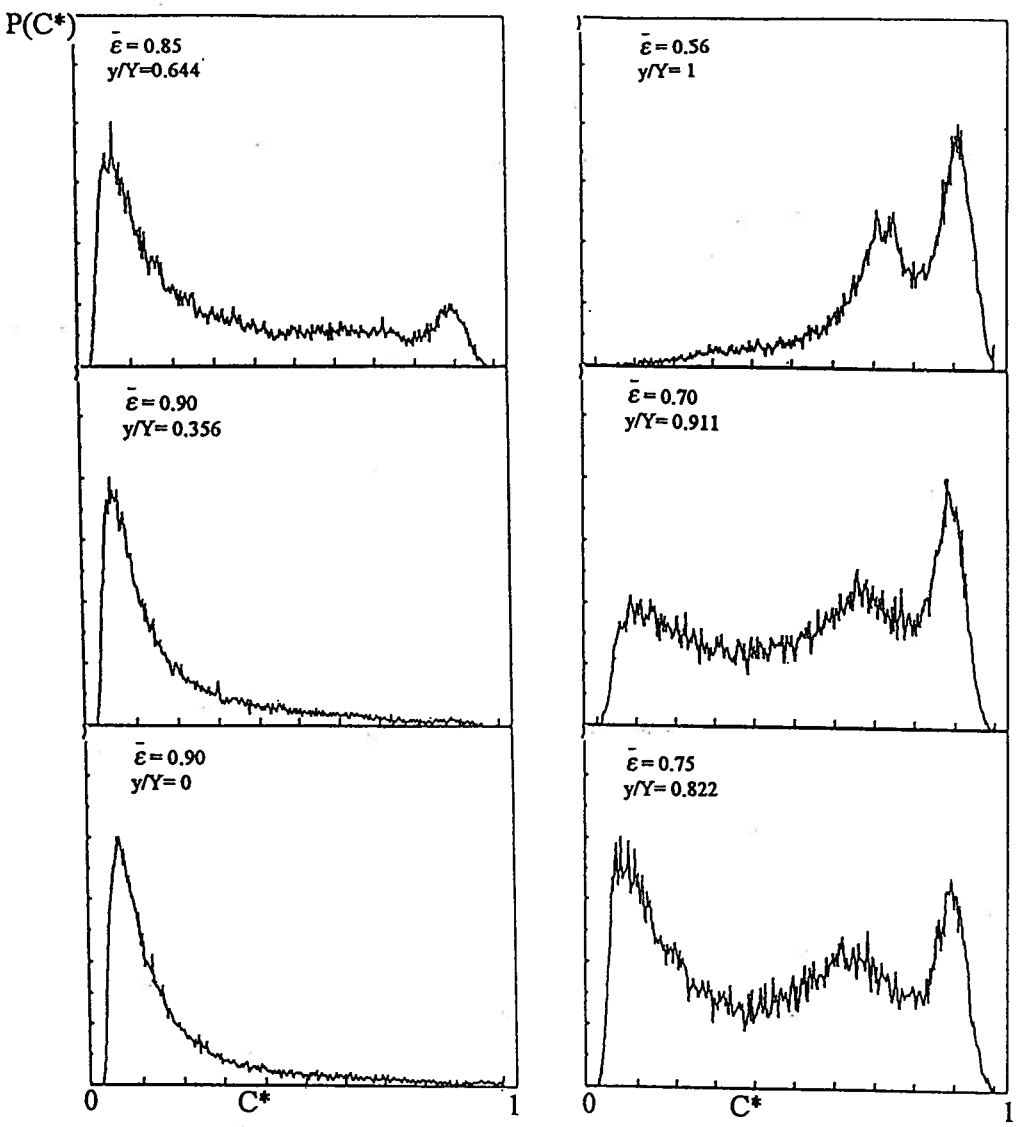

Fig. 3.23. Lateral profile of probability distribution of local time-mean particle concentration, $C^* = (1-\varepsilon)/(1-\varepsilon_o)$ for U_g=5.5 m/s, G_s=40 kg/m^{2}s, x/X=0 and z=0.79 m. C*=1 corresponds to packed bed particle concentration, i.e. ε_o=0.43.

near the wall. The locations of the peaks of the probability distribution curves for the annulus shift greatly from right to left. In the core, a much smaller shift is observed, indicating that the axial profile of voidage is more uniform than at the wall. Trimodal distributions are observed at locations a small distance inward from the wall, suggesting intermittent bulk downflow, particle streamers and dilute suspension in this region.

Figure 3.17 indicates that particle concentration is highest in the corner. As demonstrated in Fig. 3.24, the particle concentration in the corner has a wider distribution of particle concentration than midway between opposite walls. At high solids circulation rate and low superficial gas velocity, the instantaneous voidage in the corner can be as low as that of a loose packed bed. This is not present at low solids circulation rate or high superficial gas velocity.

Asymmetry of lateral voidage distributions was found at the top of the riser as shown in Fig. 3.25. The probability distribution of voidage is wider at the wall than in the core. Only one dominant peak is observed at all lateral positions. A voidage equal to the packed bed value, as indicated by C*=1 in Fig. 3.25, is found near the wall at the particle exit side.

3.3.3 Intermittency Index Profiles

Although the standard deviation provides a quantitative measure of the variability of local voidage, it is difficult to explain the nature of the two-phase flow in circulating fluidized beds in terms of the standard deviation, because the time-mean voidage varies from point to point. An intermittency index was introduced by Brereton and Grace (1993) to provide a more useful comparison of the two-phase nature of the flow. It is defined as:

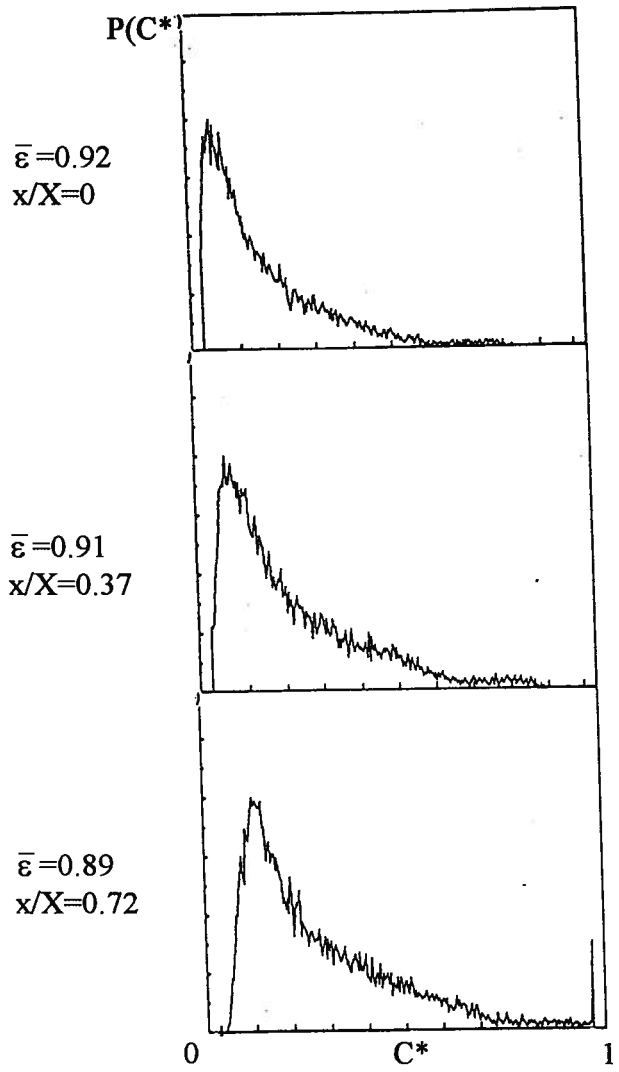

Fig. 3.24. Lateral profile of probability distribution of local time-mean particle concentration, $C^* = (1-\varepsilon)/(1-\varepsilon_o)$ at the wall for U_g=7.0 m/s, G_s=40 kg/m^{2}s, y/Y=-1, z=6.20 m. C*=1 corresponds to packed bed particle concentration, i.e. ε_o=0.43.

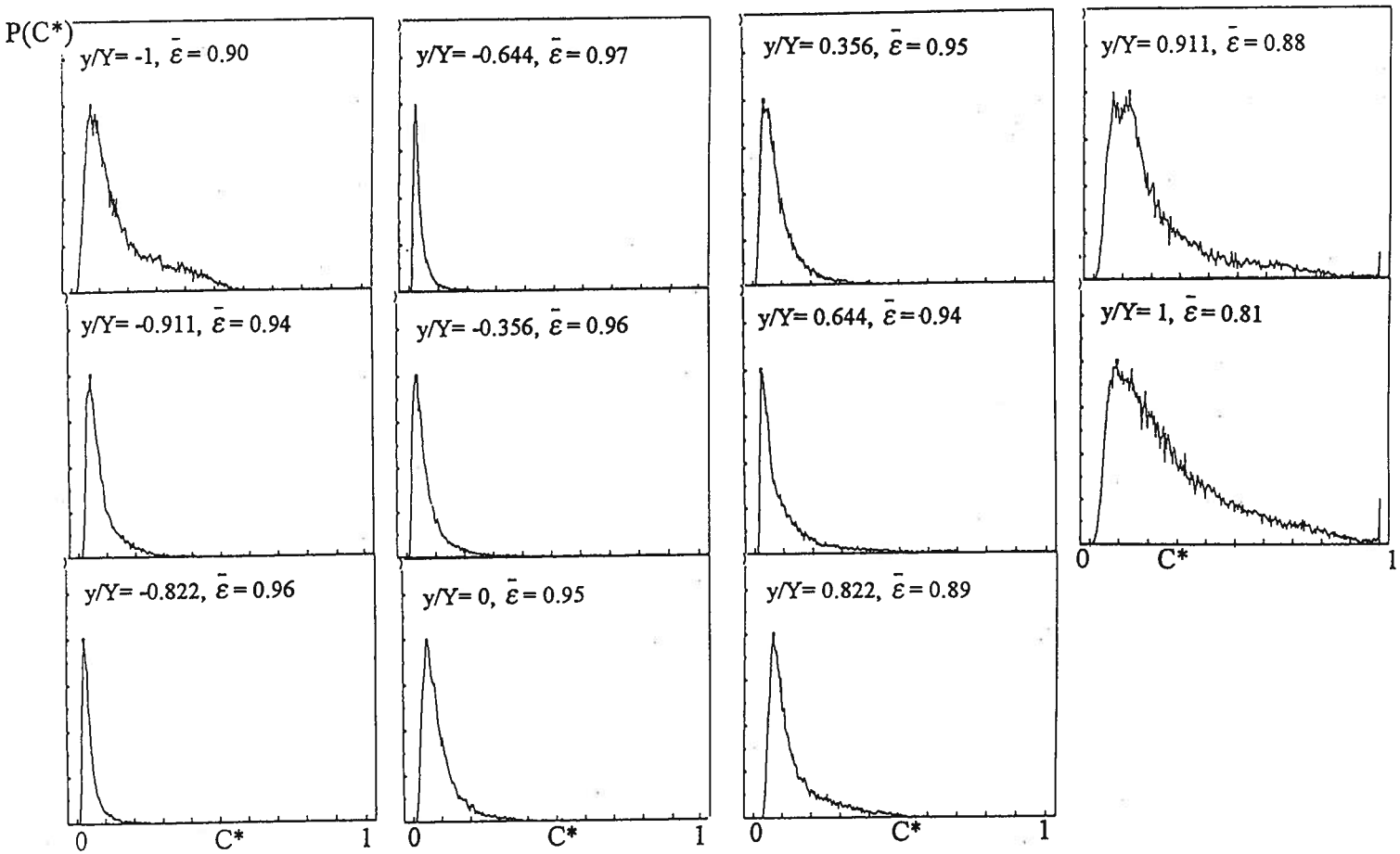

Fig. 3.25. Probability distribution of local time-mean voidage at the top of the riser for U_g=5.5 m/s, G_s=40 kg/m^{2}s, x/X=0, z=8.89 m. C*=1 corresponds to packed bed particle concentration, i.e. ε_o=0.43.

$$\gamma = \frac{\begin{pmatrix}\text{Standard deviation of density fluctuations}\\ \text{at a given point}\end{pmatrix}}{\begin{pmatrix}\text{Standard deviation of density fluctuations}\\ \text{for fully segregated two-phase flow with}\\ \text{identical time-mean density at the same point}\end{pmatrix}} = \frac{\sigma}{\sigma^*} \tag{3.11}$$

The standard deviation for fully segregated two-phase flow, where the local voidage alternates between only two values, one corresponding to the voidage at minimum fluidization and the other to unity, can be shown to be

$$\sigma^* = \rho_{mf}\sqrt{(\overline{\rho}_{susp}/\rho_{mf})(1-\overline{\rho}_{susp}/\rho_{mf})} \tag{3.12}$$

where ρ_{mf} is the bed density at minimum fluidization and $\overline{\rho}_{susp}$ is the time-average point density.

σ^* is a useful normalizing factor because it is the maximum possible value of the standard deviation for a specific voidage.

Lateral profiles of intermittency indices at different heights are shown in Fig. 3.26. Except at the bottom of the riser, γ is lower in the interior, showing the flow to be more homogeneous there than near the wall. Because of the entrance effect, γ increases towards the axis at a height of 0.25 m. High γ values near the wall indicate large fluctuations of voidage. According to the probability profiles of voidage indicated in Figs 3.21 and 3.22, there are two dominant peaks near the wall at the bottom of the riser, while only one peak is found in the central region where γ is lower.

Near the bottom of the riser, γ increases from the wall until it reaches a maximum and then decreases towards the axis. The location of the maximum γ, indicating highest heterogeneity, is

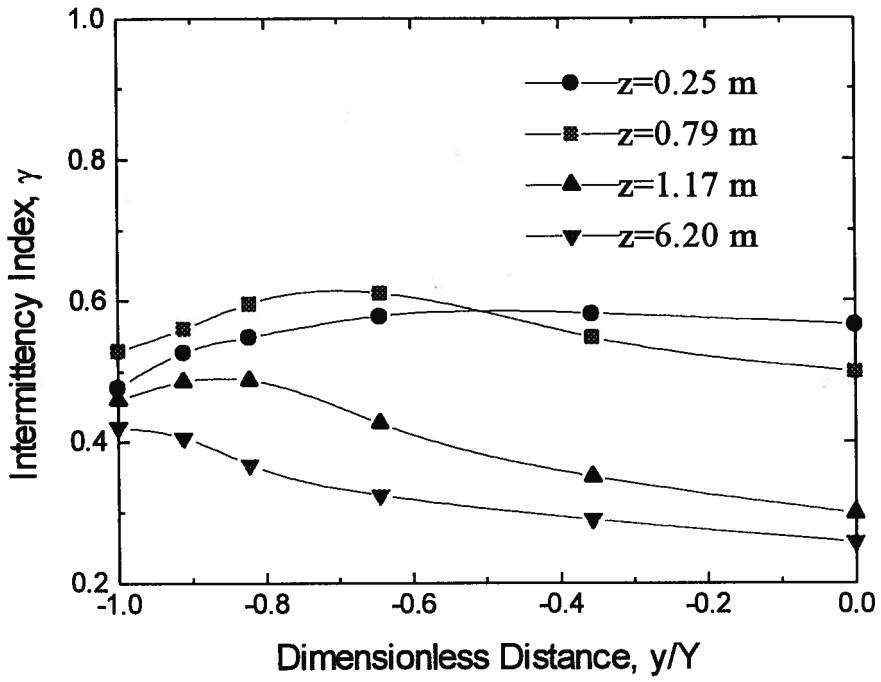

Fig. 3.26. Lateral profiles of intermittency index at four levels for x/X=0, U_g=5.5 m/s, G_s=40 kg/m^{2}s.

close to the boundary between the core and annulus where the shear rate is highest. The locations of trimodal probability distribution of particle concentration, shown in Fig. 3.23 are quite close to the locations of these maximum γ values.

Figure 3.27 shows the axial profiles of intermittency index γ both at the center and at the wall. It is seen that γ gradually decreases with increasing height. The high value of γ at the bottom shows high heterogeneity of flow with intermittent occurrence of dense phase and dilute phase. Flow becomes more homogeneous towards the top of the riser. At the bottom, as indicated in Fig. 3.26, the cross-sectional distribution of γ is more uniform than at higher locations.

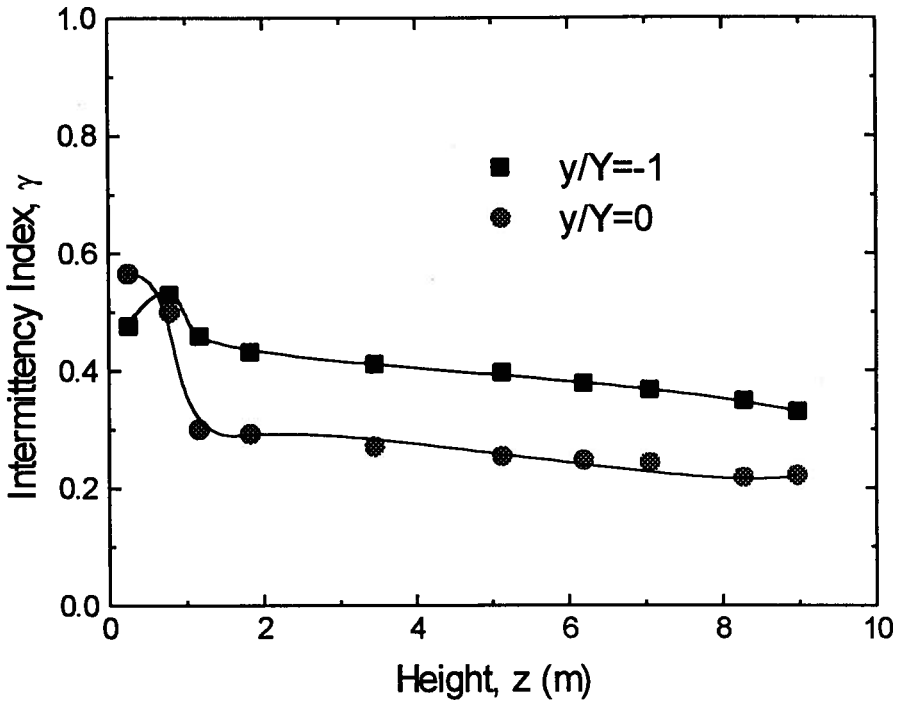

Fig. 3.27. Axial profiles of intermittency index at the wall and at the axis of the column for x/X=0, U_g=5.5 m/s, G_s=40 kg/m^{2}s.

As shown in Fig. 3.28, the intermittency index in the corner is higher than at other locations at the same level. However, there is only a small difference between γ in the corner and elsewhere near the wall, despite the much higher particle concentration in the corner, suggesting that the heterogeneity of flow in the corner is not substantially different from that at other locations near the wall.

The lateral profile of intermittency index at the top of the riser is asymmetric due to the exit effect as illustrated in Fig. 3.29, with γ higher on the exit side than on the opposite side. This may occur because, as described above, particles pile up in the horizontal duct connecting the

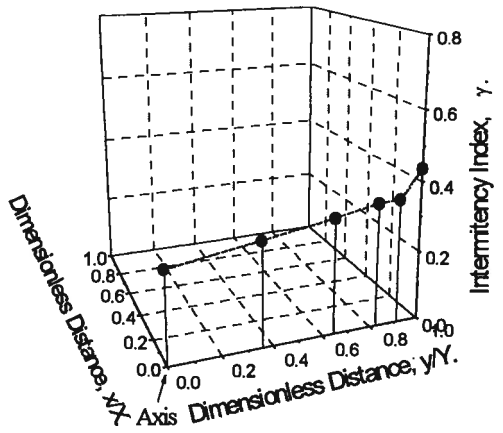

x/X=0

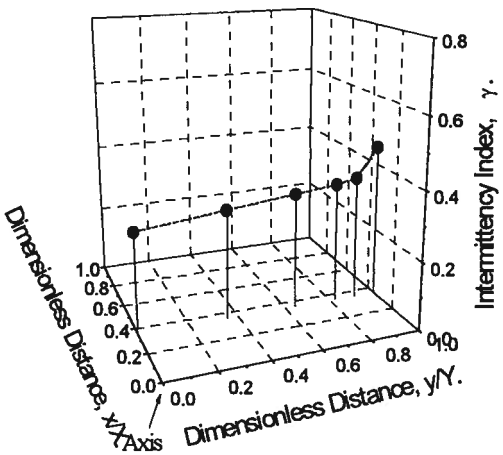

x/X=0.37

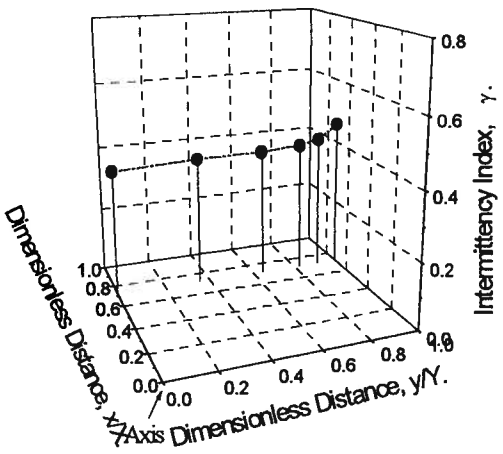

x/X=0.72

Fig. 3.28. Lateral profiles of intermittency index for U_g=7.0 m/s, G_s=40 kg/m^{2}s and z=6.2 m.

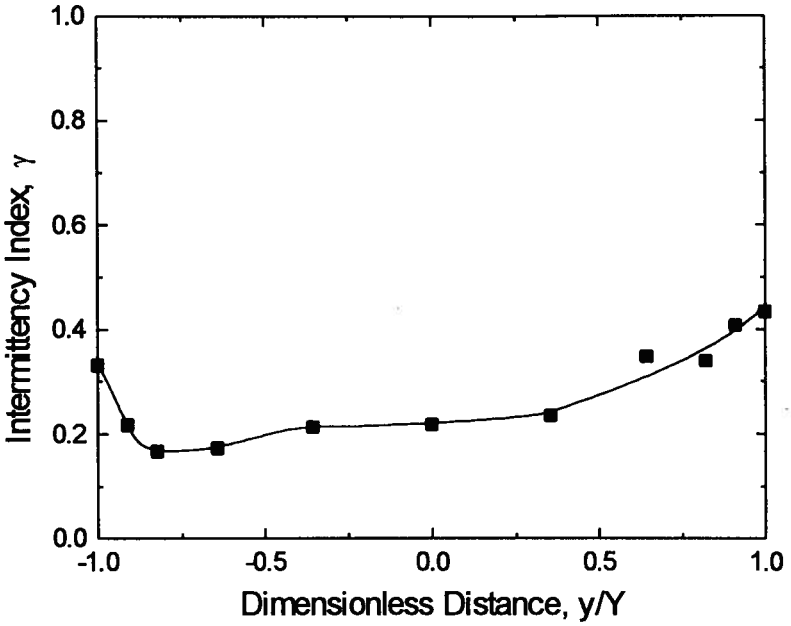

Fig. 3.29. Lateral profile of intermittency index near the top of the riser for U_g=5.5 m/s, G_s=40 kg/m^{2}s, x/X=0, z=8.98 m.

riser exit to the primary cyclone intermittently slip backwards and descend along the wall on the exit side (Glicksman et al., 1993).

3.4 Summary

Similar to results in risers of circular cross-section, the voidage at the bottom of the riser is low and gradually increases towards the top. Local time-mean voidage decreases with increasing solids circulation rate and/or decreasing gas velocity. The superficial gas velocity and solids circulation rate exert more influence on the voidage at the wall than in the core. The riser exit causes an asymmetric lateral distribution of voidage near the top of the riser with the time-mean voidage on the exit side being lower than on the opposite side.

The lateral profiles of voidage show that time-mean voidages are not always highest on the axis of the column. The voidage sometimes follows an "M-profile", reaching a maximum at a location of about 0.6 to 0.8 of the half-width of the column and then decreasing slightly towards the center. Voidages in the corners of the column are lower than elsewhere.

At lower locations, frequency distributions of voidage near the wall tend to be bimodal. Closer to the axis, only one dominant peak is observed. The voidage distribution becomes narrower as one moves from the wall towards the axis, indicating that the particle concentration is more uniform in the core. Trimodal distributions are observed a small distance inward from the wall, suggesting that bulk downflow, particle streamers and dilute suspension coexist in this region. Wider distributions of particle concentration are also found in the corner.

The intermittency index, γ is used to characterize the heterogeneity of the flow. Flow in the core tends to be more homogeneous than at the wall of the riser. Flow tends to become less heterogeneous with increasing height.

Chapter 4

Velocity Profiles

4.1 Introduction

Particle velocities affect mixing, heat and mass transfer as well as erosion in circulating fluidized beds. Bader et al. (1988) used a Pitot tube to measure local particle velocities. Both the solids flux profile and the radial profile of axial particle velocity in the riser were found to be parabolic. However, because of the large gas-solid slip velocity and interference caused by a relatively large probe, a Pitot tube is not an accurate instrument for measuring particle velocities. It can also be easily blocked by fine particles.

Monceaux et al. (1986) measured local solid fluxes in a circulating fluidized bed with a sampling probe and detected axisymmetric mass flux profiles as well as downward solid fluxes near the wall. Rhodes et al. (1988), using a sampling probe, found that there is a possibility of downward solids flux in the wall region. Both downward and upward solid fluxes decreased with height in the riser. They explained this in terms of transfer of solids from the core to the wall region. Measurements have been made by Bolton and Davidson (1988) using scoops to collect particles in the falling film.

Laser Doppler anemometry (LDA) has been used by many workers to detect particle velocity in gas-solid systems. LDA employs frequency information from light scattered by particles passing through a fringe or interference pattern to determine particle velocities. The light beam can be divided into two equal intensity beams by a beam splitter and surface mirror. The two beams are made to cross in a small region causing fringes. Particles passing through the

intersection region scatter light towards the collecting optics. From the frequency detected by a photomultiplier, the velocity can be calculated.

The major advantage of LDA is that it can provide accurate and instantaneous local particle velocities. This technique also has the advantage of being insensitive to the absolute intensity of scattered light. However, in regions of high particle concentration, light beams may be blocked by particles. LDA measurements are usually restricted to flows with very low volumetric concentrations (Yianneskis, 1987), limiting its utilization in circulating fluidized beds. The method can sometimes be used to measure particle velocities in the upper region of a riser where the voidage is high. It cannot currently be employed to measure particle velocities in the bottom region of circulating fluidized beds, except right at the wall, and it works best with particles one or two orders of magnitude smaller than typical CFB particles which follow the fluid motion closely. It is therefore not well suited to circulating fluidized beds. The laser Doppler technique was used by Yang et al. (1990) to measure local particle velocities in a dilute circulating fluidized bed. They found that the average cross-sectional mean axial particle velocity increased with increasing gas velocity and/or decreasing solid circulation rate. The laser Doppler technique provides accurate and instantaneous local particle velocities. It is insensitive to the absolute intensity of scattered light over a broad range.

Photographic and video techniques are widely used to study particle behaviour in fluidized beds. These methods are based on the analysis of particle images. These techniques can provide such information as particle velocity, direction of motion and acceleration. To obtain particle velocity, the distance between successive images of the same particle is determined, and the distance is divided by the time interval between the two images. However, the method needs tedious and sometimes difficult analysis, even with the help of advanced image-analysis software. The particle acceleration can be obtained by a similar method.

Small, fast-moving particles are difficult to photograph, unless careful consideration is given to proper illumination as well as to the interpretation of the images produced. Effects to consider are the illumination intensity, particle size and particle velocity. For contrast purposes, back illumination can be used so that recorded particles will appear as black dots or a dark dash on a bright background (Kirkman and Ryley, 1969). Photographic techniques can be used in two-dimensional risers or in risers of square cross-section. They cannot be employed in regions where particle concentrations are very high such as the bottom region of circulating fluidized bed risers. In circulating fluidized beds, highly concentrated downward moving particle streamers may also block light from reaching the camera.

High speed video techniques have been used to study particle motion at the wall of cold model circulating fluidized beds (Arena et al., 1989; Rhodes et al., 1990; Zheng et al., 1992). A descending velocity of 0.3-0.4 m/s was obtained for particle swarms in contact with the wall, while a velocity of about 1 m/s was found for particles descending a few millimeters from the wall (Rhodes et al., 1990). This method was also employed by Arena et al. (1989) a circulating fluidized bed with a two-dimensional riser to investigate solids flow structures. Wirth et al. (1991) employed a video camera and tracer particles and found that the particle descending velocity at the wall of their riser was about 2 m/s. The biggest advantage of the high speed video technique is that there is no disturbance of the flow field in the riser. However, this technique is generally limited to studies in two-dimensional cold model equipment. No on-line data can be obtained. In addition, photographic techniques are difficult to apply to the interior regions of circulating fluidized beds.

Zheng et al. (1992) developed a microcomputer-controlled multi-colour stroboscopic photography system to study particle motion in the region adjacent to the wall in CFB risers. Successive red, blue and yellow images of white tracer particles in beds of black particles were

used to provide such information as particle velocity and their directions of motion in the wall region in CFB risers.

Tracer technology, employing, for example, radioactive particles, can also be used to measure particle velocities. Detecting sensors for the tracer particles are usually located at different heights. Particle velocity can be obtained from the vertical distance between two sensors divided by the time interval that a tracer particle needs to travel through the distance. Large particles are usually required to obtain signals strong enough to be detected by sensors. No lateral/radial particle velocities can usually be obtained.

Fibre optic probes were used by Hartge et al. (1988), Horio et al. (1988), Ishii et al. (1990), Nowak et al. (1990), and Rhodes et al. (1990) to measure particle velocities in circulating fluidized bed risers of circular cross-section. Particles generally move upwards in the core of the riser. Particle velocity decreases from the center towards the wall, with negative values of time-averaged velocity very near the wall, i.e. particles move mostly downwards adjacent to the wall. This technique has the advantages of simplicity, high accuracy and low cost. A fibre optic particle velocity probe was therefore employed for our particle velocity measurements in a riser of square cross-section.

Previous research (e.g. Brereton et al., 1986; Schnitzlein and Weinstein, 1988; Wu et al., 1991; Chapter 3) has indicated that the geometry of the riser has considerable influence on the hydrodynamics of CFBs. Although risers of square cross-section are widely used in industry, especially for CFB combustion, very little research has been carried out in risers of non-circular cross-section. In this chapter, results of our experimental study on both lateral and axial particle velocity profiles are presented. This extends the work reported in Chapter 3 in which we have determined voidage profiles with the same particles and operating conditions in the same riser.

4.2. Fiber Optic Particle Velocity Probe

Particle velocity in circulating fluidized beds can be measured using the fiber optic and signal processing system shown in Fig. 4.1. The fibre or bundle B in the middle is used to project light to illuminate the particles. Fibers A and C serve as carriers of light reflected from the particles to two photomultipliers, and the signals from the photomultipliers are then fed to a correlation analyzer. The transit time t_{AC} is read as the maximum of the cross-correlation function. With the fiber at an effective separation length, l, the particle velocity is calculated as:

$$v_p = \frac{l}{t_{AC}} \tag{4.1}$$

This method has been employed by Oki et al. (1975), Patrose and Caram (1982), and Kojima et al. (1989) to measure particle velocities in fluidized beds. The disadvantage of cross-correlation is its long computation time. High accuracy requires a high sampling frequency and long computing times. For low particle velocity measurement, the maximum cross-correlation coefficient is difficult to obtain (Hartge et al., 1988). For the measurement of high particle velocities, less accuracy is usually obtained because of limited sampling frequency. The distance between fibers A and C, l also requires careful consideration. For small l, measurement accuracy is low and high sampling frequency is required. For large l, the maximum cross-correlation coefficient is usually low. The diameter of the optic fibers is usually greater than the particle diameter. Cross-correlation is then often used to measure the velocity of a group of particles. If particles are distributed uniformly in the riser, this method fails because no cross-correlation method can be obtained. This method can also be employed for the measurement of single large particles.

Another signal processing method is to use peak detectors to obtain the time interval t_{AC}. This method can be used to measure the velocity of single particles. When a particle passes

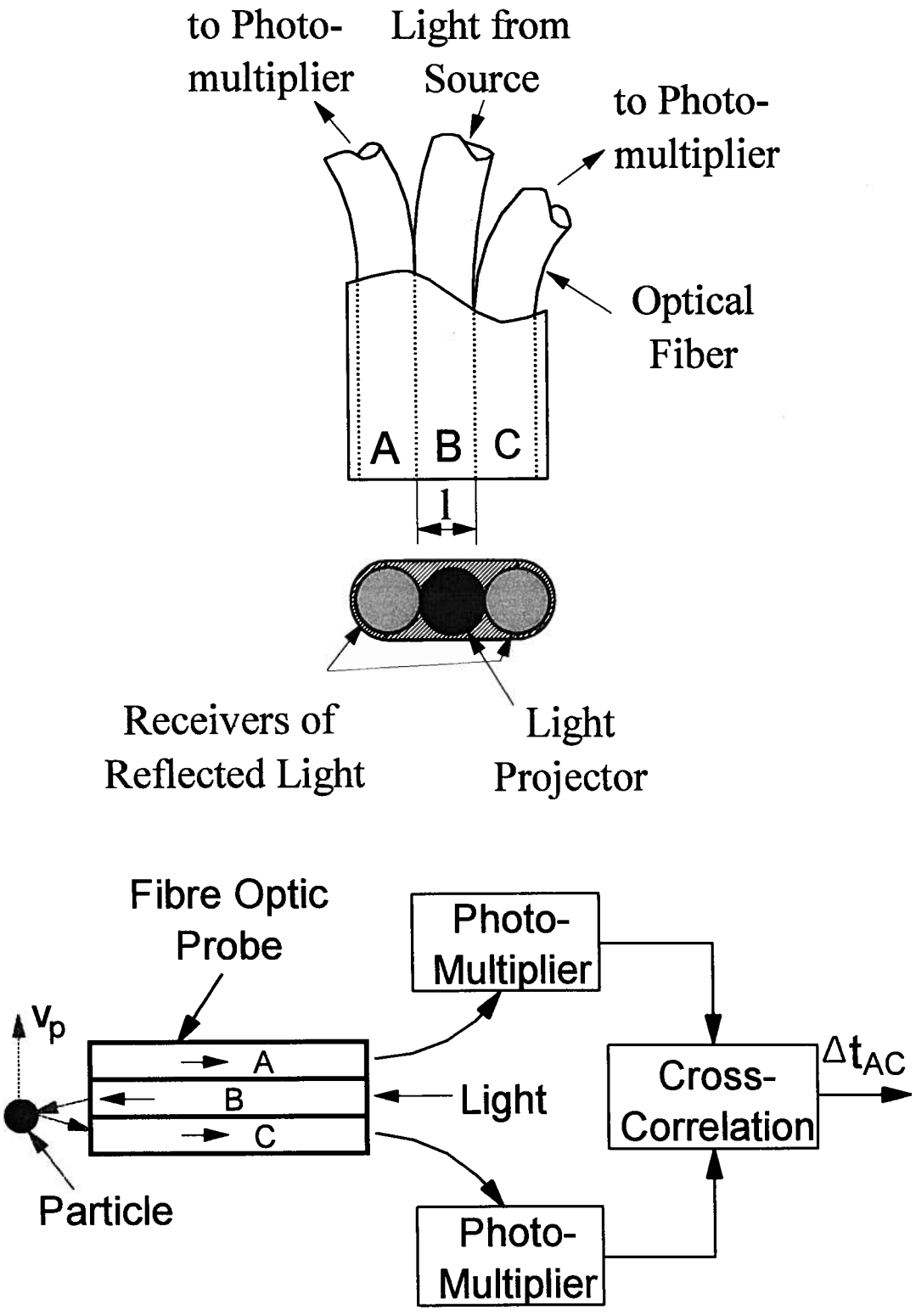

Fig. 4.1. Schematic of fiber optic and signal processing system used to measure particle velocity.

through the tip of the probe, reflected light is carried to two photomultipliers by the pair of optic fibers. Each signal has a peak. Peak detectors can be used to determine the time interval between the two peaks, allowing the particle velocity to be estimated. The advantage of this signal processing method is that the signals can be processed by a hardware-electric circuit instead of software, so that the processing time can be much shorter. To use this method, the diameter of the optical fibers must be chosen carefully to ensure that the dominant signals are from single particles. This method works well for measurements in spouted beds (He et al., 1995) because of the large particle size and unique particle moving direction. However, in circulating fluidized beds, particles are smaller than in spouted beds and the optical fibers cannot be too small; moreover there is an influence of particles surrounding the measured particle. For example, light carried to photomultipliers from probes A and C in Fig. 4.1 may not be reflected from the same particle. To overcome this problem, a five-fibered probe has been developed in this work.

As shown in Fig. 4.2, each of the five fibres is a silicon optical fibre having a diameter of 200 μm. The similarity between the fibre size and the particle diameter allows measurements from single particles and optimizes the signal-to-noise ratio. The probe consists of a horizontal cylindrical portion of diameter 2 mm and length 0.3 m leading to a 10 mm long head of cross-section 0.5 mm wide by 1.8 mm high. Light is delivered via fibres B and D, and then reflected by particles through fibres A, C and E to three separate photo-multipliers. Signals from the photo-multipliers are carried to peak detectors. Separate measurements of particle velocity are available from the A and C fibre signals and from the C and E signals. A velocity is only accepted if these two measured velocities are within a certain tolerance, taken here to be 1% of each other, i.e.

$$v_p = \frac{v_{AC} + v_{CE}}{2} \qquad \text{for} \quad 2\left|\frac{v_{AC} - v_{CE}}{v_{AC} + v_{CE}}\right| \le 0.01 \tag{4.2}$$

where $v_{AC} = \lambda_{AC}/t_{AC}$ and $v_{CE} = \lambda_{CE}/t_{CE}$ (4.3)

with λ_{AC} and λ_{CE} being the effective separation distance between A and C and between C and E, respectively, and t_{AC} and t_{CE} being the corresponding transit times determined from the peak detectors.

This probe and validation procedure minimize errors caused by light reflected to transmitting fibres from different particles, a problem encountered by three-fibre probes. The

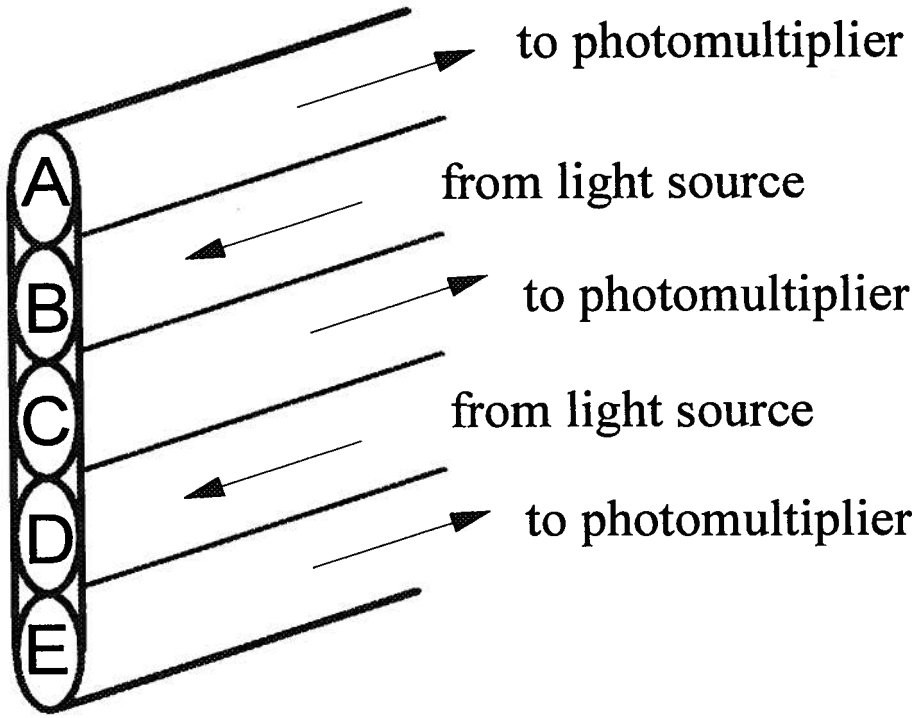

Fig. 4.2. Schematic of five-fibre optical particle velocity probe.

technique also ignores data from particles which are not travelling vertically upwards or downwards, i.e. it determines the velocity of particles travelling in a vertical direction rather than the vertical component of all particles passing the probe.

The system was calibrated by gluing some particles to a thin circular plate and then rotating the plate at different angular velocities. An oscilloscope was used to find the actual velocity of the measured particle. Thus, the effective optical distance between fibres can be obtained. The calibration indicated that the effective optical distance differs somewhat from the geometric distance between fibres. Manufacturing flaws such as fibres not being perfectly parallel and differences in fiber diameter are probably responsible for this difference. Calibration is necessary for accurate measurement.

To provide comparisons with the voidage profiles, measurements of particle velocity were taken at the same locations as the voidage measurements presented in Chapter 3, i.e. at heights of 0.25, 0.79, 1.83, 3.45, 5.13, 6.20, 7.06, and 8.98 m above the distributor. Lateral profiles were attained by performing measurements at 0.0, 26.0, 47.0, 60.0, 66.5, and 73 mm from the riser axis. The coordinates for figures are illustrated in Fig. 2.1.

Unlike the voidage measurements described in Chapter 3, a dark column is not required for the measurement of particle velocity. As for the voidage measurements, a special fitting was employed to mount the fibre optic probe to the riser so that the probe could be moved laterally without shutting down the CFB system. After the measuring system and a personal computer are hooked up, measurements can be started. For each measurement, 2000 samples are usually taken to obtain mean values for both ascending and descending particle velocities. Each measurement was repeated six times to check the reproducibility.

4.3 Experimental Results and Discussion

The particle velocity distribution determined by the fibre optic particle velocity probe for a typical case is shown in Fig. 4.3. From the optical fibre measuring system, one can obtain the velocities of both ascending and descending particles, as well as the relative numbers of particles travelling upwards and downwards.

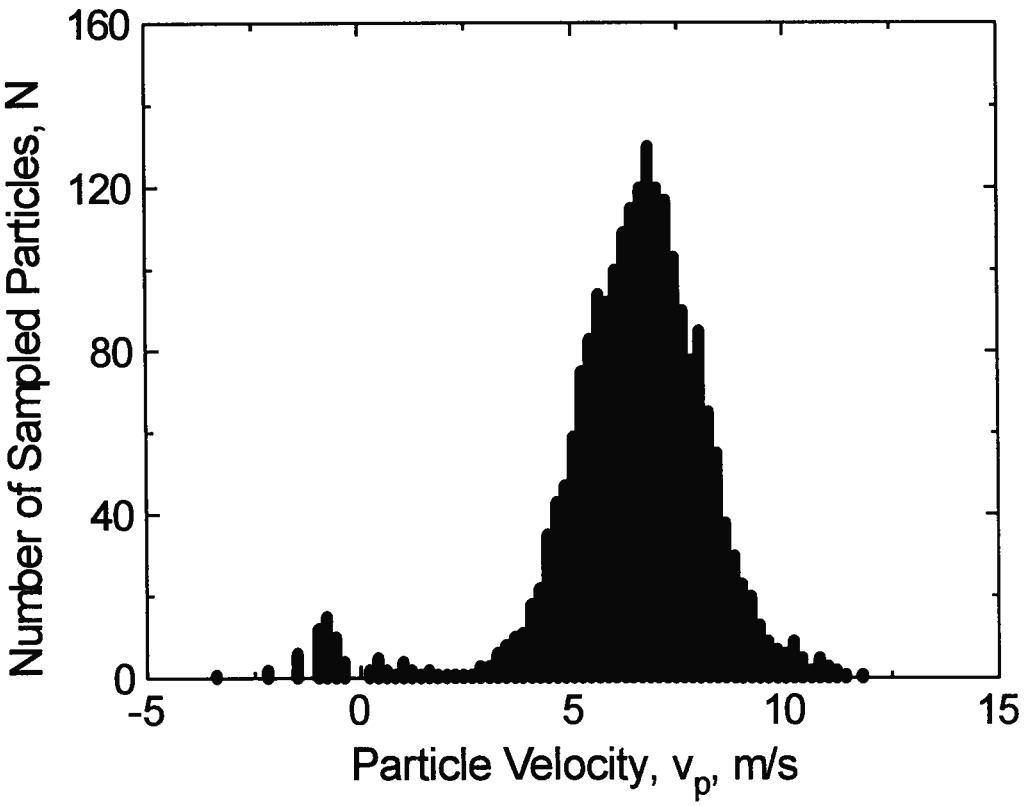

Fig. 4.3. Particle velocity distribution for U_g=5.5 m/s, G_s=40 kg/m^{2}s, x/X=0, y/Y=0, z=6.2 m. Mean particle velocities: upwards: 7.1 m/s, downwards: -1.6 m/s. Number of sampled particles: upwards: 1949, downwards: 51.

4.3.1 Lateral Profiles of Particle Velocity

Lateral profiles of vertical particle velocities are shown in Figs 4.4 and 4.5. As expected, the ascending particle velocity reached a minimum at the wall and gradually increased towards the center of the column. The non-uniformity no doubt occurs because of the no slip condition for gas, causing a lateral profile of gas velocity, and because the particle concentration is higher near the wall (Hartge et al., 1986; Weinstein et al., 1986; Hartge et al., 1988; Chapter 3). Profiles were symmetric about the axis at this height.

The influence of solids circulation rate on particle velocity profile is shown in Fig. 4.4. In the central region of the riser, the ascending particle velocity increased with increasing solids

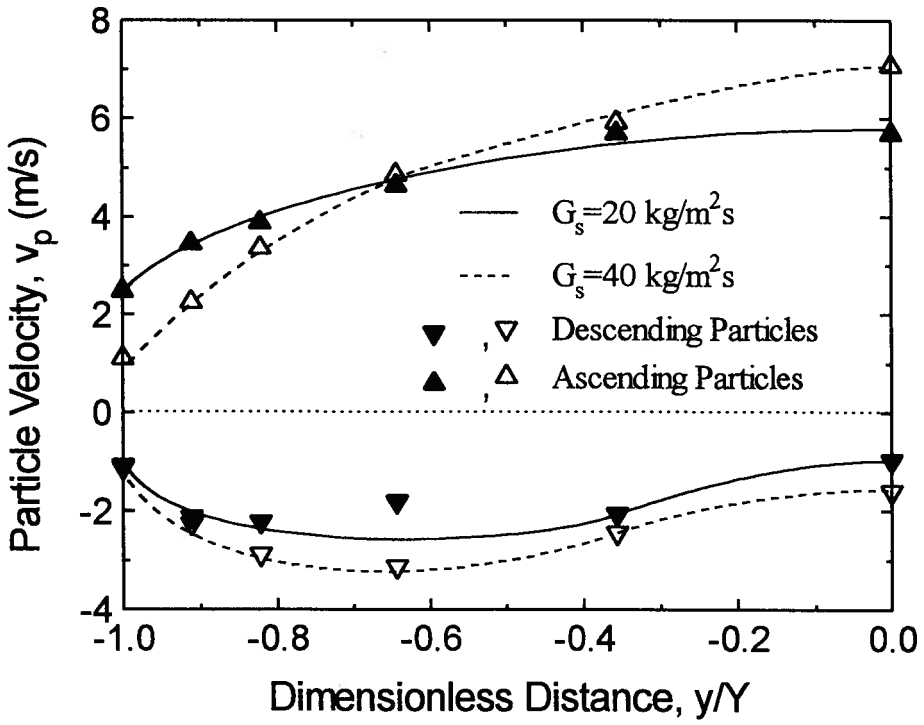

Fig. 4.4. Lateral profiles of local particle velocities for different solids fluxes: U_g=5.5 m/s, z=6.2 m, x/X=0.

circulation rate. This is because the gas velocity increases with solids circulation rate in the central region of the riser (Yang et al., 1993). Near the wall, however, the ascending particle velocity decreased with increasing solids circulation rate. As reported in Chapter 3, particle concentration increased with increasing solids circulation rate, with greater changes near the wall. Since there were more highly concentrated particles aggregates near the wall, the gas-solids slip velocity is higher there. Because the gas velocity near the wall decreases with increasing solids circulation rate (Yang et al., 1993), the ascending particle velocity decreased, while the magnitude of the descending particle velocity increased slightly with increasing solids circulation rate.

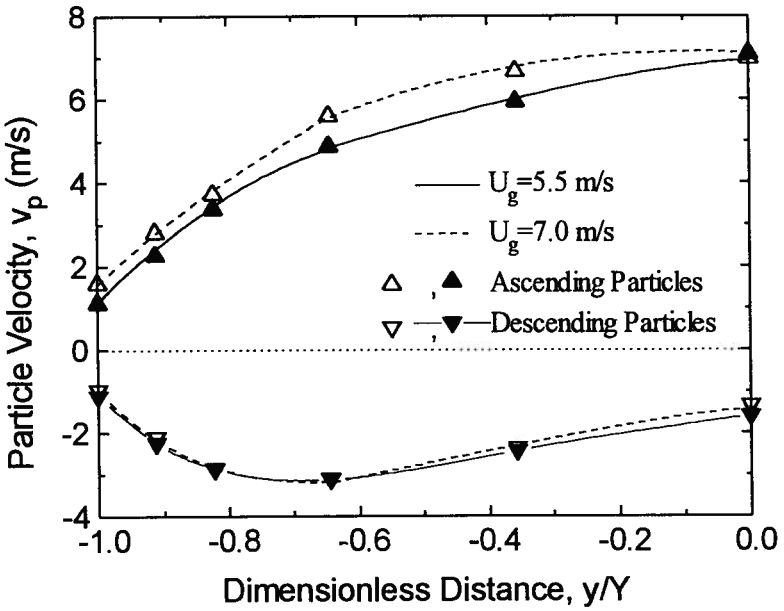

Fig. 4.5. Lateral profiles of particle velocities for different superficial gas velocities: G_s=40 kg/m^{2}s; z=6.2 m, x/X=0. For coordinates see Fig. 2.1.

Figure 4.5 shows the influence of superficial gas velocity on the lateral particle velocity profile. As expected, the ascending particle velocity increased with increasing superficial gas velocity. However, the descending particle velocity changed very little as the superficial gas velocity was varied over a limited range (5.5 to 7.0 m/s).

The lateral profiles of particle velocity in Figs 4.4 and 4.5 can be compared with the results of Hartge et al. (1988) obtained in a column of circular cross-section using an optical probe and those reported by Wang et al. (1993) using a particle dynamic analyzer. Similar trends were recorded. Near the axis, the ratio of the particle velocity at the axis to the superficial gas velocity v_p/U_g in the developed region of the riser is around 1 to 1.3. For smaller particles of lower particle terminal velocity such as FCC, v_p/U_g can be considerably higher (Bader et al., 1988; Hartge et al., 1988; Yang et al., 1993). Measurements of local average particle velocities by Yang et al. (1993) and Hartge et al. (1988) show that particle velocities decreased monotonically with radial distance, becoming negative (downwards) near the wall. This work shows that when descending and ascending particle velocities were measured separately in a column of square cross-section, the magnitude of the average velocity of descending particles increased from the wall to a maximum at around 0.7 of the half-width of the column and then decreased towards the axis.

Lateral profiles showing the local percentage of sampled particles which are being carried upwards (rather than descending) are shown in Figs. 4.6 and 4.7. The percentage of ascending particles increased from the wall to the center. Almost all particles moved upwards in the central region of the riser, while most particles moved downwards near the wall. Given the lateral particle concentration profiles presented in Chapter 3 for the same riser with the same particles, the lateral profiles of particle velocities in Figs. 4.4 and 4.5, and the profiles in Figs. 4.6 and 4.7 showing the proportions of rising and falling particles, it is clear that a core-annulus flow structure exists in a square CFB riser, as in risers of circular cross-section. In the dilute core of the riser, particles are

uniformly distributed and most particles travel upwards. Surrounding the core, there is an annular dense region near the wall where particle concentration is higher and most particles travel downwards.

As shown in Fig. 4.6, the fraction of particles which are ascending decreased significantly when the solids circulation rate was increased from 20 to 40 kg/m²s. More change was observed near the wall than in the central region. This is because the gas velocity near the wall decreases with increasing solids circulation rate (Yang et al., 1993), while the particle concentration in the same region increased greatly with increasing solids circulation rate as shown in Chapter 3. The thickness of the annular region, defined here as the distance from the wall to location where the

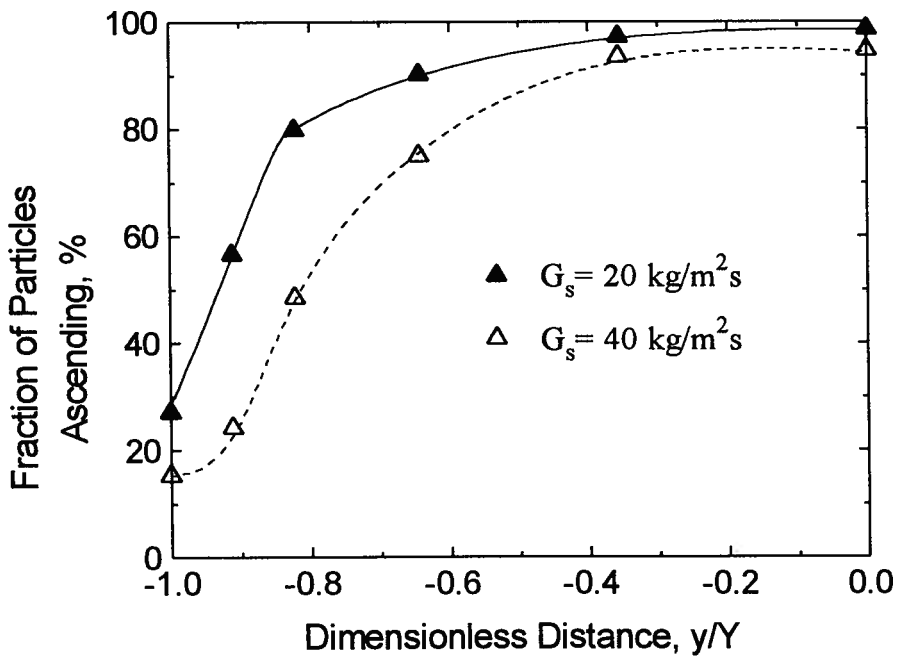

Fig. 4.6. Lateral profiles of fractions of particles travelling upwards for different solids fluxes: U_g= 5.5 m/s, z=6.2 m, x/X=0.

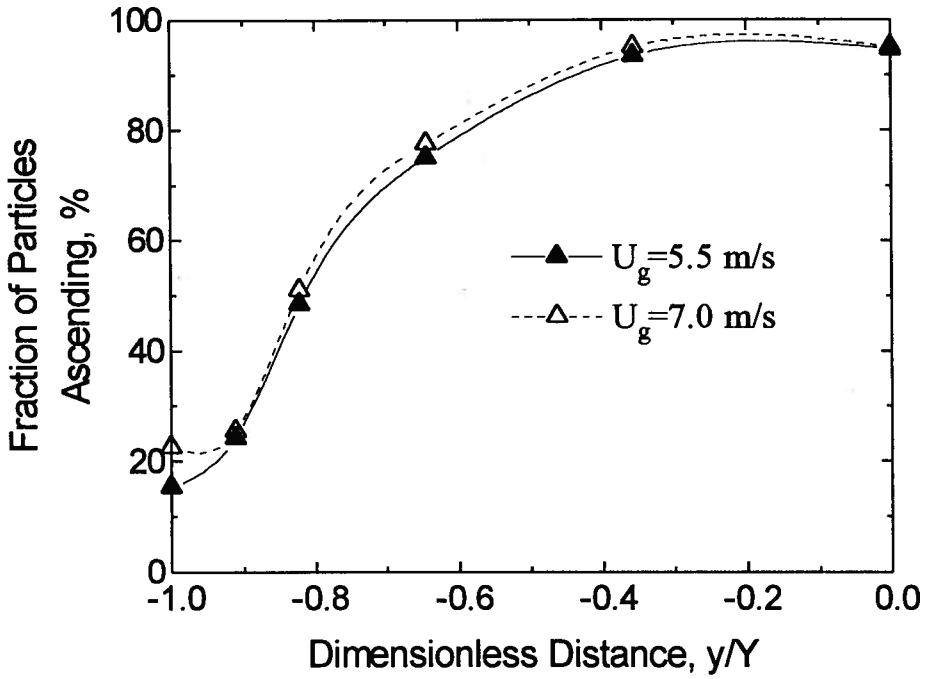

Fig. 4.7. Lateral profiles of fractions of particles travelling upwards for different superficial gas velocities: G_g=40 kg/m^{2}s, z=6.2 m; x/X=0.

vertical time-mean particle velocity is zero, also increased with increasing solids circulation rate. Therefore, more particles move downwards near the wall of the riser with increasing solids circulation rate. Figure 4.7 indicates that the superficial gas velocity had little influence on the profiles of fraction of particles travelling upwards for the conditions studied.

4.3.2 Axial Profiles of Particle Velocity

Figures 4.8 and 4.9 show axial profiles of particle velocities and sampled particle fractions at the wall and at the center of the riser respectively. The bars indicate the reproducibility of the velocity measurements based on six measurement time intervals, each producing 2000 data points.

In the developing zone at the bottom of the riser, the magnitudes of both the ascending and descending particle velocities increase with height. Similar results were obtained by Hartge et al. (1988) for a column of circular cross-section. As indicated in Fig. 4.8, there was also a deceleration zone near the exit of the riser where the magnitudes of both ascending and descending particle velocities decreased. At the wall, the fraction of particles descending increased with height at the bottom of the riser, then decreased, and finally increased again at the top of the riser. These trends are consistent with the profiles of particle concentration presented in Chapter 3.

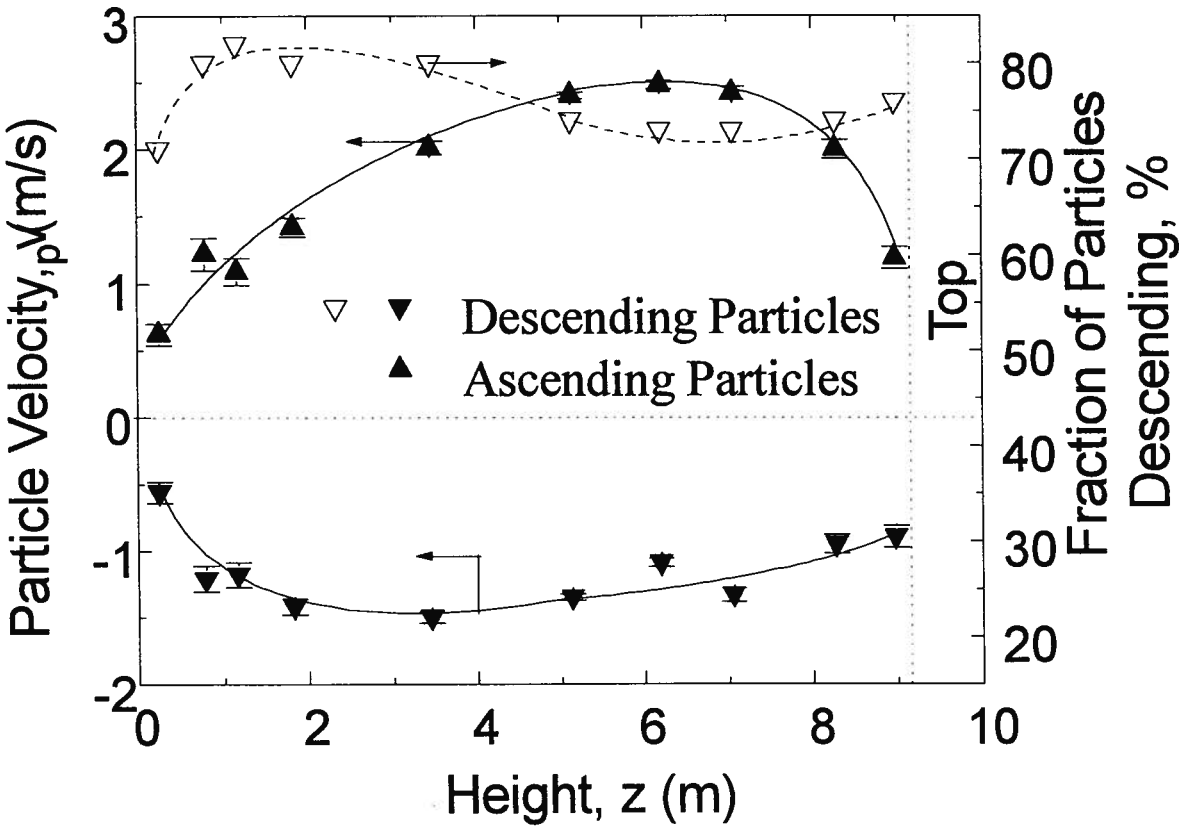

Fig. 4.8. Vertical profiles of particle velocities and fraction of particles descending along wall of column: U_g=5.5 m/s, G_s=20 kg/m^{2}s, x/X=0, y/Y=-1.

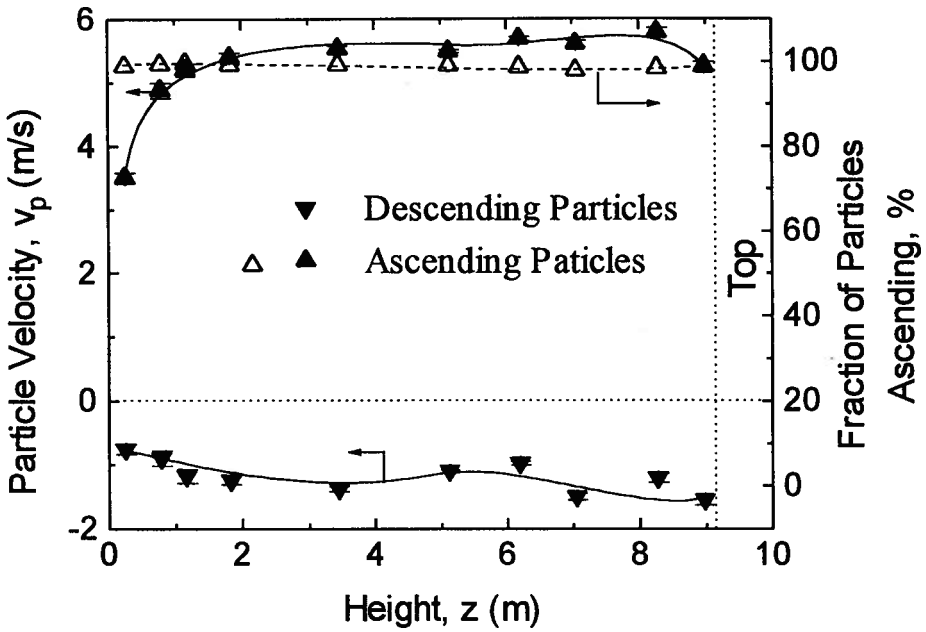

Fig. 4.9. Vertical profiles of particle velocities and fraction of particles ascending along axis of column: U_g=5.5 m/s, G_s=20 kg/m^{2}s, x/X=0, y/Y=0.

Figure 4.9 indicates that along the axis of the riser, the fraction of particles travelling upwards hardly changed with height. This is consistent with particle concentration measurements in the same column (see Chapter 3) which indicate that the particle concentration is relatively uniform in the core of the riser.

4.3.3 Wall-Layer Particle Descending Velocity

The velocities of particles descending at the wall are seen to be in the range of -0.8 to -1.5 m/s. This magnitude is similar to the magnitude of downward wall velocities summarized by Wu et al. (1990) and by Senior and Brereton (1992) for previous work by other authors with columns

of circular cross-section and is influenced very little by the operating conditions such as solids circulation rate and superficial gas velocity. However, at a small distance, e.g. 3 mm, from the wall of the riser, it was found that the magnitude of the descending particle velocity could be significantly greater than 2.5 m/s.

Downward moving clusters are generally believed (Yerushalmi et al., 1977; Brereton and Stromberg 1986; Horio et al., 1988; Hartge et al., 1988; Rhodes et al., 1990; Li et al., 1991) to form wall layers in CFB risers. In spite of the fact that the structure and motion of the clusters play very important roles with respect to such processes as heat transfer and erosion at the wall of CFB risers, the size, velocity, density and other attributes of particle clusters near the wall are not well known. Li et al. (1991) reported that the diameter of clusters is several millimeters. Clusters of dimension 2 to 3 mm* were found by Wei et al. (1993). Horio et at. (1993) illustrated, in a riser of 200 mm inner diameter, that the cluster size was roughly 1/20 to 1/10 the column diameter. Clusters as large as 15 mm* have been found by Horio et al. (1993). As demonstrated in Chapter 3, with observed particle downflow near the wall, the voidage of the wall layer is usually in the range 0.6 to 0.9.

As shown in Fig. 4.10, a cluster near the wall of a CFB riser can be modelled as a spheroidal assembly. One can then perform a force balance with five forces acting vertically: gravitational force (F_G), drag (F_D), wall friction (F_w), buoyancy (F_B), and a force F_C due to momentum exchange between the cluster and the surrounding flow. If the cluster is approximated as a spheroid with its symmetry axis oriented vertically, one can write equations for these forces as follows.

gravitational force:

* Not clear whether this is a diameter or length.

$$F_G = -\frac{4\pi}{3} a^2 b g \rho_p (1-\varepsilon_c)$$

$$= -\frac{4\pi}{3} a^3 E_r g \rho_p (1-\varepsilon_c) \tag{4.4}$$

where a and b are the horizontal and vertical semiaxes of the spheroidal cluster, respectively, E_r=b/a, g is the gravitational acceleration, ρ_p is the solids density, and ε_c is the internal voidage of the cluster.

drag force:

$$F_D = \frac{\pi}{2} C_D \rho_g a^2 u_{rel}^2 \tag{4.5}$$

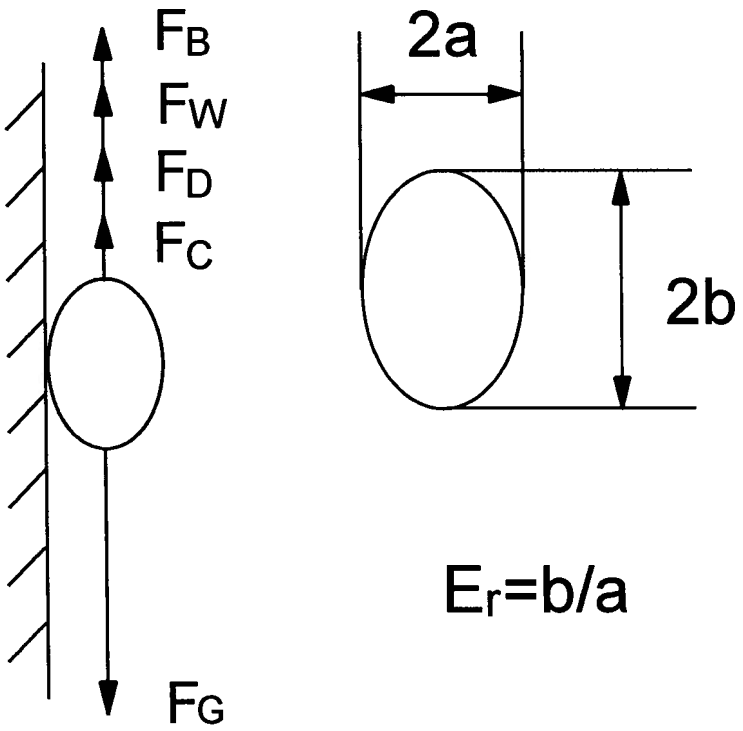

Fig. 4.10. Vertical forces on spheroidal clusters near the wall.

where u_{rel} is the relative velocity between the gas and particles, ρ_g is the density of gas, and C_D is drag coefficient. Flow of gas through the cluster has been neglected, i.e. the cluster has been treated as if it were a solid spheroid.

An expression for drag on solid spheroidal bodies was developed by Militzer et al. (1989). The correlation can be considered as a modified version of an expression for drag on spheres (Militzer et al., 1989) in which the influence of variation in shape and flow regime are accounted for:

$$C_{DS} = \left[\frac{24}{Re}(1+0.15Re^{0.687}) + \frac{0.42}{1+4.25\times10^4\,Re^{-1.16}}\right]\frac{4+E_r}{5}$$

$$\left[1.00+0.00096\frac{Re}{E_r} - 0.000754\,Re\,E_r + \frac{0.0924}{Re} + 0.00276E_r^{\,2}\right] \qquad (4.6)$$

where $Re = \frac{2\rho_g a u_{rel}}{\mu_g}$ is the Reynolds number and μ_g is the viscosity of gas. In this study, Equation (4.6) was used within its limits of applicability ($0.2 \le E_r \le 5.0$ and $1 \le Re \le 200$). Considering the influence of particle concentration (Wallis, 1969), C_D can be estimated from the drag coefficient of single spherical particle C_{DS} as:

$$C_D = C_{DS}\,\varepsilon_{out}^{-4.7} \qquad (4.7)$$

where ε_{out} is the effective outer voidage of clusters which can be calculated as

$$\varepsilon_{out} = \frac{\varepsilon - \varepsilon_c}{1-\varepsilon_c} \qquad (4.8)$$

where ε is the overall local voidage as measured by the fibre optic voidage probe. Since there is

no correlation available to calculate C_D for spheroidal particles considering the influence of particle concentration, Equation (4.7) is employed here to estimate the effect of multiple clusters.

wall friction force

$$F_W = \pi E_r a^2 \tau \tag{4.9}$$

where τ is shear stress on the cluster, N/m^2. Figure 4.11 shows the shear stress on the wall due to descending particle flow determined by Van Swaaij et al. (1970). Assuming $u_c=v_p$, a linear regression has been done to obtain the following correlation:

$$\tau = k\rho_p(1-\varepsilon)u_c \tag{4.10}$$

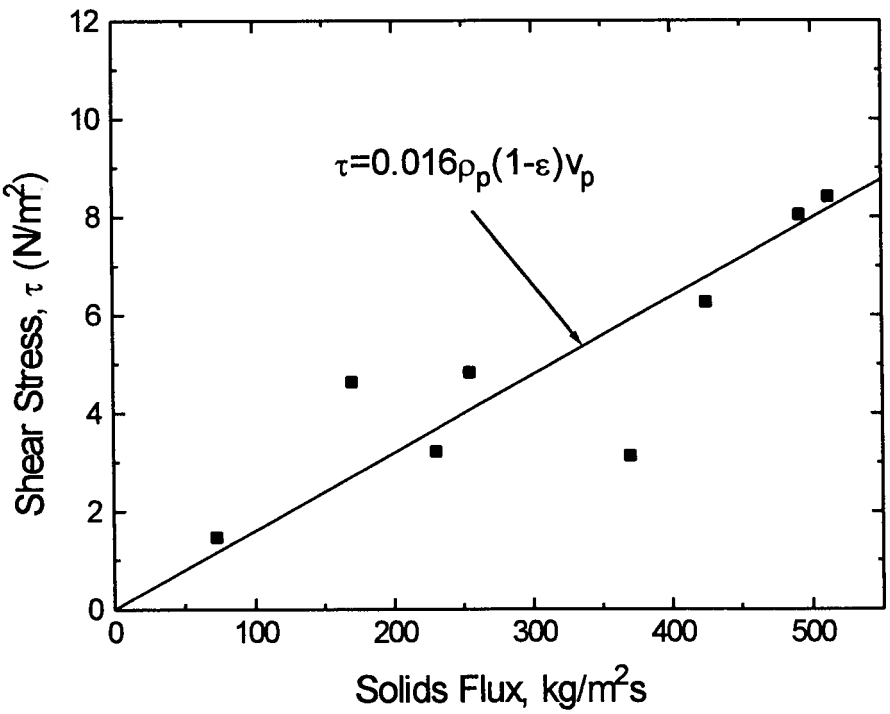

Fig. 4.11. Shear stress on the wall of the riser by downflowing particles vs. solids flux adapted from Van Swaaij et al. (1970).

where τ is shear stress, N/m^2; k=0.016 is a constant, m/s and u_c is the velocity of the cluster, m/s. Assume gas velocity is zero, $u_c=u_{rel}$.

The rate of momentum transfer required to accelerate the cluster by collisions is equal in magnitude to the decelerating force on the surrounding flow. Assume particles entering the cluster collide with all particles in the unit. The force on the cluster is then:

$$F_C = G_{ho}(u_c - v_{pc})(\pi ab)$$

$$= G_{ho}(u_c - v_{pc})(\pi a^2 E_r) \tag{4.11}$$

where G_{ho} is the lateral solids flux from the adjacent dilute phase to the cluster flow, and v_{pc} is the vertical velocity of solids entering the cluster.

buoyancy

$$F_B = -\frac{4\pi}{3} a^2 b\, g\rho_g (1-\varepsilon_c)$$

$$= -\frac{4\pi}{3} a^3 E_r\, g\rho_g (1-\varepsilon_c) \tag{4.12}$$

When the cluster near the wall reaches its terminal velocity, we have:

$$F_G - F_D - F_W - F_C - F_B = 0 \tag{4.13}$$

To solve the non-linear equation, Equation (4.13), for the cluster velocity, u_c, the Newton-Raphson method was employed. v_{pc} in Equation (4.11) is assumed zero based on the fact that the vertical particle velocity at the boundary between the core and annulus can be taken as zero (see section 4.3.4 below). According to cross-flow measurements presented in Chapter 7, the solids flux entering the annulus from the core is of order 1/10 of the solids circulation rate. For both

Ottawa sand particles of particle density ρ_p= 2640 kg/m^3 and mean size $\bar{d}_p$=213 μm and FCC particles of ρ_p= 1600 kg/m^3 and $\bar{d}_p$=70 μm, the cluster descending velocity was calculated from the force balance as a function of the voidage and the diameter of the cluster for U_g=5.5 m/s and G_s=40 kg/m^{2}s. The relative contributions with the various force terms for a cluster of E_r=1, ε =0.8, ε_c=0.7 and a=3 mm are listed in Table 4.1.

Table 4.1 Relative contributions of each force component for a cluster of E_r=1, ε=0.8, ε_c=0.7 and a=3 mm, assuming F_G=1.

	Ottawa Sand	FCC
F_G	1	1
F_C	0.47	0.56
F_W	0.42	0.32
F_D	0.11	0.12
F_B	<0.001	<0.001

The model results for spherical clusters of both Ottawa sand and FCC particles are shown in Figs 4.12 and 4.13. It is seen that in addition to the particle density, the size and the internal voidage of the cluster are also very important parameters influencing the descending velocity of clusters. With increasing cluster diameter, the predicted descending velocity increases. The effect of decreasing internal cluster voidage is to increase the descending velocity of the cluster. Near the wall of CFB risers, clusters of large and/or dense solids have greater descending velocity.

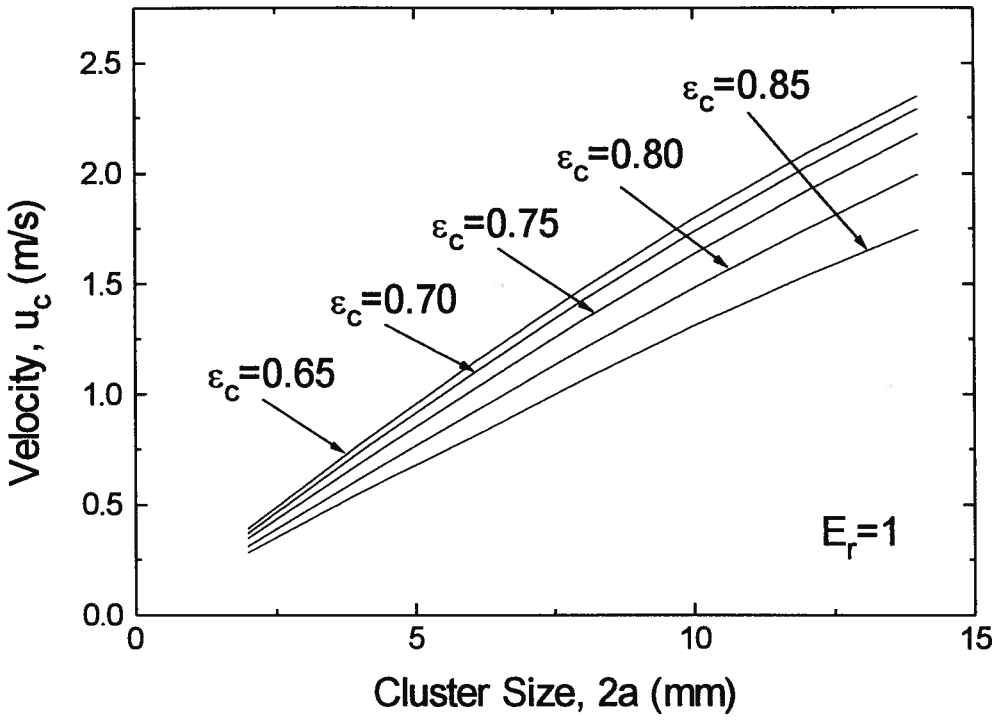

Fig. 4.12. Simulation of the descending velocity of a spherical cluster, i.e. E_r=1, vs. diameter and cluster internal voidage for Ottawa sand particles: ε=0.9, U_g=5.5 m/s and G_s=40 kg/m^{2}s.

Comparison of Figs 4.12 and 4.13 indicates that for the same size and voidage, Ottawa sand clusters have higher velocities of descent than FCC clusters.

From the voidage measurements in the developed region given in Chapter 3, the time-mean voidage near the wall for U_g=5.5 m/s and G_s=40 kg/m^{2}s is around 0.9; and ε_c is roughly 0.85. The measured particle descent velocity near the wall is in the range of 0.8 to 1.5 m/s from Fig. 4.12. The corresponding cluster size 2a is in the range of 6.5 to 12 mm which is in reasonable accord with the experimental data of Horio et al. (1993). In general, the model predictions for

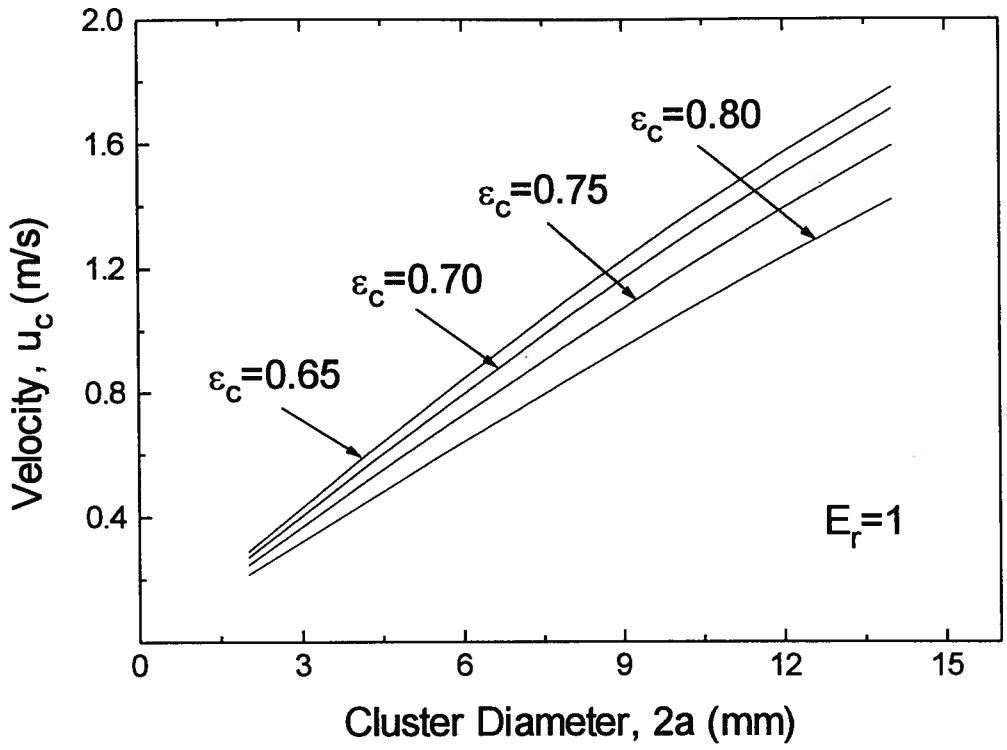

Fig. 4.13. Simulation of the descending velocity of a spherical cluster, i.e. E_r=1, vs. diameter and cluster internal voidage for FCC particles: ε=0.9, U_g=5.5 m/s and G_s=40 kg/m^{2}s.

both Ottawa sand and FCC particles agree well with experimental results of other researchers as indicated in Table 4.2.

Since clusters in CFB risers are not spherical, simulation has been done to test the sensitivity of the descending cluster velocity to its aspect ratio. With clusters taken as spheroidal with vertical axis of symmetry, the ratio of vertical semiaxis to horizontal semiaxis, E_r, was varied from 0.5 to 5, covering the range in which the correlation for drag coefficient C_D, i.e. Equation (4.6), is applicable. Calculations have been made for both Ottawa sand and FCC particles with

ε_c=0.75 and horizontal semiaxis a=6 mm. The simulation results are shown in Fig. 4.14. It is seen that the descending cluster velocity increases with E_r which means the longer the cluster, the faster it descends because the drag coefficient C_D decreases with increasing E_r. However, for E_r>1, since F_c and F_w increase with E_r because of the increase in surface area, no dramatic change in u_c with E_r is predicted.

Table 4.2. Descending particle velocities near the wall of CFB risers measured by various researchers.

	Riser size	Measuring method	d_p (μm)	ρ_p (kg/m^3)	U_g (m/s)	G_s (kg/m^3)	u_c (m/s)
Horio et al. (1988)	300 mm id	Fibre optic probe	60	1000	1.17, 1.29	11.7, 11.25, 11.75	0.5-1.8
Bader et al. (1988)	305 mm id	Pitot tube	76	800	3.7 - 6.1	98 - 195	0.5-1.8
Hartge et al. (1988)	400 mm id	Fibre optic probe	85, 120	1500, 2600	2.9, 3.7	30, 49	0.5-2.0
Ishii et al. (1989)	N.S.	Fibre optic probe	N.S.	N.S.	1.29	N.S.	0.6-1.1
Wu et al. (1989)	152 mm id	High-speed cinematography	171	2650	7	N.S.	1.26
Wirth et al. (1991)	170 x 170 mm^2	Video camera	50, 90, 200	N.S.	1.9	N.S.	2
Yang et al. (1992)	140 mm id	LDV	54	1550	1.8 - 4.3	22 - 92	0.5-1.2
Rhodes et al. (1992)	305 mm id	High-speed video camera	74.9	2456	3 - 5	2 - 80	1.0

N.S.=not specified.

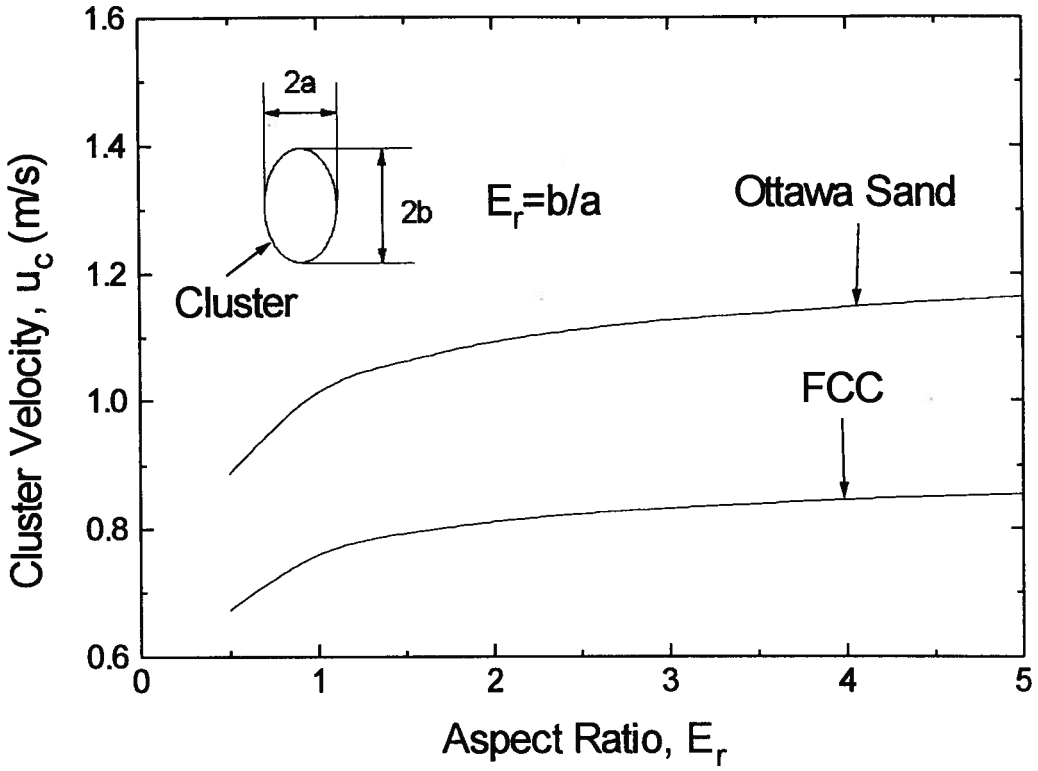

Fig. 4.14. Predicted velocity of downflowing particle clusters near the wall vs. height-to-width ratio, E_r, for ε_c=0.75 and a=6 mm.

4.3.4 Core-Annulus Boundary

CFB risers of both circular and rectangular cross-section are commonly described in terms of a core-annulus flow structure, where there is a dilute core in which most particles travel upwards surrounded by a dense annular wall layer in which most particles move downwards. However, there is a lack of consistency in the way that the boundary between the core and the

annular wall layer has been defined by different researchers. To be able to compare results from the literature, it is important to adopt a common definition.

There are two common ways of determining the boundary between the core and the annular downflow wall layer. One group of researchers (Hartge et al., 1988; Ishii et al., 1989; Yang et al., 1992) defined the boundary between the core and the annular wall layer as the location where the time-average vertical particle velocity is zero. Others (Rhodes et al., 1988; Herb et al., 1992; Miller and Gidaspow, 1992) measured vertical solids fluxes, usually by means of solids sampling probes, and defined the core-annulus boundary as the location where the vertical net solids flux is zero

The time-mean vertical component of particle velocity and voidage are given by

$$\bar{v}_p = \frac{1}{T}\int_0^T v_p dt \tag{4.14}$$

and $$\bar{\varepsilon} = \frac{1}{T}\int_0^T \varepsilon dt \tag{4.15}$$

while the local vertical solids flux is

$$G_s = \frac{\rho_p}{T}\int_0^T v_p(1-\varepsilon)dt \tag{4.16}$$

Only if v_p and ε are uncorrelated would it be possible to write

$$G_s = \rho_p \bar{v}_p(1-\bar{\varepsilon}) \tag{4.17}$$

However, there is considerable evidence that there is a strong correlation between the instantaneous local voidage, ε , and the vertical component of particle velocity, v_p, especially in the vicinity of the wall where periods of upward solids velocity (positive v_p) tend to be associated

with high local voidage while downward moving particles (negative v_p) tend to be associated with streamers and clusters, and hence lower ε. Given this, equation (4.17) is not expected to be valid, meaning that G_s and $\overline{v}_p$ are not proportional to each other and are unlikely to reach 0 at the same location.

Experiments with a sampling probe were carried out to measure the core-annulus boundary defined in terms of the location of zero vertical solids flux. The sampling system is illustrated in Fig. 4.15. The inside diameter of the sampling probe is 6.5 mm. A graduated cylinder served as sample collector so that the amount of sample obtained in a certain time period can be read directly from the graduations. During sampling, two valves shown in Fig. 4.15 were fully open and particles are carried from the riser to the collector through the sampling probe due to the pressure difference between the inside and the outside of the CFB riser. The upward and downward solids fluxes were measured by pointing the open end of the probe downwards and upwards, respectively. The net vertical solids flux was determined from the difference between the upward and the downward solids fluxes.

Bierl et al. (1980) found that isokinetic sampling is not necessary under conditions of relatively dilute flow of large CFB particles of 61 μm. Rhodes (1990), Miller and Gidaspow (1992) investigated the influence of the suction velocity of the sampling probe and found that nonisokinetic sampling probe can be employed in CFB risers to measure the net vertical solids flux. A non-isokinetic sampling system has been employed to measure the net vertical solid flux in this study.

The particle velocity data, coupled with the data for the voidages from Chapter 3 and the fractions of particles ascending and descending, allows the relative upward and downward fluxes and the thickness of the downflowing annulus layer to be determined. The axial profile of the

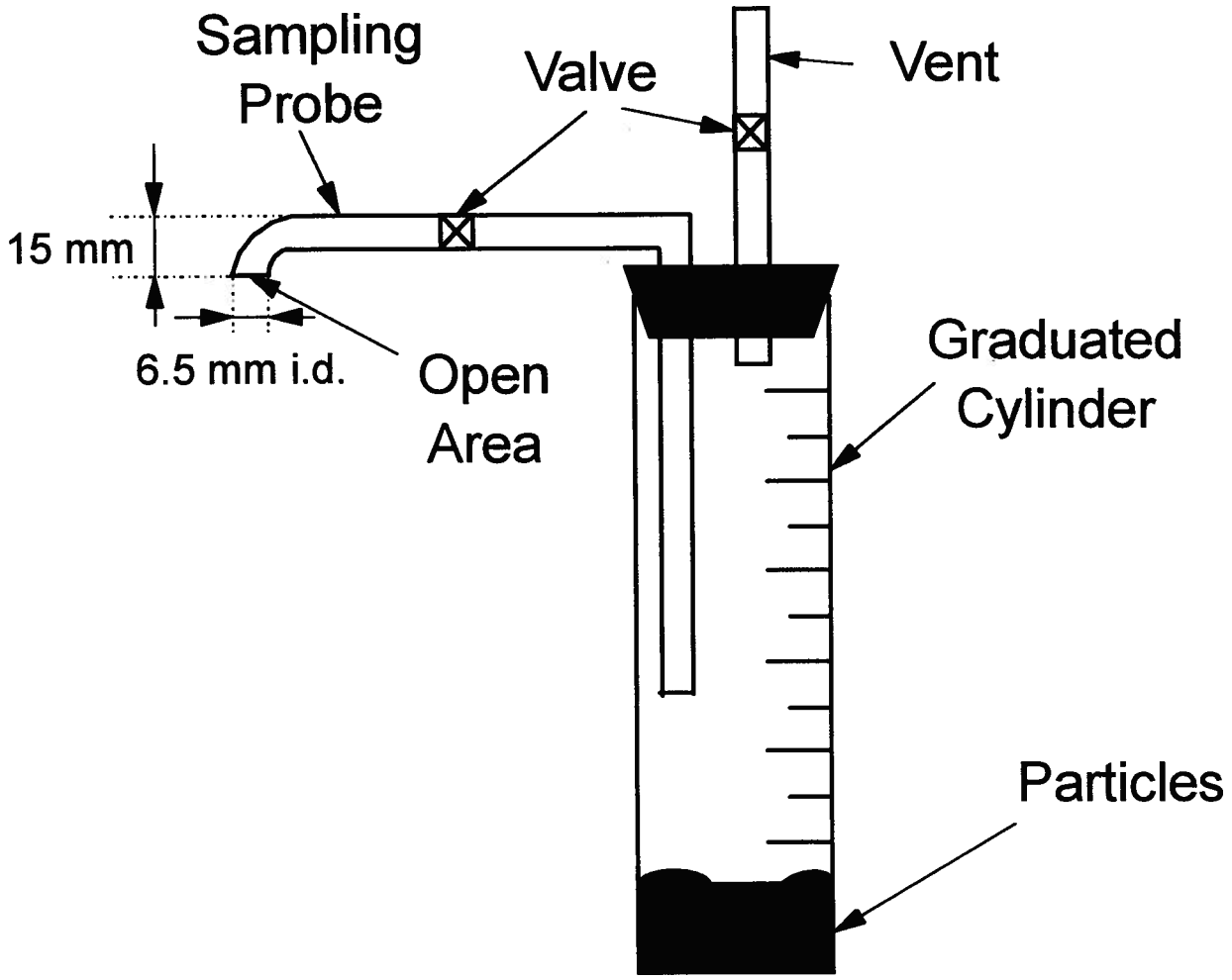

Fig. 4.15. Schematic of the sampling system to measure net vertical solids flux.

annulus thickness for U_g= 5.5 m/s and G_s= 40 kg/m²s is shown in Fig. 4.16. The core/annulus boundary has been taken as the location where the time-mean particle velocity is zero. Figure 4.16 also shows the axial profiles of wall layer thickness obtained from solids flux measurements. It is seen that, along the entire height of the riser, the wall layer obtained from the flux measurement is

always thicker than from the vertical velocity measurement. The difference between the two wall layer thicknesses decreases with height near the bottom and increases in the upper part of the riser. Recall that near the bottom of the riser, there is a particle acceleration region, while near the top, there is a deceleration region.

As indicated in Fig. 4.16, the wall layer thicknesses determined from both measurement techniques first decreased with height from the bottom until a minimum was reached about 4 m above the distributor, then increased towards the top. Near the bottom, the net lateral solids flux must have been outwards towards the wall of the riser, causing the annulus thickness to increase as the wall layers descended towards the bottom. On the other hand, in the upper portion of the

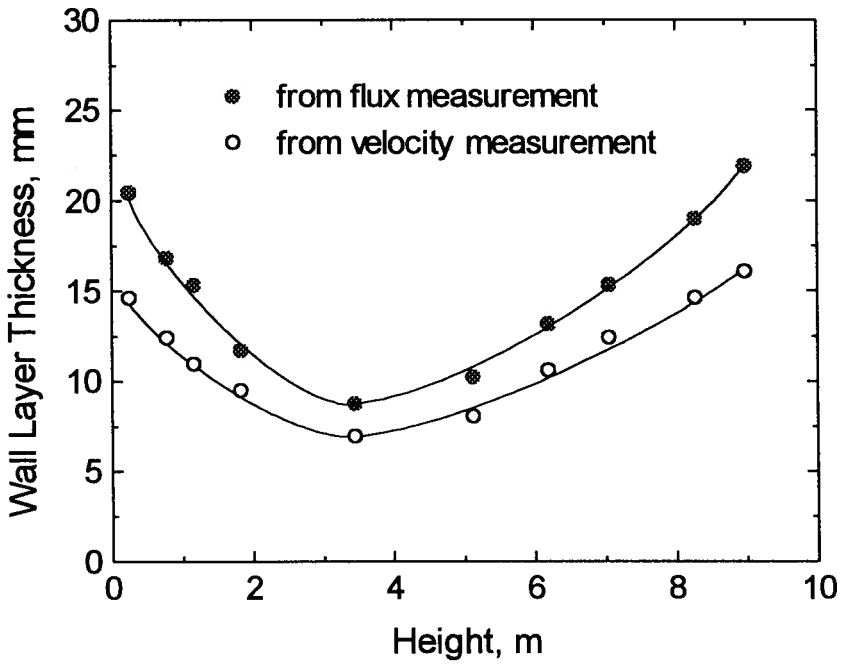

Fig. 4.16. Axial profiles of annular wall layer thickness for U_g=5.5 m/s, G_s= 40 kg/m^{2}s, x/X=0.

riser, many particles reaching the top are reflected downwards along the wall. Net solids fluxes were then inwards towards the axis of the column as wall layers are stripped of particles as they descend.

Figure 4.17 plots the wall layer thickness versus lateral position along the wall. The difference between the measured wall layer thicknesses from the two methods is greatest near the corner of the riser. Figures 4.16 and 4.17 clearly indicate that there is a significant difference between the zero vertical particle velocity boundary and the zero-vertical-net-solids-flux boundary in CFB risers. This difference must be considered when comparing data obtained using the two different techniques.

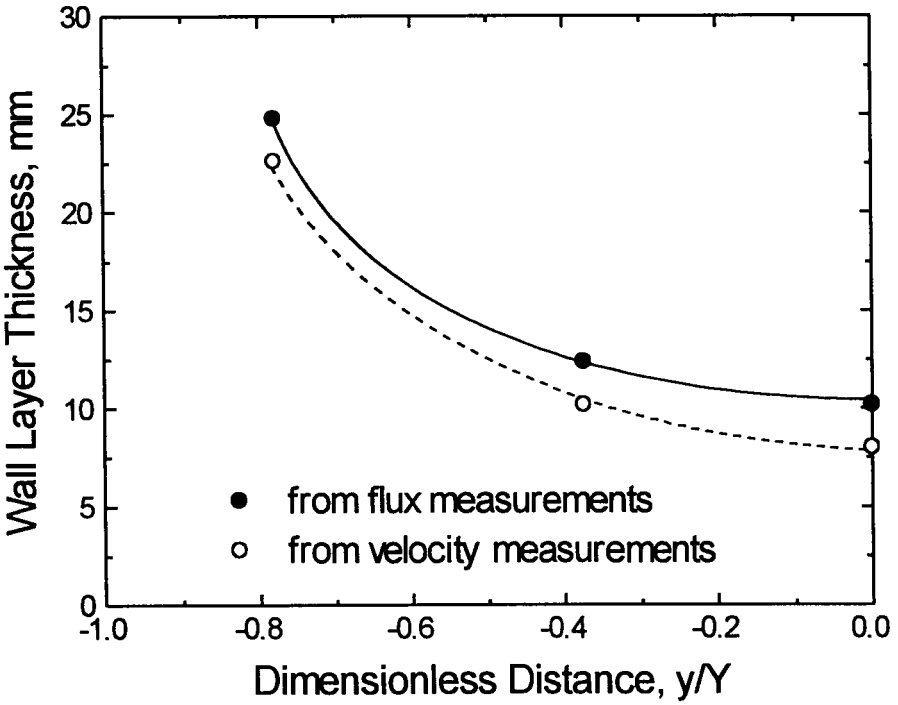

Fig. 4.17. Lateral profiles of annular wall layer thickness for z=5.13 m, U_g=5.5 m/s, G_s= 40 kg/m^{2}s.

Although the axial and lateral distributions of the core-annulus boundary obtained from the two measurement methods exhibit similar trends, it is believed that the core-annulus boundary is better defined as the location where the vertical net solids flux is zero because the core-annulus flow structure is usually described as a core where most particles travel upwards surrounded by an annular wall layer where particles generally travel downwards. However, in the following paragraphs only the results based on measurements from the fibre optic particle velocity probe are presented, because this chapter mainly discusses particle velocity.

Figure 4.18 shows that the mean ascending particle velocity near the corner was somewhat lower, while the magnitude of the descending particle velocity in the corner was higher than mid-way between opposite walls. The same trend was obtained at a height of 6.20 m. The magnitudes of the velocities of the descending particles at z=5.13 and 6.20 m were around 1.8 m/s. Wang et al. (1993) found that instantaneous particle velocities in the corners of a square riser did not exhibit any systematic trend, while the results given above are time-average values. As noted in Chapter 3 and consistent with the relative numbers of ascending and descending particles, the particle concentration in the corner was relatively high because descending particles are well protected in the corners where the gas velocity is reduced. Since the wall layer is thicker in the corner, the effective cluster size is expected to be greater than elsewhere along the wall. According to the theoretical model, the descending velocities of clusters in the corner must be higher because of lower cluster voidages and larger cluster sizes.

To check the accuracy of the experimental data, net solids fluxes were estimated by integration using the voidage profile data from Chapter 3, together with particle velocity profiles and fractions of particles rising and falling from this chapter, all for U_g = 5.5 m/s. The integrated values of net solids fluxes are 37.2 and 38.0 kg / m^2s for heights of 5.13 and 6.2 m with G_S= 40

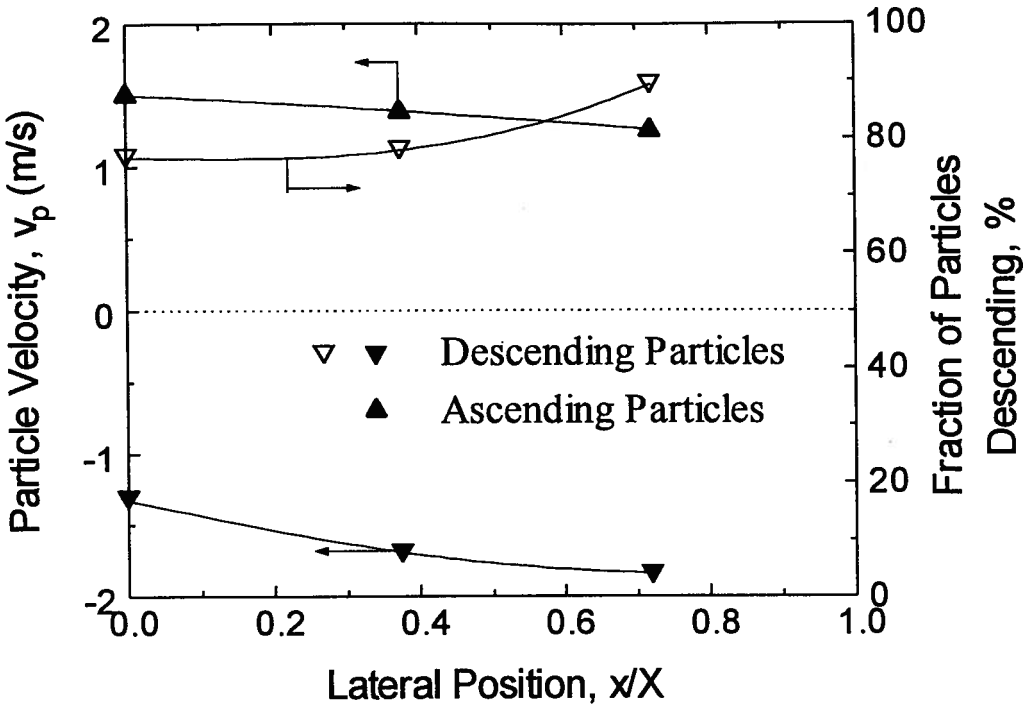

Fig. 4.18. Lateral profiles of velocities and fraction of particles descending near the wall of column: U_g=5.5 m/s, G_s=40 kg/m^{2}s, z=5.13 m, y/Y=1.

kg/m^{2}s, and 19.1 kg/m^{2}s for z=6.2 m with G_S= 20 kg/m^{2}s. The calculated fluxes are sufficiently close to the preset values of G_s that they add to the confidence in the data.

Lateral profiles of mean vertical particle velocity appear in Fig. 4.19. Particles near the wall are seen to travel mostly downwards, while most particles are conveyed upwards in the core. In the corner, particles moved downwards faster and the thickness of the downflow wall layer was greater than mid-way between facing walls. Wall layer thicknesses based on the values of y/Y where v_p=0 are shown in Fig. 4.20 for U_g=5.5 m/s and G_s=40 kg/m^{2}s.The shape of the outer wall layer is indicated in the insert. Note the increased thickness of the wall layer in the corners.

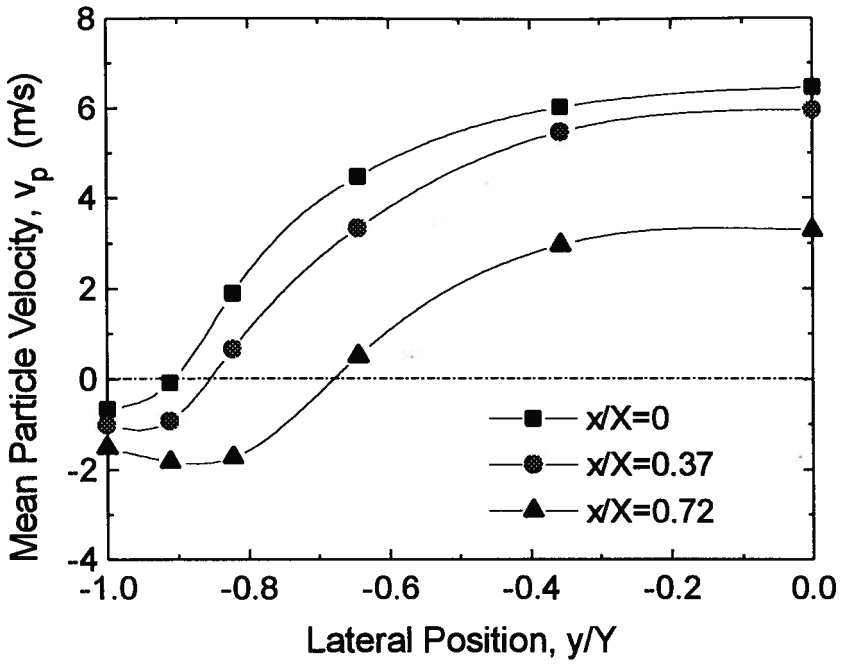

Fig. 4.19 Lateral profiles of mean particle velocity: z=5.13 m, U_g=5.5 m/s, G_s=40 kg/m^{2}s.

The magnitudes of the average particle velocity in the core for the developed region have been compared with the predictions of a semi-empirical hydrodynamic model developed by Senior and Brereton (1992). This model assumes a constant voidage and a constant downward particle velocity in an outer annular layer, with a uniform dilute suspension in the core where particles travel upwards at a constant velocity equal to the core gas superficial velocity minus the terminal settling velocity. The wall layer thickness is assumed to be uniform at any height. The gas velocity is assumed to increase linearly from the wall in the annulus region and to be constant in the core. The predicted average particle velocity in the core of the developed region for U_g=5.5 m/s and G_s=40 kg/m^{2}s is around 4.0 to 4.2 m/s for conditions corresponding to the riser employed in the

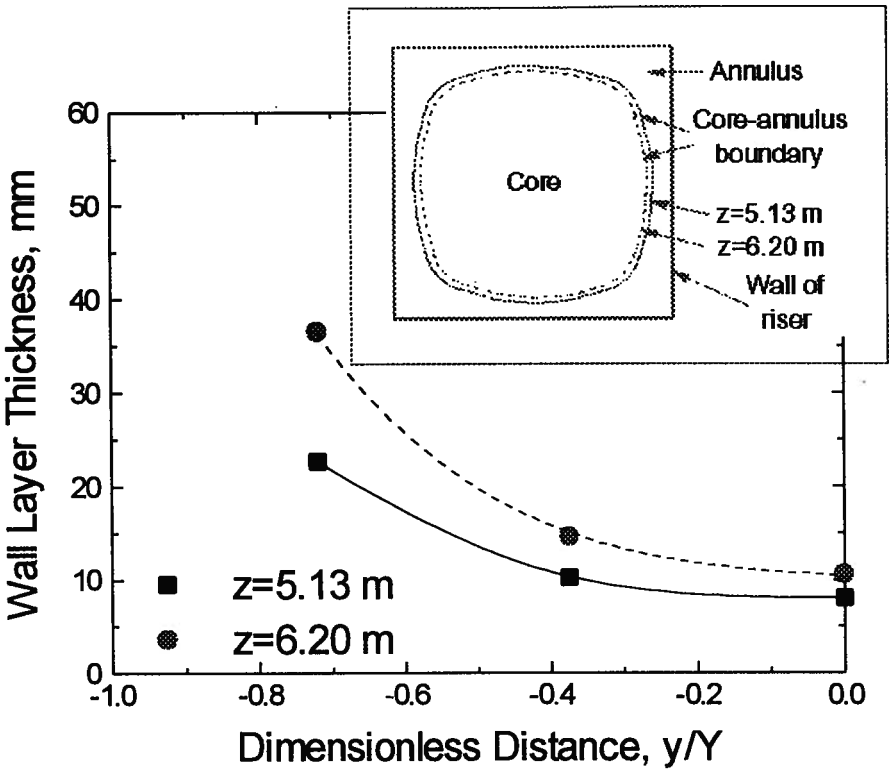

Fig. 4.20. Lateral profiles of annular wall layer thickness for: U_g=5.5 m/s, G_s=40 kg/m^{2}s. Insert shows shape of wall layer boundary at two different heights assuming symmetry around axes.

present study, except near the top. The corresponding experimental average particle velocity in the core was in range of 3.5 to 4.2 m/s, in good agreement with the predictions. On the other hand, the thickness of the annular wall layer for the developed region calculated from the model was several times smaller than the experimental value.

4.3.5 Exit Effect

Lateral profiles of particle velocities and fraction of sampled particles ascending near the top of the riser are presented in Fig. 4.21. Because of the presence of the exit, these profiles are not symmetric around y/Y=0. Instead, the location of the maximum ascending particle velocity is shifted somewhat to the exit side. Also, the thickness of the annular wall layer obtained by measuring particle velocity was thinner on the exit side than on the opposite side. In the annular zone, the magnitude of the average velocity of descending particles was smaller on the exit side than on the opposite side. These results are consistent with the gas flow pattern for an abrupt exit proposed by Brereton (1987).

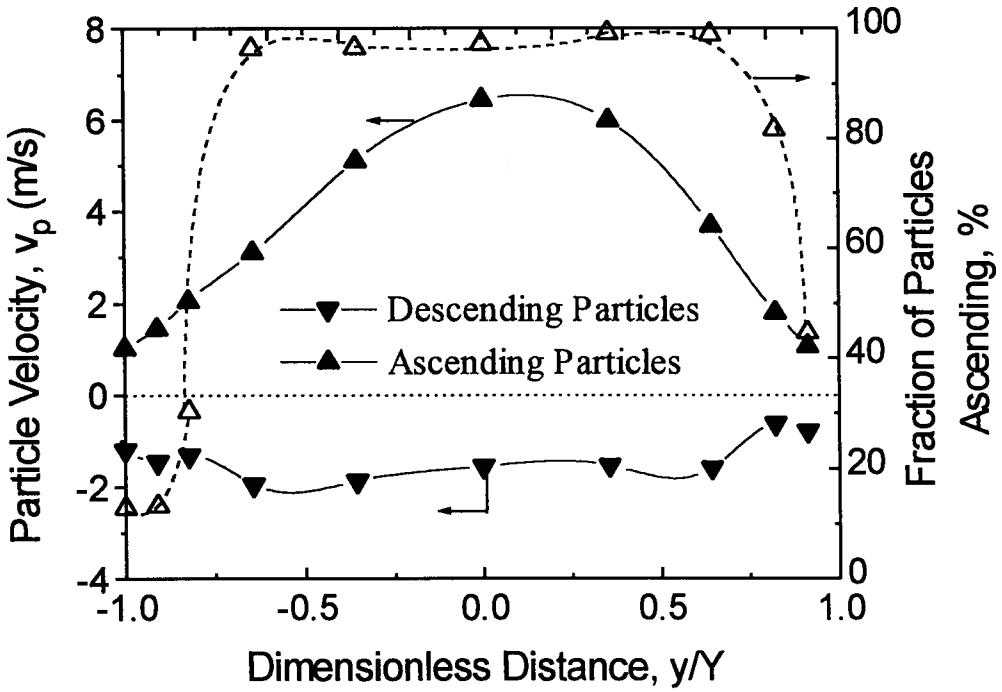

Fig. 4.21. Lateral profiles of particle velocities and fraction of particles ascending at top of column: U_g=5.5 m/s, G_s=40 kg/m^{2}s, z=8.98 m, x/X=0.

Figure 4.22 shows the influence of solids circulation rate on the lateral profiles of particle velocities at the top of the riser. With increasing solids circulation rate, the ascending particle velocity in the center of the riser increased, and the location of the peak corresponding to the maximum ascending particle velocity shifted slightly towards the exit side. The magnitude of the descending particle velocity also increased somewhat with increasing solids circulation rate.

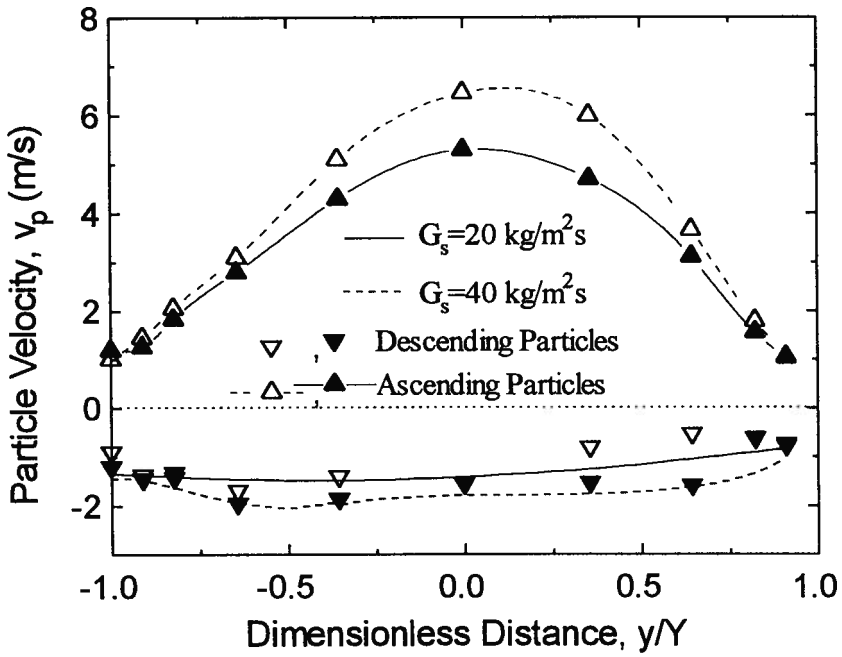

Fig. 4.22. Lateral profiles of local particle velocities at top of column for different solids fluxes: U_g=5.5 m/s, z=8.98 m, x/X=0.

4.4 Summary

An optical particle velocity measuring probe made of five 200 μm silicon optical fibers was used to measure vertical particle velocity and the fractions of ascending and descending particles. The probe was 2 mm in diameter and 0.3 m in length with a 10 mm long head of cross-section 0.5 mm by 1.8 mm.

As expected, the ascending particle velocity was lower at the wall and it gradually increased towards the center of the column. In the central region of the riser, the ascending particle velocity increased with increasing solids circulation rate. Near the wall, the ascending particle velocity decreased while the descending particle velocity increased slightly with increasing solids circulation rate. The ascending particle velocity increased with superficial gas velocity. However, the descending particle velocity did not change much as the superficial gas velocity was varied from 5.5 to 7.0 m/s, showing a small drop.

The particle velocity data, coupled with the data for the ascending and descending particles, allows the relative upward and downward fluxes and the thickness of the annulus layer to be determined. The annulus thickness first decreases from the bottom until a minimum is reached 3 to 4 m above the distributor, then increased towards the top. The wall layer thickness was greater when based on solids flux measurements than when based on the position where the time-mean particle velocity was zero. The percentage of particles which are ascending increased from the wall to the axis. The fraction of particles descending increased significantly when the solids circulation rate was increased from 20 to 40 kg/m^2s. The annulus thickness also increased with solids circulation rate.

In a developing zone at the bottom of the riser, both upward and downward particle

velocities were found to increase with height. The development length on the axis of the riser was less than at the wall. The presence of the exit led to asymmetric profiles of particle velocities and of the fractions of sampled ascending particles at the top of the riser. The location of the maximum upward particle velocity shifted somewhat to the exit side, while the annular wall layer was thinner on the exit side than on the opposite side. In the annular zone, the magnitude of the velocity for descending particles was smaller on the exit side than on the opposite side.

The ascending particle velocity was lower near the corner, while the descending particle velocity was greater than mid-way between facing walls. Towards the corner, a greater fraction of particles moved downwards. The downward particle velocities at the wall were in the range 0.8 to 1.5 m/s, influenced very little by solids circulation rate and superficial gas velocity. However, at a small distance, e.g. 3 mm, from the wall of the riser, the downward particle velocity could be significantly higher.

A theoretical model has been established to predict the descending cluster velocity near the wall of the riser. The simulation results show that the descending velocity increases with the size and the density of clusters. Clusters of Ottawa sand particles are predicted to have higher descending velocities than clusters of FCC particles. Elongated clusters are predicted to descend more quickly than spherical ones of similar cross-sectional area.

Chapter 5

Influence of Wall Roughness on the Hydrodynamics

5.1 Introduction

In Chapters 3 and 4 basic hydrodynamics, i.e. voidages and particle velocities, in the CFB riser are discussed. All these results are for a riser with smooth inside wall surfaces. However, the inner surfaces of commercial CFB reactors can be quite rough (e.g. in CFB combustors with refractories), with roughness elements sometimes exceeding particle diameter by several times. Roughness could have a significant influence on the hydrodynamics, which could in turn alter mixing, gas-solids contacting and heat and mass transfer in circulating fluidized bed processes.

Glicksman et al. (1991) reported that protrusions as small as one particle diameter can cause a change in the particle concentration in a circulating fluidized bed. Protrusions were believed to lead to an increase in solids concentration at the top of a hot column. No other early work has been reported on this topic.

An experimental study has been carried out on hydrodynamics in a riser with rough inner walls. Fiber optic probes were employed to measure particle concentrations and particle velocities. Both probes could be moved horizontally at a series of ports along the riser wall. The probes are described in Chapters 3 and 4. In this chapter, the influence of wall roughness is determined by comparing the experimental results from a riser having rough inside wall surfaces with corresponding results from the earlier chapters for the same riser with smooth inner surfaces.

5.2 Experimental Set-up

Sheets of sand-paper were affixed to all four inner walls of the riser, from the bottom to the top, to provide a rough wall surface. The walls were completely covered, i.e. including the plexiglass windows. Double-sided tape was used to affix the sand-paper to the walls. The top of the column was also covered with sandpaper.

Wirth et al. (1991), using a γ-ray technique and Lints and Glicksman (1993), using a particle impact probe, reported that a gas layer exists between downward-moving particle swarms and the wall. They claim that the thickness of this gas layer is usually less than one particle diameter. The protrusions which were found by Glicksman et al. (1991) to influence the hydrodynamics were of order one particle diameter thick. In circulating fluidized bed combustors, the refractory roughness may be greater than 10 times the particle size. In large-scale industrial CFB units wall roughness is likely to influence hydrodynamics primarily near the wall. It seems likely that roughness elements of the same order of size as the particle will have great influence on the flow in the wall region. Therefore, wall roughness of the same order as particle diameter was chosen in the present work. The coarse sand-paper (Grit 40), had roughness elements approximately 0.45 mm in size, i.e. about twice the particle diameter.

5.3 Experimental Results and Discussion

From initial tests, the roughness of fresh sand-paper changed slightly because of erosion during the first hour of exposure to CFB conditions. However, after the first hour, no apparent further change in the roughness of the sand-paper was found. These tests indicate that particles do make contact with the walls to some extent, causing some erosion of the sand-paper. However, the degree of contact with the wall may not be very extensive, so that the findings do not necessarily contradict the earlier work of Wirth et al. (1991) and Lints and Glicksman (1993)

described above. The circulating fluidized bed system was operated for 1.5 h before any measurements were taken to ensure that the roughness of the sand-paper did not change appreciably during the experiments.

In our experiments, net solids circulation rates of 40 and 60 kg/m^2s and superficial gas velocities of 5.5 m/s and 7.0 m/s were chosen. These operating conditions and the sand particles were identical to those employed in Chapters 3 and 4. Each voidage data point again corresponds to five 60 s intervals of sampling at a frequency of 483 Hz, while each particle velocity datum was obtained from five separate measurements of 2000 validated samples.

Smooth-wall and rough-wall data were compared at the 90% and 95% confidence levels using the t-test. Confidence intervals were determined for both the bed voidage and particle velocity measurements based on repeat measurements. The ranges of time-mean average values for groups of repeated measurements are small as indicated by the bars on the points shown below. The confidence interval of each datum in this work is within the range shown by the reproducibility bars. The t-test is used below to examine the significance of differences between the smooth-wall and rough-wall column.

Axial profiles of differential pressures measured by U-tube manometers for both rough- and smooth-walled riser are shown in Fig. 5.1. Except near the bottom and the top of the column, no distinguishable variation between the two curves is found. As illustrated in Fig. 5.1, the different pressure drop for the column having rough walls seems to be slightly lower near the bottom, while wall roughness appears to increase the pressure drop somewhat near the top. However, the difference is so small that no firm conclusion can be drawn.

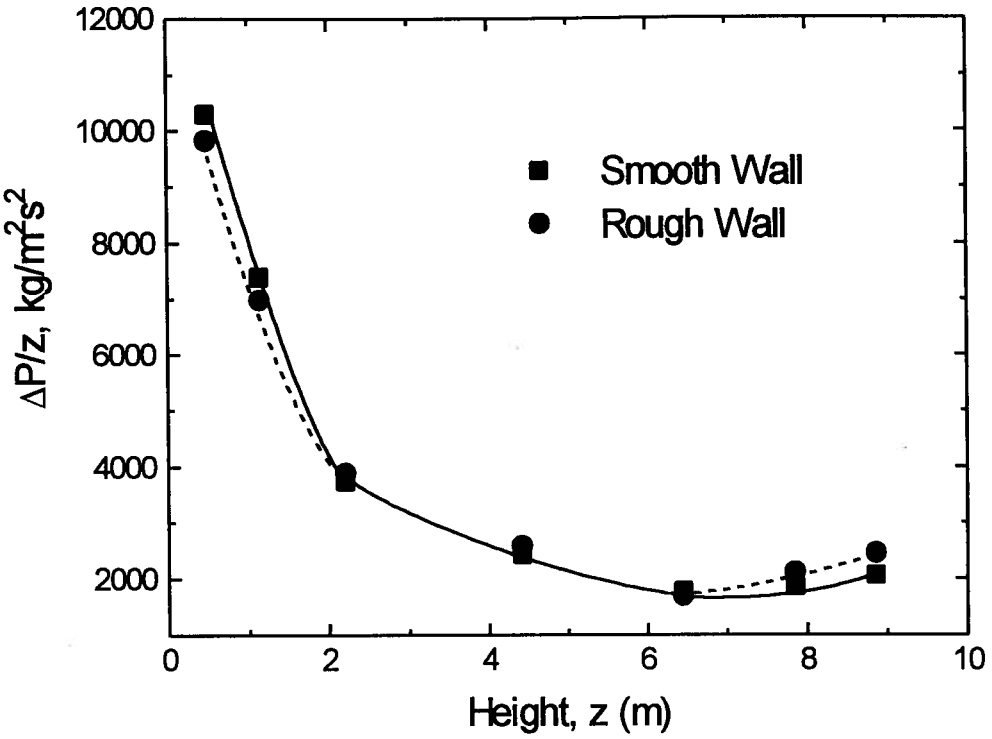

Fig. 5.1. Comparison of axial profiles of voidages obtained from differential pressure measurements for smooth- and rough-walled risers for U_g=5.5 m/s and G_s=40 kg/m^{2}s.

5.3.1. Voidage Profiles

Axial profiles of voidage are shown in Figs 5.2 and 5.3. Coordinates are the same as in Fig. 2.1. The reproducibility shown by the bars indicates the maximum and minimum of five repeat measurements, each lasting 60 s and consisting of 28,980 data points, for each position and condition. For all our data the 95% confidence interval is always smaller than the interval shown by the bars. Axial profiles of voidage near the walls of the riser with rough walls and with smooth walls are compared in Fig. 5.2. The differences between the rough and smooth walls are clearly greater than can be explained on the basis of experimental error. Except at the top of the riser, the

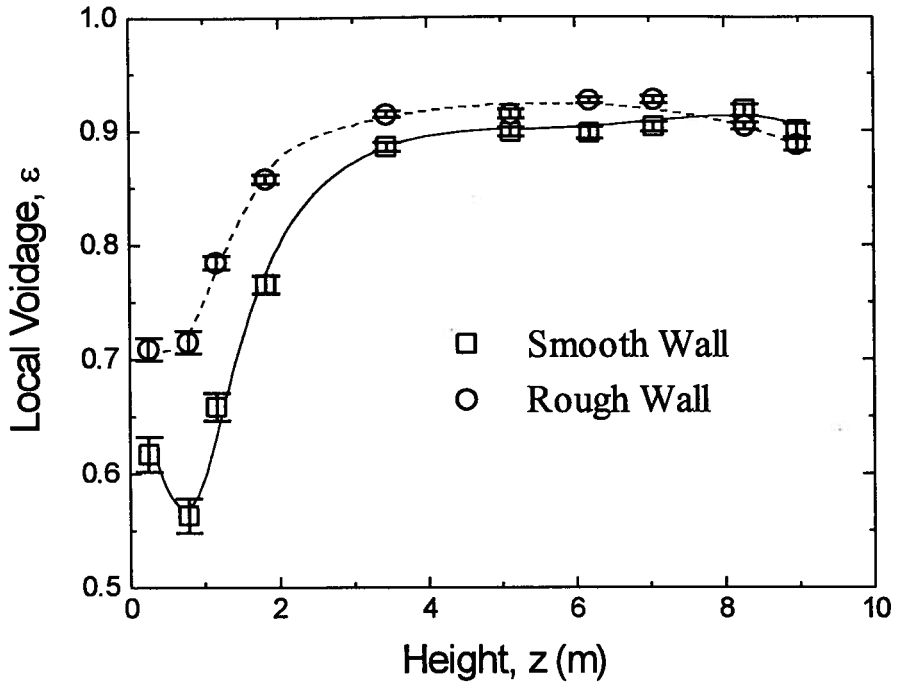

Fig. 5.2. Axial profiles of time-mean local voidage at wall of the riser for x/X=0, y/Y=-1, U_g=5.5 m/s, G_s=40 kg/m^{2}s.

voidage near the rough wall was greater than near the smooth surface. This may be because rough walls cause more turbulence and more disruption of the particle flow near the wall.

Figure 5.3 gives the axial profile of voidage along the axis of the riser. The t-test indicates that there is no distinguishable difference between the rough and smooth wall results from the bottom to the top of the riser. Figures 5.2 and 5.3 suggest that wall roughness only influences voidage in the wall region significantly.

As illustrated in Chapter 3, a bimodal probability distribution of particle concentration can sometimes be obtained, with one peak likely corresponding to particle downflow in swarms and

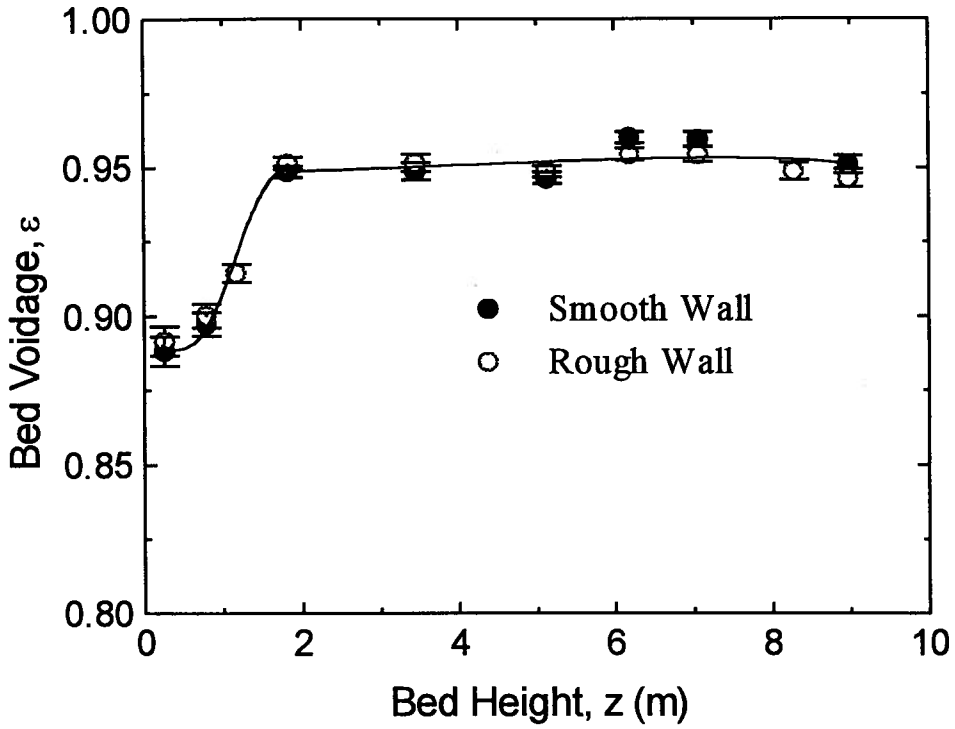

Fig. 5.3. Axial profiles of time-mean voidage along the axis of the riser for x/X=0, y/Y=0, U_g=5.5 m/s, G_s=40 kg/m^{2}s.

the other to bulk downflow of particles. As indicated in Fig. 5.4, particle concentration measurements adjacent to a rough surface show that distributions of particle concentration were neither bimodal nor trimodal. Instead, a single peak always appeared both at the wall and at the column axis over the entire height. This indicates that wall roughness may change the character of particle downflow near the wall. The single peak in the probability distribution indicates a more homogenous flow near the rough wall.

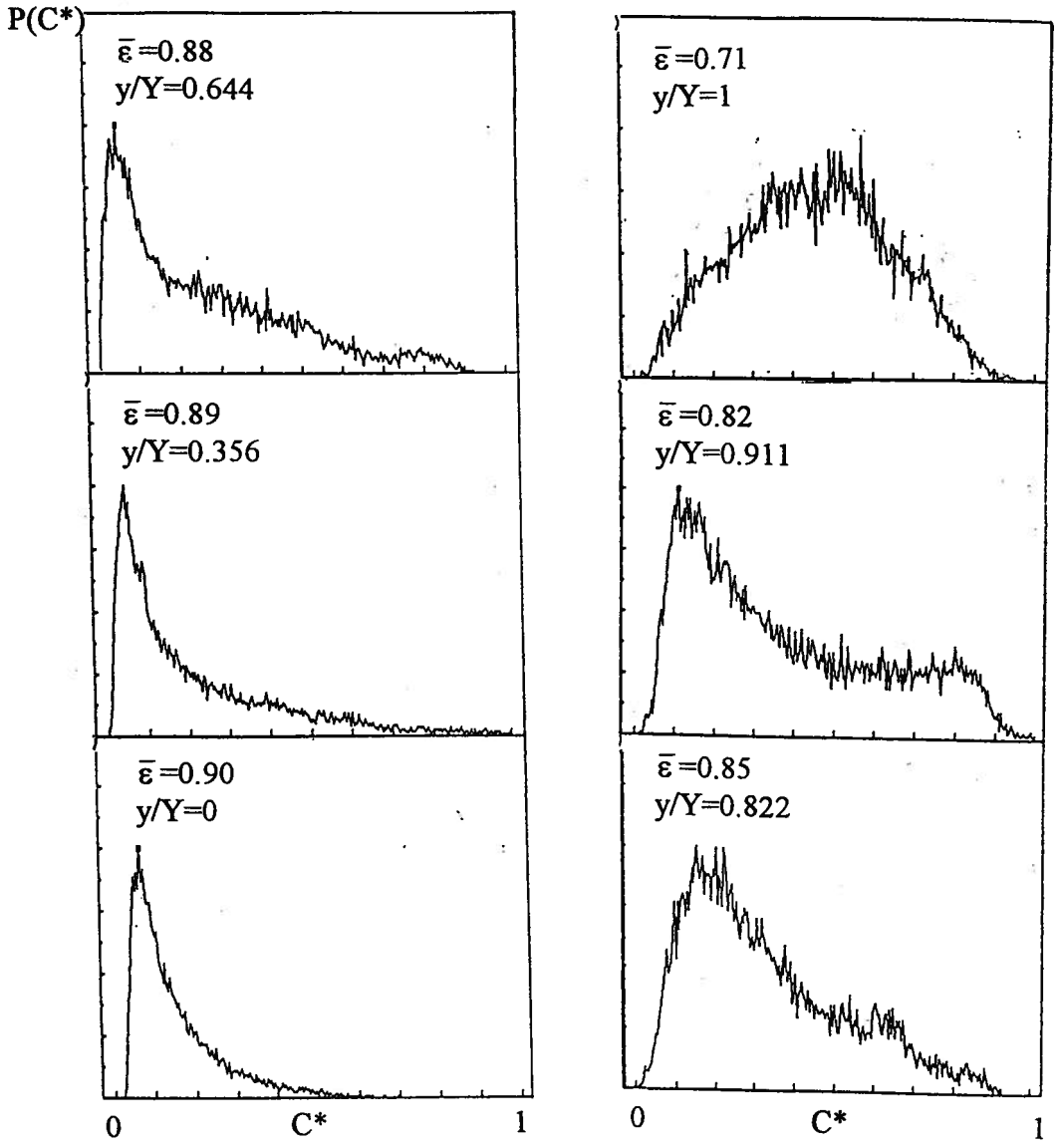

Fig. 5.4. Lateral profiles of probability distribution of local time-mean particle concentration, $C^* = (1-\varepsilon)/(1-\varepsilon_o)$ for U_g=5.5 m/s, G_s=40 kg/m^{2}s, x/X=0 and z=0.79 m. C*=1 corresponds to the packed bed particle concentration, i.e. ε=0.43.

Lateral profiles of voidage appear in Figs 5.5 and 5.6 for z=7.06 m and 8.98m, respectively. Wall roughness is seen to increase the voidage near the wall, but it has little influence near the axis of the riser. More uniform profiles were obtained for the rough wall surface. For smooth walls, indicated by the solid curve in Fig. 5.5, the voidage is not always highest on the axis of the riser. Instead, the voidage sometimes reaches a maximum at a location of about 0.6 to 0.8 of the half-width of the column and then decreases slightly towards the center. As described in Chapter 3, turbulence generated at the shear boundary is probably at the root of this M-shaped distribution. The measurements for the rough wall surface indicate a significantly flatter profile in

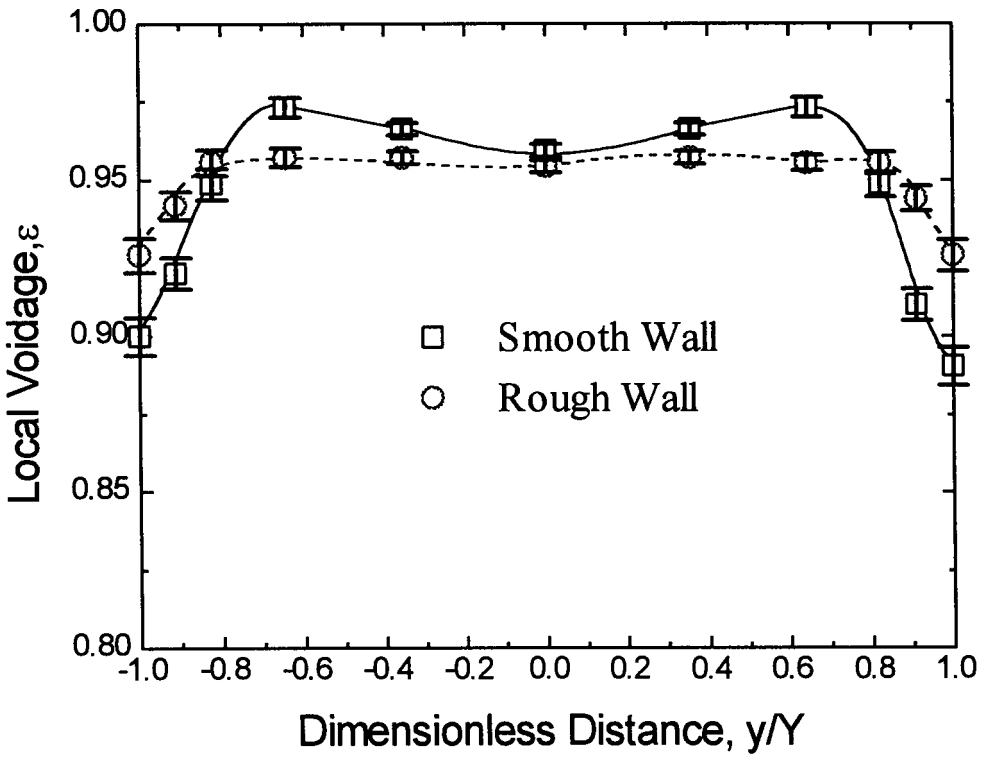

Figure 5.5. Lateral profiles of time-mean local voidage for x/X=0, z=7.06 m, U_g=5.5 m/s, G_s=40 kg/m^{2}s.

the interior of the column. Near the rough walls, because of turbulence generated by wall roughness, compared to the riser of smooth walls, particle downflows are likely to be more disrupted and to have higher voidage.

Because of the exit effect, asymmetric lateral profiles of voidage are found near the exit for both the rough and smooth wall surfaces, as indicated in Fig. 5.6. The t-test at a 95% confidence level shows that wall roughness appears to cause a slight decrease in voidage at the wall near the top of the column. No significant influence of wall roughness on voidage in the core has been found at z=8.98.

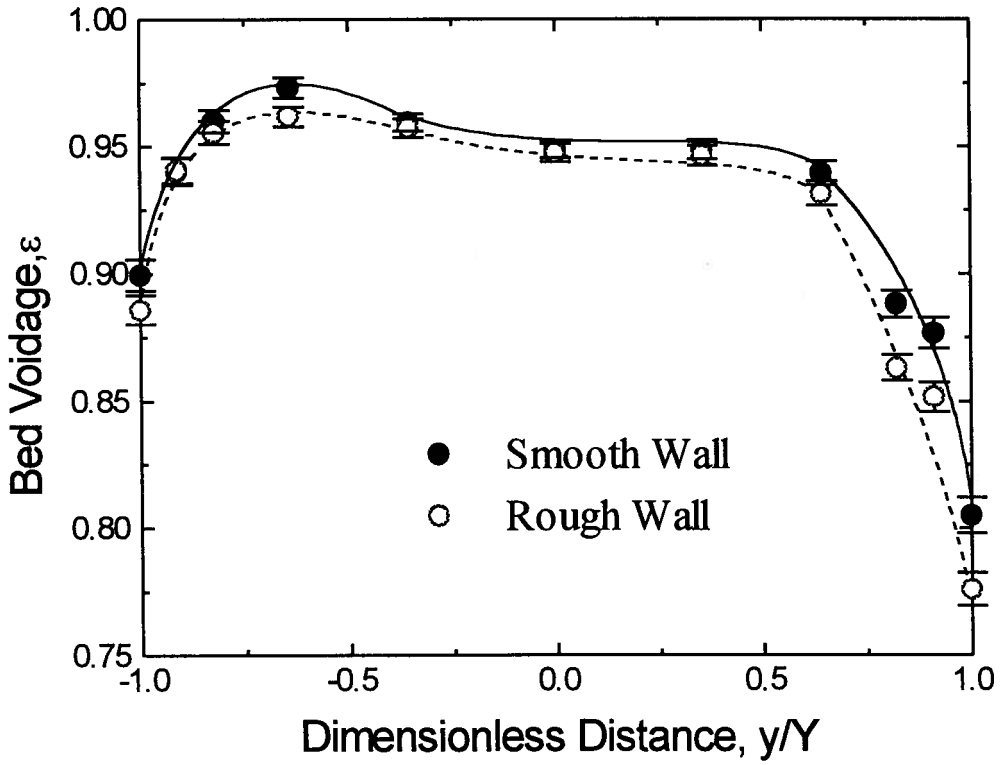

Fig. 5.6. Lateral profiles of time-mean voidage near the exit of the riser for x/X=0, z=8.98 m, U_g=5.5 m/s, G_s=40 kg/m^{2}s.

Figure 5.7 shows the influence of wall roughness on the voidage near the corner of the column. Towards the corner, the voidage for the rough walls was found to be somewhat higher than for the smooth-walled column, with the changes becoming larger towards the corner. It seems likely that this is due to augmented turbulence caused by the roughness of both walls forming the corner.

5.3.2 Intermittency Index Profiles

As described in Chapter 3, the intermittency index introduced by Brereton and Grace (1993) may be used to characterize the homogeneity of the flow in circulating fluidized beds. Axial profiles of intermittency index at the wall and at the axis of the column are presented in Figs. 5.8 and 5.9 respectively. At the wall of the riser, except near the top, the intermittency index for the rough wall surface is lower than for the smooth surface. Wall roughness creates turbulence which tends to deform descending particle swarms, making the gas-particle flow near the wall more uniform. This suggests that flow at the wall is more homogeneous with the rough wall surfaces. As discussed in section 5.3.1, a similar conclusion has been obtained from the probability distribution of voidage.

The intermittency index along the axis of the riser, shown in Figure 5.9, does not change much except near the bottom and top of the riser. The rough surfaces lead to a small decrease in intermittency index near the bottom and an increase near the top. Therefore, except near the bottom and the top, wall roughness has no significant influence on either the magnitude of voidage or the flow structure near the axis of the riser.

Near the top of the riser, however, higher values of intermittency index were obtained for the rough wall surfaces, as indicated in Figs 5.8 and 5.9, suggesting a more heterogeneous flow.

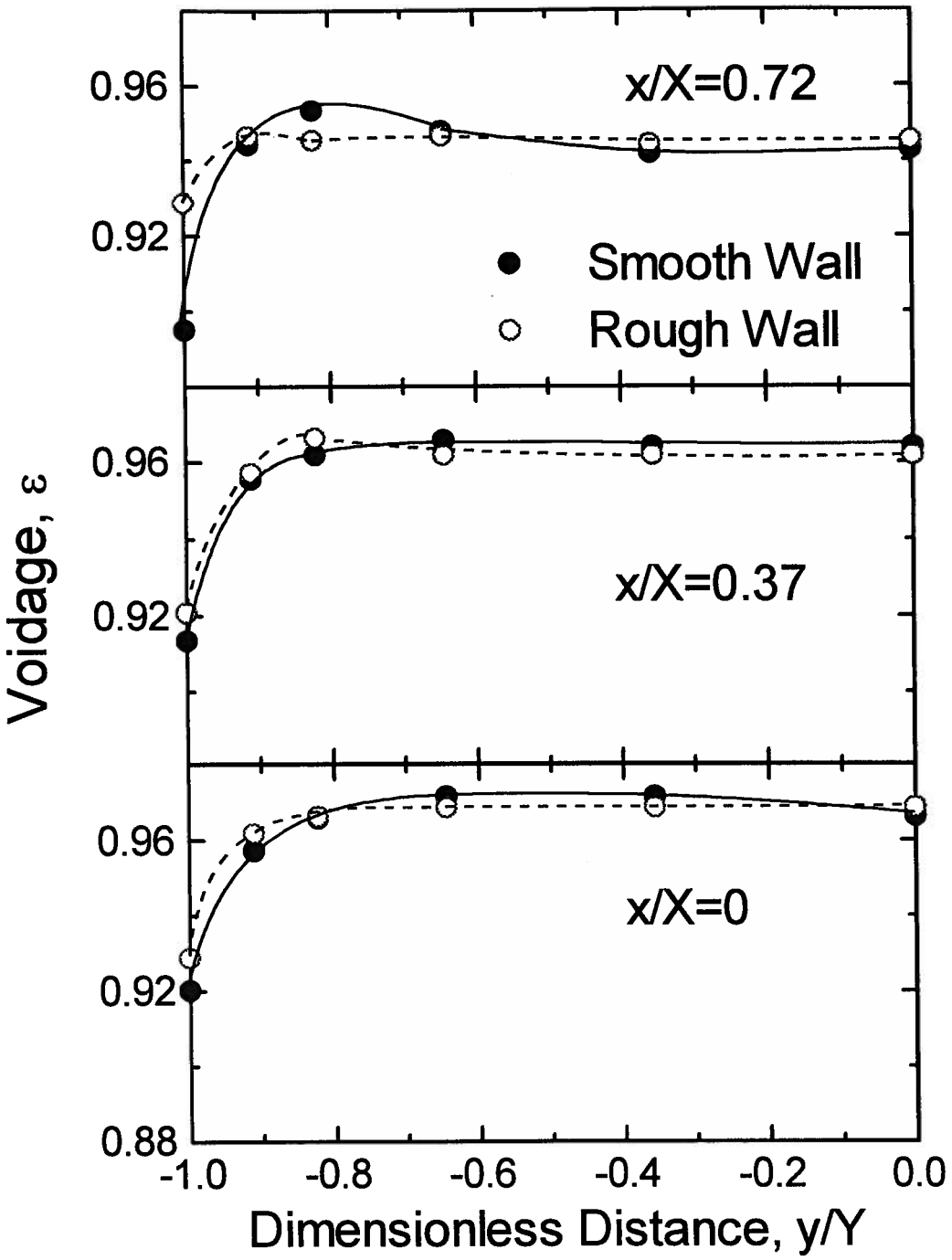

Fig. 5.7. Lateral profiles of time-mean voidage showing corner effect for z=6.2 m, U_g=7.0 m/s, G_s=40 kg/m^{2}s.

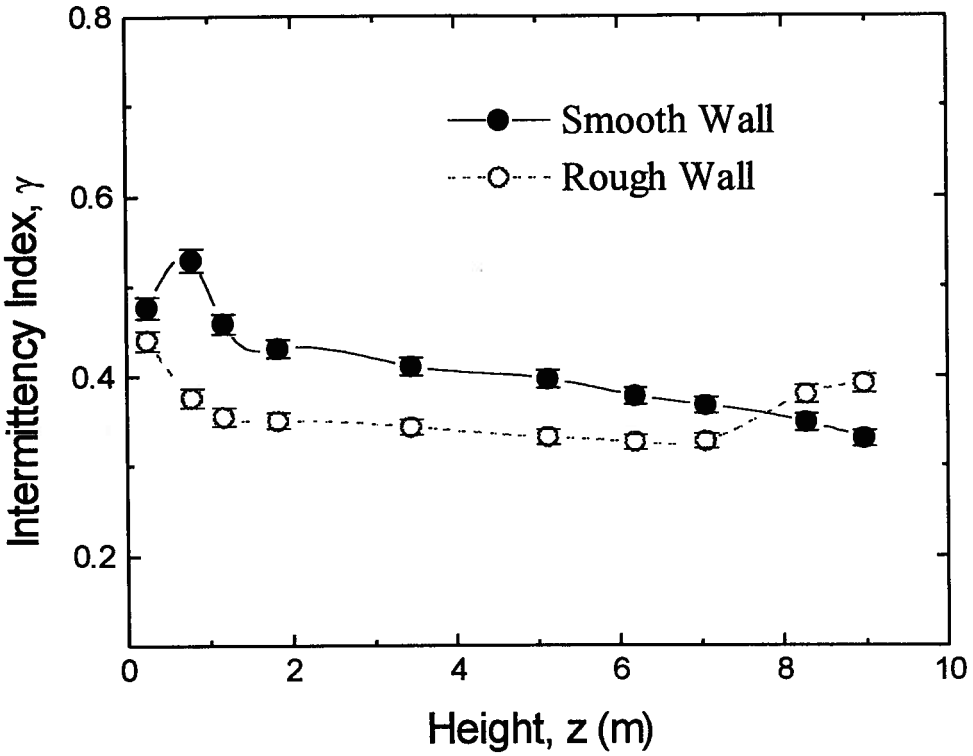

Fig. 5.8. Axial profiles of intermittency index at the wall for x/X=0, y/Y=-1, U_g=5.5 m/s, G_s=40 kg/m^{2}s.

Asymmetric lateral profiles of intermittency index near the exit of the riser are shown in Fig. 5.10. The intermittency index profile is flatter for the rough wall surfaces. The significant increase in γ near the exit shows a change in flow structure. For both rough and smooth walls, the intermittency index on the exit side is higher than on the opposite side. As noted in Chapter 3, this may be because of particles piling up in the horizontal duct connecting the riser exit to the primary cyclone and intermittently slipping backwards to descend downwards along the wall on the exit side (Glicksman et al., 1993).

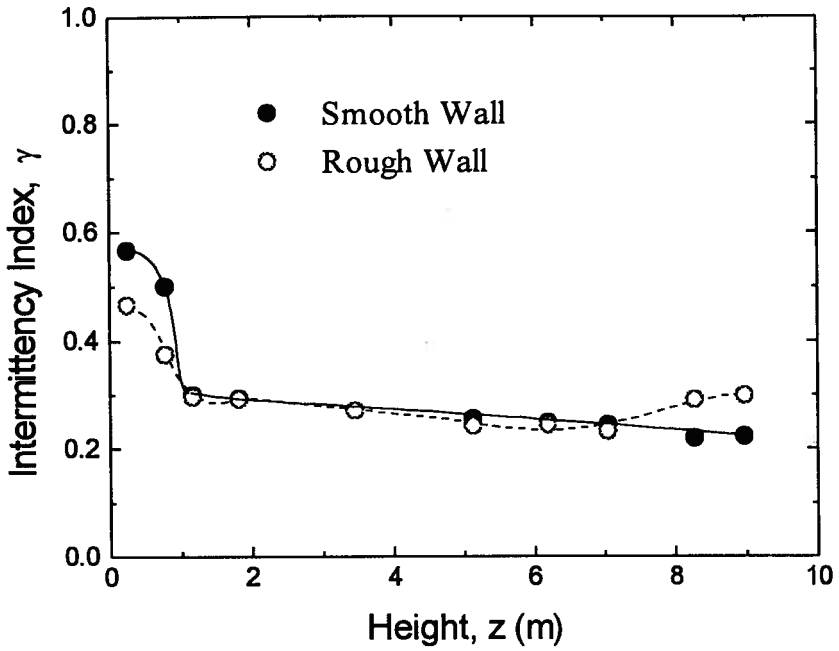

Fig. 5.9. Axial profiles of intermittency index along the axis for x/X=0, y/Y=0, U_g=5.5 m/s, G_s=40 kg/m^{2}s.

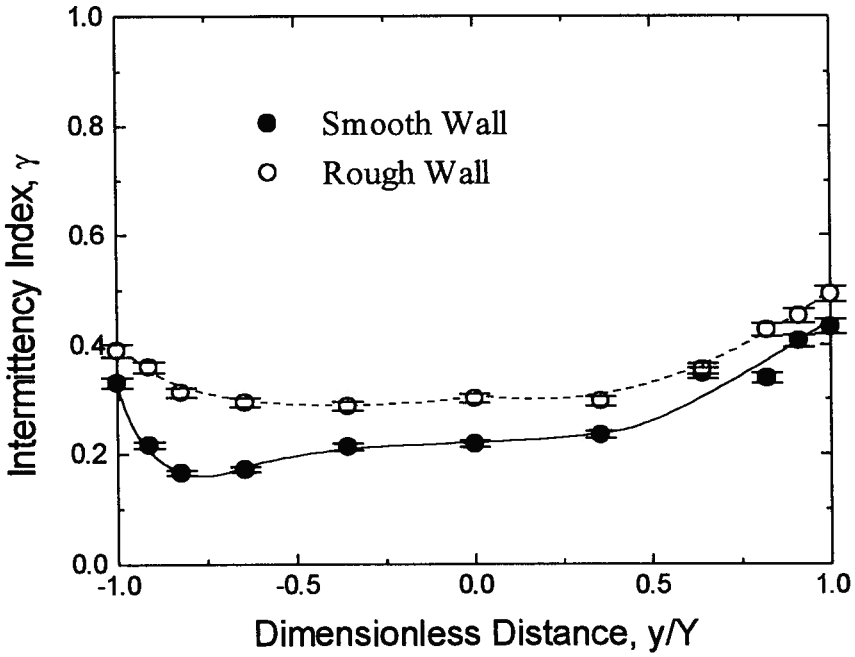

Fig. 5.10. Lateral profiles of intermittency index near the riser exit for x/X=0, z=8.98 m, U_g=5.5 m/s, G_s=40 kg/m^{2}s.

As in Chapter 3, the intermittency index in the corner of the riser is higher than at other locations at the same level. Figure 5.11 shows that lower intermittency indices are obtained in the corner of the riser with rough walls. This again suggests that flow is somewhat more homogeneous with rough walls.

5.3.3 Particle Velocity Profiles

Lateral profiles of particle velocity 6.2 m above the distributor are illustrated in Fig. 5.12. At this level, the ascending particle velocity was higher for the rough wall. Similar results were obtained for other levels. In the core, this is probably because of a higher gas velocity caused by a thicker downflow wall layer for the rough wall surface at the same superficial gas velocity. The magnitude of the velocities of particles descending close to the wall (y/Y=-0.60 to -0.95) were somewhat lower for the rough wall, probably due to the increase of the voidage of the particle downflow, while wall roughness had no significant influence on the velocity of descending particles at the wall. Near the axis, with a confidence level of 90%, descending particle velocities appear to be higher for the rough wall surface than for the smooth surface. However, the influence can be neglected at a confidence level of 95%, although it must be remembered that there are few descending particles there.

Lateral profiles of the fraction of particles which are ascending appear in Fig. 5.13. Greater influence of wall roughness was found in the outer part of the riser. Little change was found right at the wall and near the axis of the column. If we ignore a possible bias in the results from the velocity probe (Chapter 4), the rough wall appears to produce a thicker wall layer where most particles move downwards.

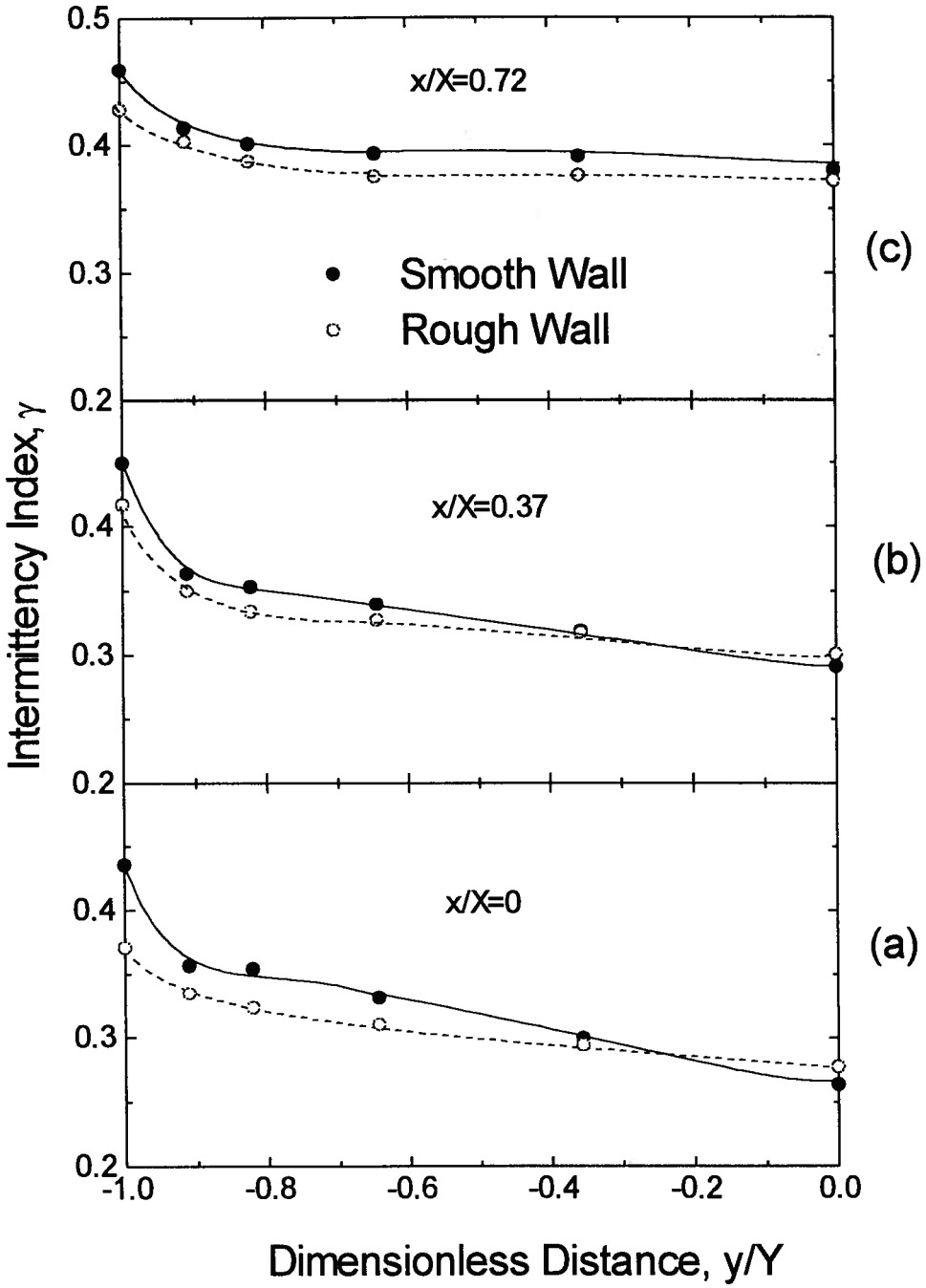

Fig. 5.11. Lateral profiles of intermittency index for z=6.20 m, U_g=7.0 m/s, G_s=40 kg/m^{2}s.

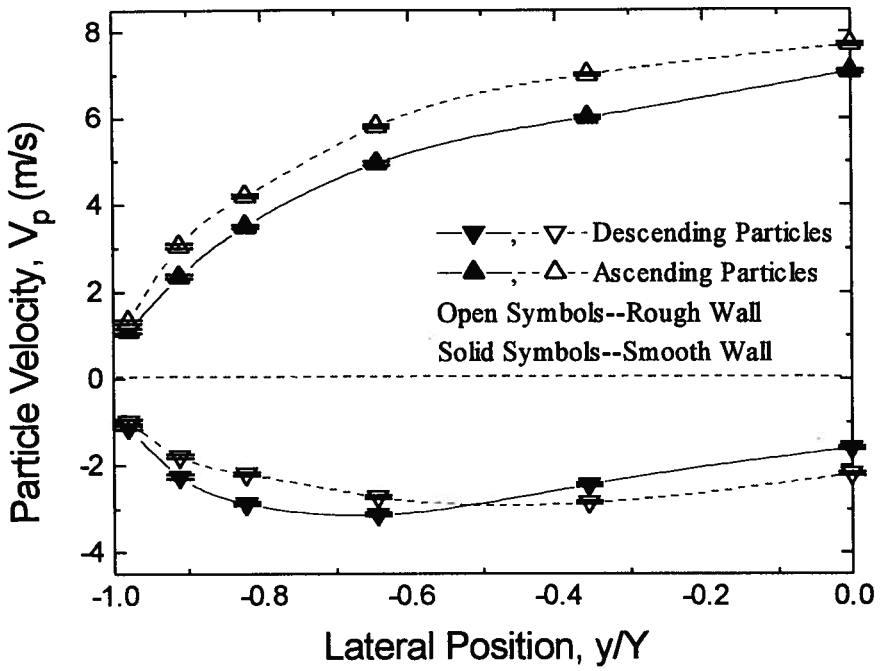

Fig. 5.12. Lateral profiles of particle velocity for x/X=0, z=6.2 m, U_g=5.5 m/s, G_s=40 kg/m^{2}s.

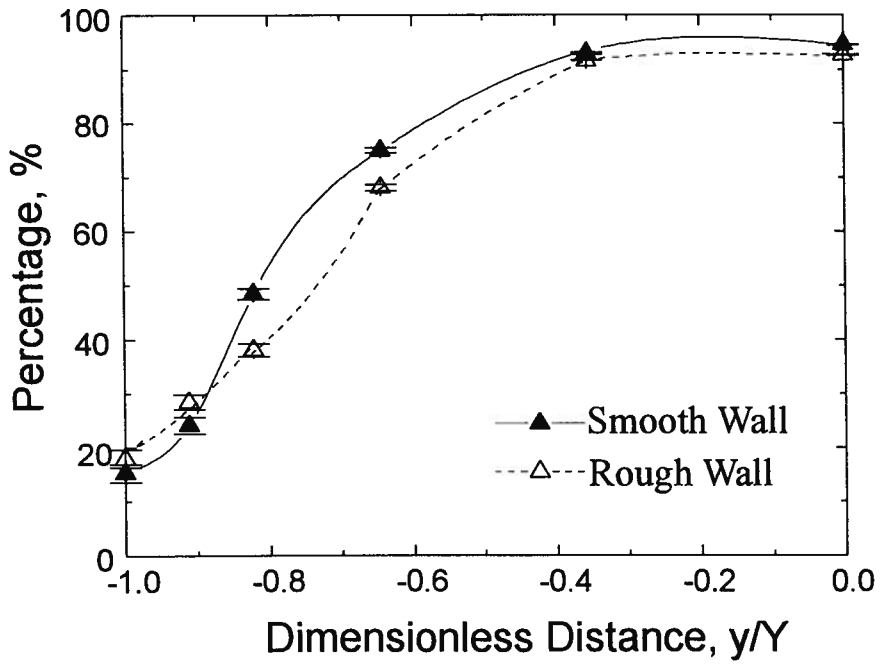

Fig. 5.13. Lateral profiles of fraction of particle which are ascending for x/X=0, z=6.2 m, U_g=5.5 m/s, G_s=40 kg/m^{2}s.

As for the smooth riser (Chapter 4), numerical integrations, involving the particle concentrations, ascending and descending particle velocities, and fractions of the ascending and descending particles, were carried out for the rough wall riser at the heights of 5.13 and 6.20 m to see whether the calculated net particle flux matched the preset value of 40 kg/m^{2}s. The latter was determined from the descent of identifiable particles in the standpipe as proposed by Burkell et al. (1987). Integration results of 36.8 and 38.2 kg/m^{2}s were obtained, respectively, again within 10% of the "true" value, helping to validate the experimental results.

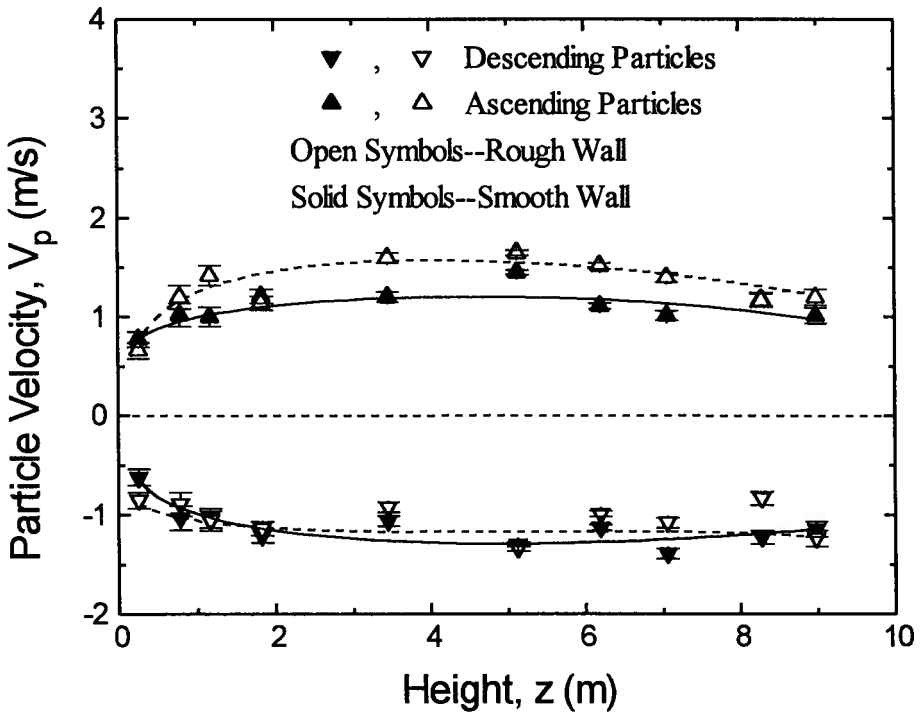

Fig. 5.14. Axial profiles of particle velocity at the wall for x/X=0, y/Y=-1, U_g=5.5 m/s, G_s=40 kg/m^{2}s.

Axial profiles of particle velocity at the wall and at the axis are compared for rough and smooth walls in Figs 5.14 and 5.15, respectively. The reproducibility of the data was again determined by making five separate measurements for each position and condition, each of 2000 data points. It is seen from Fig. 5.14 that the velocity of particle downflow at the wall, usually in the range of 0.8 to 1.5 m/s, did not change appreciably with wall roughness. This is also confirmed by t-tests at significance levels of both 10% and 5% illustrated by a sample calculation in Appendix I for the heights interval of 3.45 to 8.28 m, where particle velocity was found to be virtually independent of height. It is not known whether roughness elements of size larger than 0.45 mm would have a significant influence on the velocities of particle descending near the wall. As demonstrated in Appendix I, the t-test has been used to examine the influence of wall

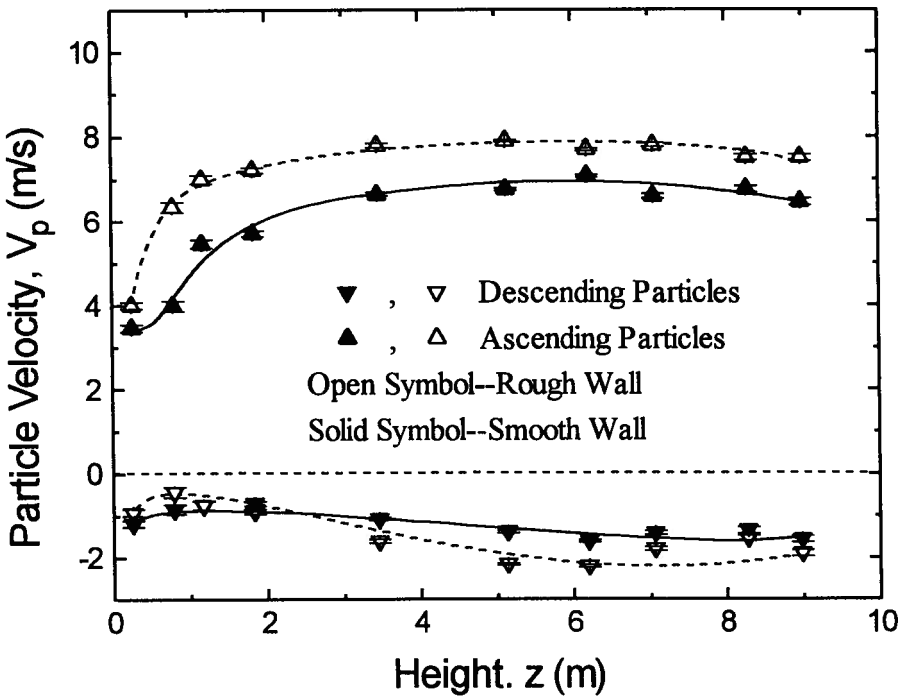

Fig. 5.15. Axial profiles of particle velocity along the axis for x/X=0, y/Y=0, U_g=5.5 m/s, G_s=40 kg/m^{2}s.

roughness on the velocities of particles descending along the axis of the riser at z=3.5 to 8.3 m. The result of the test indicates that wall roughness influences the velocities of descending particles at a confidence level of 90%; but the influence can be neglected at a confidence level of 95%.

Figures 5.14 and 5.15 suggest that there are significant differences between the smooth and rough wall cases. Ascending particle velocities, both along the axis and at the wall, were somewhat higher for the rough walls than for smooth walls. There was a deceleration zone near the top of the riser for both rough and smooth walls. The general trend for the riser with rough walls is similar to that for the smooth-walled riser.

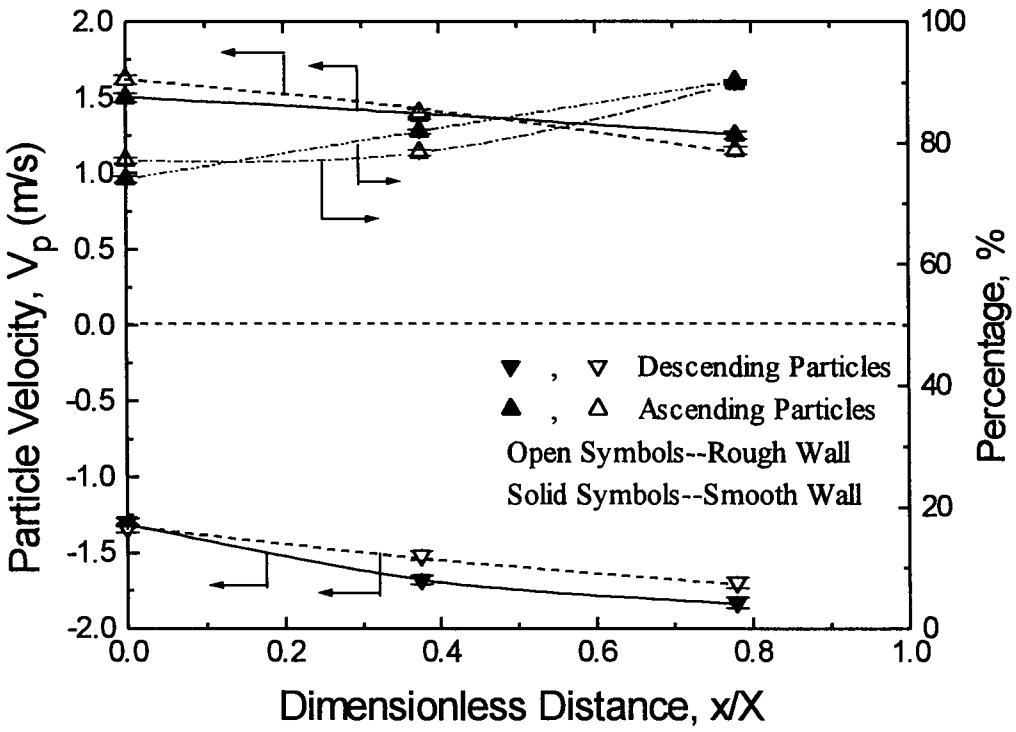

Fig. 5.16. Lateral profiles of velocities and fractions of rising particles showing corner effect for y/Y=-1, z=5.13 m, U_g=5.5 m/s, G_s=40 kg/m^{2}s.

The influence of wall roughness on particle velocity in the corner is shown in Fig. 5.16. The magnitudes of velocity of particles descending in the corner are slightly lower in the rough-walled riser. This is probably associated with the fact that the concentration of descending particles in the corner is lower for the rough wall. The influence of wall roughness on ascending particle velocities has not been found to be significant. Figure 5.16 also indicates the fractions of ascending particles near the corner of the rough-walled column. Wall roughness is seen to cause little change.

As shown in Fig. 5.17 asymmetric lateral profiles of particle velocity were obtained near the exit of the riser, similar to the riser with smooth walls. At a confidence level of 95%, the

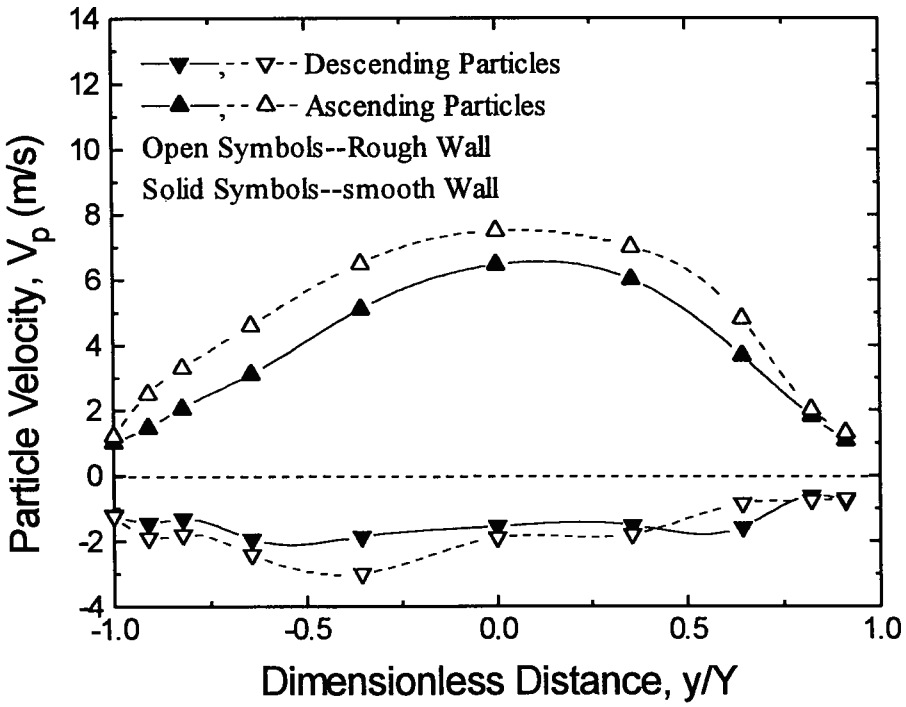

Fig. 5.17. Lateral profiles of particle velocity at the top for x/X=0, z=8.98 m, U_g=5.5 m/s, G_s=40 kg/m^{2}s.

ascending particle velocities were higher for the riser with rough walls, while descending particle velocities did not change significantly. A somewhat more symmetric profile was obtained for the rough wall.

5.4 Summary

Roughness elements were found to have some influence on the voidage and velocity of particles in a riser of square cross-section, especially near the wall:

1. For rough walls, the voidage was higher near the wall, except near the top of the riser where rough surfaces led to a small decrease in voidage. Wall roughness had little influence on the voidage near the axis of the column. More uniform lateral profiles of voidage were obtained for the rough-walled riser. Wall roughness increased the voidage in the corner. No bimodal probability distributions of particle concentration were found for the rough wall.

2. Near the wall, the intermittency index for the rough wall was found to be lower than for the smooth wall. Except near the bottom and top of the riser, wall roughness did not appreciably alter the intermittency index on the axis of the column. However, the intermittency index was lower near the bottom and higher near the top of the column for rough walls and was somewhat lower in the corner of a column with rough walls.

3. The t-test shows that ascending particle velocities both at the wall and the axis of the riser were higher for the rough-walled riser. The magnitude of the particle velocity of descent near the wall did not change appreciably at confidence levels of 90% and 95%. On the axis, at a confidence level of 90%, the wall roughness was found to increase the velocities of descending particles at z=3.5 to 8.3 m, while the influence can be neglected at a confidence level of 95%. The velocity of

particle downflow in the corner of the riser was slightly lower with rough walls. Near the top of the riser, at a confidence level of 95%, the ascending particle velocities were higher, while descending particle velocities did not change significantly for the rough wall.

Chapter 6

Influence of Membrane Wall

6.1 Introduction

Membrane walls are commonly employed as heat transfer surfaces to remove heat from CFB combustors. Membrane walls are composed of parallel tubes connected with fins to form a wall as indicated in Fig. 6.1. This geometry may well influence the dynamics of gas and particle flows in CFB risers. Wu et al. (1990) reported that particles were stripped off a flat smooth wall by upflowing gas more readily than off a membrane surface where downflowing particles appear to be protected in the fin region. Local heat transfer coefficients near a membrane wall have been investigated by Andersson and Leckner (1992) and Lockhart et al. (1995). Distributions of heat

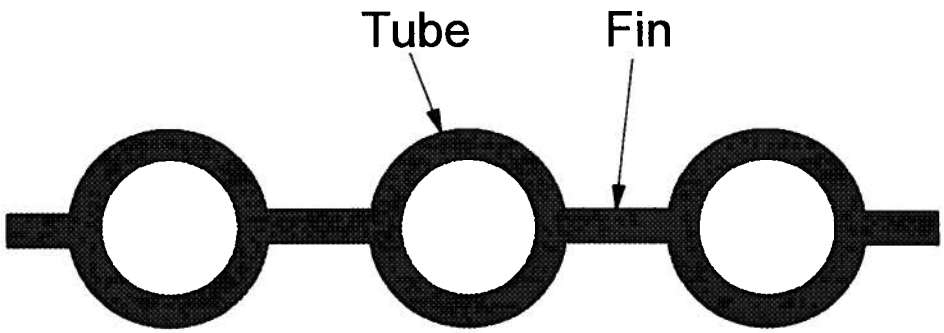

Fig. 6.1. Configuration of membrane wall. Tubes are normally vertical.

transfer coefficient near the membrane wall were found to be non-uniform. Andersson and Leckner (1994) observed highly concentrated particle downflow with a long residence time in the fin area.

Despite the importance of the membrane wall geometry to CFB combustors, little research has been conducted to determine the influence of the membrane wall geometry on the hydrodynamics in CFB risers. No detailed local hydrodynamics near the membrane wall have been reported. To better understand the heat transfer mechanism and erosion near the membrane wall, a better picture of local flow structure is needed. In this study, simulated membrane walls have been installed in the experimental cold model CFB riser described in detail in Chapter 3 to investigate the influence of this geometry on local hydrodynamics. Both voidage and particle velocity near the membrane walls were measured using the fibre optic probes described in detail in Chapters 3 and 4. Both probes could be inserted and moved horizontally using three ports around the membrane tubes. Experimental results from the membrane-walled riser are compared with the smooth flat-wall results obtained in the same riser.

6.2 Experimental Set-up

Half-round plexiglass rods of diameter 1" (25.4 mm) were affixed by double-sided tape to all four inner walls of the CFB riser, extending from bottom to top, to simulate a membrane wall surface. The ratio of rod diameter, d, to the pitch, p was set at 0.75, i.e. p=33.9 mm, where p is the distance between the centrelines of two adjacent fins. Measurements around the membrane tube were conducted at points A, B and C in Fig. 6.2, where α=48.1 for point B. Lateral profiles of voidage and particle velocity were also measured along the three lines shown in Fig. 6.2 from y=0 to the wall through a specially designed window. The window can be moved to cover frames at four different heights, allowing measurements of voidage and particle velocities along the height of the riser. The coordinates in Fig. 6.2 are the same as those defined in Fig. 2.1.

6.3 Experimental Results and Discussion

For convenience of comparison, operating conditions identical to those in the same riser of smooth wall surface were adopted, i.e. superficial gas velocities of 5.5 and 7.0 m/s, and solids circulation rates of 40 and 60 kg/m^{2}s. The solid particles were also the same as those in the earlier experiments with the smooth flat-walled riser. Particle properties are described in Chapter 3.

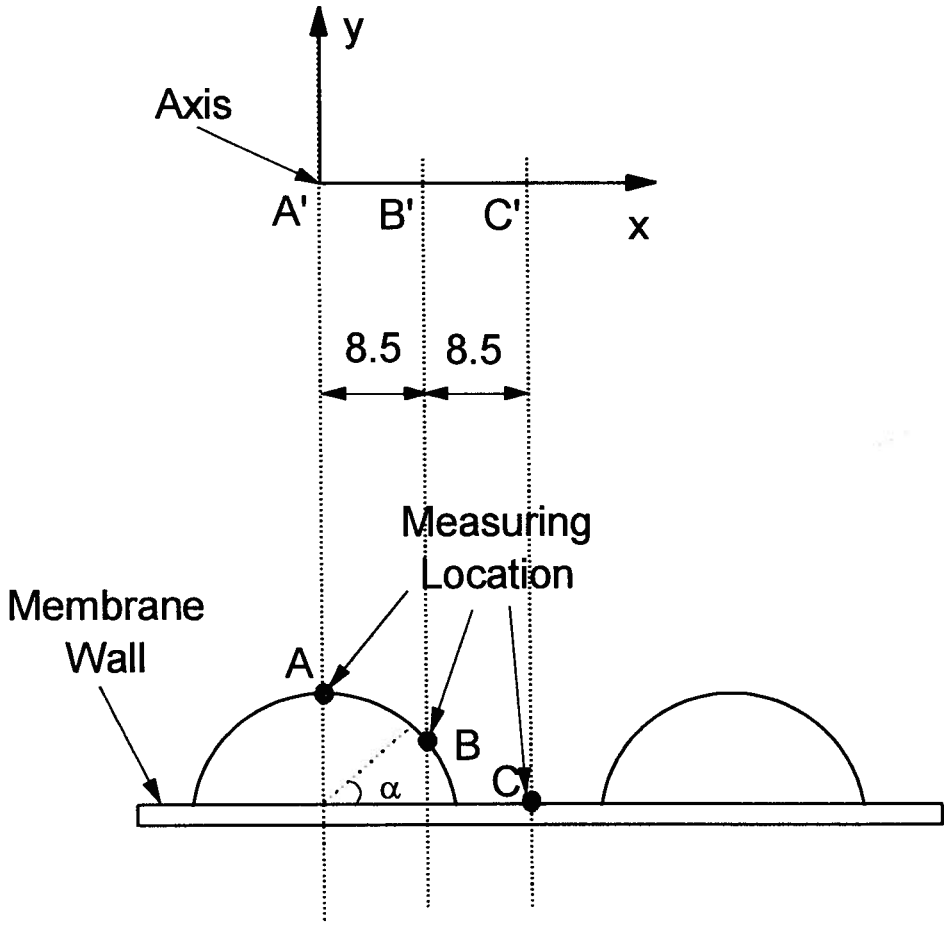

Fig. 6.2. Schematic of the window allowing measurements near membrane wall.

As in to Chapter 5, each data point for both voidage and particle velocity has been obtained from the average of five separate measurements, each involving many individual determinations. The reproducibility of the data obtained for the membrane wall riser is indicated by bars showing the range between the maximum and minimum of the sample. The 95% confidence interval of each datum in this chapter is within the range shown by the reproducibility bars. The t-test has been employed to compare the membrane wall and flat wall results at a confidence level of 95%.

6.3.1 Voidage Profiles

Axial profiles of time-mean voidage near the membrane wall on the fin (α=0), on the side (α=48.1) and on the crest (α=90.0) are shown in Fig. 6.3. There is a non-uniform voidage distribution around the crest of the membrane wall. The voidage in the fin area is lower than near the crest and also lower than near the wall of the riser with a flat smooth wall surface (Chapter 3). The voidage near the crest is higher than for the flat wall (see Chapter 3) for the same operating conditions, U_g=7.0 m/s and G_s=40 kg/m^{2}s. Similar to the corners of the riser in Chapter 3, particles in the fin region are well protected in the valleys formed by the fin and two adjacent tube surfaces and are therefore relatively difficult to strip off the wall. This protection is not relevant for particles near the crest of the membrane tube. As a consequence, streamers of high particle concentration are more easily formed in the fin region of the membrane wall, while on the crests of the membrane wall, streamers are easily disturbed by upflowing gas, leading to higher voidage near the crest. For the same reason, the particle renewal rate is higher near the crest region and lower along the fin of the membrane wall compared to the flat wall (Chapter 3) in the same riser.

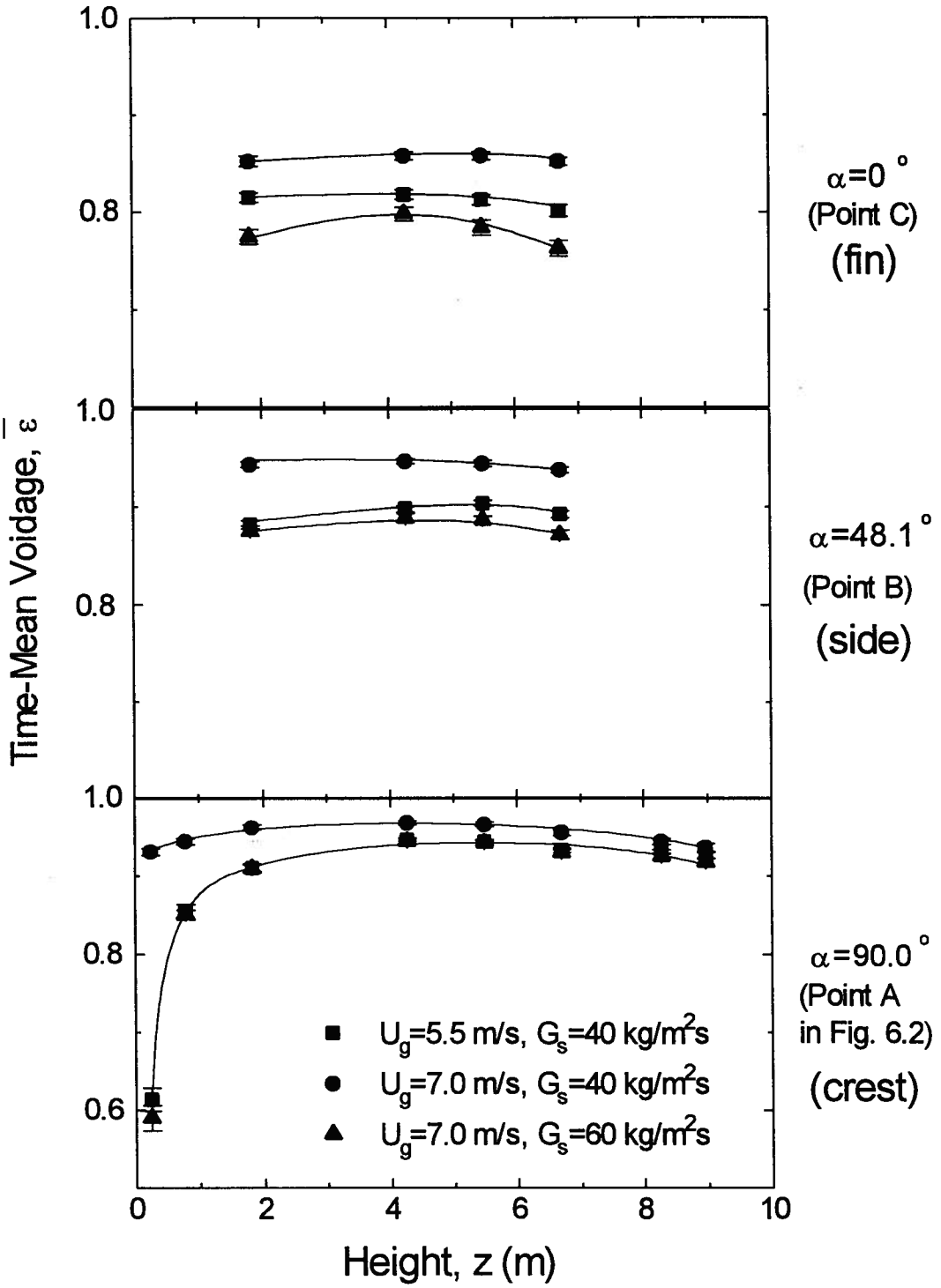

Fig. 6.3. Axial profiles of time-mean voidage near membrane wall showing influence of operating conditions.

The influence of superficial gas velocity and solids circulation rate is also indicated in Fig. 6.3. As for in the riser with flat walls investigated in Chapter 3, the voidage in both the fin and the crest regions increased with increasing superficial gas velocity and decreasing solids circulation rate, showing that particle streamers are influenced by the operating conditions as expected.

A polar plot of voidage profile around the membrane tube is given in Fig. 6.4. It is seen that voidage increases with α from C in the fin region through B to A at the crest because, as discussed above, streamers in the fin region are well protected, while the crest region is totally exposed. The disturbance of the upflowing gas on particle streamers near the membrane wall increased with α.

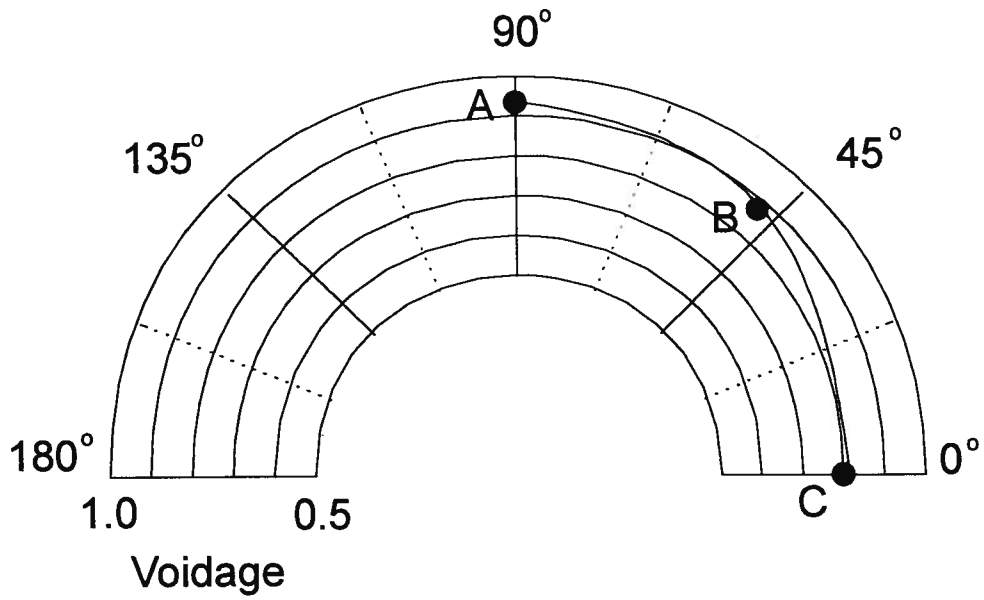

Fig. 6.4. Voidage profiles near membrane wall for z=6.7 m, U_g=5.5 m/s and G_s=40 kg/m^{2}s.

Lateral profiles of voidage for z= 6.7 m, U_g=5.5 m/s and G_s=40 kg/m^{2}s are plotted in Fig. 6.5. The voidage is always lower near the wall and increases towards the axis. The membrane surface only influences voidage significantly in the vicinity of the wall. From y=45 to 60 mm, for the same lateral position y, near the wall, voidage increases from AA' through BB' to CC'. This is probably because of the greater distance from CC' to the wall. However, for the same distance from the wall, voidage decreases from AA' to CC'. As indicated in Fig. 6.5, the voidage at y=0 with membrane walls is around 0.96, very close to the value (0.96) obtained for the same operating conditions with flat walls in Chapter 3. Thus, the membrane wall has very little influence on the voidage at the axis. No M-shaped lateral voidage profiles similar to those described in Chapter 3 were found when the membrane wall riser was used.

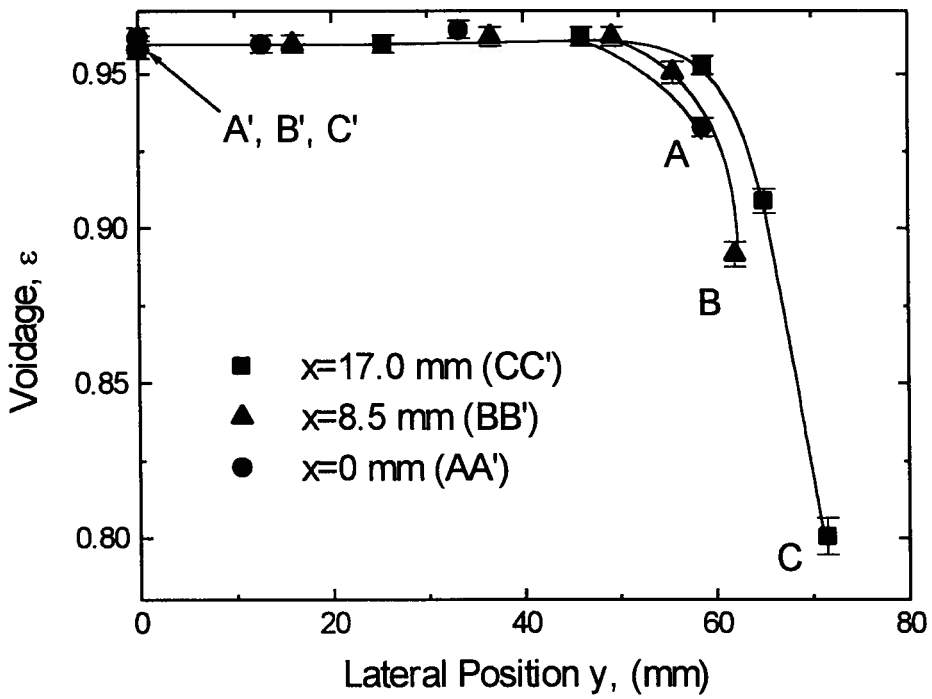

Fig. 6.5. Lateral voidage profiles for z=6.7 m, U_g=5.5 m/s and G_s=40 kg/m^{2}s along the three parallel dashed lines shown in Fig. 6.2.

6.3.2 Intermittency Index Profiles

In Chapter 3, the intermittency index, γ, introduced by Brereton and Grace (1993), is used to describe the flow heterogeneity in CFB risers. Lateral profiles of the intermittency index in the membrane-walled riser given in Fig. 6.6 indicate that γ is generally higher near the outer wall and gradually decreases towards the interior. The lower γ in the core indicates a more homogeneous flow. Near the membrane wall, γ is highest in the fin region suggesting that the largest relative fluctuations of voidage occur there.

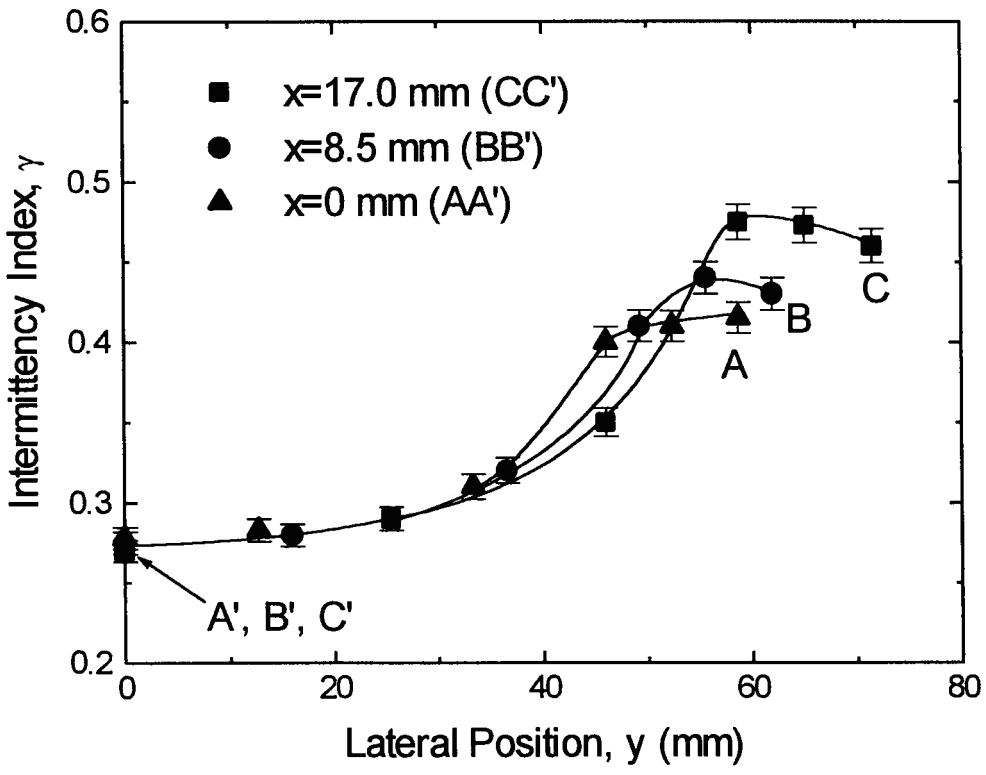

Fig. 6.6. Lateral profiles of intermittency Index for z=6.7 m, U_g=5.5 m/s and G_s=40 kg/m^{2}s. For positions of profiles see Fig. 6.2.

As indicated in Fig. 6.6, for the lateral intermittency index profile along CC', i.e. for x=17.0 mm, γ increases from the fin of membrane wall until it reaches a maximum and then decreases towards the center. The maximum γ, indicating highest flow heterogeneity, occurs close to the core-annulus boundary where there are large voidage fluctuations. As described in Chapter 3, similar lateral γ profiles were obtained near the bottom of a riser with flat walls.

6.3.3 Particle Velocity Profiles

Profiles of axial ascending and descending mean particle velocities and the fraction of particles which were descending near the membrane wall are plotted in Fig. 6.7. Similar to particle velocities for the riser with flat walls, the magnitudes of both ascending and descending particle velocities increase first from the bottom with height and then decrease near the top because of the end effect discussed in Chapter 4. The fraction of descending particles decreases somewhat with z near the bottom and then increases near the top. Near the membrane wall, the ascending particle velocity is highest in the crest region and lowest in the fin region. The fraction of descending particles is considerably higher in the valley of the membrane wall than at the crest.

As discussed in Chapter 3, the descending particle velocity near the flat wall in the CFB riser is in the range of 0.8 to 1.5 m/s. This range is also valid for particles near the crest of the membrane tube; however the magnitude of the descending particle velocity in the fin area, as indicated in Fig. 6.7, was greater than 2 m/s. This is consistent with the elevated particle concentration in the fin region. The measurements of both particle velocity and voidage indicate that particle behaviour in the fin region is similar to that near the corners of the flat-walled riser where voidage and ascending particle velocity are low, while velocity and fraction of descending particles are relatively high.

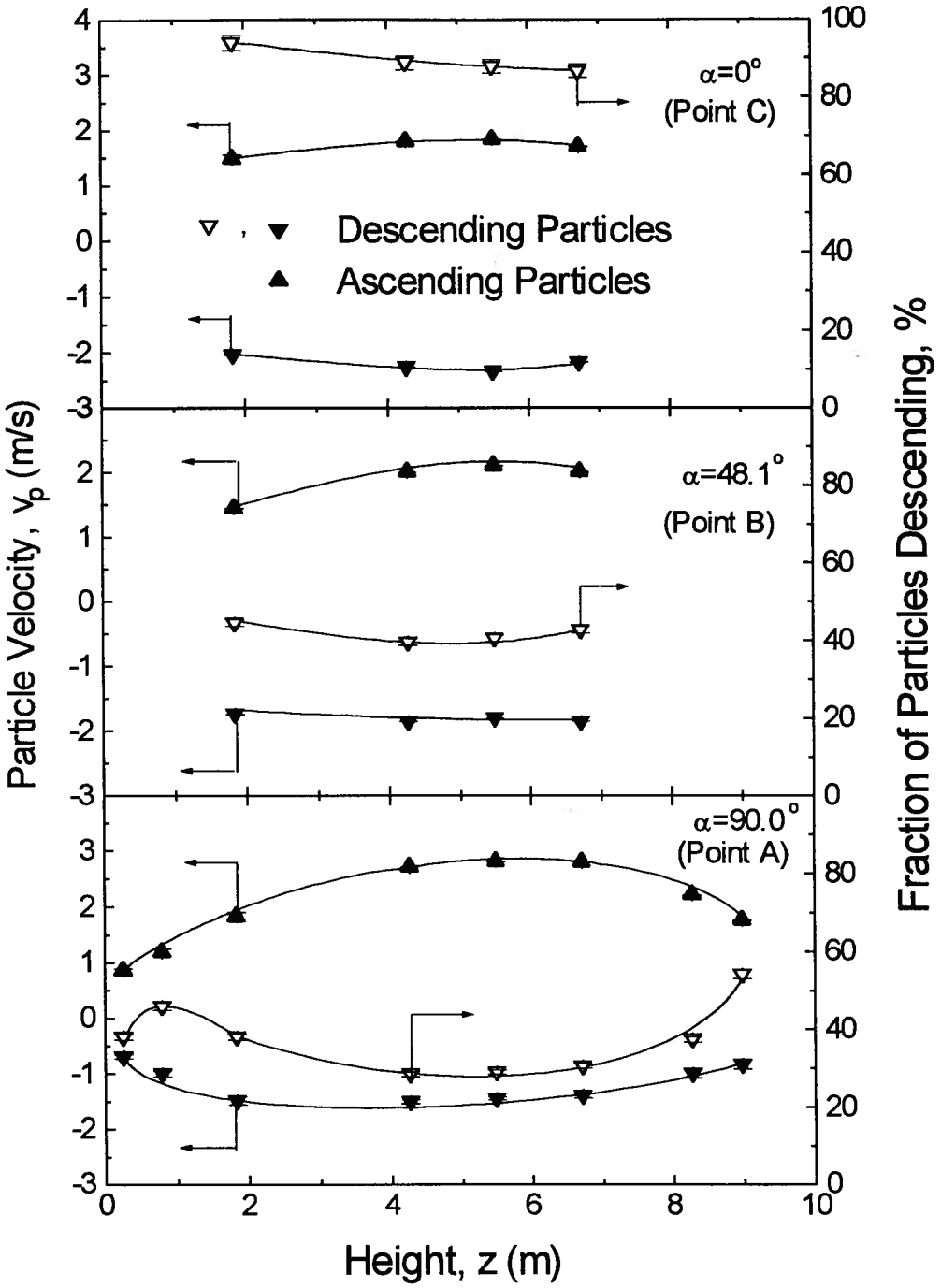

Fig. 6.7. Axial profiles of vertical particle velocity and fraction of particles which are descending for U_g=5.5 m/s and G_s=40 kg/m^{2}s.

The voidage and particle velocity results confirm the explanation of heat transfer phenomena near membrane walls. In particular for short surfaces (Lockhart et al., 1995) local heat transfer coefficients are higher on the fin while for long heat transfer surface (Andersson and Leckner, 1992) the heat transfer coefficient in the fin region is lower than on the crest because the particle renewal rate along the fin is low, causing the particles there to approach the same temperatures as the heat transfer surface.

Lateral profiles of time-mean particle velocities and fraction of descending particles near the membrane tube for U_g=5.5 m/s and G_s=40 kg/m^{2}s are shown in Fig. 6.8. The magnitude of the particle descending velocity and the fraction of descending particles decrease as one moves from the fin to the crest near the membrane tube. The ascending particle velocity, however, increases with α.

Fig. 6.9 illustrates the lateral profiles of time-mean particle velocities along AA', BB' and CC' at z=6.7 m, for U_g=5.5 m/s and G_s=40 kg/m^{2}s. As for the lateral voidage profiles, the influence of the membrane wall on the particle velocity and on the fraction of descending particles, is only significant near the wall. The fraction of descending particles increases monotonically towards the wall. Near the wall, the magnitude of the descending particle velocity and the fraction of descending particles increased with x (see Fig. 6.2). Similar to the riser with flat walls (Chapter 4), the magnitude of the descending particle velocity first increases from the axis with increasing y because the gas velocity decreases laterally (Yang et al., 1993); after a maximum is reached the magnitude of the descending particle velocity decreases towards the wall, probably because of wall friction, while the particle ascending velocity decreased monotonically towards the wall.

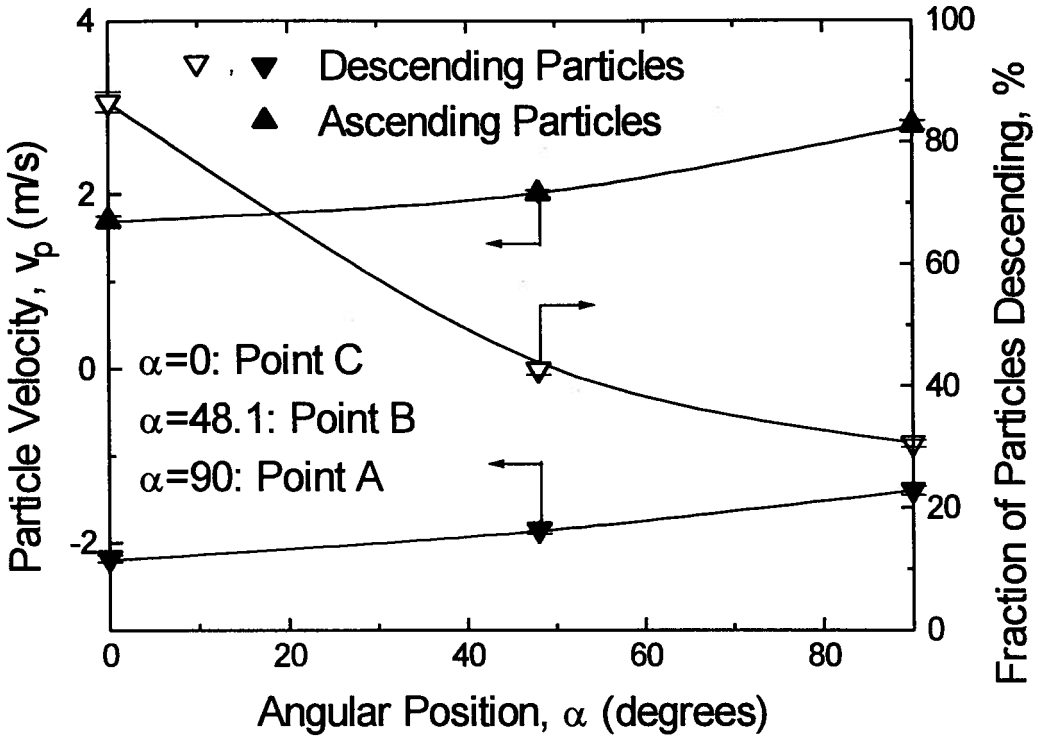

Fig. 6.8. Lateral profiles of particle velocities and fraction of descending particles near the membrane tube for z=6.7 m, U_g=5.5 m/s, G_s=40 kg/m^{2}s and z=6.7 m.

6.4. Summary

Membrane walls influence voidage and particle velocity in a CFB riser of square cross-section. Similar to corners, the valley or trough formed by the fin and two adjacent membrane tubes protects particles from upflowing gas. There is very little influence of the membrane walls on the voidage and particle velocity in the core of the riser. Particle streamers tend to move downwards along the fin in the protected valleys formed by the riser wall and two adjacent

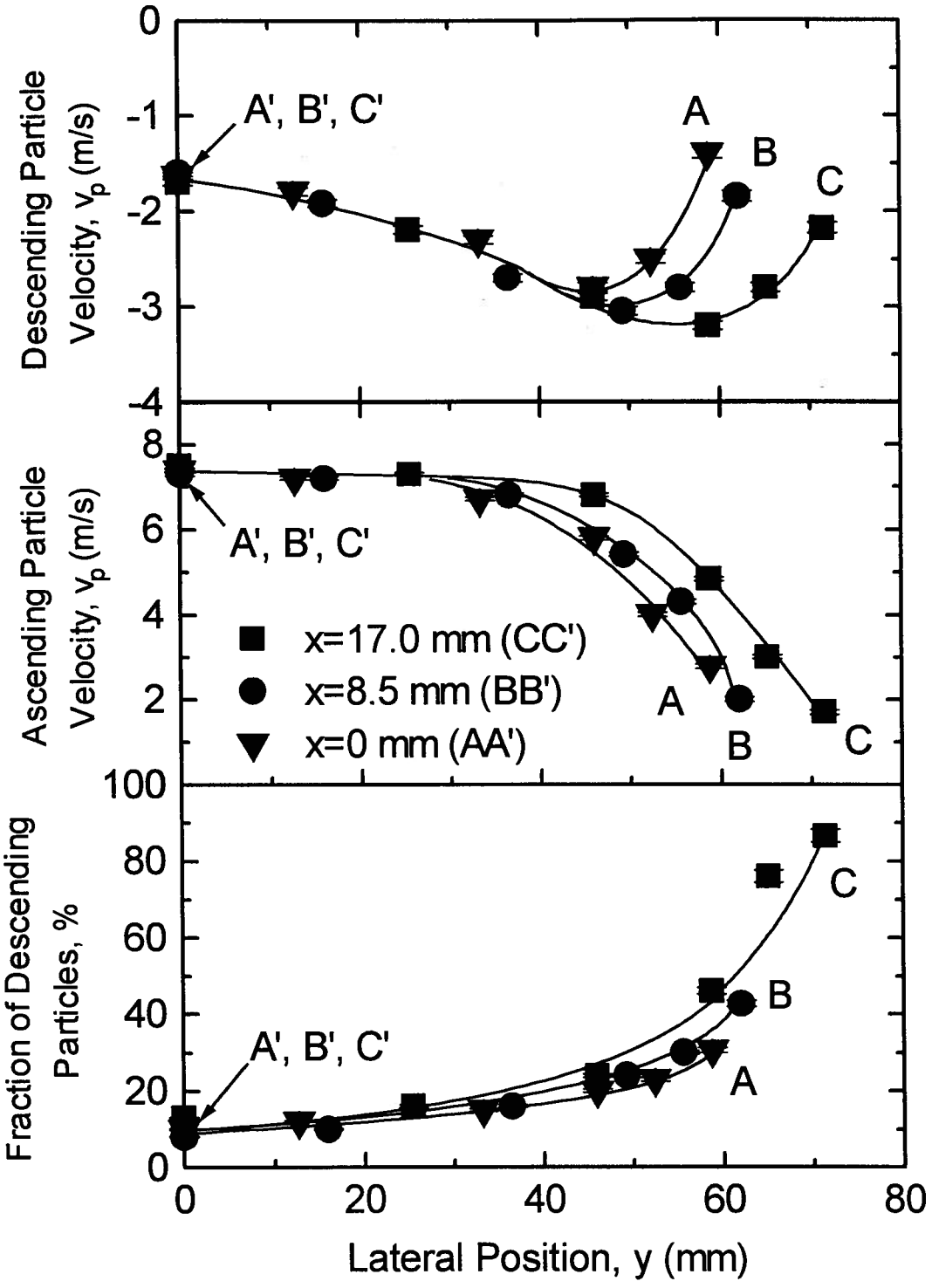

Fig. 6.9. Lateral profiles of particle velocities and fraction of descending particles for z=6.7 m, U_g=5.5 m/s and G_s=40 kg/m^{2}s.

membrane tube surfaces. Along the surface, the particle concentration is highest in the fin area and lowest on the crest of the tube. The intermittency index is generally high near the membrane wall and it decreases towards the axis. The magnitude of γ in the fin region is higher than near the crest, indicating more heterogeneous flow in the fin region. The magnitude of the downflowing particle velocity is highest in the fin area and lowest in the crest area along the membrane tube.

Chapter 7

Particle Cross-Flow, Lateral Momentum Flux and Lateral Velocity

7.1 Introduction

A core-annulus distribution of particle concentration has been detected in CFB risers of both circular and rectangular cross-sections (Gajdos and Bierl, 1978; Weinstein et al., 1986; Dry, 1986; Brereton, 1987; Horio et al., 1988; Hartge et al., 1988; Chapters 3 and 4). Time-mean vertical solids fluxes in circulating fluidized bed risers are upwards in the core and usually downwards near the wall (Monceaux et al., 1986; Rhodes et al., 1988; Chapter 4).

Solids are exchanged between the core and the annulus in CFB risers (Brereton et al., 1987; Berruti and Kalogerakis, 1989; Leckner and Andersson, 1992; Herb et al., 1992). Solids cross-flow affects suspension-to-surface heat transfer by determining particle renewal rates. Cross-flow also influences the thickness of the annulus zone, wall coverage and the voidage of streamers near the wall. It may also affect erosion of the wall.

Despite the importance of lateral flow, very little systematic research has been carried out on solids cross-flow. The only reported experimental data were obtained by Qi and Farag (1993) who used a sampling probe and reported that the radial particle flux near the wall was surprisingly large, even higher than the axial solids circulation flux in their riser. There is clearly a need to confirm the magnitude of the cross-flux. In addition, no data on net lateral solids flux nor on horizontal momentum have been reported for a riser of square cross-section.

This chapter consists of two parts. In the first, a sampling probe was used to measure lateral solids mass fluxes in a circulating fluidized bed riser of square cross-section. In the second,

lateral solids momentum fluxes were determined by a piezoelectric probe. The combined results are then used to estimate lateral particle velocities along the riser axis.

7.2 Equipment and Instrumentation

Experiments were carried out in the same cold model circulating fluidized bed riser as in Chapters 3 and 4. See Chapter 2 for details. Ottawa sand particles of mean diameter 213 μm, particle density 2640 kg/m^3 and loosely packed bed voidage 0.43 were again used as the bed material.

7.2.1 Sampling Probe

As illustrated in Fig. 7.1, a sampling probe similar to that used by Qi and Farag (1993) was employed to measure the cross-flow solids mass flux. The sampling system consists of a sampling probe, a sample collector and purging air. The inside diameter of the sampling probe is 6.3 mm. It is inserted into the riser at an angle of 45 to the axis. Since the angle of repose of the sand particles is less than 35 , sampled particles pass through the probe tube freely without blockage. The plane of the open area is vertical to ensure that only particles travelling laterally are captured. The upper part of the open area is covered as indicated in Fig. 7.1 to prevent particles hitting the upper inside surface of the probe from bouncing out. The open area of the probe is 38 mm^2. A modified graduated cylinder is employed to collect the sampled particles.

Before each measurement, the solids sampling probe is purged by air to ensure that the channel is free of solids. The system is then checked to make sure that it is well sealed because any leakage may lead to great error, as indicated below. When the CFB system is operating

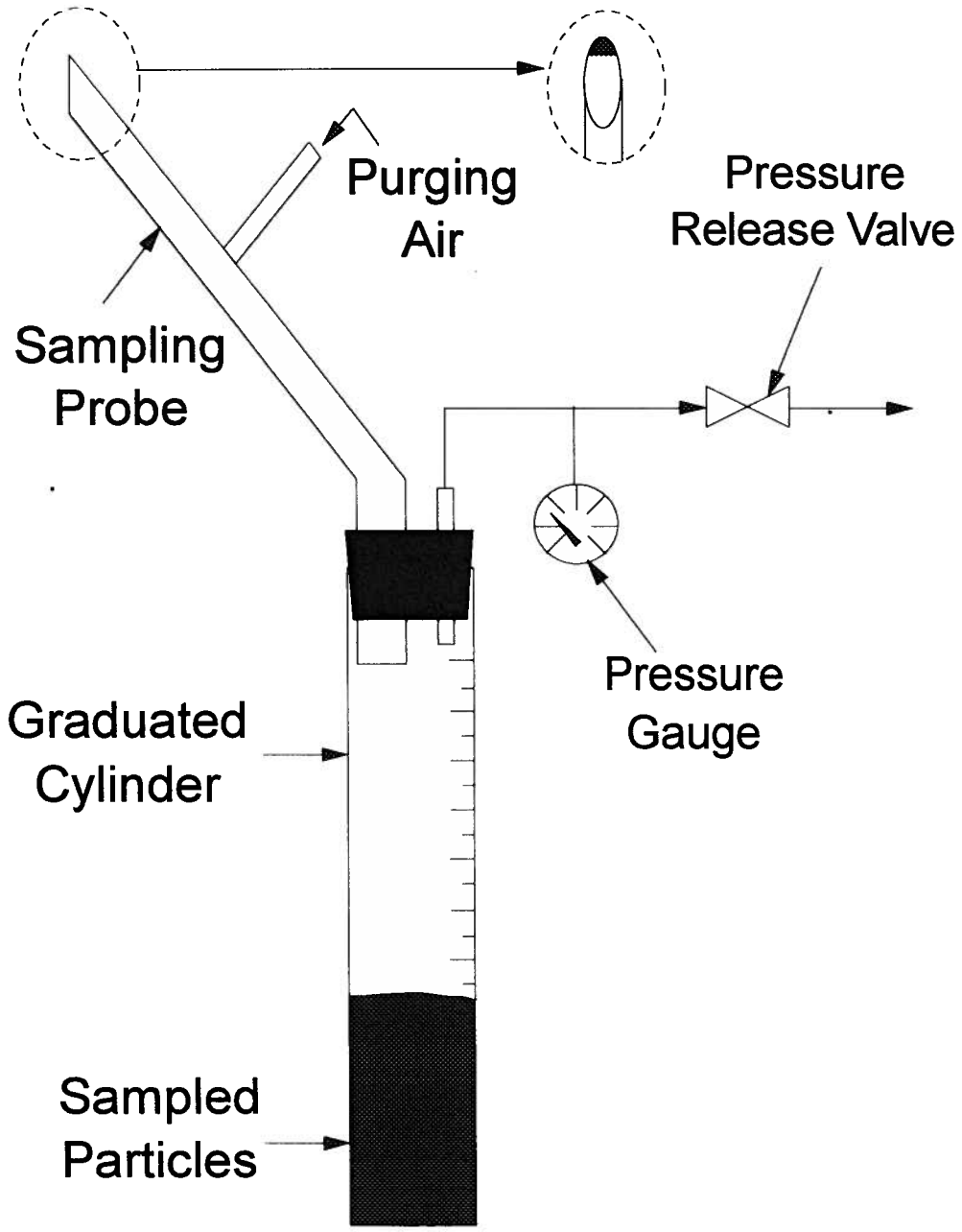

Fig. 7.1. Schematic of the solids sampling probe.

steadily, the purging air is turned off to initiate sampling. After a sampling interval, which is usually 0.5 to 5 minutes, the purging air is re-established to stop the sampling. The cross-flow flux is then simply

$$G_h = \frac{V(1-\varepsilon_o)\rho_p}{At} \tag{7.1}$$

where V is the volume of particles collected, ρ_p is the particle density, A is the open area of the sampling probe, ε_0 is the bulk voidage and t is the sampling time.

7.2.2 Piezoelectric Probe

A piezoelectric probe was used to determine particle lateral momentum fluxes. When a piezoelectric crystal is deformed by mechanical forces, the crystal develops an electrical potential. When the piezoelectric probe is used to measure solids cross-flow in a circulating fluidized bed, the impact of cross-flow particles causes deformation of the piezoelectric crystal, and an electrical charge is thus developed. The electrical charge produces an electrical potential from which the momentum flux of the cross-flow particles can be obtained. The electrical signal is logged by a computer for data processing.

The structure of the piezoelectric probe is shown in Fig. 7.2. Clamped by an o-ring, the piezoelectric crystal is placed at the mouth of a stainless steel enclosure. Since the crystal is very fragile, a thin steel disk having the same area as the crystal is glued to its surface to absorb the impacts. This steel disk was only 0.5 mm thick in order to minimize the reduction in sensitivity of the piezoelectric crystal. To prevent unwanted interference by particles hitting other parts of the probe, the piezoelectric crystal is backed by soft sponge to absorb the energy of unwanted particle

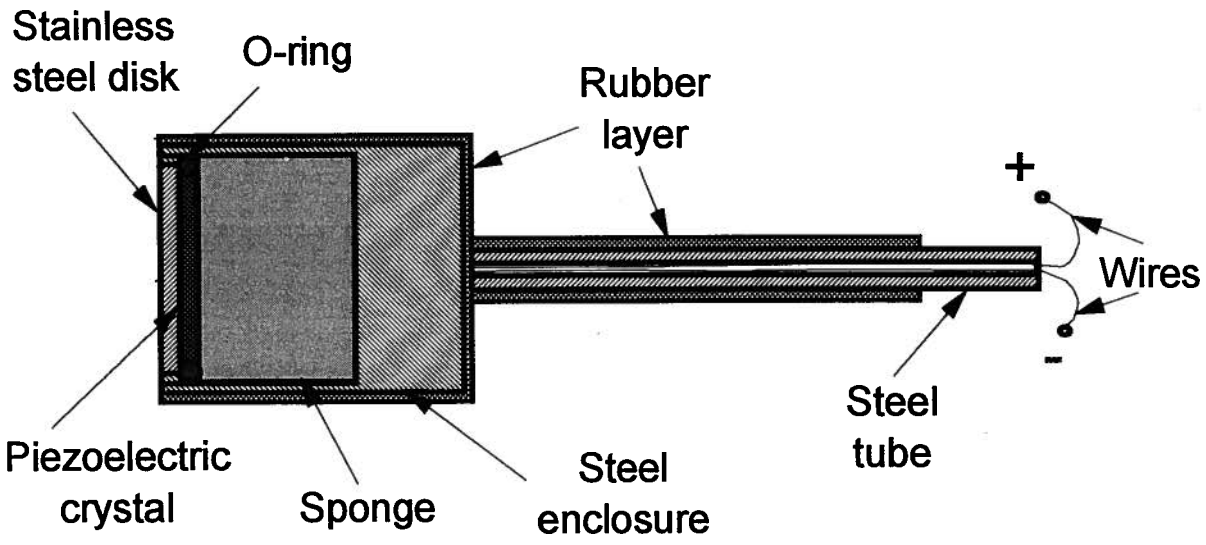

Fig. 7.2. Schematic of the piezoelectric solids momentum flux probe.

impacts. To reduce the influence of unwanted particle impact further, the outside surface of the head of the probe, except for the measuring surface, is covered by rubber. Two wires connected to the piezoelectric crystal are protected by a steel tube. Signals are then transmitted to an amplifying circuit and thence to a computer for logging. The amplifying circuit and a typical trace for the piezoelectric probe are provided in Appendix III.

The cylindrical head of the probe has an outside diameter of 10 mm and a length of 18 mm. The diameter of the circular particle impact area of the probe is 7.5 mm. The outside diameter of the steel tube which supports the head of the probe is 3 mm. The total length of the probe is 300 mm.

A calibration system developed for the piezoelectric probe is illustrated in Fig. 7.3. Particles leaving the side of a small fluidized bed impinged on the piezoelectric probe through a

guiding tube. Previous studies (e.g. Martin and Davidson, 1983; Geldart et al., 1984) have shown that the flow rate of gas-solids suspension leaving a fluidized bed through an orifice due to pressure difference ΔP across the orifice can be estimated as:

$$Q = A_0 C_{DC} \sqrt{\frac{(2\Delta P)}{\bar{\rho}}} \tag{7.2}$$

where A_0 is the cross-sectional area of the orifice, C_{DC} is the discharge coefficient, and $\bar{\rho}$ is the average suspension density given by

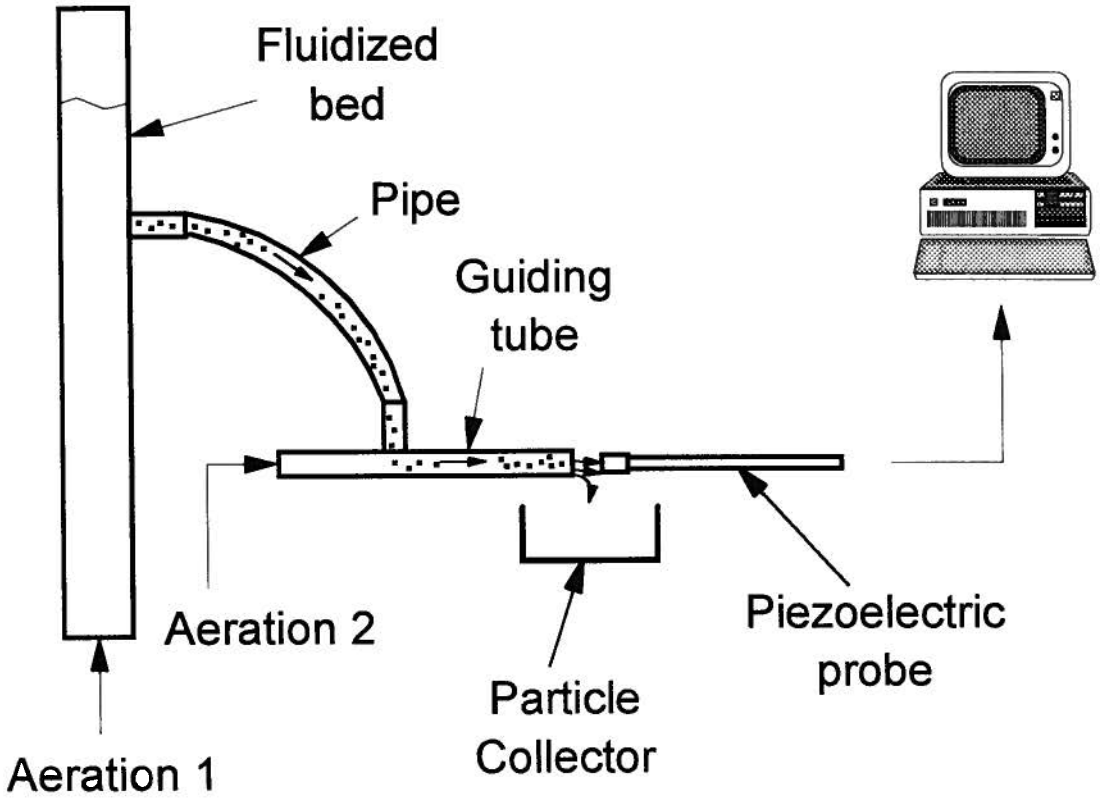

Fig. 7.3. Calibration system for the piezoelectric solids momentum flux probe.

$$\overline{\rho} = (1-\varepsilon)\rho_p + \varepsilon\rho_g \tag{7.3}$$

Here ε is the average voidage, ρ_g is the gas density and ρ_p is the particle density. The flowrate of gas-solid flow is thus:

$$\dot{m}_p = Q\overline{\rho}$$

$$= A_o C_{DC}\sqrt{(2\Delta P)\overline{\rho}} \tag{7.4}$$

ΔP and/or $\overline{\rho}$ in Equation (7.4) can be varied by changing the superficial gas velocity, while the particle velocities at the surface of the piezoelectric probe are controlled by changing the gas velocity at the Aeration 2 location in Fig. 7.3. The characteristics of the system were determined before it was used to calibrate the piezoelectric probe. The flow rate of particles striking the piezoelectric probe was measured by weighing the particles delivered by the guiding tube in a given time interval, while the particle velocity at the measuring location of the piezoelectric probe was measured by a fibre optic particle velocity probe, as described in detail in Chapter 4.

A calibration curve for the piezo-electric probe has been obtained as shown in Fig. 7.4. The electrical potential, E, developed by the piezoelectric crystal is seen to be proportional to the momentum flow of solids striking the surface of the piezoelectric probe, i. e.

$$E = C\dot{m}_p v_p \tag{7.5}$$

where C is a constant and v_p is the velocity of solids striking the probe normal to the surface. A linear regression has been performed, yielding a calibration curve with a correlation coefficient of 0.9985 and standard deviation of 0.0689. The detailed particle velocities and solids fluxes used in the calibration of the piezo-electric probe are given in Table 7.1.

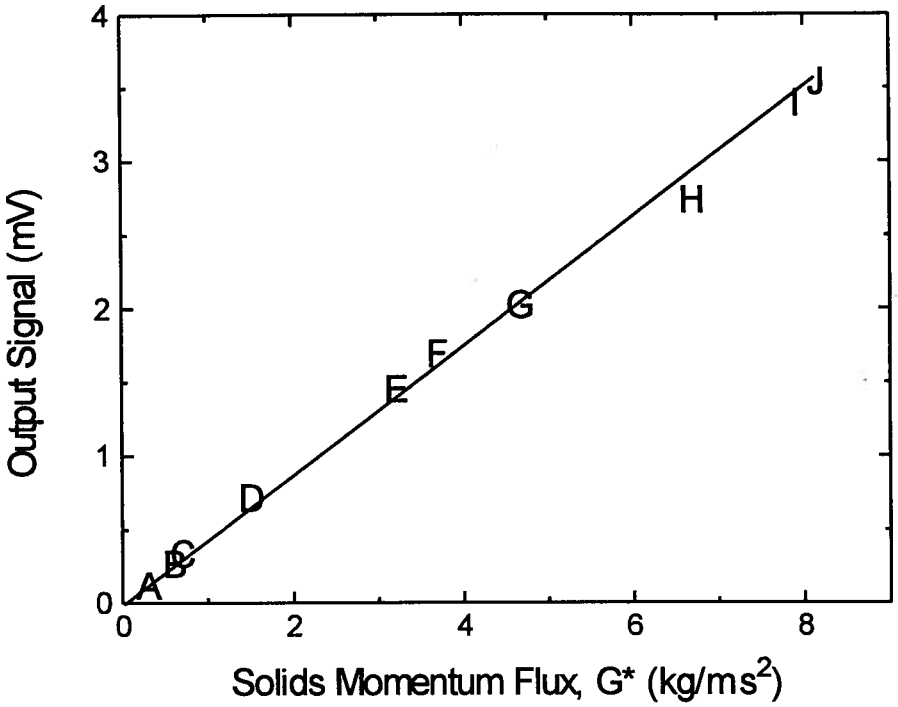

Fig. 7.4. Calibration curve of piezo-electric probe.

Table 7.1. Particle velocity and solids fluxes used in calibration of piezo-electric probe.

	A	B	C	D	E	F	G	H	I	J
Particle velocity, m/s	0.6	0.6	0.6	1.3	2.1	3.1	1.2	3.7	3.7	2.1
Solids flux, kg/m^2s	0.5	1.0	1.1	1.1	1.5	1.2	3.9	1.8	2.1	3.9

7.3 Experimental Results and Discussion

7.3.1 Solids Cross-Flow Mass Flux

Axial profiles of solids cross-flow mass fluxes at the axis and the wall of the riser are shown in Figs 7.5 and 7.6, respectively. Similar to axial particle concentration profiles in CFB risers, the solids cross-flow flux was highest at the bottom of the riser. It decreased with height between the bottom and 1.5 m above the distributor, remained nearly unchanged from z=2 m to 6 m, and finally increased slightly towards the top. The greatest change in flux was observed in the bottom region of the riser where particle concentration and particle velocity changed greatly. As shown in Figs 7.5(b) and 7.6(b), the solids cross-flow flux decreased with increasing superficial gas velocity. A greater influence is observed at both the bottom and the top. Figures 7.5(a) and 7.6(a) indicate that the solids cross-flow increases with solids circulation rate, with a greater increase near the bottom of the riser. The outward solids cross-flow flux is higher at the wall than at the axis. The lateral solids flux at the axis of the riser is much smaller than the axial solids circulation flux along the whole riser, while in the dense region at the bottom, the lateral flux at the wall can be of the same order of magnitude as the solids circulation rate. The finding reported by Qi and Farag (1993) that the lateral net solids flux near the wall can be higher than the (axial) solids circulation flux could not be verified in this work.

Lateral profiles of solids cross-flow mass fluxes are shown in Fig. 7.7. Note that only outward flux could be measured at y/Y=1, but the corresponding inward flux can be obtained from the condition that the net flux at the wall is zero. Similar to lateral profiles of particle concentration, both the inward and the outward solids fluxes reached a minimum at the axis and increased laterally towards the wall. Near the wall, where particle concentration is highest, particle-particle collisions are more frequent, leading to higher solids cross-flow. The magnitude

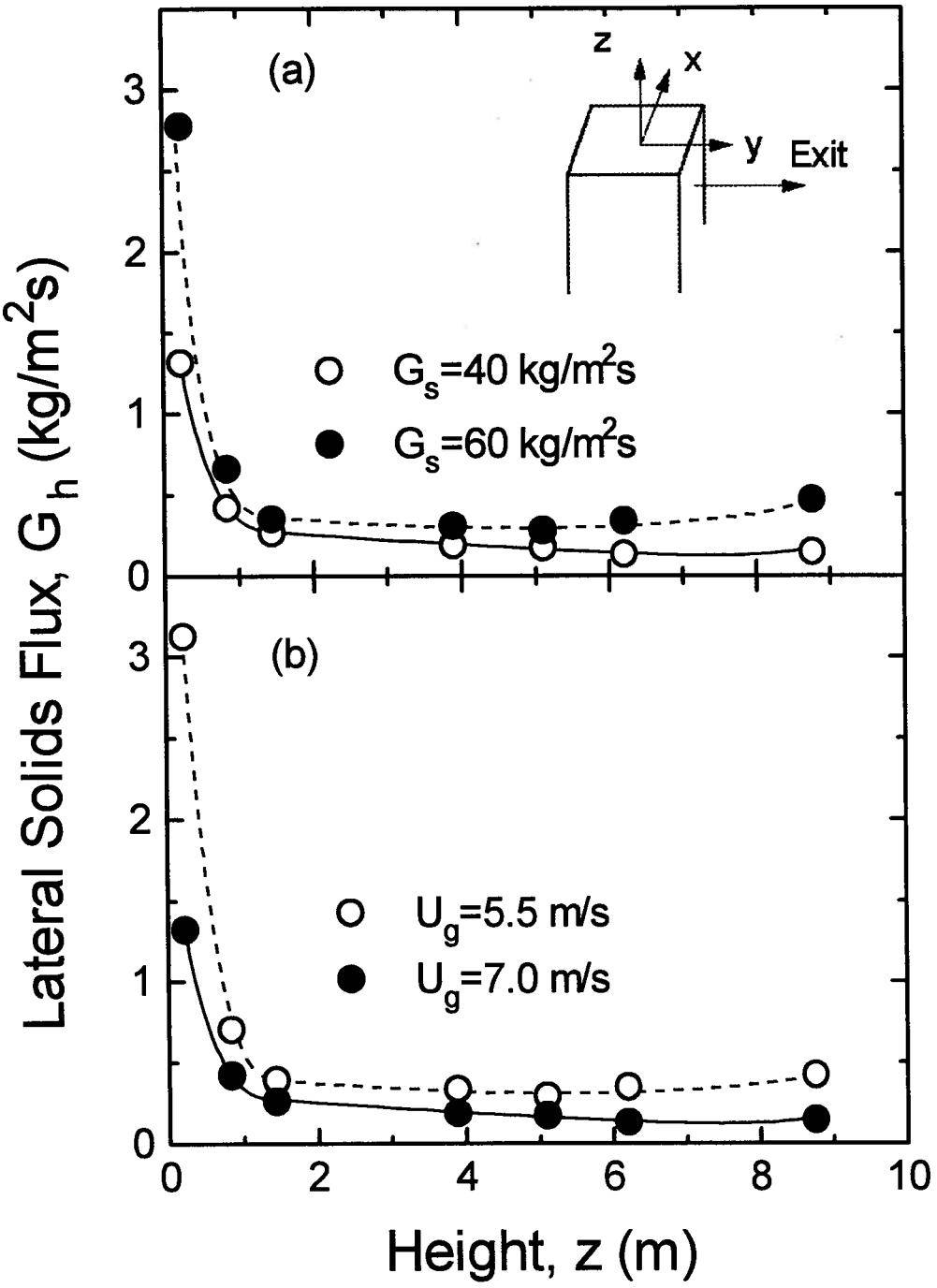

Fig. 7.5. Axial profiles of solids cross-flow flux on the axis (x=y=0) showing the influence of operating conditions: (a) U_g=7.0 m/s; (b) G_s=40 kg/m^{2}s.

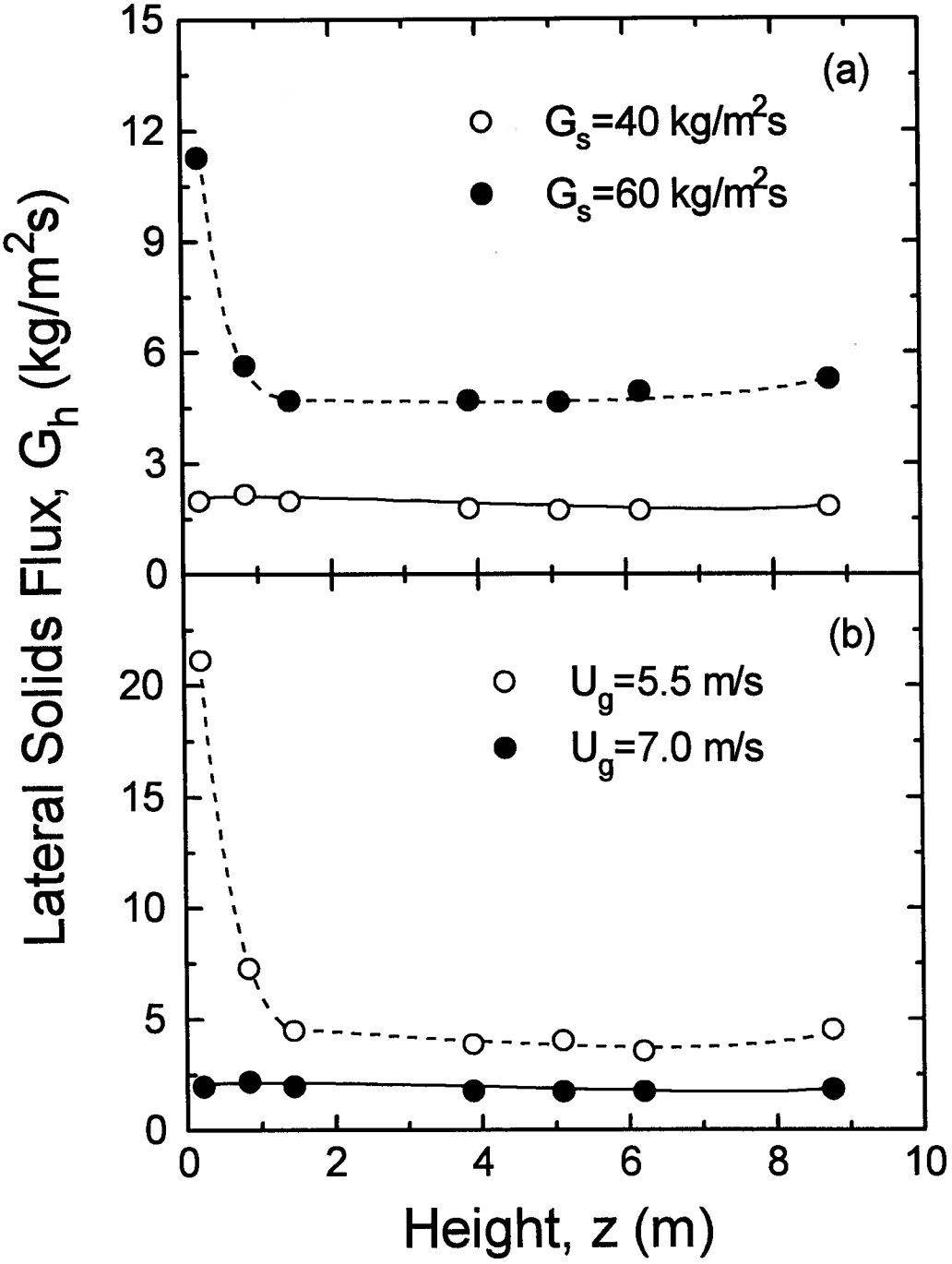

Fig. 7.6. Axial profiles of outward solids cross-flow flux at wall (x/X=0, y/Y=1) showing the influence of operating conditions: (a) U_g=7.0 m/s; (b) G_s=40 kg/m^{2}s.

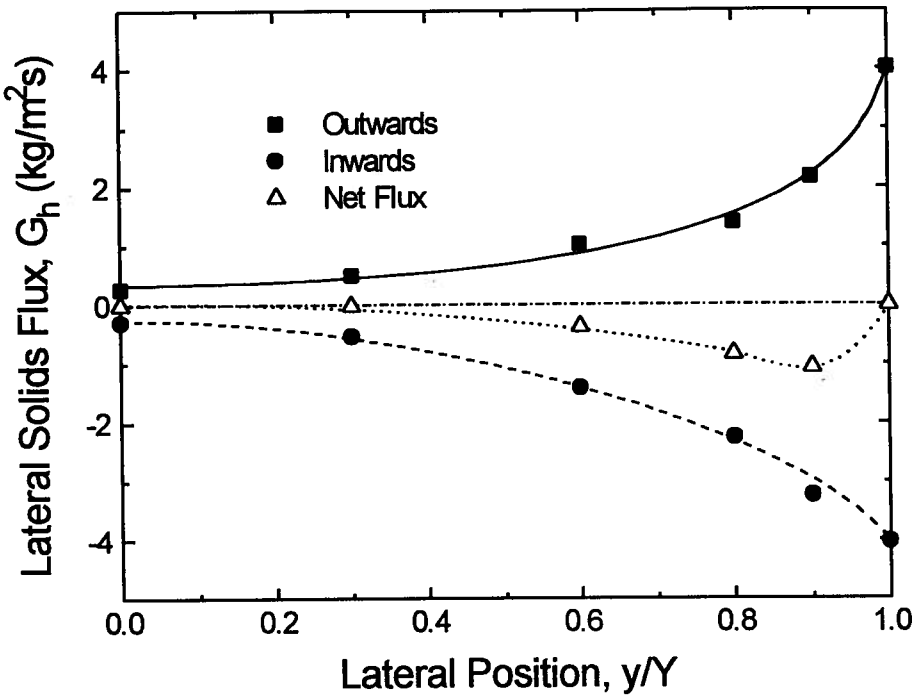

Fig. 7.7. Lateral profiles of solids cross-flow flux for x/X=0, z=6.2 m, U_g=5.5 m/s, G_s=40 kg/m^{2}s.

of the net solids cross-flow flux, obtained by subtracting the outward solids flux from the inward flux, first increases as one moves outwards from the axis, then decreases after a maximum is reached near the core-annulus boundary. Visual observations showed that near the axis of the riser, the sampled particles entered the sampling probe in a relatively regular manner, suggesting homogenous solids cross-flow near the axis. Near the wall, however, the sampled particles entered the probe in irregular clumps, indicating a heterogeneous flow structure. Near the bottom of the riser, the solids cross-flow flux was more heterogeneous than at higher locations, consistent with the lateral intermittency index profiles obtained from particle concentration data by Brereton

and Grace (1993) in a riser of circular cross-section and data reported in Chapter 3 for the same square cross-section riser.

As indicated in Fig. 7.8(a), the magnitude of both the inward and outward lateral solids fluxes increased when the solids circulation rate was increased from 40 to 60 kg/m^{2}s. Figure 7.8(b) shows that both the outward and the inward solids cross-flow flux decreased with increasing superficial gas velocity. The difference is greatest near the wall, presumably because particle concentration varies most at the wall as the superficial gas velocity or solids circulation rate is varied.

The influences of the superficial gas velocity and solids circulation rate on the lateral profiles of net solids lateral fluxes 6.2 m above the distributor are shown in Fig. 7.9. At this level, the net solids flux was inwards towards the axis, except at the wall itself and at the axis where it was 0. The magnitude of the net lateral solids flux increased with decreasing superficial gas velocity and/or increasing solids circulation rate. However, the location of the maximum net solids flux near the core-annulus boundary did not change appreciably with solids circulation rate or superficial gas velocity.

Lateral profiles of net solids cross-flow fluxes at different heights are plotted in Fig. 7.10. It is seen that near the bottom of the riser, the net lateral solids fluxes are outwards from the axis towards the wall, while in the upper portion of the riser, the net lateral solids fluxes are inwards towards the axis. This is consistent with the lateral profile of the wall layer thickness obtained in the same riser for the same operating conditions (Chapter 4). In the lower part of the riser, since the net lateral solids fluxes are outwards towards the wall and particles in the annular wall layer travel downwards, wall layer thickness becomes thicker towards the bottom. In the upper part of the riser, however, wall layer thickness increases with height because the net lateral solids flux is

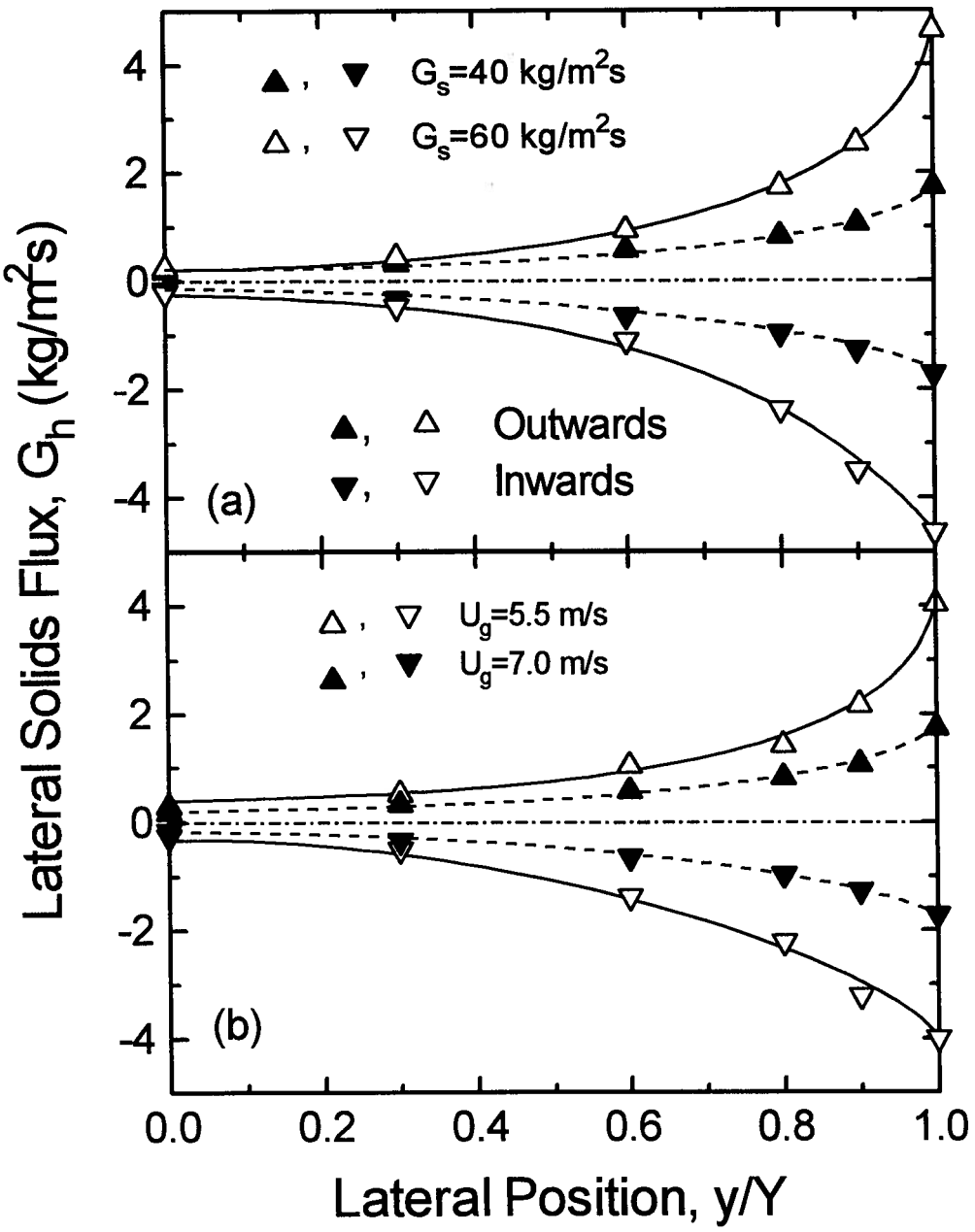

Fig. 7.8. Lateral profiles of solids cross-flow flux for x/X=0, z=6.2 m: (a) U_g=7.0 m/s; (b) G_s=40 kg/m^{2}s.

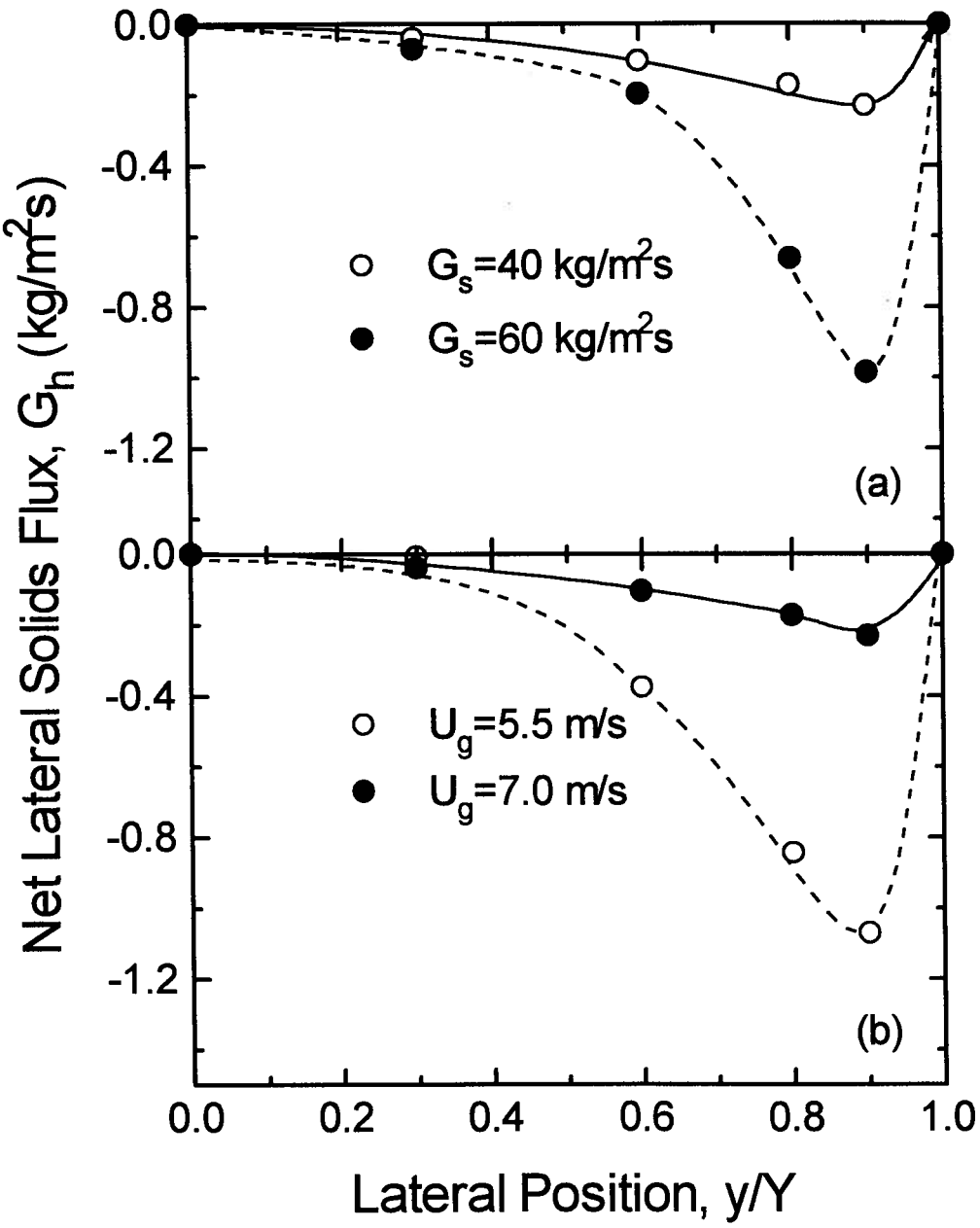

Fig. 7.9. Lateral profiles of net cross-flow solids flux for x/X=0, z=6.2 m: (a) U_g=7.0 m/s; (b) G_s=40 kg/m^{2}s.

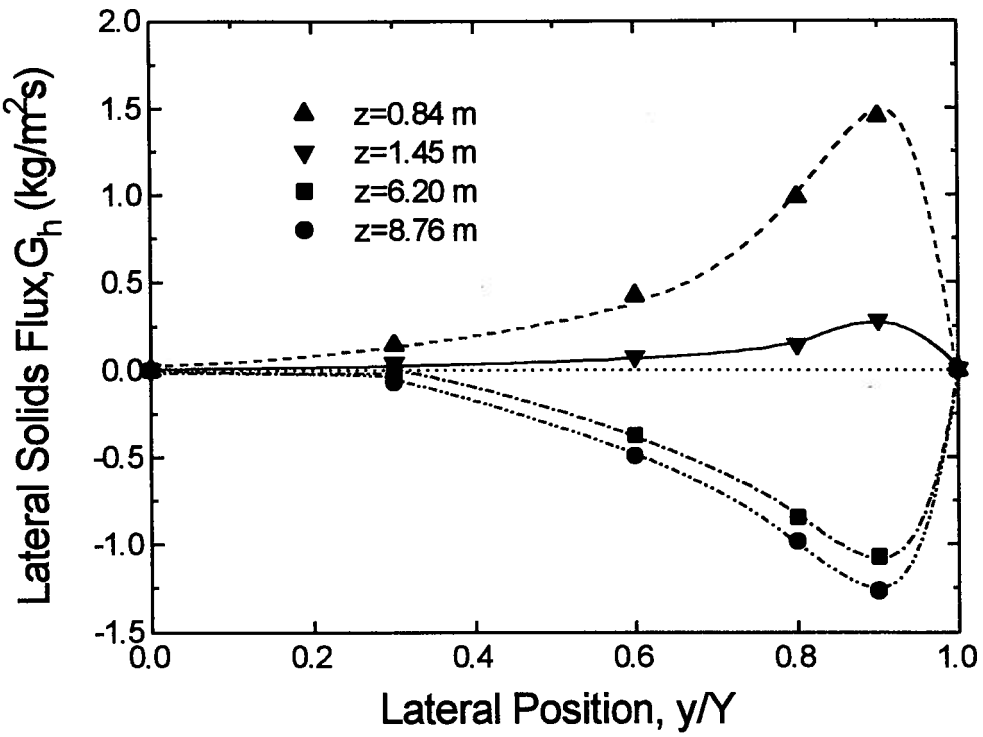

Fig. 7.10. Lateral profiles of net solids cross-flow flux at different heights for x/X=0, U_g=5.5 m/s, G_s=40 kg/m^{2}s.

inwards towards the axis. At some intermediate level, between 3 and 4 m above the distributor for U_g=5.5 m/s and G_s=40 kg m^{2}s, the wall layer thickness reaches a minimum and the net lateral solids flux is expected to be zero, i.e. the lateral inward solids flux equals the lateral outward flux. Note that since limited data were obtained near the wall, the locations where the net lateral solids mass fluxes reached maxima may not be exactly as shown in Figs 7.7, 7.9 and 7.10.

The net lateral solids mass fluxes obtained near the core-annulus boundary at different heights have been compared with the results of a semi-empirical hydrodynamic model developed

by Senior and Brereton (1992). The model successfully predicts that the direction of the net lateral solids mass flux is outward towards the wall near the bottom, while being inward towards the axis near the top of the riser. The detailed comparison is provided in Appendix II. Although a number of papers (e.g. Harris and Davidson, 1994) have considered particle cross-flow, there appear to be no other published predictive models with which to compare our experimental data.

The local voidage, particle velocity and annulus thickness data presented in Chapters 3 and 4 allow time-mean vertical solids flow rates in both the core and annulus to be determined at 5.13 and 6.20 m above the distributor for U_g=5.5 m/s and G_s=40 kg/m^{2}s. By subtracting these two, the net solids exchange between the core and annulus between two levels can then be obtained. The estimated net solids cross-flux is 1.3 kg/m^{2}s outwards, which agrees very well with an integrated mean value of about 1 kg/m^{2}s outwards.

Figure 7.11 shows that both the inward and outward solids cross-flow fluxes are higher near the corner of the column than midway between opposite walls. These profiles are quite similar to particle concentration profiles reported in Chapter 3 for the same height in the same riser with the same operating conditions. It appears that lateral particle movement reaches a maximum in the corner region.

The net lateral solids flux profiles near a corner are shown in Fig. 7.12. It is seen that there is a greater lateral solids exchange towards the corner than elsewhere at the same cross-section. At this height, z=6.2 m, the net lateral solids fluxes were inwards towards the axis. Experiments conducted at a lower level where the net lateral solids fluxes were outwards towards the wall gave similar results, again showing higher fluxes near the corner.

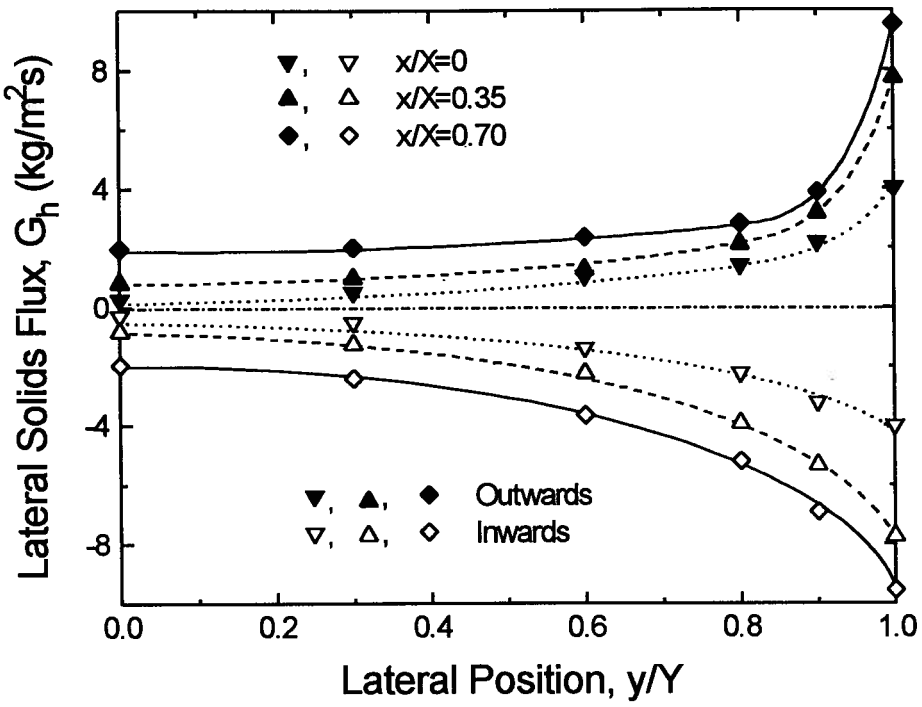

Fig. 7.11. Lateral profiles of solids cross-flow flux for z=6.2 m, U_g=5.5 m/s, G_s=40 kg/m^{2}s.

In Figs 7.7 to 7.12, the net vertical solids flux was either 40 or 60 kg/m^{2}s for each of the curves shown. In each case, the measured solids lateral flux (inwards, outwards or net) is seen to be at least an order of magnitude smaller than the corresponding vertical net flux. This finding differs significantly from that of Qi and Farag (1993) who, as noted above, reported lateral fluxes of similar magnitude as, and sometimes in excess of, their vertical fluxes.

In order to explain this discrepancy a test was carried out to check the sensitivity of the sampling probe to the pressure difference between the sample collector and the location inside the riser where samples were obtained. As shown in Fig. 7.13, the magnitudes of solids cross-flow

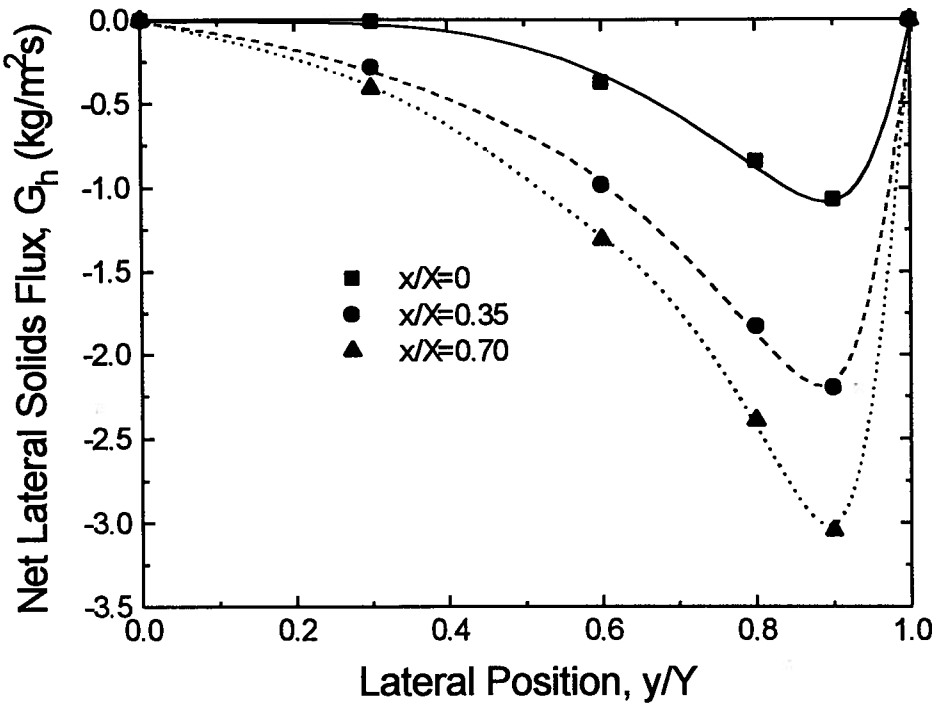

Fig. 7.12. Lateral profiles of net solids cross-flow flux for z=6.2 m, U_g=5.5 m/s, G_s=40 kg/m^{2}s.

fluxes obtained both near the wall and at the axis were very sensitive to this pressure difference. The measured value of the lateral solids flux at the axis with the pressure release valve, shown in Fig. 7.1, fully open for U_g=5.5 m/s, G_s=40 kg/m^{2}s at 0.77 m above the distributor was as much as 6.6 times the value with the system fully sealed, while near the wall the measured lateral solids flux with the pressure release valve fully open was 3.6 times greater than with the system properly sealed. It is possible that even a small amount of air leakage from the receiver or connecting tubing employed by Qi and Farag could have caused much higher efflux of particles into their sampling system, accounting for the substantial measured fluxes. However, as discussed in

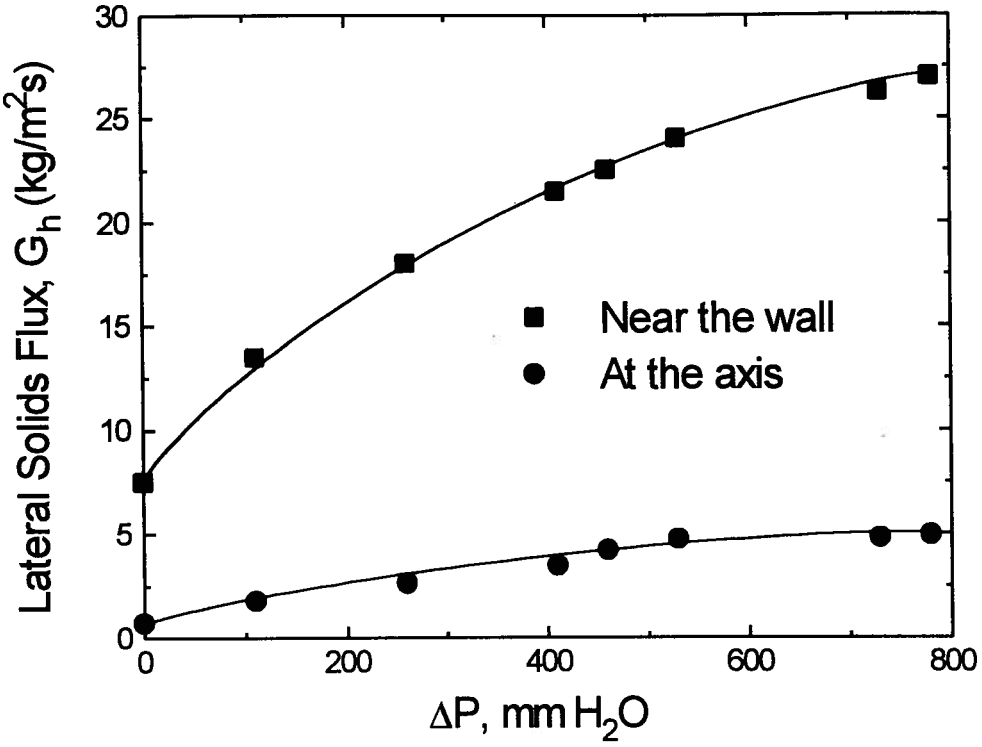

Fig. 7.13. Sensitivity of solids cross-flow to pressure difference for U_g=5.5 m/s, G_s=40 kg/m^{2}s, x/X=0, z=0.77 m.

Chapter 4, the net solids flux obtained from the difference between inward and outward fluxes is not much influenced by the leakage. Further measurements of cross-flow flux by other workers or with other experimental techniques are needed to confirm the magnitude of the cross-flow flux. In our view it is unlikely that lateral fluxes could be as high as the corresponding vertical fluxes.

7.3.2. Lateral Momentum Flux

Lateral solids momentum fluxes were measured using the piezoelectric probe described above by dividing the momentum flow by the corresponding sensing area. Axial profiles of lateral

momentum flux appear in Fig. 7.14. These indicate that the lateral solids momentum flux increases first from the bottom of the riser and then decreases towards the top. Figure 7.14 also shows that the lateral solids momentum flux increased with increasing solids circulation rate and with decreasing superficial gas velocity. These trends are the same as the influence of these operating variables on the lateral solids mass flux shown in Fig. 7.5.

Figure 7.15 plots horizontal profiles of lateral solids momentum flux midway between opposite walls of the riser at a height of 6.2 m above the gas distributor. It is seen that the lateral solids momentum flux increases slightly in moving away from the axis until a maximum is reached at about 30 to 50% of the distance to the wall of the riser. It then decreased sharply towards the wall. Near the axis, there are relatively few particles present (Chapter 3) and this likely explains the minimum there. Particles move mostly downward in streamers at the wall, shielding the wall from impacts of horizontally moving particles. There are, however, occasional pulses when the piezoelectric probe is flush with the wall indicating that some individual particles do penetrate through to collide with the wall from inside the riser. Limited by the sensitivity of the piezoelectric probe, the minimum solids momentum flux which can be detected is 0.12 kg/m s^2. The lateral solids momentum flux is low at the wall, less than the 0.12 kg/m s^2 minimum level of measurement.

Horizontal profiles of lateral momentum flux are shown in Fig. 7.16 for three different distances from the axis (i.e. x/X=0, 0.35 and 0.70), all at z=6.2 m. These measurements demonstrate that the lateral solids momentum flux is higher midway between parallel walls than near one of the walls. The piezo-electric probe at the wall and near the corner showed that some particles struck the measuring surface of the probe causing spikes in the output signals; however, the average output of the probe was essentially zero except near the very bottom of the riser, indicating lateral solids momentum fluxes less than the lower limit of measurement, 0.12 kg/m s^2.

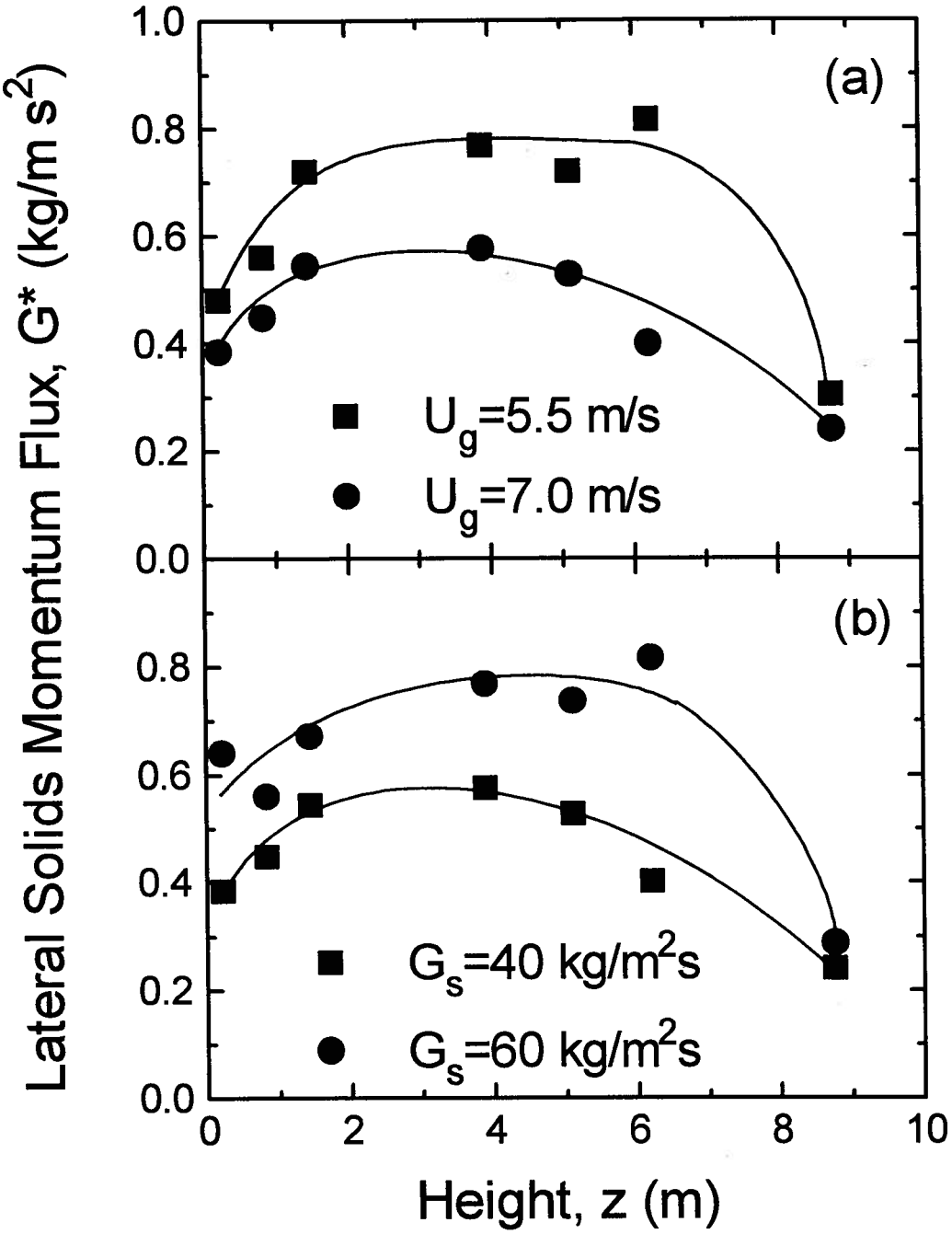

Fig. 7.14. Axial profiles of lateral solids momentum flux about the axis (x=y=0): (a) G_s=40 kg/m^{2}s; (b) U_g=7.0 m/s.

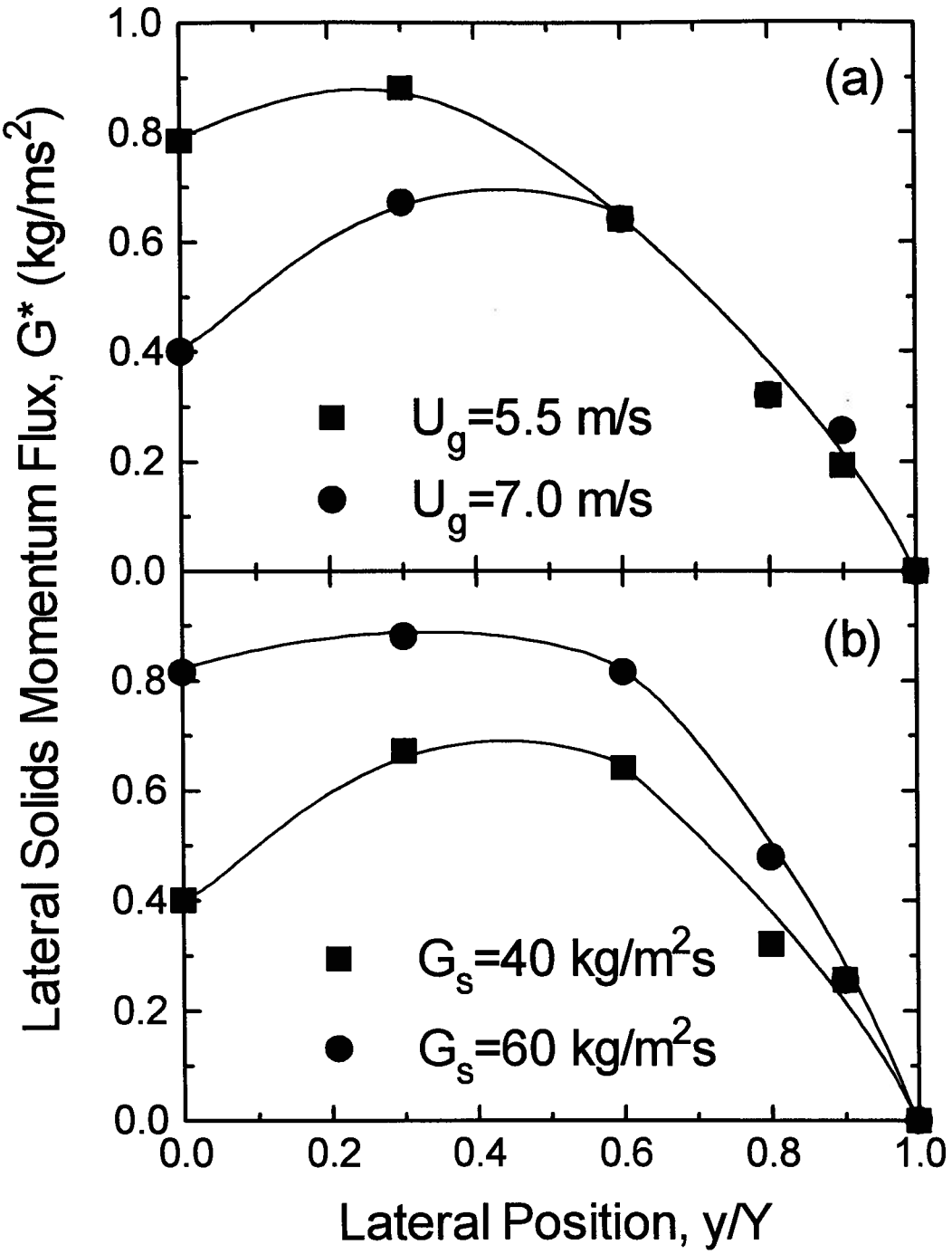

Fig. 7.15. Horizontal profiles of lateral solids momentum flux for x/X=0, z=6.2 m: (a) G_s=40 kg/m^{2}s; (b) U_g=7.0 m/s.

7.3.3. Lateral Particle Velocity

If one divides the lateral solids momentum flux by the corresponding lateral solids mass flux, one obtains a quantity which we may call

$$v^* = \frac{\frac{1}{A_p T}\iint \rho_p v_h^2 (1-\varepsilon) dA dt}{\frac{1}{AT}\iint \rho_p v_h (1-\varepsilon) dA dt} \tag{6}$$

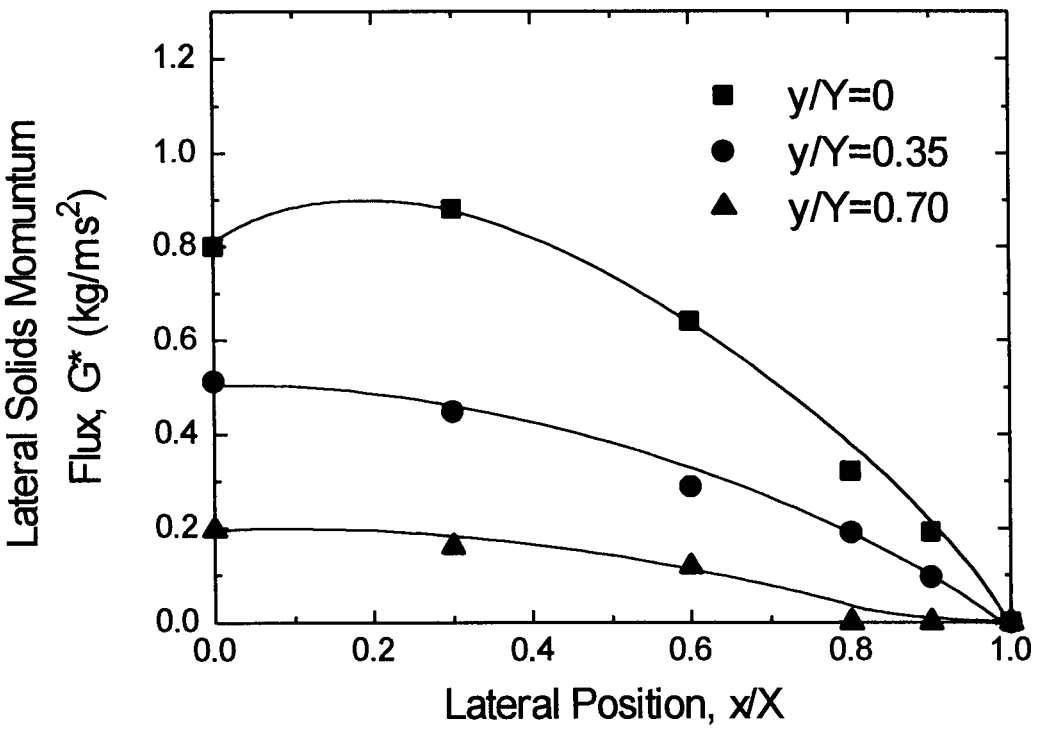

Fig. 7.16. Horizontal profiles of lateral solids momentum flux for z=6.2 m, U_g=7.0 m/s, G_S=40 kg/m^{2}s.

where T is sampling duration, v_h is the horizontal component of particle velocity normal to the probe surface and A_p is the sensing area of the piezoelectric probe. If v_h and ε were to be uncorrelated, then for small measurement areas $v^*=v_h$. In general, we do not expect v_h and ε to be uncorrelated. However, the correlation should be minimal along the axis of the column, especially in the upper part of the riser.

Hence, we can estimate the lateral component of particle velocity at x=y=0 by dividing the lateral solids momentum flux by the lateral solids mass flux. The results are shown in Fig. 7.17. Similar to the axial velocity profiles of particles travelling vertically (Zhou et al., 1994) the horizontal component of particle velocity on the axis increased with height near the bottom of the column, then decreased near the top. More significant changes in lateral particle velocities were found at the bottom of the riser where particles accelerated and at the top where particles decelerated. Between 3 and 7 m above the distributor, lateral particle velocities did not change very much with height and averaged 2 to 3 m/s, somewhat less than half of the corresponding average vertical ascending particle velocity (Chapter 4). These lateral particle velocities are higher than might be expected. Since these are the first experimental data for lateral particle velocities, it is important that other work be done to confirm values of this magnitude. As shown in Fig. 7.17(a), the lateral particle velocity decreased when the solids circulation rate increased from 40 to 60 kg/m^{2}s, presumably because of a stronger damping effect caused by an increase in particle concentration. Not surprisingly, the lateral particle velocity increased as the superficial gas velocity increased from 5.5 to 7.0 m/s (Fig. 7.17(b)).

7.4 Summary

The data in this chapter are especially useful in allowing estimates to be made of particle interchange rates between the dilute core and the more concentrated wall regions and in providing data for testing of future hydrodynamic models.

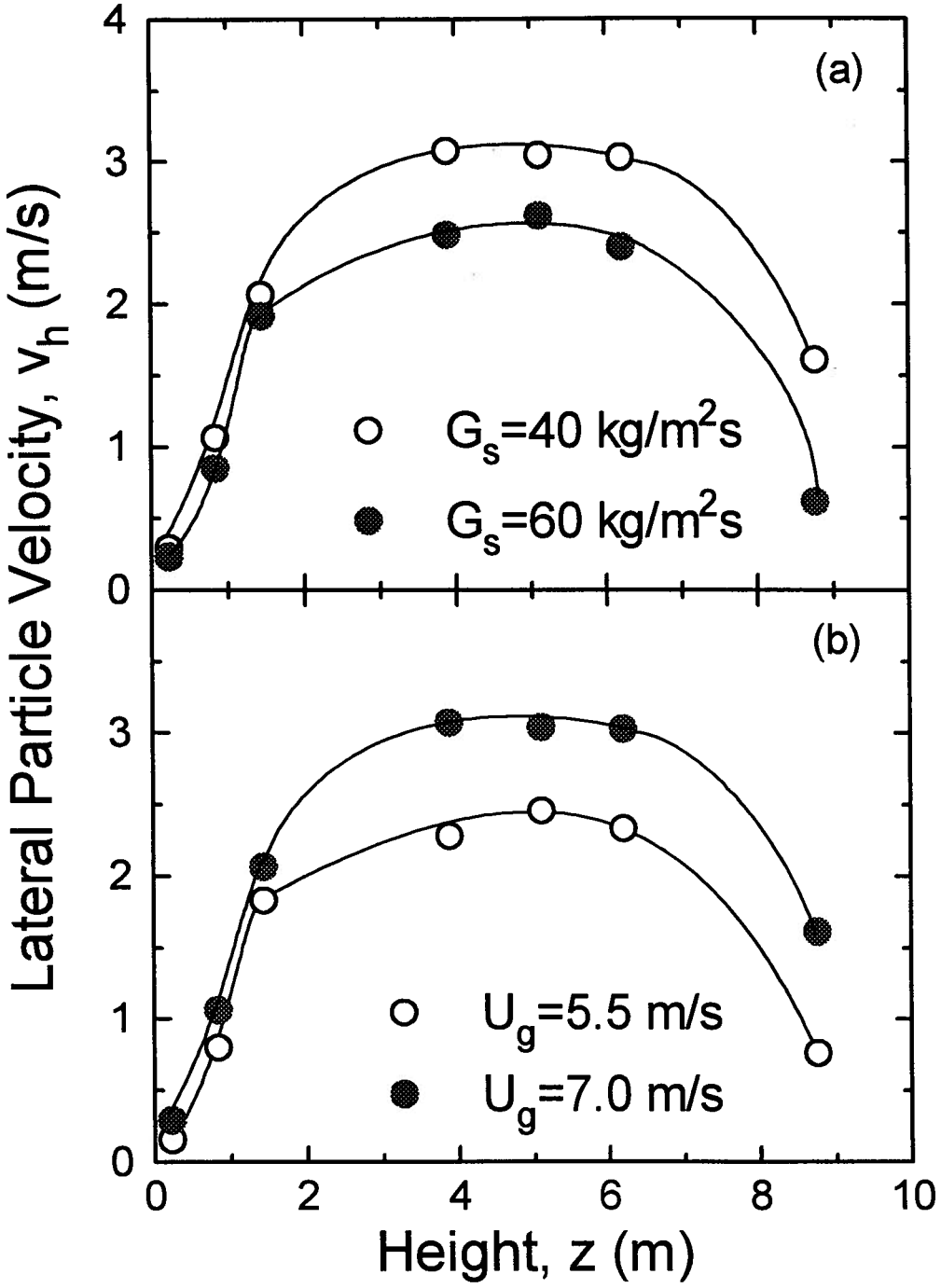

Fig. 7.17. Axial profiles of lateral particle velocity about the axis (x=y=0): (a) U_g=7.0 m/s; (b) G_s=40 kg/m^{2}s.

Measurements of lateral solids mass fluxes, lateral momentum flux and lateral velocities were carried out in a circulating fluidized bed riser of square cross-section. Except at the very bottom of the riser, cross-flow fluxes were always substantially lower than (axial) net circulation fluxes, but high enough to assure considerable interchange between the wall and core regions. Lateral fluxes were highest at the bottom of the riser, relatively constant at intermediate heights, then increased slightly near the top. Higher fluxes were found near the corners than mid-way between opposite walls. Lateral fluxes tended to be higher at a higher solids circulation rate and at a lower superficial gas velocity for the range of conditions studied. The net solids mass flux was outwards towards the outer wall near the bottom and inwards in the upper part of the riser.

The lateral solids momentum flux was found to increase with height at the bottom of the riser and then to decrease towards the top. A maximum lateral solids momentum flux was reached at about 30 to 50% of the way from the axis to the wall of the riser. The lateral solids momentum flux increased with increasing solids circulation rate and with decreasing superficial gas velocity.

The estimated average lateral component of particle velocity along the axis of the riser reached a maximum about half way up the column with a magnitude somewhat less than half the corresponding velocity of vertically ascending particles measured in Chapter 4 for the same column with the same particles.

Chapter 8

Conclusions and Recommendations

8.1 General Conclusions

Most previous research on circulating fluidized beds has been carried out in risers of circular cross-section, although square columns are widely used commercially in CFB combustors. Despite the influence of column geometry on hydrodynamics in CFB risers, experimental and modelling results obtained from circular risers are commonly used in the design and operation of CFBs. To improve the understanding of the influence of column geometry on hydrodynamics, a CFB riser of 146 × 146 mm^2 square cross-section and 9.14 m height was designed and constructed to study the hydrodynamics.

The basic voidage and particle velocity profiles in a riser with flat and smooth walls have been determined to study the influence of corners on the square column on hydrodynamics. The experimental results in this thesis, giving local voidages, vertical and some horizontal particle velocity data, vertical fluxes and horizontal fluxes, all for identical operating conditions, presented in Chapters 3, 4 and 7, provide the most comprehensive mapping of CFB hydrodynamics for any given column. It is clear that there are complex interrelations between the various quantities and regions. The influences of wall roughness and membrane walls on hydrodynamics were also investigated by comparing the results with voidage and velocity profiles from the same column with flat smooth walls.

In Chapters 3 and 4, particle concentration and particle velocity profiles have been studied extensively. Fibre optic probes have been employed to measure both voidage and particle velocity. As in risers of circular cross-section, the voidage is low near the bottom of the riser and increases with the height. The particle concentration is higher near the wall than towards the axis. End

effects, appear to be similar to those in circular columns. M-shaped lateral voidage profiles, also applicable to in risers of circular cross-section by close scrutiny of data from previous studies, appear to be more prominent in the square riser. The particle concentration in the corners of the column is higher than at other locations on the same cross-section. The probability distribution of voidage and intermittency index have been used to characterize the nature of flow in the CFB riser. Bimodal and trimodal probability distributions of voidage have been found. The particle flow has been found to be more heterogeneous with high fluctuation of voidage near the core-annulus boundary.

Ascending and descending particle velocities, together with the proportion of particles travelling upwards and downwards were measured using a newly developed five-fibre optical particle velocity probe. A core-annulus structure was found to exist in the riser of square cross-section, but the shape of the boundary was no longer circular. The thickness of the wall layer, in which most particles were descending, decreased with height from the bottom of the riser and, after a minimum was reached, increased towards the top. There is a substantial difference between core-annulus boundaries defined in terms of the location where the time-mean vertical particle velocity is zero and the position where the net vertical solids mass flux is zero. A model to predict the descending velocity of wall clusters gives good results. Simulations for both Ottawa sand and FCC particles show good agreement with the experimental data. Particle density and the configuration of the cluster are both predicted to influence the velocity of clusters.

The influence of wall roughness on the hydrodynamics in the CFB riser is elucidated in Chapter 5. Statistical methods are used to analyze the data. The voidage near the rough wall has been found to increase, while there was negligible change in voidage near the axis of the riser. Lateral voidage profiles for the rough walls were more uniform than for smooth walls. Wall roughness led to higher particle ascending velocities, while the velocity of particle downflow near the wall did not change appreciably with wall roughness.

Chapter 6 demonstrates that membrane walls influence voidage and particle velocities in the CFB riser. As for the corners of the square riser where voidage is low and downflowing particle velocity is high, the valleys or troughs formed by the riser wall and two adjacent membrane tubes appear to protect wall-layer downflowing particles from the gas. Particles in the valleys then descend further on average before being stripped off into the core upflow. This part of the work helps explain local heat transfer measurements for membrane surfaces in CFB risers.

Solids lateral fluxes were measured using a sampling probe, and the results appear in Chapter 7. Except at the very bottom of the riser, cross-flow mass fluxes were always substantially lower than (axial) net solids circulation fluxes, but high enough to assure considerable interchange between the wall and core regions. Lateral fluxes were highest at the bottom of the riser, relatively constant at intermediate heights, then increased slightly near the top. The solids mass flux is high near the wall, while even higher fluxes were found near the corners than mid-way between opposite walls. The net solids mass flux was outwards towards the outer wall near the bottom of the riser and inwards in the upper part of the riser. The direction change of the net lateral solids flux is consistent with the measured axial profile of wall layer thickness presented in Chapter 4.

A piezo-electric probe was developed to measure lateral solids momentum flux. It has been found that the lateral solids momentum flux increased with height at the bottom of the riser and then decreased towards the top. There was a maximum in the lateral profile of lateral solids momentum flux at about 30 to 50% of the way from the axis to the wall of the riser. The lateral solids momentum flux increased with increasing solids circulation rate and with decreasing superficial gas velocity for the range of conditions investigated.

Taken together, the various chapters provide a comprehensive picture of the flow structure of the CFB riser of square cross-section. The various aspects are shown together in schematic form in Fig. 8.1.

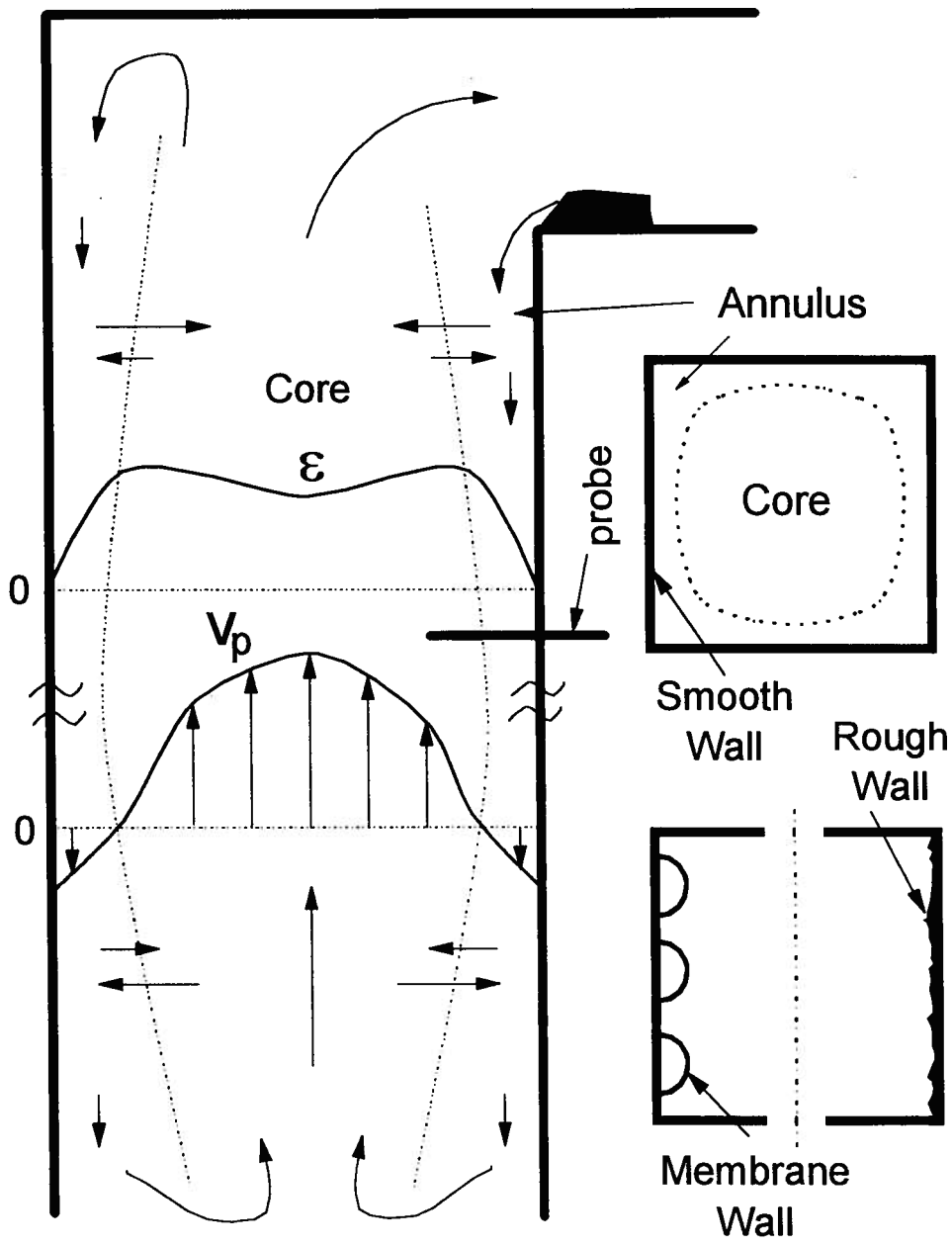

Fig. 8.1. Schematic of flow structure of a CFB riser of square cross-section.

8.2 Recommendations

Proper terminology and clear definitions for many common concepts such as wall layer and particle aggregates are needed and should be unified to reduce misunderstandings between researchers. To achieve this, a better understanding of CFB phenomena is needed.

Until now, most hydrodynamic studies in CFBs have been concentrated on the solids phase because of the development of electrical and optical techniques for solid phase measurements and the difficulty in determining gas phase behaviour. More work is needed to understand the gas-phase hydrodynamics.

For solids-phase hydrodynamic studies, more work is recommended on new configurations and baffles to improve the performance of CFBs. The influence of particle size distribution on the hydrodynamics in CFBs should also be investigated, although some work has already been done in conventional fluidized beds. More accurate, reliable and non-interfering measurement techniques are needed to further investigate particle aggregates and wall layer particle downflows.

With more experimental data available and a better understanding of CFB phenomena, theoretical analysis can also be improved. A better and comprehensive hydrodynamic model for CFBs is needed for the sake of both design and operation of CFB reactors. The results given in this thesis may be useful to validating such a model.

Nomenclature

a, b	Semiaxes of the spheroidal cluster, m
A	Open area of the sampling probe, m^2
A_l	Cross-sectional area of the standpipe in which the identified particles are descending, m^2
A_s	Cross-sectional area, m^2
A_t	cross-sectional area of the riser, m^3
A_o	Cross-sectional area of the orifice, m^2
A_p	Sensing area of the piezoelectric probe, m^2
C, C_0, C_1, C_2	Constants
C_D	Drag coefficient
C_{DC}	Discharge coefficient
C_{DS}	Single particle drag coefficient
C_p	Particle concentration, kg/m^3
C_v	Particle volumetic concentration
C*	Local relative particle concentration = $(\rho_{susp}-\rho_g)/(\rho_{mf}-\rho_g)$
d_f	Diameter of particle concentration probe,mm
d_p	Mean particle diameter, m
d_p^*	Dimensionless particle diameter=$A_r^{1/3} = d_p(\rho_g \Delta\rho g / \mu_g^2)^{1/3}$
E_r	Ratio of b to a
E	Electric potential developed by the piezoelectric crystal, mV
F_C	Force on cluster because of momentum transfer, N
F_D	Drag force, N
F_G	Gravitational force, N

F_B	Buoyancy, N
F_W	Wall friction force, N
g	Acceleration due to gravity, m/s^2
G*	Lateral solids momentum flux, $kg/m^2 \cdot s$
G_h	Solids cross-flow mass flux, $kg/m^2 \cdot s$
G_{ho}	Lateral solids flux from the adjacent dilute phase to cluster flow, $kg/m^2 s$
G_s	Solids circulation rate, $kg/m^2 s$
H	Bed height, m
H_o	Height of packed bed, m
k	Constant
l_{AC}	Effective separation length, m
L	Height of expanded bed, m
L_i	Known distance, m
L_o	Height of packed bed, m
$\dot{m}_p$	Solids mass flowrate, kg/s
N	Number of sampled particles
N_{Up}	Number of sampled ascending particles
N_{Down}	Number of sampled descending particles
P(C*)	Relative probability of C*
Q	Solids volumetric flow rate, m^3/s
Re	Reynolds number
t	Sampling time, s
t_i	Time for the identified particles to traverse the known distance, s
t_{AC}, t_{CE}	Transit time for particle to move from optical fibres A to C, C to E as shown in Fig. 4.2, s
T	Sampling duration, s
u_c	Velocity of cluster, m/s

u_{rel}	Relative velocity between the gas and particles, m/s
U	Output of the fibre optic voidage probe, volt
U_g	Superficial gas velocity, m/s
U_{mf}	Minimum fluidization velocity, m/s
U_{TR}	Transport velocity, m/s
U_g^*	Dimensionless gas velocity=$U_g(\rho_g^2 / \Delta\rho g\mu_g)^{1/3}$
V	Volume of sampled particles, m^3
v*	Ratio of lateral solids momentum flux/lateral solids mass flux, m/s
v_h	Horizontal component of particle velocity normal to probe surface, m/s
v_p	Particle velocity, m/s
v_{pc}	Vertical velocity of solids entering cluster, m/s
v_T	Particle terminal velocity, m/s
v_{AC}, v_{CE}	Particle velocity obtained from fibres A and C, C and E, m/s
$\bar{v}_p$	Time-mean of vertical component of particle velocity, m/s
V_S	Threshhold, volt
x, y	Coordinates as shown in Fig. 2.1
z	Vertical coordinate measured from the primary air distributor
X, Y	Half-width of column cross-section, m
ΔL	Difference in height, m
ΔP	Pressure difference, N/m^2
Δt	Time interval, s
ΔW	Cumulative weight of particles passing through the cross-sectional area A_s, kg
$\Delta\rho$	Difference in density=ρ_p-ρ_g, kg/m^3
α	Angle, degree
γ	Intermittency index defined by Equation (3.11)
ϕ	Dimensionless radius=r/R

ε	Local voidage
ε_c	Internal voidage of the cluster
ε_o	Packed bed voidage
ε_{out}	Outer voidage of clusters
$\overline{\varepsilon}$	Time-mean voidage
$\overline{\varepsilon}_{av}$	Cross-sectional average voidage
$\overline{\varepsilon}_o$	Cross-sectional average voidage at the solids re-entering location
ε_{mf}	Voidage at minimum fluidization
ζ	Decay constant, m
λ_{AC}, λ_{CE}	Effective optical separation distance between fibres A and C, C and E, m
ρ_{bulk}	loosely packed particle density, kg/m^3
$\overline{\rho}$	Average suspension density, kg/m^3
ρ_{mf}	Bed density at minimum fluidization, kg/m^3
ρ_g	Gas density, kg/m^3
ρ_p	Particle density, kg/m^3
$\overline{\rho}_{susp}$	Time-average point suspension density, kg/m^3
σ	Standard deviation of density fluctuations for fully segregated two-phase flow with identical time-mean density at the same point, kg/m^3
σ^*	Normalizing factor = $\rho_{mf}\sqrt{(\overline{\rho}_{susp}/\rho_{mf})(1-\overline{\rho}_{susp}/\rho_{mf})}$, kg/m^3
τ	Shear stress, N/m^2

References

B. Andersson and B. Leckner (1992), "Experimental methods of estimating heat transfer in circulating fluidized bed boilers". *Int. J. Heat Mass Transfer*, **35**, 3353-3362.

B. Andersson and B. Leckner (1992), "Local lateral distribution of heat transfer on tube surface of membrane walls in CFB boilers". In: Circulating Fluidized Bed Technology IV, ed. A. Avidan, 368-373, in press.

Arena, U., A. Cammarota, A. Marzocchella and L. Massimilla (1989), "Solids flow structure in a two-dimensional riser of a circulating fluidized bed". *J. of Chem. Engng of Japan* **22**, 236-241.

Arena, U., A. Cammarota and L. Pistone (1986), "High velocity fluidization behavior of solids in a laboratory scale circulating fluidized bed". In: *Circulating Fluidized Bed Technology*, ed. P. Basu, Pergamon, Toronto, pp.119-125.

Bader, R., J. Findley and T.M. Knowlton (1988), "Gas-solids flow patterns in a 30.5-cm-diameter circulating fluidized bed". In: *Circulating Fluidized Bed Technology II*, ed. P. Basu and J. F. Large, Pergamon, Oxford, pp.123-137.

Bai, D. R., Y. Jin, Z. Q. Yu and J. Zhu (1992), "The axial distribution of the cross-sectional averaged voidage in fast fluidized beds". *Powder Technol.* **71**, 51-58.

Bai, D. R., Y. Jin and Z.Q. Yu (1991), "Gas-solids flow pattern in circulating fluidized beds".. *Chem. Reaction Engng Technol.* 7, 303-316.

Baumgarten, P.K. and R.L. Pigford (1960), "Density fluctuations in fluidized beds". *AIChE J.* **6**, 115-123.

Berruti, F., N. and Kalogerakis (1989), "Modelling of the internal flow structure of circulating fluidized beds". *Can. J. Chem. Engng* **67**, 1010-1014.

Bi, X., (1994), "*Flow Regime Transition in Gas-Solid Fluidization and Transport*". Ph.D. dissertation, University of British Columbia, Vancouver, Canada.

Bierl, T.W., L.J. Gajdos, A.E. McIver, and J.J. McGovern, (1980), *Studies in support of recirculating fluidized bed reactors for the processing of coal.* DOE Report FE-2449-11, Carnegie-Mellon Univ., Pittsburgh.

Boiarski, A. A. (1985), "Fibre optic particle concentration sensor", *SPIE, Fibre Optic and Laser Sensors III*, **566**, 122-125.

Bolton, L. W. and J. F. Davidson (1988), "Recirculation of particles in fast fluidized risers". In: *Circulating Fluidized Bed Technology II*, ed. P. Basu and J.F. Large, Pergamon, Oxford, pp.139-153.

Brereton, C.M.H. and L. Stromberg (1986), "Some aspects of the fluid behavior of fast fluidized beds". In: *Circulating Fluidized Bed Technology*, ed. P. Basu, Pergamon, Toronto, pp.133-143.

Brereton, C.M.H. (1987), *Fluid mechanics of high velocity fluidized beds.* Ph.D. dissertation, University of British Columbia, Vancouver, Canada.

Brereton, C.M.H. and J.R. Grace (1993), "Microstructual aspects of the behaviour of circulating fluidized beds". *Chem. Engng Sci.* **48**, 2565-2572.

Brereton, C.M.H. and J.R. Grace (1994), "End effects in circulating fluidized bed hydrodynamics". In: Circulating Fluidized Bed Technology IV, ed. A. Avidan, in press.

Burkell, J.J., J.R. Grace, J. Zhao, and C. J. Lim (1988), "Measurement of solids circulation rates in circulating fluidized beds". In: *Circulating Fluidized Bed Technology II*, ed. P. Basu and J.F. Large, Pergamon, Oxford, pp.501-509.

Burkell, J.J. (1986), Solids Circulation Rate Measurement in a Circulating Fluidized Bed. Master's dissertation, University of British Columbia, Vancouver, Canada.

Cen, K., J. Fan, Z. Luo, J. Yan and M. Ni (1988), "The prediction and measurement of particle behavior in circulating fluidized beds". In: *Circulating Fluidized Bed Technology II*, ed. P. Basu and J. F. Large, Pergamon, Oxford, pp.213-221.

Dry, R. J. (1986), "Radial concentration profiles in a fast fluidized bed". *Powder Technol.* **49**, 37-44.

Gajdos, L. J. and T. W. Bierl (1978). *Studies in support of recirculating fluidized bed reactors for the processing of coal.* Topical Report on Work Performed under DOE Contract No.EX-C-76-01-2449, Carnegie-Mellon Univ., Pittsburgh.

Geldart, D. (1972), "The effect of particle size and size distribution on the behaviour of gas-fluidized bed", *Powder Technol.*, **6**, 201-215.

Geldart, D. (1973), "Types of gas fluidization," *Powder Technol.*, 7, 285-292.

Geldart, D., N., Harnby and A.C. Wong (1984) "Fluidization of cohesive powders", *Powder Technol.* **37**, 25-37.

Gel'perin, N. I., V. G. Aynshteyn, L. I. Krupnik, Z. N. Memedlyayev and S. V. Yefimova (1976), "Structure and heat transfer in turbulent gas suspension flows". *Heat Transfer-Soviet Research* **8**, 77-86.

Glicksman, L. R., D. Westphalen, K. Woloshun, T. Ebert, K. Roth, M. Lints, C. M. H. Brereton, and J. R. Grace (1991), "Experimental scale models of circulating fluidized bed combustors," *Proc. 11th Intern. Conf. Fluidized Bed Combustion*, Montreal, ASME, New York, 1169.

Glicksman L. R., M. Hyre and D. Westphalen (1993), "Verification of scaling relations for circulating fluidized beds". In: *Proc. 12th Inter. Conf. on Fluidized Bed Combustion*, ed. L. N. Rubow, ASME, New York, pp.69-80.

Grace, J.R. and J. Tuot (1979), "A theory for cluster formation in vertically conveyed suspensions of intermediate density," *Trans. I. Chem. Engrs.*, **57**, 49-54.

Grace, J.R. (1982), "Fluidized bed hydrodymanics," Chapter 8.1 in the Handbook of Multiphase Flow, G. Hetsroni ed., Hemisphere, Washington.

Grace, J.R. (1986), "Contacting modes and behaviour classification of gas-solid and other two-phase suspensions," *Can. J. of Chem. Eng.*, **64**, 353-363.

Grace, J.R. (1990), "High-velocity fluidized bed reactors," *Chem. Eng. Sci.*, **45**, 1953-1966.

Hartge, E.-U., D. Rensner and J. Werther (1988), "Solids concentration and velocity patterns in circulating fluidized beds". In: *Circulating Fluidized Bed Technology II*, ed. P. Basu and J. F. Large, Pergamon, Oxford, pp.165-180.

Hartge, E.-U., Y. Li and J. Werther (1986), "Analysis of the local structure of the two phase flow in a fast fluidized bed". In: *Circulating Fluidized Bed Technology*, ed. P. Basu, Pergamon, Toronto, pp.153-160.

He, Y., S. Qin, C.J. Lim and J.R. Grace (1994), "Particle velocity profiles and solid flow patterns in spouted beds". *Can. J. Chem. Eng.*, **72**, 561-568.

Herb, B., S. Dou, K. Tuzla and J. C. Chen (1992), "Solid mass flux in circulating fluidized beds". *Powder Technol.* **70**, 197-205.

Horio, M., K. Morishita, O. Tachibana and N. Murata (1988), "Solid distribution and movement in circulating fluidized beds". In: *Circulating Fluidized Bed Technology II*, ed. P. Basu and J. F. Large, Pergamon, Oxford, pp.147-154.

Horio, M., H. Kuroki and M. Ogasawara (1993) "The flow structure of a three-dimensional circulating fluidized bed observed by the laser sheet technique" 86-91, 4CFB

Ishii, H. and I. Murakami (1990), "Evaluation of the scaling law of circulating fluidized beds in regards to cluster behaviors". In: *Circulating Fluidized Bed Technology III*, ed. P. Basu, M. Horio and M. Hasatani, Pergamon, Oxford, pp.125-130.

Jin, Y., Z. Yu, C. Qi and D. Bai (1988), "The influence of exit structures on the axial distribution of voidage in fast fluidized bed". In: *Fluidization '88: Science and Technology*, ed. M. Kwauk and D. Kunii, Science Press, Beijing, pp.165-173.

Karri, S.B.R. and T.M. Knowlton (1990), "A practical definition of the fast fluidization regime". In: *Circulating Fluidized Bed Technology III*, ed. P. Basu, M. Horio and M. Hasatani, Pergamon, Oxford, pp.67-72.

Kato, K., T. Takarada, T. Tamura and K. Nishino (1990), "Particle holdup distribution in a circulating fluidized bed". In: *Circulating Fluidized Bed Technology III*, ed. P. Basu, M. Horio and M. Hasatani, Pergamon, Oxford, pp.145-150.

Kennedy, J.B. and A.M. Neville (1986), "Basic statistical methods for engineers and scientists", 3rd Edition, Harper and Row, New York.

Kojima, T., K.-I. Ishihara, Y. Gulin and T. Furusawa (1989), "Measurement of solids behavior in fast fluidized bed". *J. Chem. Engng Japan* **22**, 341-346.

Krohn, D.A. (1982), "Intensity modulated fibre optic sensors overview", *SPIE, Fibre Optic and Laser Sensors IV*, **718**, 2-11.

Leckner, B. and B. A. Andersson (1992), "Characteristic features of heat transfer in circulating fluidized bed boilers", *Powder Technol.* **70**, 303-314.

Li, J., Y. Tung and M. Kwauk (1988), "Axial voidage profile of fluidized beds in different operating regions". In: *Circulating Fluidized Bed Technology II*, ed. P. Basu and J. F. Large, Pergamon, Oxford, pp.537-544.

Li, Y. and M. Kwauk (1980), "The dynamics of fast fluidization". In: *Fluidization*, ed. J. R. Grace and J. M. Matsen, Plenum Press, New York, pp.537-544.

Lints, M. C. and L. R. Glicksman (1993), "Parameters governing particle-to-wall heat transfer in a circulating fluidized bed," *Proc. 4th Intern. Conf. on Circulating Fluidized Beds*, Pennsylvania, USA, 350-312.

Lischer, D. J. and M. Y. Louge (1992), "Optical fiber measurements of particle concentration in dense suspensions: calibration and simulation". *Applied Optics* **31**, 5106-5113.

Lockhart, C., J. Zhu, C.M.H. Brereton, C.J. Lim and J.R. Grace (1995), "Local heat transfer, solids concentration and errosion around membrane tubes in a cold model circulating fluidized bed", *Int. J. Heat Mass Transfer*, in press.

Louge, M., D. J. Lischer and H. Chang (1990), "Measurements of voidage near the wall of a circulating fluidized bed riser". *Powder Technol.* **62**, 269-276.

Louge, M. Y., E. Mastorakos and J. T. Jenkins (1991), "The role of particle collision in pneumatic transport". *J. Fluid Mech.* **231**, 345-359.

Martin, P.D. and J.F. Davidson (1983), "Flow of powder through an orifice from a fluidized bed", *Chem. Eng. Res. Des.* **61**, pp.162-166.

Matsen, J.M. (1982), "Mechanisms of choking and entrainment". *Powder Technol.*, **31**, 21-33.

Matsuno, Y., H. Yamaguchi, T. Oka, H. Kage and K. Higashitani (1983), "The use of optic probes for the measurement of dilute particle concentration: calibration and application to gas-fluidized bed carryover". *Powder Technol.* **36**, 215-221.

Miller, A. and D. Gidaspow (1992), "Dense, vertical gas-solid flow in a pipe". *AIChE J.* **38**, 1801-1815.

Militzer, J. J.M. Kan, F. Hamdullahpur, P.R. Amyotte and A.M. Al Taweel (1989), "Drag coefficient for axisymmetric flow around individual spheroidal particles". *Powder Technol.*, **57**, 193-195.

Monceaux, L., M. Azzi, Y. Molodtsof, J. F. Large (1986), "Overall and local characterisation of flow regimes in a circulating fluidized bed", in Circulating Fluidized Bed Technology, eds. P. Basu, Pergamon, Toronto, pp.185-191.

Morooka, S., K. Kawaznishi and Y. Kato (1990), "Holdup of flow pattern of solid particles in freeboard of gas-solid fluidized bed with fine particles". *Powder Technol.*, **26**, 75-82.

Nakajima, M., M. Harada, M. Asai, R. Yamazaki and G. Jimbo (1990), "Bubble fraction and voidage in an emulsion phase in the transition to a turbulent fluidized bed", In: *Circulating Fluidized Bed Technology III*, ed. P. Basu, M. Horio and M. Hasatani, Pergamon, Oxford, pp.4-2-1 - 4-2-6.

Nowak, W., H. Mineo, R. Yamazaki and K. Yoshida (1990), "Behavior of particles in a circulating fluidized bed of mixture of two different sized particles". In: *Circulating Fluidized Bed Technology III*, ed. P. Basu, M. Horio and M. Hasatani, Pergamon, Oxford, pp.219-224.

Oki, K., T. Akehata and T. Shirai (1975), "A new method for evaluating the size of moving particles with a fibre optic probe", *Powder Technol.*, **18**, 171-178.

Patrose, B. and H.S. Caram (1982), "Optical fibre probe transit anemometer for particle velocity measurements in fluidized beds". *AIChE J.*, **28**, 604-609.

Perales, J.F., T. Coll, M.F. Llop, L. Puigjaner, J. Arnaldos and J. Casal (1991), "On the transition from bubbling to fast fluidization regimes," Circulating Fluidized Bed Technology III, P. Basu, M. Horio and M. Hasatani eds., Pergamon Press, Toronto, pp.73-78.

Qin, S. and G. Liu (1982), "Application of optical fibers to measurement and display of fluidized systems". In: *Fluidization, Science and Technology*, ed. M. Kwauk and D. Kunii, Science Press, Beijing, China, pp.258-267.

Randelman, R., A. Benkrid and H.S. Caram (1983), "Investigation of the solid flow pattern in a spouted bed", In: *AIChE Symp. Ser.*, **83**, 23-28.

Reh L. (1972), "Fluidized bed processing". *Chem Eng Prog*, **67**, 58-63.

Reh, L., and J. Li (1990), "Measurement of voidage in fluidized beds by optical probes". In: *Circulating Fluidized Bed Technology III*, ed. P. Basu, M. Horio and M. Hasatani, Pergamon, Oxford, pp.163-169.

Rhodes, M. (1990), "Modelling the flow structure of upward-flowing gas-solids suspensions". *Powder Technol.* **60**, 27-38.

Rhodes, M. J. and D. Geldart (1986), "The hydrodynamics of circulating fluidized beds". In: *Circulating Fluidized Bed Technology*, ed. P. Basu, Pergamon, Toronto, pp.193-206.

Rhodes, M., H. Mineo and T. Hirama (1992), "Particle motion at the wall of a circulating fluidized bed", *Powder Technol.* **70**, 207-214.

Rhodes, M. J., H. Mineo and T. Hirama (1990), "Particle motion at the wall of 305 mm diameter riser of a cold model circulation fluidized beds". In: *Circulating Fluidized Bed Technology III* (P. Basu, M. Horio and M. Hasatani, Eds.), Pergamon, Oxford, pp.171-176.

Riley, C. A. and M. Louge (1989), "Quantitative capacitance measurements of voidage in gas-solid flows". *Particulate Sci. Technol.* 7, 51-59.

Rowe, P.W. and B.A. Partridge (1965), "An X-ray study of bubbles fluidized beds". *Trans. Instn. Chem. Engrs*, **43**, 157-175.

Schnitzlein, M. G. and H. Weinstein (1988), "Flow characterization in high-velocity fluidized beds using pressure fluctuations". *Chem. Engng Sci.* **43**, 2605-2614.

Senior, R. C and C.H.M. Brereton (1992), "Modelling of circulating fluidized-bed solids flow and distribution". *Chem. Engng Sci.*, **47**, 281-296.

Senior, R. (1992), *Circulating fluidized bed fluid and particle mechanics: modelling and experimental studies with application to combustion.* Ph.D. dissertation, University of British Columbia, Vancouver, Canada.

Takeuchi, H., L. Hirama, T. Chiba, J. Biswas and L.S. Leung (1986), "A quantitative regime diagram for fast fluidization". *Powder Technol.*, **47**, 195-199, 1986.

Tsuji, Y., Y., Morikawa and H. Shiomi (1984), "LDV measurements of an air-solid two-phase flow in a vertical pipe". *J. Fluid Mech.* **139**, 417-434.

van der Ham, A.G.J., W. Prins and W.P.M. van Swaaij (1992), "Hydrodynamics of a pilot plant scale regularly packed circulating fluidized bed". *AIChE Symp. Ser.* **89**, No.296, 53-72.

van Swaaij, W.P.M., C. Buurman and J.W. van Breugel (1970), "Shear stresses on the wall of a dense gas-solids riser". *Chem. Engng Sci.*, **25**, 1818-1820.

Wang, T., Z.J. Lin, C.M. Zhu, D.C. Liu and S.C. Saxena (1993), "Particle velocity measurements in a circulating fluidized bed". *AIChE J.* **39**, 1406-1410.

Wang, Z., D. Bai and Y. Jin (1992), "Hydrodynamics of cocurrent downflow circulating fluidized bed". *Powder Technol.* **70**, 271-275.

Wei, F., Y. Jin and Z. Yu (1993) "The visualization of macro structure of the gas-solids suspension in CFB", 708-723 4th Int. conf. on Circulating Fluidized beds, Sedney, Australia.

Weinstein, H., M. Meller, M.-J. Shao and R.J. Parisi (1984), "The effect of particle density on holdup in a fast fluid bed". In: AIChE Symp. Ser., No.234, Vol.80, 52-59.

Weinstein, H., R.A. Graff, M. Meller and M.J. Shao (1994), "The influence of the imposed pressure drop across a fast fluidized bed", United Eng. Trustees, Inc., D. Kunii and R. Toei, eds, pp.299-306.

Weinstein, H., M. Shao and M. Schnitzlein (1986), "Radial variation in solid density in high velocity fluidization". In: *Circulating Fluidized Bed Technology* (P. Basu, Ed.), Pergamon, Toronto, pp.201-206.

Werther, J. (1993), "Fluid mechanics of large-scale CFB units". In: *Circulating Fluidized Bed Technology IV*, ed. A. Avidan, in press.

Wilson, C. (1972), "Applied statistics for engineers", Applied Science Publishers Ltd., London.

Wirth, K. -E., M. Seiter and O. Mqlerus (1991), "Concentration and velocities of solids in areas close to the walls in circulating fluidized bed systems". *VGB Kraftwerkstechnik* **10**, 824-828.

Wu, R. L., C. J. Lim, J. R. Grace and C. M. H. Brereton (1990), "Instantaneous local heat transfer and hydrodynamics in a circulating fluidized bed". *Int. J. Heat Mass Transfer* **34**, 2019-2027.

Wu, R., 1989, *Heat transfer in circulating fluidized beds*. Ph.D. dissertation, University of British Columbia, Vancouver, Canada.

Yang, Y.-L, Y. Jin, Z.-Q. Yu, J.-X. Zhu and H.-T. Bi (1993), "Local slip behaviors in the circulating fluidized bed". *AIChE Symp. Ser.* **89**, 81-90.

Yang, Y., Y. Jin, Z.-Q Yu, Z. Wang (1990), "Sectional averaged particle velocity profile in low-density circulating fluidized beds". *Chem. Reaction Engng and Technol.* **6**, 30-35.

Yang, Y.-L, Y. Jin, Z.-Q. Yu and Z.-W. Wang (1992), "Investigation on slip velocity distributions in the riser of dilute circulating fluidized bed". *Powder Technol.* **73**, 67-73.

Yerushalmi, J., D.H. Turner and A.M. Squires (1976), "The fast fluidized bed". *Ind. Eng. Chem. Process Des. Dev.*, **15**, 47-51.

Yerushalmi, J. and N.T. Cankurt (1979), "Further studies of the regimes of fluidization". *Powder Technol.*, **24**, 187-205.

Yianneskis, M. (1987), "Velocity, particle sizing and concentration measurement techniques for multi-phase flow". *Powder Technol.* **49**, 261-269.

Yousfi, Y. and G. Gau (1974), "Aerodynamique de l'écoulement vertical de suspensions concentr ées gaz - solides - I. Régimes d'écoulement et stabilité aerodynamique," *Chem. Eng. Sci.*, **29**, 1939-1946.

Zhang, W. and Y. Tung (1991), "Radial voidage profiles in fast fluidized beds of different diameters". *Chem. Engng Sci.*, **46**, 3045-3052.

Zheng, Z., J. Zhu, J. R. Grace, C. J. Lim and C. H. Brereton (1992), "Particle motion in circulating fluidized beds via microcomputer-controlled colour-stroboscopic photography". In: *Fluidization VII* (O. E. Potter and D. J. Nicklin), Engineering Foundation, New York, pp.781-789.

Appendix I

Statistical Methods used to Analyse Voidage and Particle Velocity Data

I.1 χ^2 Test

I.1.1 Theory

The χ^2 test can be used to investigate the variance of the population. To perform the χ^2 test, we compare values E and O drawn from two populations. The value of χ^2 is obtained from

$$\chi^2 = \sum \frac{(O-E)^2}{E} \tag{I.1}$$

where O is an observed value and E is a hypothetical (expected) value.

The calculated value is then compared with tabulated values of χ^2 given in standard statistics texts. At a specified level of significance, if the latter values are not exceeded by the calculated value, it is concluded that it is not possible to reject the hypothesis that the two populations are drawn from the same overall population.

I.1.2. Sample Calculation

Results of voidage measurements for U_g=4.5 m/s and G_s=20 kg/m^{2}s obtained in two different days at both wall and axis of the riser with smooth inner walls at height z=0.79 m above the distributor are shown in Table I.1. Ten samples at duration 60 s for each day were recorded.

Table I.1 χ^2 test for voidage data from two different days at both wall and axis of riser for U_g=4.5 m/s, G_s=20 kg/m^{2}s, z=0.79 m.

	At Wall		On Axis	
	Day 1 (O_{11})	Day 2 (O_{12})	Day 1 (O_{21})	Day 2 (E_{22})
	0.774	0.785	0.955	0.951
	0.793	0.757	0.96	0.945
	0.789	0.762	0.947	0.949
	0.761	0.785	0.957	0.955
	0.763	0.757	0.950	0.953
	0.780	0.782	0.952	0.948
	0.782	0.759	0.954	0.952
	0.764	0.769	0.958	0.950
	0.778	0.760	0.949	0.955
	0.767	0.779	0.959	0.947
Mean (E)	0.775	0.770	0.954	0.950
Standard Deviation	0.0112	0.0120	0.00448	0.00334
Calculated χ^2	0.00146	0.00168	0.00019	0.00011
Value of χ^2 at a significance level of 99%	2.088	2.088	2.088	2.088
Mean (E) of Days 1 and 2	0.773		0.952	
Calculated χ^2	1.62×10^{-5}		8.40×10^{-6}	
Value of χ^2 at a significance level of 99%	1.57×10^{-4}		1.57×10^{-4}	
Conclusion	Over 99% sure that there is no significant difference between ten samples in each day, and data from Days 1 and Day 2,			

The χ^2 test is performed to examine whether there is a significant difference between the two populations.

I.2 t Test

I.2.1 Theory

The t test is generally used to compare the mean values of two small populations (<30) whose variance σ^2 is unknown. Define the random variable t as

$$t = \frac{z}{\sqrt{\chi^2/\nu}} \tag{I.2}$$

$$\text{with} \quad z = \frac{|\mu - \bar{x}|}{\sigma/\sqrt{n}} \tag{I.3}$$

where μ is the population mean; $\bar{x}$ is the sample mean; n is the sample size, σ is the standard deviation, and ν is the number of degrees of freedom = n-1.

It can be shown (Kennedy and Neville, 1986) that from equation (I.2), the following equation can be drawn:

$$t = \frac{|\bar{x}_1 - \bar{x}_2|}{s_d} \tag{I.4}$$

$$\text{where } s_d = s_c\sqrt{\frac{n_1 + n_2}{n_1 n_2}} \tag{I.5}$$

and $$s_c^2 = \frac{(n_1 - 1)s_1^2 + (n_2 - 1)s_2^2}{n_1 + n_2 - 2} \qquad \text{(I.6)}$$

At a certain level of significance, usually 5% (confidence level 95%), if the calculated value of t is greater than the corresponding tabulated value (available in standard statistics texts), it can be concluded that there is a significant difference between the two means, $\overline{x}_1$ and $\overline{x}_2$.

I.2.2 Sample Calculation

The t test is conducted to examine the influence of wall roughness on the particle descending velocities at the wall and on the axis of the riser for U_g=5.5 m/s and G_s=40 kg/m^{2}s at heights of 3.45, 5.13, 6.20, 7.06 and 8.28 m above the distributor. It is shown in Table I.2 that at a confidence level of 95%, wall roughness has no significant influence on particle descending velocity both at the wall and on the axis. However, at a confidence level of 90%, wall roughness is found to influence descending particle velocities on the axis, while having no influence on descending particle velocities at the wall.

Table I.2. t test for particle descending velocities for U_g=5.5 m/s and G_s=40 kg/m^{2}s at wall and on axis of riser.

	Particle Descending Velocity, v_p, at Wall (m/s)		Particle Descending Velocity, v_p, on Axis (m/s)	
Height (m)	Smooth Wall	Rough Wall	Smooth Wall	Rough Wall
3.45	-1.06	-0.92	-1.07	-1.61
5.13	-1.30	-1.34	-1.38	-2.16
6.20	-1.13	-0.99	-1.61	-2.20
7.06	-1.39	-1.08	-1.41	-1.79
8.28	-1.23	-0.83	-1.35	-1.54
ν	4		4	
s_c	0.166		0.256	
s_d	0.129		0.198	
$\lvert\bar{v}_{p1} - \bar{v}_{p2}\rvert$	0.190		0.496	
Calculated t Value	1.58		2.51	
Tabulated t Value for significance level of 10%	2.132		2.132	
Tabulated Value for significance level of 5%	2.776		2.776	
Conclusion	Not significantly different at a confidence level of 90%		Different at confidence level of 90%, while not different at a 95% confidence level	

Appendix II

Comparison Between Measured Lateral Solids Mass Flux and Model Predictions by Senior and Brereton (1992)

A comparison between the measured net lateral solids mass flux for U_g=5.5 m/s and G_s=40 kg/m^{2}s and the results of a semi-empirical hydrodynamic model developed by Senior and Brereton (1992) for risers of circular cross-section is shown in Fig. II.1. The hydraulic radius of the square riser was used in the model calculation. Since secondary air must be introduced in the model calculations, while no secondary air was employed in the experiments, the ratio of primary to secondary air, R_{air}, was set at 9999, i.e. the secondary air was only 0.01% introduced 1 m above the distributor for the predictions shown in Fig. II.1. The model successfully predicts that the direction of the net lateral solids mass flux is outward towards the wall near the bottom, while being inward towards the axis near the top of the riser. While there is reasonable agreement over most of the height, there is a significant difference between the experimental and modelling results near the bottom and the top of the riser.

Tests with R_{air} from 1 to 9999 at a constant total amount of air introduced into the riser show that the predicted net lateral solids flux near the bottom and the top of the riser decreased only by 10%, indicating that the predicted lateral solids mass fluxes near the bottom and the top were insensitive to R_{air}. This is expected because the model considers turbulent flow near the bottom of the riser, while the measurements, as indicated in Chapters 3 and 4, show a core-annulus flow structure even at the very bottom of the square riser. The rapid decrease of the percentage of core over the total cross-sectional area near the bottom and the top of the column appears to be responsible for the high predicted lateral solids mass flux.

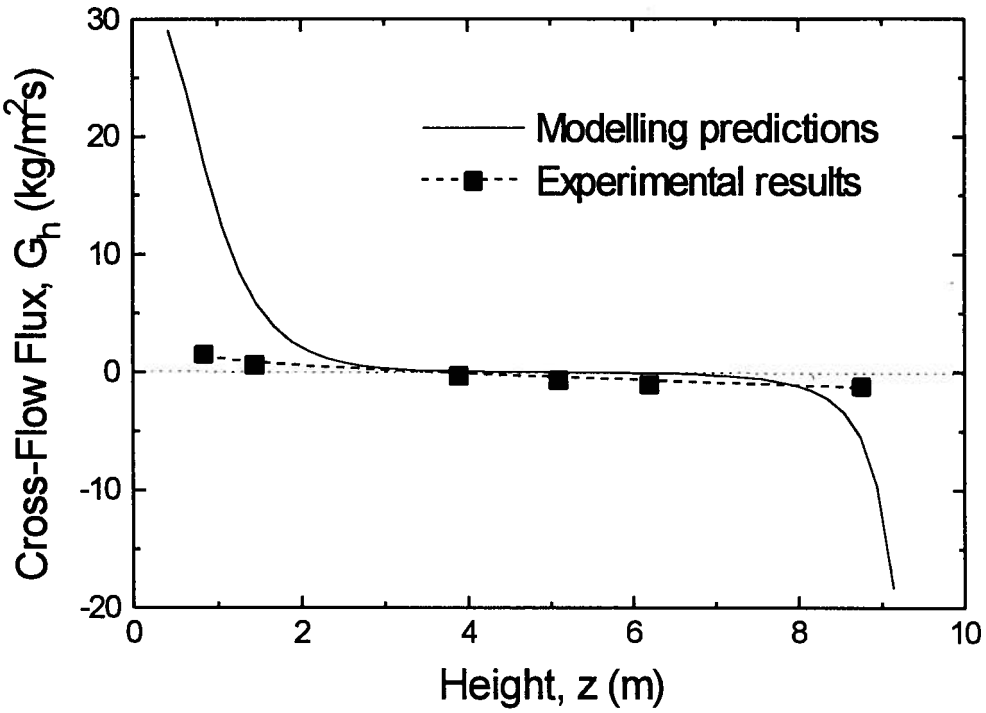

Fig. II.1. Comparison between measured net lateral solids mass fluxes and model predictions by Senior and Brereton (1992) for U_g=5.5 m/s and G_s=40 kg/m^{2}s

Appendix III

Amplifying Circuit and a Sample Trace for the Piezoelectric Probe

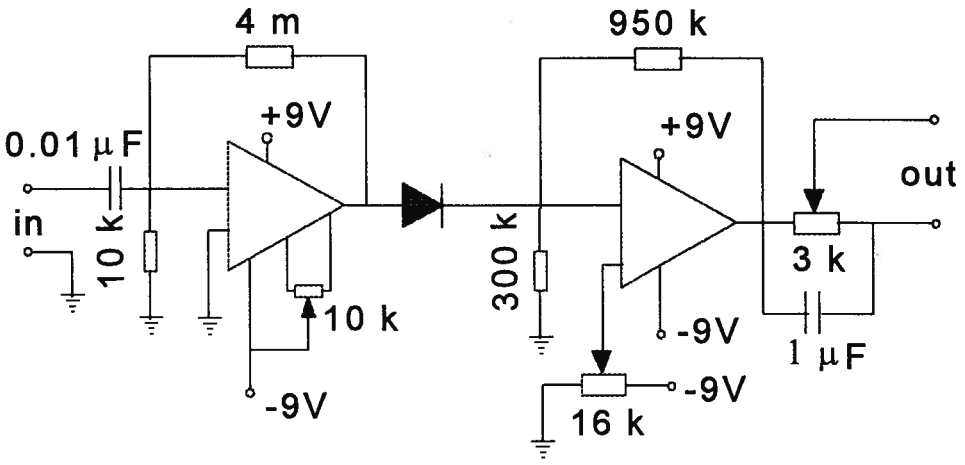

Fig. III.1. Amplifying circuit with input resistance of $10^{12}\Omega$ for the piezoelectric probe.

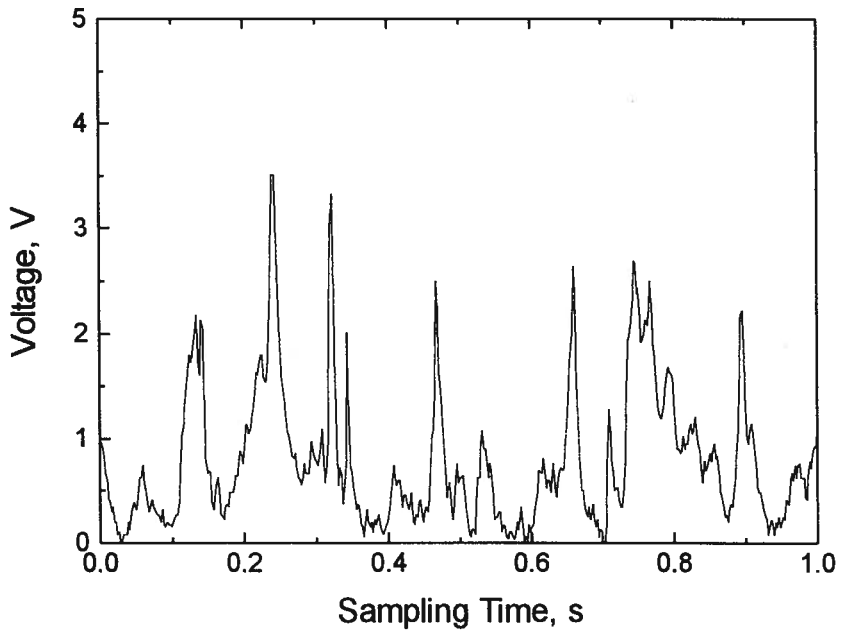

Fig. III.2. Typical trace for piezoelectric probe for U_g=7.0 m/s, G_s=60 kg/m^{2}s, x/X=0, y/Y=0.3 and z=6.2 m.